# Experimental Investigation and Modeling of Integrated Tri-generation Systems

by

Eda Cetinkaya

A Thesis Submitted in Partial Fulfillment
of the requirements for the Degree of

Doctor of Philosophy

in

The Faculty of Engineering and Applied Science

Mechanical Engineering Program

University of Ontario Institute of Technology

Oshawa, Canada

# Abstract

Energy demand in the world is increasing with population growth and higher living standards. Today, the need for energy requires a focus on renewable sources without abandoning fossil fuels. Efficient use of energy is one of the most important tasks in modern energy systems to achieve. In addition to the energy need, growing environmental concerns are linked with energy is emerged. Multi-purpose energy generation allows a higher efficiency by generating more outputs with the same input in the same system. Tri-generation systems are expected to provide at least three commodities, such as heating, cooling, desalination, storable fuel production and some other useful outputs, in addition to power generation.

In this study, an experimental investigation of gasification is presented and two integrated tri-generation systems are proposed. The first integrated tri-generation system (System 1) utilizes solar energy as input and the outputs are power, fresh water and hot water. It consists of four sub-systems, namely solar power tower system, desalination system, Rankine cycle and organic Rankine cycle (ORC). The second integrated tri-generation system (System 2) utilizes coal and biomass as input and the outputs are power, fuel and hot water. It consists of five sub-systems: gasification plant, Brayton cycle, Rankine cycle, Fischer-Tropsch synthesis plant and an organic Rankine cycle (ORC). Experimental investigation includes coal and biomass gasification, where the experimental results of synthesis gas compositions are utilized in the analysis of the second systems.

To maximize efficiency, heat losses from the system should be minimized through a recovery system to make the heat a useful commodity for other systems, such as ORCs which can utilize the low-grade heat. In this respect, ORCs are first analyzed for three different configurations in terms of energy and exergy efficiencies altering working fluids to increase the power output.

Among two types of coal and one type biomass tried in the laboratory scale experimental set-up, Tunçbilek-Ömerler is found to be superior to Konya-Ilgın coal in terms of the highest amount of hydrogen in the synthesis gas composition. As biomass, wheat straw is gasified, which shows higher exergetic efficiency in comparison to Konya-Ilgın coal.

Based on theoretical analysis conducted for the integrated systems, System 2 is found to be more efficient in terms of energy and exergy in comparison with System 1. However, when local needs are taken into account, fresh water can be a desirable useful output where solar irradiation is high. Both systems are compared to conventional and co-generation systems having the same inputs to quantify the improvement in efficiency. System 1 has an energy efficiency of 69% and an exergy efficiency of 58%, whereas System 2 has an energy efficiency of 71% and an exergy efficiency of 73%. When single generation is obtained from the same inputs, it is observed that the energy and exergy efficiencies drop drastically down to 34% and 42% for System 1; 33% and 42% for System 2, respectively.

**Keywords:** Tri-generation, exergy analysis, optimization, solar power tower, gasification, Fischer-Tropsch synthesis

# Acknowledgements

First of all, I would like to express my deep gratitude to my supervisor Dr. Ibrahim Dincer for his patient guidance, encouragement and useful critiques of this research work. I am particularly grateful for the assistance given by Dr. Murat Aydin, not only for his technical knowledge, but also showing me how to differentiate the important things and keep the most basic questions in mind. My grateful thanks are also extended to Ahmet Ozbilen and Sadi Hamut for their help in the analysis process and providing the best social environment I had in Oshawa. I would also like to thank Dr. Calin Zamfirescu, for his advice and assistance in keeping my progress on schedule.

I would like to express my very great appreciation to the people for their help and support during the preparation of this thesis, especially Canan Acar for her contributions on reviewing and formatting.

I would also like to extend my thanks to the kind people working in TÜBİTAK Marmara Research Center, for their help for the experiments, tests and software installation: Dr. Hayati Olgun, Hakan Karatas, Murat Baranak, Omer Faruk Gul, Isil Isik Gulsac, Serhat Gul, Dr. Salih Obut and Yeliz Cetin. This journey would not have been possible without their help and support.

Finally, I wish to thank my father Selim Cetinkaya and my brother Emre Cetinkaya for their support and encouragement throughout my life, their support has been vital, and I shall never forget it.

# Table of Contents

# List of Figure Captions

# List of Table Captions

# Nomenclature

| | |
|---|---|
| A | area [$m^2$] |
| C | seawater reverse osmosis plant capacity [$m^3/h$] |
| C | coefficient |
| E | energy [kJ] |
| $\dot{E}$ | energy rate [kW] |
| ex | specific exergy [kJ/kg] |
| $\dot{E}x$ | exergy rate [kW] |
| g | gravitational acceleration [$m^2/s$] |
| G | Gibbs free energy [kJ] |
| h | specific enthalpy [kJ/kg] |
| H | enthalpy [kJ] |
| I | solar irradiation [$W/m^2$] |
| i | interest rate |
| K | equipment cost coefficient |
| m | mass [kg] |
| $\dot{m}$ | mass flow rate [kg/s] |
| M | molecular weight [kg/kmol] |
| N | number of operation hours in a year [h] |
| P | pressure [kPa] |
| q | specific heat transfer [kJ/kg] |
| Q | heat [kJ] |
| $\dot{Q}$ | heat rate [kW] |
| $R_u$ | universal gas constant [kJ/kmol-K] |
| R | scaling factor |
| s | specific entropy [kJ/kg K] |

| | |
|---|---|
| $S$ | entropy [kJ/K] |
| $\dot{S}$ | entropy rate [kW/K] |
| $t$ | time [s] |
| $T$ | temperature [K] |
| $U$ | overall heat transfer coefficient [W/m$^2$K] |
| $u$ | volumetric-specific energy of the blackbody radiation [kJ/m$^3$] |
| $v$ | volume [m$^3$] |
| $V$ | velocity [m/s] |
| $w$ | weight [N] |
| $W$ | work [kJ] |
| $\dot{W}$ | power [kW] |
| $Z$ | purchase equipment cost [$] |
| $\dot{Z}$ | cost rate associated with the sum of capital investment [$/h] |
| $z$ | elevation [m] |

## Greek Letters

| | |
|---|---|
| $\alpha$ | chain growth probability |
| $\Delta$ | change in variable |
| $\varepsilon$ | emissivity |
| $\mu$ | mole fraction of hydrocarbons |
| $\eta$ | efficiency |
| $\sigma$ | Stefan-Boltzmann constant |
| $\rho$ | mass concentration |
| $\varphi$ | maintenance factor |

## Subscripts

| | |
|---|---|
| 0 | surroundings |
| a | aperture |
| b | boundary |
| c | collector |
| C | Carnot |
| cv | control volume |
| des | destruction |
| Desal | desalination |
| diss | dissipated |
| E | expander |
| e | electricity |
| en | energy |
| ex | exergy |
| f | formation |
| gen | generated |
| HE | heat engine |
| H | high |
| heat | heater |
| in | input |
| k | component |
| L | low |
| max | maximum |
| out | output |
| P | pump |
| Q | heat |

| | |
|---|---|
| R | receiver |
| rev | reversible |
| s | sun |
| Turb | turbine |

## Superscripts

| | |
|---|---|
| 0 | dead state |
| ch | chemical |
| n | equipment lifetime [years] |

## Acronyms

| | |
|---|---|
| ASF | Anderson-Schulz-Flory |
| BTL | biomass-to-liquid |
| CFC | chlorofluorocarbon |
| CHP | combined heat and power |
| CTL | coal-to-liquid |
| DAF | dry ash-free basis |
| DS ORC | double-stage organic Rankine cycle |
| DS ORC-R | double-stage organic Rankine cycle with reheating |
| EES | engineering equation solver |
| ER | equivalence ratio |
| ERD | energy recovery devices |
| FT | Fischer-Tropsch |
| FTS | Fischer-Tropsch synthesis |
| GA | genetic algorithm |
| GCV | gross calorific value |

| | |
|---|---|
| GHG | greenhouse gas |
| GTL | gas-to-liquid |
| GWP | global warming potential |
| HCFC | hydrochlorofluorocarbon |
| HEX | heat exchanger |
| LHV | lower heating value |
| MW | molecular weight |
| NCV | net calorific value |
| ODP | ozone depletion potential |
| ORC | organic Rankine cycle |
| TRC | trilateral Rankine cycle |

# Chapter 1: Introduction

All forms of living organisms rely on an external source of energy to survive. Green plants and some special bacteria undergo photosynthesis by absorbing sun light. Humans and animals need the chemical energy in food combined with oxygen to be able to live and grow. Energy conversion in the body ends up in the form of heat and work.

From keeping houses warm to running a factory, energy is a crucial need of human activity. Billions of people use energy to improve their living standards. While energy demand increases together with population growth and demands for better living standards, climate change raises deeper concerns related to fossil-fuel based energy use. Most countries in the world desperately keep importing resources from very few countries. The economic competition and environmental concerns have lead researchers to find a reliable and affordable solution to this problem. The key points to the possible solution can be summarized as energy efficiency, sustainable development, energy security, and diversity of energy supply.

Energy efficiency offers lower fuel costs, lower investment costs in energy infrastructure, more independency from imported fossil fuels, reduction of greenhouse gas emissions and local air pollution. Efficient use of energy can be adopted in buildings, appliances, transport, industry, and lighting by highlighting the full potential. For example, insulating a house will reduce the cost of fuel and electricity consumption, as well as emissions of flue gas by maintaining the same comfort for residents [1].

In addition to the power and heat produced by co-generation systems, tri-generation systems offer one more useful output from the system, such as fresh water, cooling, hydrogen, drying or fuel. However, it should be noted that the benefit obtained from the additional output should be weighed against the increase in overall cost and emissions of the system. Therefore, it would be beneficial to consider these criteria in the final decision making process.

## 1.1 Importance of Energy

Energy is one of the most important parts of our daily life and makes the existence of ecosystems, human civilization and life itself possible. We carelessly plug in power adapters of appliances like a refrigerator or computer, but what happens before the electricity reaches the power outlets in our homes? Energy related issues are one of the most important problems facing 21st century society. With the advent of industrialization and globalization, the demand for energy has increased exponentially over the past decades.

According to statistics by the International Energy Agency, between 2010 and 2015, the world population is projected to increase 5.6% while the energy consumption is estimated to increase 9.2%. Currently, the world relies heavily on fossil fuels, such as oil, gas and coal, which provide almost 80% of global energy demand [2], to meet its energy requirements. Fossil fuels and limited natural resources that will essentially become extinct are extravagantly consumed [3].

Moreover, coal consumption has also increased significantly over the past years. Altough the share of coal in the world electricity generation is projected to drop from 40% to 36% from 2010 to 2040, it will still be the largest source of total electricity consumption [4]. For example, if electricity access is provided by 2030 to the 1.3 billion people [5] in the world who are currently without power, more than half of the fuel required to provide additional on-grid connections would be generated by coal. In the future however, policies may be developed to encourage more environmentally friendly alternatives through air quality regulations or carbon penalties. If the efficiency of coal-fired power plants is increased by 5% higher than expected, it would result in reduction of global power plant carbon dioxide emissons by 8%. More efficient use of coal would secure the position of coal in the future energy generation mix and reduce the associated impact on climate change.

Energy is a prerequisite for access to safe potable water, where the survival of future generations is tied significantly to its availability and usage. Today, the international community must reflect on, propose and pursue solutions to answer the associated challenges. Through the new solutions that stand out among so many others, it can be seen that water and energy are at the heart of the world’s security in the future [6]. Energy production is expected to double along with a 50% increase in water demand by the year 2050 [7]. In 2010, the United Nations declared that access to clean water and sanitation is a basic human right. On the contrary, 2.6 billion people lack access to basic sanitation, where half of the world population is estimated to be deprived of safe drinking water and basic sanitation by 2015 [8]. Currently, 884 million people do not have access to safe drinking water.

Various countries promote energy efficiency in both energy supply and demand in many areas such as transport, buildings, industry and home appliances. They also take action by utilizing renewable energy sources, including wind, solar and biomass. On the other hand, several developing countries claim that their economies are highly dependent on the production and consumption of fossil fuels, which leads to difficulties in transforming their energy systems into high-efficiency, low carbon emission systems. Thus, specific national circumstances and the level of economic development affect national actions and policies. Biomass and solar energy [9] are examples of further energy-related action rural communities and developing countries can take. The import and export of fossil fuels between countries may also lead to political conflicts, revealing the need for greater energy independence.

In terms of environmental impacts, fossil fuel utilization and cement production are approximated to cause 337 billion metric tons of carbon release to the atmosphere since the industrial revolution in 1760, where half of the overall emissions were released after the mid-1970s [3]. Today, the global population is almost seven times higher than that of 1760 [10].

Up-to-date gasoline and oil prices [11] are shown for selected countries in Figure 1.1. Recent political transitions in the Middle East can be accountad as one of the reasons for the increase in average oil price to $105 per barrel in 2013 [4]. Estimations predict that oil prices will increase to $163 per barrel by 2040. High oil prices are expected to cause changes in consumer preferences for liquid fuels, encouraging the use of less energy, alternative forms of energy, and higher efficiency. To satisfy demand, liquid fuels other than petroleum products are expected to gain importance, such as coal-to-liquid and gas-to-liquid fuels as well as biofuels. The U.S. and Brazil plan to produce biofuels to substitute a portion of petroleum liquids, while China plans to produce liquid fuels by coal-to-liquid processes. Advanced technologies enable liquid fuel production for previously inaccessible regions, where high oil prices make it economically feasible.

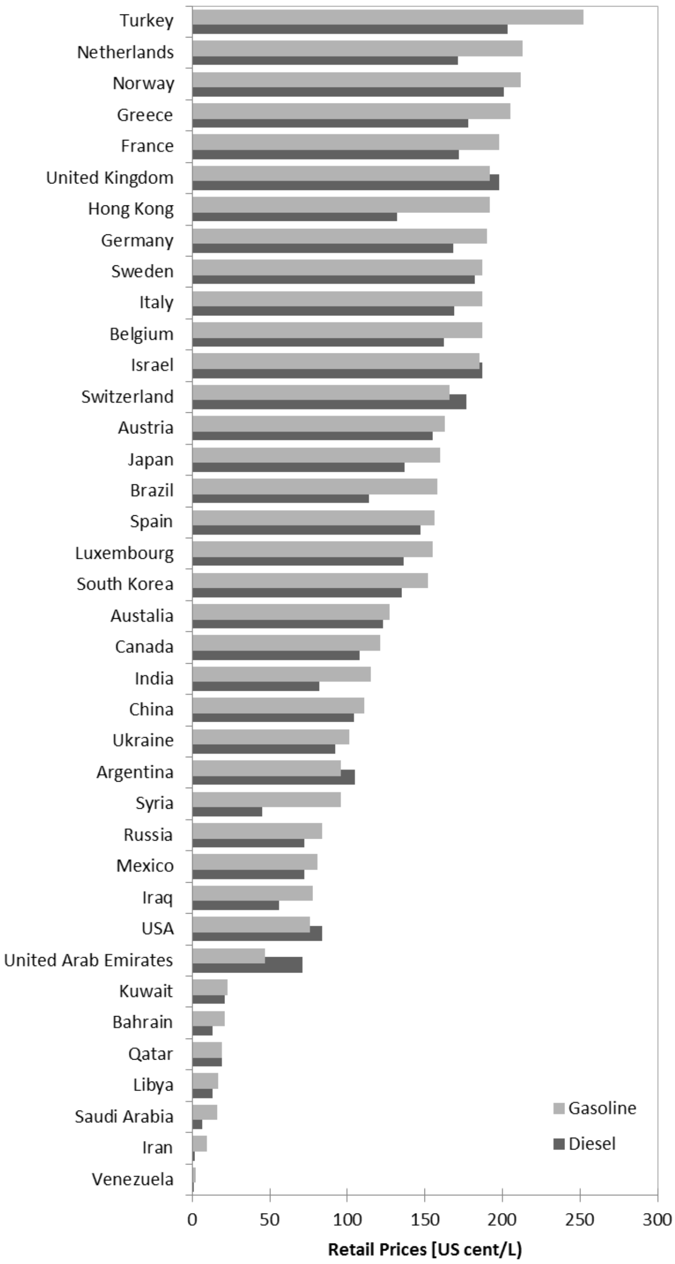

**Figure 1.1** Diesel and gasoline prices of selected countries (data from [11]).

Global warming is a heavily discussed topic mainly because of fossil fuel consumption. Climatic changes driven by human activities (especially greenhouse gas emissions) have significant direct negative effects on the environment and contribute to over 160,000 deaths per year from side-effects associated with climate change, which is estimated to double by 2020 [12].

Thus, based on this pervasive use of global energy resources, energy sustainability is becoming a global necessity and is directly linked to the broader concept of sustainability that affects all of human civilization [13]. This brings importance to renewable energy sources and efficient production and use of energy.

## 1.2 Motivation and Objectives

Energy is an essential part of life for people, communities, countries and the world. Efficient use of energy sources can be a key solution by considering the useful outputs, as well as cost and environmental impact. Tri-gerenation systems draw interest in this regard. In this section, motivation and objectives of this study are demonstrated in both general and specific forms.

### 1.2.1 Motivation

Since the industrial revolution, energy has gained significant importance while the energy comsumption rate has increased considerably. Since then, economic, environmental and technical concerns related to energy have been expressed and significant attention is paid both locally and globally. The cost and environmental impacts of power generation raise concerns about the global future of energy utilization and its effect on the environment, human health and the economy. Solutions such as efficient use of energy and renewable resources have thus become a major option.

Fossil fuels are still the predominant source of power generation; especially coal, which has the highest share among these resources. Coal is the most abundant fossil fuel in the world as well as the most common primary energy source utilized in power plants. It also contributes significantly to greenhouse gas emmisions based on current power generation techniques. Therefore, increasing efficiency and applying low-carbon emission techonologies can reduce the associated environmental impact considerably. Currently, gasification is one of the most promising methods to make use of coal with higher efficiency and lower environmental impact.

Due to strict emmision regulations and concerns related to the environment and human health, renewable energy sources are becoming more popular throughout the world. Solar energy applications are one of the emerging technologies based on its availability, low cost and environmental impact during the operation, especially for off-grid utilization.

Petroleum and gas fields are concentrated in several locations, while the rest of the world depends on a select few countries for access to these resources. This can create problems for economies of countries that lack these resources, or political fragility in between. There are several ways to avoid conflict: more efficient use of oil and gas, producing these fuels by utilizing a carbonaceous feed-stock or utilizing less fuel. Utilizing coal or biomass as feed-stock, gasification followed by Fischer-Tropsch synthesis is an option to produce liquid fuels locally, which can provide independence and perhaps even lower production costs than the price of imported fuels.

1996 Nobel Laureate Prof. Richard E. Smalley claims that energy must take the first place in his prioritized list [14], which consists of the top ten problems facing the world today. Energy is followed by the second problem: water. Billions of people are in need of clean water for drinking and agriculture, as well as sanitation. An increasing population requires new sources of clean water. Our planet has a vast source of water; however it contains salt, which can be separated from water with presence of energy. Thus, the second problem can be solved by utilizing energy, but without cheap energy, desalination and transportation of clean water will raise new economic problems. Thus, the cost of energy is an important parameter in addition to its presence.

Tri-generation plants gained importance recently due to their higher efficiency compared to conventional systems. Utilizing the same amount of an energy source, it is possible to obtain more useful outputs rather than only one and producing several outputs such as gaseous and liquid fuels and fresh water in addition to power and heat.

### 1.2.1 Objectives

The current thesis aims to present first an experimental investigation of coal and biomass gasification, which is very important for countries having low-grade coal supplies and excess biomass. The coal samples are selected such that their carbon and hydrogen content, as well as their higher heating values are different. One biomass sample is also tested to compare its effect on the synthesis gas composition.

Furthermore, two novel tri-generation systems are introduced: The first system utilizes solar energy and the second coal and biomass. The objectives of this study are to model these tri-generation systems thermodynamically to obtain the highest energy and exergy efficiencies for the overall system by altering some key thermodynamic parameters.

The specific objectives of this study are summazrised as follows:

- To carry out experimental analysis for gasification
    - To conduct experiments with various feedstocks as coal and biomass
    - To measure the synthesis gas composition by first monitoring $H_2$, CO, $CO_2$, $CH_4$, $O_2$, and $N_2$ outputs simultaneously, then by taking samples to detect sulfur compounds in a gas chromatograph.
    - To measure temperature, pressure, and flow rate at various points within the system while varying the exccess air ratio by keeping the bed temperature and pressure constant to obtain the best synthesis gas in terms of heating value and hydrogen content.
    - To compare the results with those presented in the literature.
- To conduct a comprehensive energy and exergy modeling of two integrated tri-generation systems
    - Solar power tower system with a steam Rankine cycle, an organic Rankine cycle and a desalination unit.
    - Biomass or coal gasification plant equipped with a combined gas-steam power plant and a Fischer-Tropsch reactor, which yields gaseous and liquid fuels such as methane, gasoline and diesel and some other distillates such as wax.
- To perform energy and exergy analyses of these two systems
    - To develeop an advanced EES code and carry out parametric studies for both thermo-mechanical and chemical exergy contents of the flows.
    - To calculate the exergy flow rate of each stream of the systems including the chemical exergies for the gasification based plant.
    - To determine the entropy generation of each component.
    - To determine the exergy destruction, exergy loss, and exergy efficiency of each component.
    - To analyze the effect of dead state conditions as well as operational parameters such as working fluid selection in ORC design.
- To calculate greenhouse gas emissions as a result of system operation by calculating carbon dioxide emissions and comparing the obtained values with

those of conventional energy systems that produce equivalent outputs separately. The objective is to show the improvement potential by employing tri-generation systems instead of conventional separate units.

# Chapter 2: Literature Review

There are various studies in the literature associated with modeling integrated systems. Tri-generation systems, gasification, desalination, hybrid thermo-chemical hydrogen production cycles, ORC, and ammonia-water based power cycles are considered. This chapter reviews important relevant publications in the literature. Such a review is necessary to validate the originality of the proposed systems in this work.

## 2.1 Tri-generation Systems

Energy systems that generate three useful outputs are known as tri-generation systems. Energy input to these systems can be supplied by one primary source or more. The purpose is to minimize waste energy and improve the sustainability of energy generation. The heat taken from a high temperature process is converted into mechanical work through a heat engine, which has a maximum efficiency equal to the Carnot cycle efficiency. Heat engines must reject heat, which can be made useful by integrating with another system to yield a higher efficiency. Tri-generation systems integrate various devices such as heat engines, heat pumps, refrigeration units, hydrogen production units, and desalination units.

Co-generation and tri-generation technologies provide better use of energy resources, while reducing greenhouse gas emissions compared to single generation of power. This also enables cost effectiveness and independence for some countries that import energy.

Co-generation is encouraged by the European Union by a directive approved by European Parliament in 2004, [15] as a part of their energy efficiency and emission reduction goal. Tri-generation has gained in importance in recent years and is becoming more common in recent publications [16-22].

An international corporation owns a quad-generation technology resulting in a 31 per cent improvement [23] in energy efficiency from 2002 to 2011. The company also targets a further 25% reduction in $CO_2$ emissions by 2015. The quad-generation plant supplies power and steam to produce hot water for production, sanitation and all other purposes, chilled water for refrigeration and air conditioning, and $CO_2$ needed for the company's soft drink production process. Excess electricity is sold to the grid.

Al-Suleiman [24] presented his Ph.D. dissertation on three novel tri-generation systems that are distinguished by the source of the heat input to the ORC and based on solid oxide fuel-cell, biomass, and solar. Electric power production, cooling, and heating were considered as products for each system. The objective of this study was defined as minimization of cost per unit exergy production. The key output parameters considered were energy efficiency, exergy efficiency, net electrical power, electrical–to-cooling ratio, and electrical-to-heating ratio, as well as the amount of carbon dioxide produced. Results show that the solar-tri-generation system has the lowest cost per unit exergy and the lowest air pollution having zero $CO_2$ emissions during operation.

Berger et al. [25] issued a patent in 2010, which proposes a multi-heat source power plant. A low-grade heat source such as a geothermal brine or waste process heat was integrated with solar collectors to provide more efficient utilization of low-medium temperature (70–200°C) sensible heat source fluids in conjunction with relatively high temperature heat sources (thermal oil heated in solar collectors at a temperature of 230°C).

Carvalho et al. [26] designed a tri-generation system to be installed in a hospital to minimize total annual cost and $CO_2$ emissions. Among those systems, the most cost-effective and the most environmentally benign were then compared to each other and one configuration was selected that meets the optimum criteria. Based on the size of the hospital and its geographical location, they assumed the annual electricity consumption, the cooling demand and the heat requirements. They ended up with several configurations, in each case, an inversely proportional relationship was observed with emission reduction and cost-effectiveness.

For a tri-generation system, it is very important to define the efficiency that represents all outputs and inputs in the most appropriate way. Exergy quantities can be added in terms of input and output to calculate the overall system efficiency. However, how can the efficiency be defined to also represent the desalination branch of an integrated system? Exergy of desalinated water at dead state temperature would be zero, which inaccurately represents the fresh water output. Therefore, one possible approach can be defined as cost equivalent ratio of outputs over inputs [27]. Alternatively an equivalent pollutant emission per unit product for grading the environmental impact of the system can be proposed not only to present each sub-system but also to compare different multi-generation systems.

An environmental impact indicator to show effectiveness of $CO_2$ emission reduction was proposed by Mancarella and Chicco [28] to assess the greenhouse gas (GHG) emissions caused by trigeneration and cogeneration systems. They compared the obtained results with conventional systems that produce the same outputs separately. They concluded that greenhouse gas emissions can be reduced by 20–35% relative to conventional systems.

In a model developed by Chua et al. [29], cooling, heating and power needs of a commercial building are supplied simultaneously by a trigeneration system. Four key sub-systems are employed: photovoltaic-thermal, solar-thermal, fuel cell, and microturbine and absorption chiller-water system. Auxiliary prime movers are designated to be an alkaline fuel cell, a photovoltaic-thermal panel and solar-thermal collectors. A multi-criteria analysis approach is adopted in terms of operation cost reduction, energy saving, and minimum environmental impact. They calculated the optimum configuration of prime mover utilization ratios that yield the lowest operation cost, maximum energy savings, and minimum carbon dioxide emissions.

Another trigeneration system for buildings was proposed based on biomass for cooling, heating and electric power generation applications in [30]. They considered a gasification system utilizing willow chips, miscanthus and rice husk as biomass fuel. Their results showed that if the power/heat ratio is in the range of 0.5 and 0.75, a trigeneration system with a biomass gasifier would be beneficial to the building system. It was economically feasible but slightly more expensive than conventional options.

The review on related literature has shown that the proposed systems in this work are original and have not been examined before.

## 2.2 Key Systems

In this section, the key systems addressed in the theoretical analysis part are explained. These systems are namely Rankine cycles and solar tower system. As

Rankine cycles, two sub-sections are covered as organic Rankine cycles and ammonia-water based power systems.

### 2.2.1 Rankine Cycles

Steam is the most common working fluid emloyed in a Rankine cycle for coal plants, nuclear plants, or natural gas plants due to its availability, low cost and high enthalpy of vaporization. On the other hand, when the highest temperature in the cycle is lower, some alternative working fluids are possible. In Section 2.2.1, Rankine cycles are discussed, in which alternate organic fluids and ammonia-water mixtures are employed as working fluids instead of steam.

#### 2.2.1.1 Organic Rankine Cycle

In this section, a number of recently published papers and theses that study different types of thermodynamic optimization of Rankine cycles with various working fluids and ammonia-water based power cycles and conversion of scroll compressor into expander are reviewed. The first section describes the main characteristics that affect the organic Rankine cycle. It is essential to study a broad range of properties, conditions, phenomena, and specifications of different thermophysical aspects that affect the overall performance of a particular system application used for electricity and hot water production from low-grade heat. Taking exergy efficiency as the objective function, Dai et al. [31] optimized an ORC for waste heat recovery with different working fluids. The analysis was made based on a genetic algorithm method. The results show that organic fluids, especially R236EA exhibit better performance compared to water for waste heat recovery systems. The best results were obtained when having saturated vapour at the turbine inlet.

ORC can be used in ranges of a few kW up to 1 MW. Schuster et al. [32] presented a study on the efficiencies of three different sized Rankine cycles: solar desalination plant with an electrical power of 3 $kW_e$, a micro-CHP plant with an electrical power of 100 $kW_e$ and a waste heat recovery from biogas digestion plant with an electrical power of 537 $kW_e$. For low cost, decentralized applications, ORC was found to be an appropriate solution.

Choosing the most appropriate working fluid for the ORC can be very advantageous for the specified heat source level. Various working fluids are considered and compared in [33] concerning their heat transfer capacity and exergy loss plus destruction to reach the maximum system efficiency. The system efficiency can be increased 8% by varying the mentioned supercritical parameters. For 150°C, the best thermal heat transfer capacity was obtained with iso-butene.

In a recent study [34], micro-organic Rankine heat engines were analyzed to identify the engine with the highest exergetic efficiency for driving a small scale reverse osmosis desalination system driven by a heat source at a temperature below 100°C. The method was built based on the combination of exergy flow graphs, exergy loss graphs, and thermoeconomic graphs that consider three working fluids: R134a, R245fa and R600. Evaporator, turbine and mixing units are the most critical components. However, modification of the simple Rankine cycle did not seem like an attractive option due to the economic disadvantages for heat sources below 100°C.

Utilizing waste heat of an operational power plant located in India, flue gas at 140°C was utilized as a heat source for the optimization study by Roy et al. [35]. R-12, R-123, and R-134a are investigated to find the best working fluid for the corresponding heat source temperature. Four units were under operation, each having a 210 MW power capacity. R-123 was found to be the best option among all in terms of work output with energy and exergy efficiencies of 25.3% and 64.4%, respectively. The optimum turbine inlet pressure was calculated to be 3.435 MPa, when the optimum work output was obtained with two phase flow in the turbine. To keep the working fluid dry, the turbine inlet pressure was corrected to 1.945 MPa. The higher the pinch point, the lower the exergy efficiency. The pinch point for the selected fluid was 5°C.

Rayegan and Tao [36] investigated the best working fluid option for solar organic cycles to obtain the maximum energy efficiency. The REFPROP 8.0 database with 117 organic fluids is considered with similar working conditions. Benzene and toluene showed the highest thermal and exergetic efficiencies both for 85°C and 130°C. The energy and exergy efficiencies of the collector can increase 30% and 5%, respectively. For the selected source temperatures, higher molecular complexity resulted in higher regenerative cycle efficiencies except for cyclohydrocarbons.

A vehicle engine emits nearly 40% of thermal energy with engine exhaust gas and converts only 30% into useful work. The rest of the fuel combustion energy is spent for the coolant system and convection as well as radiation from the engine block. Considering the amount of loss, Wang et al. [37] aimed to recover this waste heat into useful work using an ORC cycle, which can be operated with different working fluids. Nine different pure organic working fluids were selected based on their evaporating pressure and condensing temperature in the thermodynamic model built in MatLAB together with REFPROP. Net power output was set to a constant value of 10 kW using a single screw expander for heat recovery. Safety and environmental impacts were also considered in the analysis. The performances of R11, R141b, R113, and R123 are found to be slightly higher than others. Greater thermal efficiencies were achieved at lower condensing temperatures and higher evaporating pressures. Condensing temperature of the fluid should be selected so that it reaches the ambient temperature to gain the highest exergy efficiency. R245fa and R245ca were found to be the most suitable working fluids based on their safety levels and environmental impacts.

Energy recovery from low grade heat sources can be accomplished by employing ORC. Quoilin et al. [38] present a transient model, which is able to represent part-load operation and start and stop procedures. The optimized model led an overall waste heat recovery efficiency of 6.6% for the defined heat source, which was mainly due to heat exchanger performance. In the parametric study, three variables were proposed: a constant evaporating temperature, an optimized evaporating temperature depending on the actual working conditions, and a pump speed based on the expander speed. The findings showed that the greatest influence on the efficiency is caused by evaporating temperature regulation.

Mathematical models for the expander, evaporator, air cooled condenser and pump are developed to uncover the best operational conditions of an ORC utilizing R134a as working fluid by Sun and Li [39]. Several important parameters were taken into account such as working fluid mass flow rate; air cooled condenser fan air mass flow rate, and expander inlet pressure to obtain the optimal set of operating variables. Higher inlet pressure led to a higher system thermal efficiency but depends on the properties of the working fluid and the investment cost. The flow rate of the air at the inlet of the condenser fan had a lower impact on the net-work output than the working fluid mass flow rate. Both of these quantities need to be increased when increasing the heat source temperature.

A low-temperature (i.e. 80–100°C ) binary geothermal power system [40] was optimized with a program written in MatLAB using five indicators: thermal efficiency, exergy efficiency, recovery efficiency, heat exchanger area per unit power output and the levelized energy cost. Considering the same source and sink temperatures, optimized internal operation parameters were determined for different working fluids. While R123 yielded the highest thermal and exergy efficiencies in a sub-critical ORC system, R125 was found to be the best choice for a supercritical cycle in terms of efficiency and cost effectiveness, as well as excellent economic and environmental performance. Although R41 showed favourable performance, its flammability was a matter of safety concern.

Quoilin et al. [41] presented a paper on a small scale ORC in a waste heat recovery application by predicting the cycle performance with different working fluids and different component sizes. R245fa, R123, n-butane, n-pentane, R1234yf, and Solkatherm were considered as possible working fluid alternatives to find out which one among all is the most beneficial for thermodynamically and economically. The results showed that n-butane provided the largest cost effectiveness with an energy efficiency of 4.47%, while the thermodynamic optimum is obtained for the same fluid with an overall efficiency of 5.22%. The combination of both criteria can lead to a different selection of the working fluid. The cost of the expander and the evaporator can be reduced by a higher evaporating temperature, which causes a greater high-pressure vapour density. On the other hand, high density working fluids require larger component sizes, which lead to higher investment costs that cannot be seen through the specific investment cost approach.

Available low-temperature heat resources for ORC are: solar energy, geothermal energy, biomass products, surface seawater, and waste heat from various thermal processes. In their review paper, Tchanche et al. [42] presented existing applications of solar thermal electricity, solar thermal driven reverse osmosis desalination (Solar ORC-RO), duplex-Rankine cooling, solar pond power systems, ocean thermal energy conversion (OTEC), biomass combined heat and power plants (CHP), binary geothermal systems and low-grade waste heat recycling (ORC-WHR) from thermal devices and processes. Waste heat recycling was a promising method among them.

Kanoglu and Bolatturk [43] and DiPippo [44] analyzed a geothermal power plant that has a temperature of around 150-160°C, which was operational for ORC cycles. Both studies presented results on exergy efficiencies. DiPippo concluded that an ammonia based working fluid with the same inlet temperature as the ORC had a 5% larger exergetic efficiency. Kanoglu and Bollaturk [43] altered condenser pressure, turbine inlet temperature and pressure values to see their effect on exergy efficiency and work output. Low condenser pressure, low turbine inlet pressure and high turbine inlet temperature yielded a higher exergetic efficiency that was calculated for isobutene used in a binary geothermal plant.

#### 2.2.1.2 Ammonia-water Based Power Cycles

In this section, the possible optimization characteristics that have influence on the efficiency of ammonia-water cycles were reviewed.

**Table 2.1** Some candidate replacements for CFC and HCFC.

| Natural refrigerants | ODP[1] | GWP[2] |
|---|---|---|
| Air | 0 | 0 |
| Water | 0 | 0 |
| Ammonia | 0 | 0 |
| Carbon dioxide | 0 | 1 |

[1] Ozone depletion potential, taking reference value as R11=1

[2] Global warming potential, taking reference value as $CO_2$=1

As given in Table 2.1, ammonia is one of the candidate replacements for CFC (chlorofluorocarbon) and HCFC (hydro chlorofluorocarbon) regarding environmental concerns on their ODP and GWP. Ammonia has zero ODP, as well as zero GWP [45].

The ammonia-water based Rankine cycle technology can play an important role, in particular for the following objectives:

- It can have a beneficial effect on the energy intensity of industrial processes, mainly by recovering waste heat.
- It can decrease electricity and natural gas bills of dwellings.
- It can be applied to off-grid houses to provide electricity and hot water by using geothermal or solar heat.
- It can be used to convert renewable heat sources (mainly geothermal, biomass and solar sources) into electricity.

Goswami [46] proposed a 5 $kW_e$ combined power/cooling cycle that utilizes a binary ammonia/water working fluid. The cycle can be driven by renewable sources such as simple solar collectors that can provide the power needed to operate an electrolyzer and liquefier [47]. This method could extract more energy from a renewable source than those utilizing wind electricity and solar photovoltaic. The expander efficiency had a significant influence on the overall cycle efficiency. For a healthy expander selection several parameters should be considered: operating pressures and temperatures, flow rate of ammonia vapour and material compatibility with ammonia. The corrosive properties of ammonia require the use of compatible materials such as steel or aluminum instead of widely available materials such as copper, brass, and bronze. Emphasis was given to a scroll compressor that was converted into an expander. The results showed that the conversion affects expander efficiency adversely by allowing more leakage around the scroll tips. Low friction material was needed for improving the expander efficiency.

Zamfirescu and Dincer [48] made a thermodynamic assessment of a novel ammonia-water Rankine cycle used for power production purposes. In their system, the exergy content transferred from a 150°C heat source can be extracted with more efficiency through the use of ammonia-water as working fluid. Expander efficiency, ammonia concentration and the coolant flow rate was optimized to acquire the highest power output. The optimization resulted in a cycle efficiency of 30% by obtaining the highest heat recovery. On the other hand, use of steam under the same operation conditions resulted in an energy efficiency of 23%. They had taken into account that some friction losses cause a pressure drop within the cycle as well.

Wagar et al. [49] investigated the thermodynamic performance of an ammonia-water Rankine cycle for power production and heating by varying the source temperature in the range of 75-350°C, ammonia concentration up to 0.5 and the pump outlet pressure between 0 to 250 bar. The cycle energy efficiencies were obtained between 5 to 35%, where the Carnot efficiency limits the maximum efficiency at 65%.

Kim et al. [50] presented a comparative study on ammonia–water based Rankine and regenerative Rankine power generation cycles by varying ammonia mass concentration. The most important consideration was on the system temperature distributions of fluid streams in the heat exchange devices, where other important system variables were defined as net work production, mass flow rate of working fluid, and the energy and exergy efficiencies. Increasing turbine inlet pressure narrowed down the lowest workable ammonia concentrations. They concluded their work that regenerative cycles show better performance than those without regeneration in general.

### 2.2.2 Solar Power Tower

The exergy efficiency of solar systems can be calculated through numerous different methods [51]. In this regard, Petela [52] stated that the exergy of solar radiation determines the maximum work that can be extracted from an isotropic blackbody radiation enclosed in a deformable volume with perfectly reflecting walls. The theory was founded on the adoption of a photonic model of the electromagnetic radiation and on the assumption that the photon gas can be described with the kinetic theory of monoatomic gases. One of the major outcomes of this theory is that it showed that if the enclosed radiation is initially at temperature $T_1$, higher than the ambient temperature $T_2$, then the maximum work delivered by the system to achieve the dead state 2 corresponds to an isentropic expansion of the photonic gas, and it is

$$w_{1-2} = u_1\left[1 - \frac{4}{3}\frac{T_2}{T_1} + \frac{1}{3}\left(\frac{T_2}{T_1}\right)^4\right] \tag{2.1}$$

where $u_1$ is the volumetric-specific energy of the blackbody radiation in state 1.

As discussed elsewhere [53, 54], it is usually assumed that at the initial state the volume is filled with solar radiation at temperature $T_1$≅6000 K and that $T_2$≅298K is the ambient temperature at the Earth's surface. Here, the ratio $\eta_{\mathrm{P}} = w_{1-2}/u_1$ is very similar to that of Carnot efficiency for heat engines.

For example, if $T_1$=6000 K and $T_2$=298 K, one can determine that $\eta_{\mathrm{P}}$ = 0.93. However, as argued by Bejan [55] dividing the expansion work $w_{1-2}$ with the specific-volumetric internal energy of the photonic gas does not represent a heat engine efficiency in the sense commonly accepted in engineering thermodynamics but rather is a non-dimensional representation of the work introduced by Equation (2.1).

The exergy of solar radiation can be calculated differently through devising a heat engine that converts the incident radiation at source level into heat while the heat sink is the terrestrial atmosphere. This approach has been analyzed, e.g., by [56-58].

The model would require a reversible heat engine connected with a solar collector at the source side. In [56-58], it would be a safe assumption to take the sun as the only thermal contact with the solar collector. Therefore the heat flux input per unit of collector area is $\sigma(T_S^4 - T_C^4)$, where $\sigma$ is the Stefan-Boltzmann constant, $T_S$ is the sun temperature and $T_C$ is the collector temperature. Consequently, the shaft work produced by the reversible heat engine per unit of collector area is:

$$W_{rev}^{"} = \sigma(T_S^4 - T_C^4)(1 - T_0/T_C) \tag{2.2}$$

There is an optimal collector temperature [56-58] that maximizes the work generated by the Carnot cycle, $W_{rev}^{"}$. For example, for $T_0$=298 K and $T_S$=6000 K, the calculated optimum collector temperature is $Tc$=2541 K [51] and the corresponding maximum work (that is the exergy from solar radiation in the assumed system) is $W_{rev}^{"}$=62.8 MW/m$^2$. Although it is conceptually correct, the value of the predicted result shows that this model may not seem to be practical for calculating the maximum work from the insolation. The incident radiation flux on the terrestrial surface is on the order of 1 kW/m$^2$; therefore the exergy of this flux must be of the same order of magnitude.

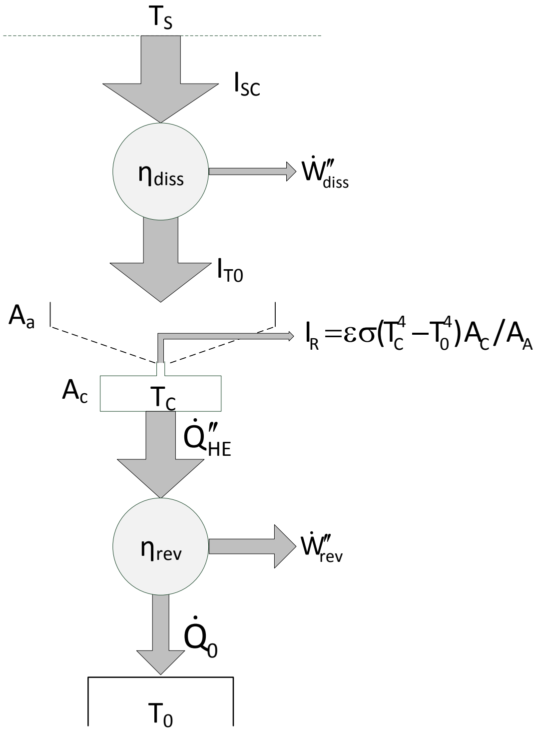

**Figure 2.1** A thermodynamic model to extract maximum work (exergy) from solar radiation (modified from [51]).

If the hot end of a heat engine were connected to the solar surface at temperature $T_S$ (using a resistance free energy transportation media) then the maximum work extracted from the sun is given by the Carnot approach as:

$$\eta_C = 1 - T_0/T_S \tag{2.3}$$

where $T_0$ is the temperature of the Earth's surface as the sink temperature.

Generally, the aforementioned model, which is conceptually correct, would not produce the right results in reality since the process is intrinsically irreversible due to the transport of solar energy through radiation [56].

The thermodynamic model proposed in Figure 2.1 is intended to consider the coupling between the atmosphere as a work and heat dissipater, and a terrestrial heat engine producing useful work from solar energy. According to this model, the solar radiation hits the outer shell of the terrestrial atmosphere with an intensity given by the solar constant $I_{SC}$ and sun temperature $T_S$. The dissipation effects in the terrestrial atmosphere can be modeled with an irreversible thermodynamic cycle with the efficiency $\eta_{diss}$, running as a brake (this means that all the produced work is dissipated). The atmosphere, i.e., the "brake," operates between the sun temperature and the temperature of the solar collector, $T_C$.

For a sun tracking collector, one can indicate the intensity of the insolation in the direction normal to beam radiation with $I_{T0}$. Since the collector points to the sun, $I_{T0}$ denotes the maximum value of the solar flux that can be received. With reference to Figure 2.1, the energy balance at the level of the concentrating solar collector can be written as follows [51]:

$$I_{T0} = Q_{HE}^{"} + I_R \tag{2.4}$$

$$I_R = \varepsilon\sigma(T_C^4 - T_0^4)A_C/A_a \tag{2.5}$$

where $I_R$ is the energy flux reradiated from the small spot area of the solar receiver and $Q_{HE}^{"}$ is the heat flux delivered by the solar collector to the heat engine. $I_R$ as well as $Q_{HE}^{"}$ are calculated with respect to per unit of aperture area $A_a$ of the solar collector.

The main role of the solar concentrator is to minimize the area of the solar receiver $A_c$ with respect to the aperture area $A_a$. This methods is utilized to reduce heat losses through radiation with respect to the useful heat flux $Q_{HE}^{"}$. An alternative way to reduce $I_R$ (which can be deduced from Equation 2.4) is by selecting a receiver surface material low emissivity ε. Thus, the purpose of a good designer would be to devise the solar collector by adopting a concentration ratio $A_a$ /$A_c$, and a material (ε) and a thermal insulation such that $I_R \ll Q''_{HE}$ or $Q''_{HE} \approx I_{T0}$ [51].

$$\eta_{diss} = \frac{W_{diss}}{I_{SC}} = \frac{I_{SC} - I_{T0}}{I_{SC}} \tag{2.6}$$

$\eta = 1 - \frac{T_0}{T_S}\frac{I_{SC}}{I_{T0}}$ (2.7)

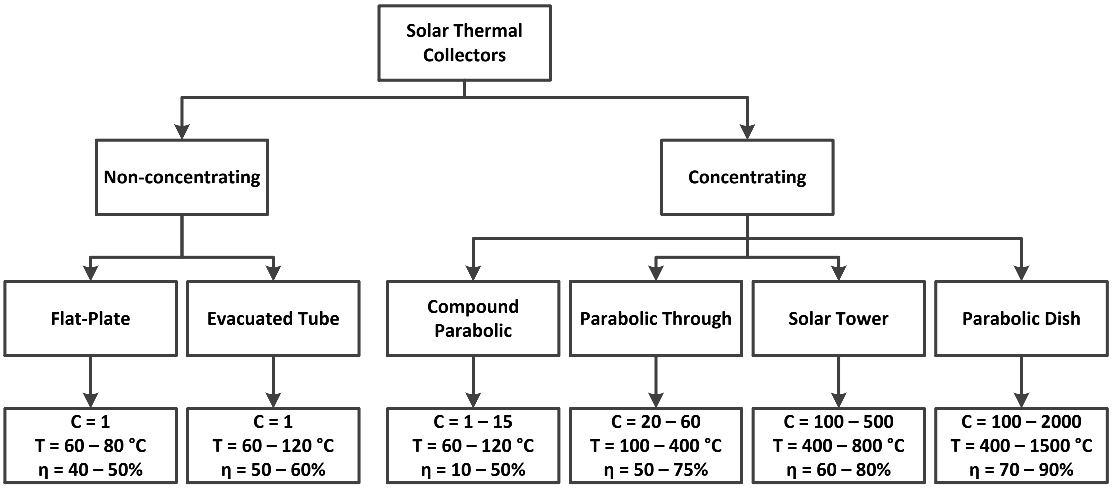

**Figure 2.2** Types of solar thermal collectors (modified from [27]).

Among the renewable technologies utilized for large-scale power production shown in Figure 2.2, concentrating solar thermal power (STP) is one of the most modular and convenient technologies available today. These are one of the most promising systems for producing solar electricity by focusing concentrated solar radiation on a heat transfer fluid to produce heat energy, and then change it to electricity in a conventional generator. This reflection and concentration of the direct solar radiation is done by a field of large mirrors onto a receiver located at the top of a tower. The system uses hundreds to thousands of sun-tracking mirrors called heliostats to reflect the incident sunlight onto the receiver, where the thermal energy is collected in a heated fluid and then the high temperature fluid is transferred to the steam generator through pipes to produce high pressure and super-heated steam to power a conventional high-efficiency steam turbine to produce electricity. These systems are currently being used to generate clean electricity over 20 $MW_e$ and are being built to increase the production up to 100 $MW_e$ and are expected to reach even 300 $MW_e$ in the near future.

Figure 2.3 shows a simple representation of a solar power tower system that consists of a molten salt thermal storage system. Xu et al. [59] present a theoretical framework for the energy and exergy analysis of solar power tower systems (using molten salt as the heat transfer fluid) and identified the thermodynamic losses in each component and determined the overall efficiency of the system. They had taken several design parameters including direct normal irradiation, the concentration ratio, and the type of power cycle in order to evaluate their effects on the energy and exergy performance of the system. They had determined that the efficiencies of the receiver as well as the overall system can be increased by increasing the direct normal irradiation and the concentration ratio. Moreover, the authors had concluded that the overall energy and exergy efficiencies of the system can be increased by integrating advanced power cycles including reheating and supercritical Rankine cycles.

In addition, Yang et al. [60] conducted further studies on solar thermal power systems using numerical simulation studies on the heat transfer characteristics of the tube receiver. They had found that the temperature distribution of molten salt and tube wall are very uneven whether in an axial or radial direction and the temperature of the inner tube wall is an important parameter for preventing the decomposition of molten salt and that the heat flux of the heating surface increases with the increase in velocity.

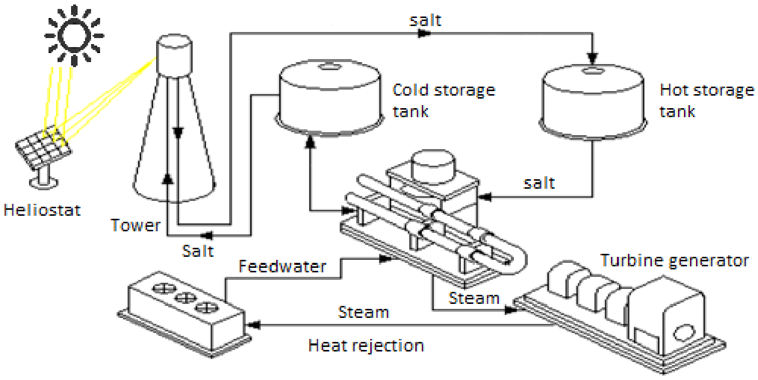

**Figure 2.3** A simple representation of solar power tower (modified from [61]).

Finally, Collado and Guallar [61] stated that, in spite of a system’s higher thermodynamic efficiency (due to higher temperatures in a central receiver), the complex optimized design of heliostat fields and the technical difficulties associated with expensive central receivers and scale-up problems may lead to some delay in the full establishment of tower systems compared to parabolic trough systems.

## 2.3 Key Processes

In this section, recent and fundamental studies in the literature on the key processes of the theoretical analysis part are provided. These systems are namely desalination, gasification and Fischer-Tropsch synthesis.

### 2.3.1 Desalination

Desalination of seawater has become a widely accepted process for procuring fresh water. However, it still requires intensive energy, which is the key parameter affecting the cost. The cost of desalination depends on capacity and type of facility, energy use, feed water, location, labour, and concentrate disposal. The most common methods for desalination are reverse osmosis, multi-stage flash distillation (accounting for 85% of production worldwide) [62]. The locations experiencing water shortages usually have significant solar energy resources, which can justify use of solar energy for desalination process.

Desalination technologies can be classified into two main groups based on their separation mechanism: thermal and membrane based technologies [63]. Thermal desalination technique requires evaporation and condensation to separate salt from water, where, on the other hand, membrane desalination technique requires utilizing a membrane through which water diffuses and the salts are almost completely retained. Desalination technologies can be classified as below [34]:

- **Thermal desalination Technologies**
  - Multi-stage flash distillation
  - Multi-effect distillation
  - Vapor compression distillation
- **Membrane desalination technologies**
  - Reverse osmosis
  - Nanofiltration
  - Electrodialysis

Among these, the most common technologies are reverse osmosis and multi-stage flash. Energy source, plant size, technology, feed water salinity and required product quality affect the cost of water produced. [64].

Reverse osmosis (RO) is a pressure driven separation through certain semi-permeable polymers. Their permeability is low for dissolved substances, whereas they are very permeable for water. The water in the feed flow is forced to permeate through the membrane by applying a pressure difference across the membrane. High feed pressure is required to overcome the feed side osmotic pressure, which varies from 15 to 25 bars for brackish water and 60–80 bars for seawater [63]. The steps of the process can be given as follows: pre-treatment, pumping, membrane separation, brine energy recovery and post-treatment. [65].

Recent applications on solar desalination processes are small-scale and decentralized. On the contrary, concentrating solar power plants are suitable for large scale desalination. From an environmental point of view, it can be utilized as an alternative source of fresh water to prevent over-exploitation of groundwater. It can be useful either by thermal or membrane process with volumetric flow rates up to several 100,000 $m^3$/day. It is expected that in twenty years, energy from solar thermal power plants will become the least expensive option for electricity generation (below 4 ct/kWh) and desalted water (below 0.4 €/$m^3$) [66].

Brine can be separated completely from the water, which creates the opportunity of no brine discharge. Renewable sources can be adopted to provide zero carbon dioxide emission for the operation. Fernández-López et al. [67] carried out a study utilizing both wind and solar energy for desalination in two steps: distillation and mechanical vapor compression. Desalted water flow rate has taken into account as 100 $m^3$/h, which resulted in a price of 0.59 €/$m^3$.

Sharqawy et al. [68] conducted a study on exergy analysis of a desalination plant. First, they defined a dimensionless exergy ratio and checked how it is affected by three parameters by changing one of them and keeping the others constant. These alterations were made in $P/P_0$ (1-5), $z/z_0$ (5-50), $T/T_0$ (1-5). They took dead state properties as $T_0$=25 C, $P_0$=1 atm, and mass fraction of the salt as $w_0$=0.035 kg/kg. Their results showed that under these conditions, the plant operates with an exergy efficiency of 7.65%.

Penate and Garcia-Rodriguez [69] analyzed technical and thermoeconomic energy optimization of an existing sea water reverse osmosis desalination plant with energy recovery devices (ERD). ERD decrease specific energy consumption, which can be installed in existing plants. Lowering the energy cost can be advantageous especially in the countries where energy prices are high. Pelton turbines and isobaric energy recovery turbines have 85-90% and 90-97% efficiency, respectively. They had analyzed constant capacity configuration with Pelton and isobaric ERD to calculate which gives the best energy efficiency. Energy cost savings were also taken into account.

### 2.3.2 Gasification

Due to both worldwide and governmental concerns on sustainable power generation, environmental legislations limit the environmental impact of the coal fired combustion systems; encouraging clean coal combustion technologies. Fluidized bed combustors (FBC) offer less emissions and more efficient energy generation with increasing utilization rate. Countries such as Turkey that have a significant reserve of low quality lignite have great interest in clean combustion technologies. Turkish lignites have high ash, volatile matter and sulfur content, which draw a non-feasible picture for conventional combustion techniques.

Thermochemical biomass conversion technologies can generally be divided into three main categories: combustion, pyrolysis and gasification. In the review article of Saidur et al. [70], it was concluded that the most effective method for converting biomass is gasification.

Gasification allows the conversion of various organic feed such as wood, agricultural residues, peat, coal, anthracite, oil residues and municipal solid waste into syn-gas, bio-oil and bio-char. Co-gasification of coal with biomass can be beneficial for several reasons: high oxygen content of biomass results in less external oxygen addition to the process. Biomass contains less ash, sulfur and nitrogen compared to coal. However, biomass has a relatively low calorific value than coal, which is not desired in the gasification process. In practical applications, biomass may be advantageous than coal in kinetic reactions regarding carbon decomposition at the same bed temperature [71].

In order to optimize the co-gasification of coal and biomass process several parameters can be varied such as feed particle sizes and the ratio of biomass to coal. Mixtures of coal and biomass have a synergistic effect regarding ash formation and harmful emissions. de Jong et al. [72] presented an experimental study on a pressurized bubbling fluidized bed gasifier that operates at a maximum pressure of 10 bar and with a maximum thermal capacity of 1.5 MW. Lower air fractions and reduced air velocity yielded a higher conversion ratio.

Gasification results in higher hydrogen content in the syn-gas when steam/fuel ratio is equal to 0.4-0.6, where 900 K was found to be the temperature results in highest hydrogen concentration [73].

Howaniec et al. [74] presented an experimental study that takes place at atmospheric pressure in a fixed bed reactor. Hydrogen concentration in the syn-gas varies between 59-67 vol. % in respect with temperature and biomass/coal mass ratio (w/w %). The highest volume of hydrogen was generated with 20/80 biomass/coal mass ratio at 900°C.

In another experimental study, Vélez et al. [75] investigated co-gasification of Colombian coal and biomass in a fluidized bed reactor. For a bed temperature of 800°C, the highest volumetric hydrogen concentration was obtained with 15% (w/w %) rice husk, where at 900°C 6% coffee husk is gasified with the highest volumetric hydrogen concentration. Carbon monoxide was measured to be 11% (v/v %) in the syn-gas.

Karatas et al. [76] investigated solely coal gasification as well as coal mixed with calcined dolomite in a bubbling fluidized bed gasifier. The same setup used in their work has been adopted in this study. Four different coal samples were gasified with and without dolomite. Gas analysis resulted and lower heating values of different gas samples were documented. The parameters varied in the study were type of the feed-stock and equivalence ratio under the same bed temperature and pressure.

Sudiro and Bertucco [11] investigated coal-to-liquid (CTL) processes. on a weight basis CTL productivity was 32.5% fuel produced per unit of feed-stock. Per unit mass of liquid fuel 4.66 kg $CO_2$ was emitted. When steam was employed as a gasification agent in a high temperature gasification reactor the synthesis gas has $H_2/CO$ molar ratio of 0.49 which must be 2 before entering the Fischer-Tropsch reactor. A water–gas shift reactor was put before the FT reactor to convert CO into $CO_2$ and hydrogen by adding steam under high pressure. This reaction increased hydrogen and also decreased CO concentrations. Both of these lead to an increase in the $H_2/CO$ ratio. It was assumed that syngas conversion was 87%.

### 2.3.3 Fischer-Tropsch Synthesis

In the last couple of decades, the conversion of syngas (CO and $H_2$) through gas-to-liquid (GTL) technology has proven to be an excellent alternative to conventional sources of liquid transportation fuels [77, 78]. This by itself, along with a world-wide growing demand for clean-burning fuels, has prompted a renewed interest in the study of FTS [79].

Industrial FT facilities are currently used for coal-to-liquid (CTL) and GTL conversion [80]. The purpose of such facilities is to convert solid or gaseous carbon-based energy sources into products that may be used as fuels or chemicals. The types of feed material that can be converted to synthesis gas (syngas) are not only limited by coal and natural gas. It is possible to employ almost any other carbon source as feed material. The conversion of biomass in a biomass-to-liquid (BTL) process and waste in a waste-to-liquid (WTL) process are very good examples of sustainable technology, since biomass represents a renewable source of energy and waste conversion is connected with the beneficial recycling of discarded material.

FTS is a catalytic process that converts syngas into a multi-component mixture of hydrocarbons. FT-derived products are excellent high-performance, clean diesel fuels, because of their high cetane number and lack of sulfur and aromatic compounds.

The need to remove the heat released by the FT reaction is a major consideration in the design of reactors suitable for syngas conversion. In this study, this heat is recycled by integrating an ORC to the FTS unit to recover the heat rejected from the exothermic reactions. The temperature level is high enough to produce electricity and hot water with an appropriate ORC unit.

There is a large capital cost associated with indirect coal liquefaction based on FTS. The break-even crude oil price for a 50,000 bbl/day crude-oil-equivalent FT-based CTL facility in 2007 was reportedly around US$50–70 [81]. The capital cost associated with GTL facilities is lower, since the conversion of natural gas into synthesis gas is less complex. Coal preparation and gasification contribute 30% or more of the capital cost, even before the price of utilities, gas cleaning, and air separation are taken into account, which brings the total for syngas preparation to more than 70% of the capital cost for CTL [82].

# Chapter 3: Experimental Investigation

In this chapter, the experimental set-up and procedure as well experimental difficulties are explained. For gasification experiments, minimum fluidization velocity is an important parameter. The calculations are provided after describing the experimental procedure. An uncertainty analysis is carried out to characterize the dispertion of the values attributed to gas analysis measurements.

## 3.1 System Description

The experimental set-up is designed and built in the Energy Institute at Marmara Research Center of TÜBİTAK (The Scientific and Technological Research Council of Turkey) Marmara Research Center that is located in Gebze, Kocaeli.  Various studies are performed on this system are published elsewhere in the literature [76, 83-85].

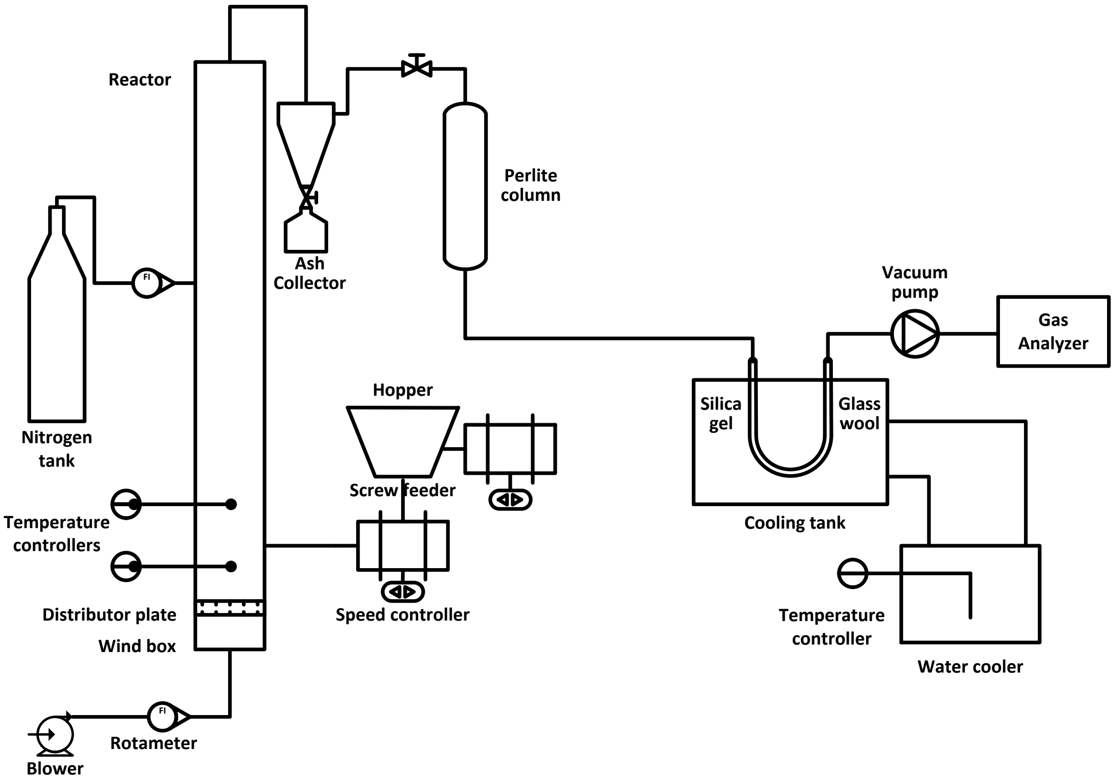

**Figure 3.1** Schematic of experimental set-up.

Gasification converts solid fuels such as coal or biomass into product gas that can be utilized in various applications. The product gas is mainly composed of CO, $CO_2$, $CH_4$, and $H_2$ and can be combusted to generate heat and work. It can also be used as a feedstock for the production of synthesis gas, liquid fuel and chemicals. The outputs of the gasifier also include particulates, tar, ammonia, and hydrogen sulfide. This analysis presents the experimental results of gasification of straw in a laboratory scale bubbling fluidized bed gasifier using air. Bubbling fluidized beds are one of the most conveniently used technologies for moderate capacities with low investment costs and operates at lower temperatures than entrained bed. In addition, it has lower agglomeration and corrosion potentials, better air and fuel mixing, less tar production than the alternatives. The effect of equivalence ratio (ER) on the quality of the product gas are investigated. The composition of the product gas is determined with an online gas analyzer which measures CO, $CO_2$, $CH_4$, $H_2$, and $O_2$ components. The lower heating value (LHV) of the product gas is calculated by using the gas composition measurements.

In the experiment, a bubbling fluidized bed gasifier is employed as shown in Figure 3.1. The setup consists of a reactor, a cyclone and two screw feeders, as well as a perlite column for filtration and a cooling tank. The height and inner diameter of the stainless-steel reactor are 2.29 m and 82 mm, respectively. Gasification is initiated through two electric heaters that wrap the gasification column. The hot parts of the reactor were well insulated with ceramic fiber blanket. At the gasification agent inlet of the reactor there is a distributor plate to provide a uniform flow stream, which lies on top of the wind box.

In the lower section of the reactor, the wind-box directs the air flow into the system through the distributor plate. The distributor plate connects the wind-box to the base of the fluidized bed above.

The bed material, silica sand is located in the centre of the unit above the distributor plate. This part is called fluidized bed. The air directed by the wind-box is routed into the sand bed via the distributor plate. The upward flow fluidizes the sand thoroughly mixing the feedstock and the sand media insuring efficient heat and material transfer.

As soon as the fluidized bed reaches the desired temperature, the furnaces are shut off while the sand media continues keeping the temperature constant throughout the gasification reactions.

To deliver the feedstock, two screw-feeders manipulated by speed controllers are used. To ensure uniform flow of the feedstock, nitrogen gas is used to balance the pressure between the feeders and the reactor. This nitrogen feed must also be measured when taking the inputs into account. Thus, a rotameter is placed at the connection between the nitrogen tank and the reactor. The air is supplied with an air blower, which again is measured with a rotameter. A thermocouple is placed into the bed to continuously measure its temperature. To capture and collect the solid particles in the synthesis gas, a cyclone is connected to the top of the reactor. The synthesis gas flows through the cyclone, after running into the perlite column where it becomes homogenous. A u-shaped glass tube is connected after the perlite column, which is filled with silica gel to avoid moisture and glass wool to avoid small particles. This u-shaped tube is immersed into a cooling tank that is filled with water kept at 20°C. There is a vacuum pump to vacuum the gas and pump it to the gas analyzer in order to determine synthesis gas composition. CO, $CO_2$, $CH_4$, $H_2$ and $O_2$ fractions of the gas can be seen on the monitor simultaneously. The percentage of $N_2$ in the gas composition can be calculated from the difference.

**Figure 3.2** Sieving silica sand into desired particle size

An inert material must be filled into the reactor to stabilize the reaction conditions. Silica sand is a widely available inert material that is chosen as the bed material in the experiments. Supplied silica sand consists of 99.2% $SiO_2$, 0.5% $Al_2O_3$, and 0.1% $Na_2O$ and has a mean particle size of 450 μm, a weight of 1082 g and a static height of 152 mm.

Silica sand is sieved to obtain a particle size that is smaller than 450 μm (Figure 3.2). The bed material is fed into the reactor until it reaches a static height of 152 mm as stated before in [76].

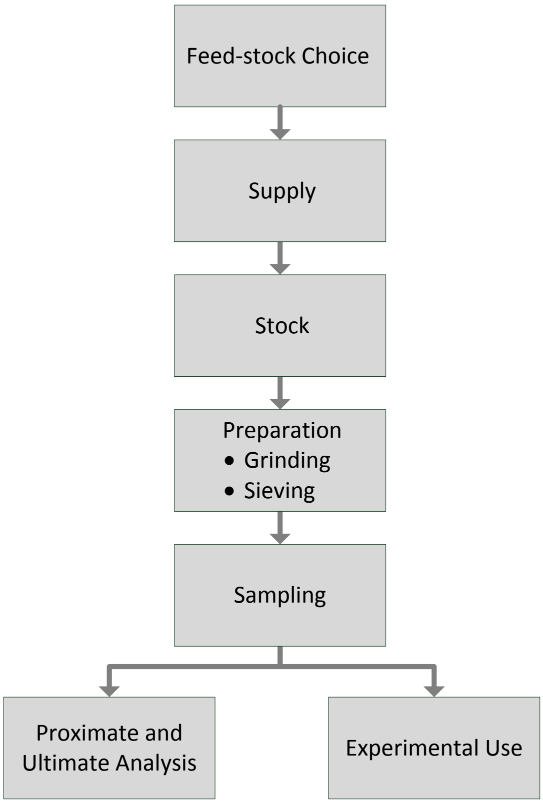

**Figure 3.3** Procedure for feed-stock preparation

The procedure followed for feedstock preparation is given in Figure 3.3, which starts with choosing the appropriate feedstock, supply, stock, preparation, sampling and experimental use, as well as analysis.

Different samples from various regions of Turkey were considered to be utilized in the experiments. Some samples were eliminated since they are already presented in the literature. Tunçlike-Ömerler and Konya-Ilgın lignite samples are chosen for difference in higher heating values. 40% of Konya-Ilgın lignite is ash, which makes the coal less valuable in terms of higher heating value, whereas low-grade lignites are widely available. As biomass sample, wheat straw is selected due to its availability and low moisture content. From the previous experience, it can be foreseen that high moisture content will result in stuck of screw-feeder. Small particles are also more feasible than large fiber-type biomass to maintain a continuous flow without wind-around.

Tunçbilek–Ömerler coal, Konya-Ilgın lignite and wheat straw are employed as gasification feedstocks. Apart from being sieved, coal samples are not introduced to any pre-treatment such as drying or screening. Proximate and ultimate analyses with calorific value of the sample are shown in Tables 3.1–3.4. ASTM D 7582-12, ASTM D 3172-07a, ASTM D 4239-12, ASTM D 5865-12, ISO 1928-09, ASTM D-5373-08, and ASTM D 3176 standards are followed to analyze the samples. Proximate and ultimate analyses of feed-stock are given in Tables 3.1-3.3, where their calorific values are shown in Table 3.4.

**Table 3.1** Ultimate analysis of coal samples employed in the experimentation.

| | **Tunçbilek-Ömerler** | | **Konya-Ilgın** | |
|---|---|---|---|---|
| **Compound** | **Dry basis [wt. %]** | **Dry ash free basis [wt. %]** | **Dry basis [wt. %]** | **Dry ash free basis [wt. %]** |
| Carbon | 73.85 | 88.40 | 52.92 | 77.46 |
| Hydrogen | 3.65 | 4.37 | 3.88 | 5.68 |
| Nitrogen | 2.76 | 3.30 | 1.12 | 1.64 |
| Sulfur | 1.42 | 1.70 | 5.73 | 8.39 |
| Oxygen | 1.86 | 2.23 | 31.68 | 6.84 |

A proximate analysis of coal and biomass samples is carried out by LECO TGA701 thermogravimetric analyzer device located at TÜBİTAK MAM Energy Institute, Coal Combustion and Gasification Laboratory, in accordance with ASTM D 5142–04 standard test method.

**Table 3.2** Proximate analysis of coal samples employed in the experimentation.

| | **Tunçbilek–Ömerler** | | **Konya-Ilgın** | |
|---|---|---|---|---|
| **Compound** | **Original basis [wt. %]** | **Dry basis [wt. %]** | **Original basis [wt. %]** | **Dry basis [wt. %]** |
| Moisture | 5.65 | - | 40.72 | - |
| Volatile matter | 32.86 | 34.83 | 30.14 | 50.85 |
| Fixed carbon | 45.96 | 48.71 | 10.36 | 17.47 |
| Ash | 15.53 | 16.46 | 18.78 | 31.68 |

**Table 3.3** Proximate analysis of biomass sample employed in the experimentation.

| | **Straw** | |
|---|---|---|
| **Compound** | **Dry basis** | **Dry ash free basis** |
| | [wt. %] | [wt. %] |
| Carbon | 44.86 | 47.66 |
| Hydrogen | 3.82 | 4.06 |
| Nitrogen | 0.73 | 0.78 |
| Sulfur | 0.11 | 0.12 |
| Oxygen | 44.59 | 47.38 |

**Table 3.4** Calorific values of coal and biomass samples employed in the experimentation.

| | **Tunçbilek–Ömerler** | | **Konya-Ilgın** | | **Straw** | |
|---|---|---|---|---|---|---|
| **Heating Value** | **Original basis [kJ/kg]** | **Dry basis [kJ/kg]** | **Original basis [kJ/kg]** | **Dry basis [kJ/kg]** | **Original basis [kJ/kg]** | **Dry basis [kJ/kg]** |
| **LHV** | 24974 | 26589 | 10565 | 16347 | N/A | 18020 |
| **HHV** | 26004 | 27543 | 12117 | 17564 | N/A | 19225 |

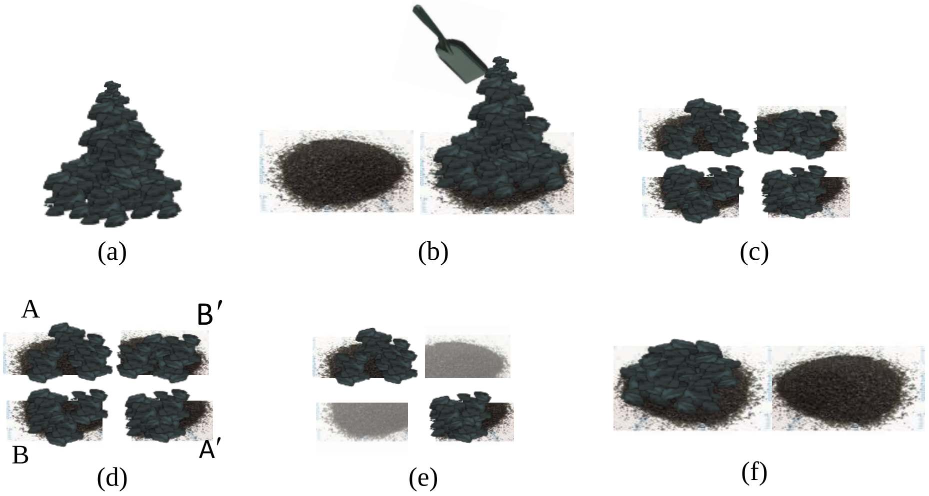

**Figure 3.4** Sampling with coning method.

Coal samples have a heterogenous distribution, which can affect the experimental results. Thus, a sampling method is adopted to minimize the associated error: The sample is first widened in a conical shape onto a horizontal, hard and smooth surface as in Figure 3.4a. Then, the coning procedure given in Figure 3.4a is repeated as Figure 3.4b. The top of the cone is flattened with the back of a shovel, and the particles are divided into four equal shares as shown in Figure 3.4c. The sample is divided into four by shares of AÁ and BB́ as shown in Figure 3.4d. Opposing BB́ part is omitted (Figure 3.4e) while keeping AÁ part as samples to be used in analysis and experiments. Procedure explained by (a)-(d) is then followed for the remaining part of the samples as illustrated in Figure 3.4f.

### 3.2 Procedure

As the first step, the reactor, distributor plate and cyclone are cleaned and silica sand is loaded into the bed, coal is loaded into the screw feeder that is in the ‘off’ position. At the second step, both heaters are turned on; nitrogen gas is purged from the outlet of the screw feeder. When the bed temperature reaches 500°C, the screw feeder is taken into the ‘on’ position and coal is started to feed into the reactor. Once a stable temperature is obtained, the gas analyzer is connected to the system to monitor the gas composition. A photograph of the experimental set-up is provided in Figure 3.5.

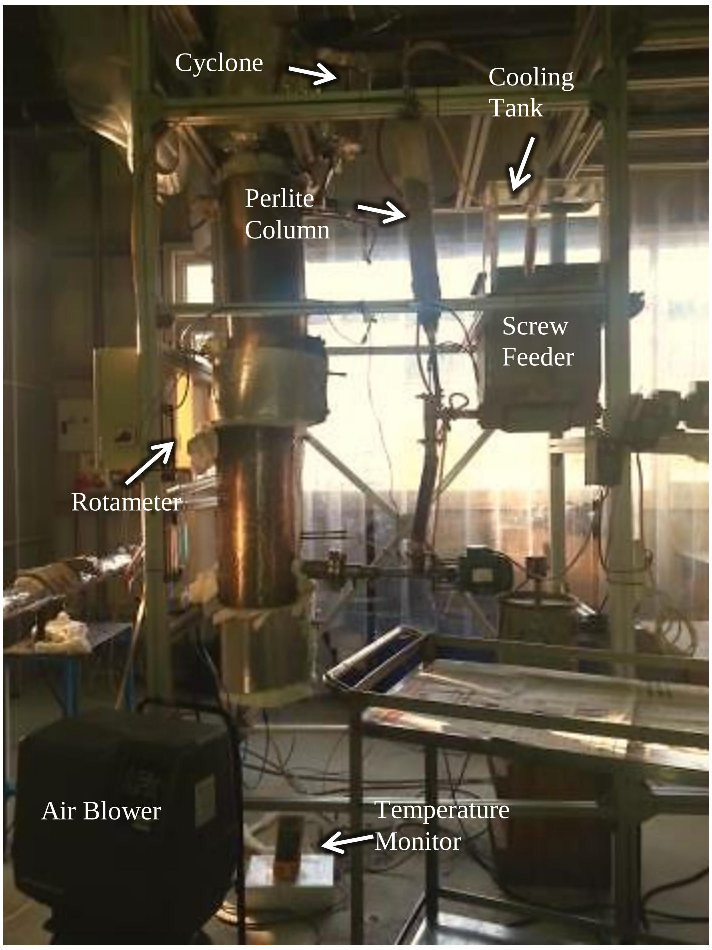

**Figure 3.5** Experimental set-up.

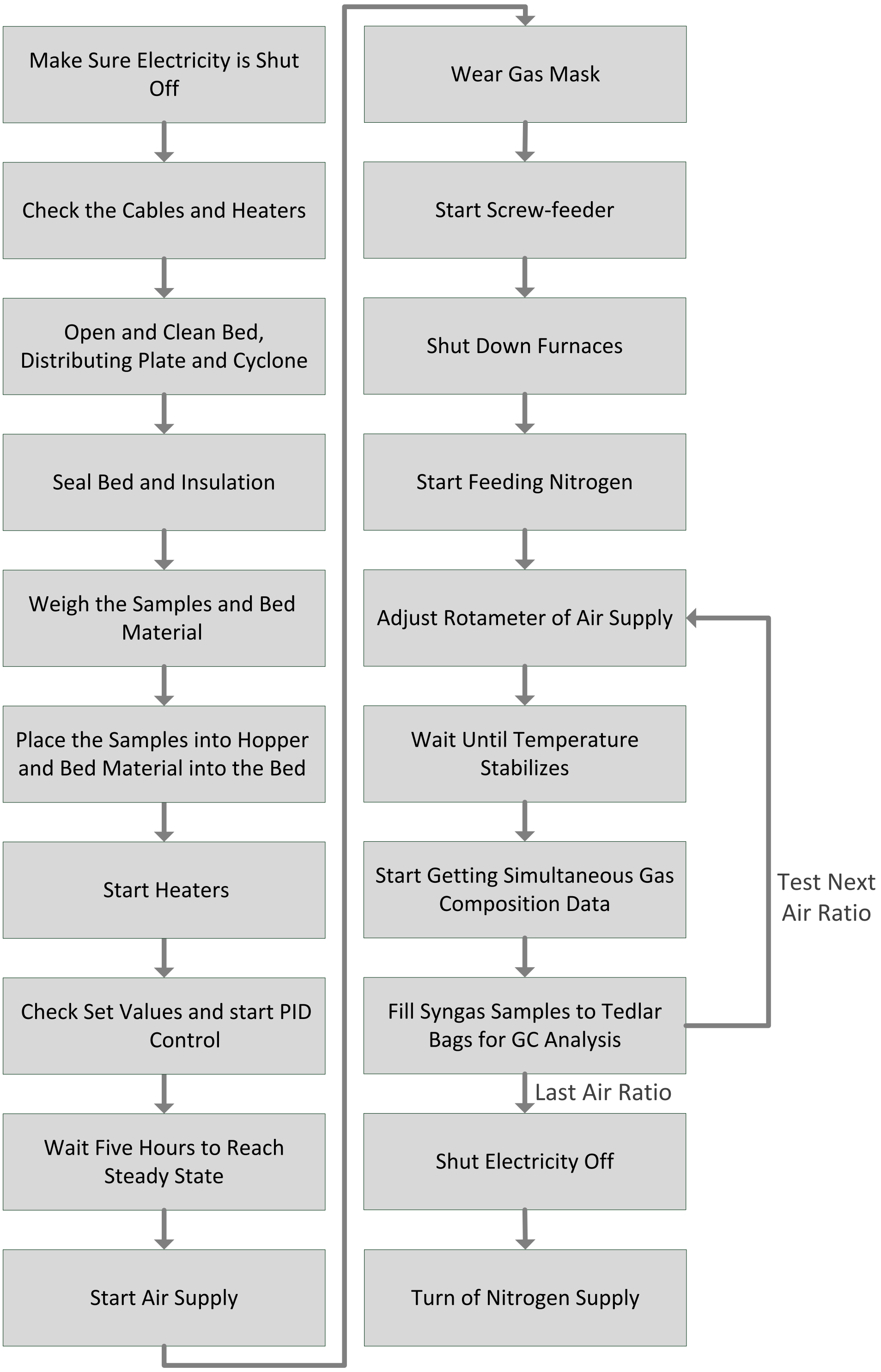

**Figure 3.6** Procedure followed during experiments.

In the experiments, the air feed rate is altered while keeping the other parameters constant: bed temperature, coal feed rate, nitrogen flow rate, air flow rate and cooling tank temperature.

Nitrogen gas and coal are fed to the reactor at a constant temperature of 20°C. Experiments are conducted with air as the gasification agent.

One of the most important parameters for gasification process analysis is the equivalence ratio, which is a dimensionless variable that shows the actual fuel/oxidant ratio normalized by the stoichiometric fuel/oxidant ratio as given as

$$ER = \frac{Fuel\ /Oxidant_{actual}}{Fuel\ /Oxidant_{stoichiometric}} \tag{3.1}$$

ER=1 represents stoichiometric combustion condition. Mixtures are categorized as 'lean,' where excess oxidant exist and therefore ER<1. On the other hand, if excess fuel is present, the mixtures are categorized as 'rich' and ER>1.

On the condition that the units of the numerator and denominator are consistent, the ratio can be calculated both in mass or molar basis. In this study, ER is calculated on mass basis.

The lower heating value of the synthesis gas is calculated through the equation below, which results in units of kJ/m$^3$.

$$LHV = \frac{282.99\,V_{CO}+802.34V_{CH_4}+241.83V_{H_2}}{0.1\times 22.4} \tag{3.1}$$

The thermal capacity of the system is 20 kW [76]. The inner diameter of the rector is 82 mm. Heating the reactor at the initial state employs two furnaces, which wrap the reactor and thoroughly cover it with insulation material to reach as close to adiabatic conditions as possible. Temperature transmitters and PID control units are integrated to the set-up to keep the temperature constant throughout the experiment. The temperature is monitored during the experiments.

**Figure 3.7** External view of the distributor plate when dismounted.

The procedure followed in the experiments is presented in Figure 3.6. Before all steps, electricity connections and switches are checked to make sure there is no electrical current or leakage. Then the cables between switches, furnaces, screw-feeders, thermocouples, temperature monitoring devices and the simultaneous data analyzer are checked.

The bed, the distributor plate (Figure 3.7) and the cyclone (Figure 3.8) were demounted and cleaned in addition to perlite column, silica and glass wool in the u-tube. As soon as the pipes and tubings are clean, the parts are assembled together and covered with insulation. Feedstock samples are weighed and placed into the hopper that is connected to two screw feeders. The purpose of two screw feeders instead of one is due to the difficulty in balancing the pressure and to set the hopper and the bed apart to prevent any pyrolysis from occurring in the pipes. Otherwise, pyrolytic oil can cover the pipes and block the movement of the feedstock.

**Figure 3.8** Cyclone cleaning before starting a new set of experiments.

There are two heaters placed around the bed to initiate the heating process before the feedstock feed. They can also be used if somehow the screw feeder encounters a discontinuity. The PID controllers are set to heat the furnaces with a heating rate of 3°C/min, to make sure that the thermostat does not exceed the set temperature and a healthy expansion rate is achieved to maintain the materials in good condition. The top screw feeder is set to the level to supply 0.85 kg/hr feed-stock. If the supply rate is increased, this can create various problems such as blockage of the feed stock in the screw-feeder as shown in Figure 3.9.

**Figure 3.9** Coal samples stuck in screw-feeder.

An approximate air ratio is calculated for stoichiometric combustion and air was set between 20-45% of the stoichiometric air needed to meet gasification conditions and the effect of different air supply ratios. Meanwhile, the nitrogen supply is turned on to prevent any blockage and ensuring a constant mass flow rate and to keep the temperature constant.

The distributor plate allows the air and nitrogen supply to pass upwards to the reactor, while keeping the bed material and feedstock on top. With the air and nitrogen flow, the feedstock and bed material particles act as a fluid flow, which is the main reason of calling this type of bed as 'fluidized bed.'

**Figure 3.10** Moist silica sand if dampens before the experiments.

When the gasification reaction starts, the furnaces are switched to the 'off' position, because gasification consists of exothermic reactions and heat is released during this process.

If the silica sand is exposed to the humidity at room conditions over a long period of time, it gets damped and becomes sticky. Thus, it inhibits the occurrence of fluidization in the gasification experiments. The photograph of this phenomenon is shown below in Figure 3.10.

After succeeding a constant temperature of 800±20°C in the bed and 730±10°C at the top heater level, the synthesis gas is navigated into the simultaneous gas analyzer device (Figure 3.11a) by changing the position of the valve at the outlet of the gasifier. The gas composition is read from the monitor as $H_2$, $CH_4$, CO, $CO_2$, $O_2$, and the $N_2$ content is found by difference. A vacuum pump is employed to suck the gas into a Tedlar bag, which is durable against corrosion caused by sulfur components for several days. The bags are labeled and sent to the laboratory for sulfur analysis using GC device shown in Figure 3.11b.

Appropriate gas masks are supplied to avoid possible harmful gas inhalation. Sulfur compounds such as $H_2S$ and COS are some of the hazardous gases, which are dangerous for human health even in trace amounts.

(a) (b)

**Figure 3.11** (a) Simultaneous gas analyzer ABB AO2040 and (b) gas chromatography device.

After finalizing the experiments, the electricity switches, air and nitrogen supplies are all turned off. The remaining feedstock samples are removed from the hopper to avoid any change in the moisture content. Relative humidity of the air can cause an undesired change in the moisture content of the feedstock, which can affect the theoretical molar balance calculations.

### 3.3 Minimum Fluidization Velocity

Kunii and Levenspiel [86] proposed a formula for calculating minimum fluidization velocity. When Reynolds Number is smaller than 20, their equation that is given below can be used to calculate the minimum fluidization velocity:

$$u_{mf} = \frac{d_p^2 \; (\rho_s - \rho_f) g \, \varepsilon_{mf}^3 \, \Phi_s^2}{150 \, \mu \, (1 - \varepsilon_{mf})} \tag{3.2}$$

where $d_p$ is mean particle diameter (0.045 cm, as calculated); $\rho_s$ is solid (sand) density (2.557 g/cm$^3$, as measured); $\rho_f$ is air density at ambient temperature 25°C (0.001184 g/cm$^3$, as taken from [87]); g is gravitational acceleration (981 cm/s$^2$ as taken from [88]); $\varepsilon_{mf}$ is void fraction at minimum fluidization (0.45, as calculated); Φs: sphericity of an average sand particle (0.75, as taken from [89]); μ is viscosity of air at ambient temperature 25°C (0.0001845 g/cm$^3$, as taken from internal library of [87]).

The mean particle diameter $d_p$ is calculated through the following equation:

$$d_p = \frac{1}{\sum \frac{f_i}{d_{p,i}}} \tag{3.3}$$

where $f_i$ is the fraction of particles with diameter $d_{p,i}$. Retsch AS200 basic sieve set is utilized to determine the particle size ranges. This set consists of nine sieves that have different aperture sizes to determine particle size, separation, and fractioning for materials such as powders, bulk materials, and suspensions. The sieves are placed in respect to their aperture sizes starting from the largest on the top to the smallest at the bottom. The smallest sieve passes through smaller particles that are not larger than 25 μm. The largest aperture size for the top sieve is 20 mm. Then the sieves are connected to the shaking device. Maximum capacity of the device is 3 kg. Sand is sieved for five minutes and then the sand between each sieve is weighed. The average aperture size of paired sieves is taken as the mean diameter for the sand in between.

The void fraction at minimum fluidization $\varepsilon_{mf}$ is calculated by

$$L_m \, (1 - \varepsilon_m) = L_{mf} \, (1 - \varepsilon_{mf}) \tag{3.4}$$

where $L_m$ is height of fixed bed (15.2 cm as measured); $\varepsilon_{mf}$ is void fraction at fixed bed (0.38 as calculated); $L_{mf}$ is height of minimum fluidization (17 cm as assumed).

The sand density is measured experimentally as explained below: First the sand is weighed. 100 ml water is measured and put into a graduate cylinder. The sand is then poured into the graduated cylinder and the final volume is read. Now, by knowing its mass and volume, the density is found by dividing its mass into its volume. Utilizing Equation 3.2, minimum fluidization velocity is calculated as below:

$$\mathrm{u_{mf}} = \frac{0.045^2 \times (2.557 - 0.001184) \times 981 \times 0.38 \times 0.75^2}{150 \times 0.0001845\ (1 - 0.38)} = 16.48\ \mathrm{cm}/s$$

$$Re = \frac{d_p\ u_{mf} \rho_f}{\mu} = \frac{0.045 \times 16.48 \times 0.001184}{0.0001845} = 4.8$$

Since Reynolds Number is found to be smaller than 20, the minimum fluidization velocity calculation is acceptable.

### 3.4 Agglomeration

Although fluidized bed gasification is a mature technology to generate energy from coal, its application to biomass has faced frequent operational problems. Most biomass fuels contain alkali metal that could cause particle agglomeration during fluidized bed operation. This problem is basically related to the content of the fuel ash, type of the employed bed material and the operating temperature within the bed. Lignocellulosic biomass feedstock, especially those containing potassium, sodium and alkali earth metals along with chlorine and sulfur in lesser extent create low melting ash within the bed [90]. Such phenomenon makes the sand particle surface sticky, at the same time the capturing and deposition rate of ash which is generated during the gasification process on the silica sand surface increases. This process improves clustering tendency of the sand particles and deteriorates the fluidization and mixing condition in the bed and generates hot spot within the bed which consequently leads to sintering and agglomeration [91].

The agglomeration behaviour influences not only the fluidization itself but also product distribution. Agglomeration of the bed materials causes defluidization which is detected by remarkable pressure drop and temperature segregation over the bed [92]. This causes serious problems such as reduction of the fluidization tendency or even causing unscheduled system shut down [93, 94]. Figure 3.12 shows the agglomeration occurred in the bubbling fluidized bed during the experimental analysis of this study.

**Figure 3.12** Agglomeration occurred in the bubbling fluidized bed.

During the experiments carried out for this study, some gas composition analysis results are found to be unexpectedly low or high. After each experimental session, the reactor is fully opened and cleaned to make sure the set-up is working accordingly. After those experiments, the reactor is opened and it is seen that blockage occurred due to agglomeration. The results obtained from those experiments are not put into calculations. This agglomeration may be considered as a result of the high ash content of Tunçbilek–Ömerler lignite, as well as its sulfur content and relative humidity experienced in the air at that particular day, which can make the silica sand sticky.

In previous gasification experiments reported in the literature [95, 96], agglomeration is identified as a problem affecting the overall quality of the process. The agglomeration problem is linked to the sodium vapour released from high-sodium containing lignites, which then form sticky sodium silicate by reacting with silica sand [97]. It is suggested that these sticky sodium silicates are responsible for the agglomeration problem and defluidization encountered during gasification experiments of high-sodium lignite. To prevent agglomeration, a possible solution is addition of an inert material to the bed, such as dolomite and limestone, where the reaction temperature is limited to 930°C. At high temperature, it is possible that agglomerated particles melt and form tar.

It is observed that inert material addition and temperature limitation results in agglomeration-free experiments. In the experiments, where agglomeration experienced, $Na_2O$ (sodium oxide) concentration in the ash is found to be as high as 6-7 wt.% [97].

### 3.5 Uncertainty Analysis

Data obtained from experimentation needs to be analyzed. The analysis result can be expressed in a simple verbal form, as well as a part of complex mathematical formulation with statistical change of the results and instrumental sensitivity.

For estimation of experimental uncertainties, Kline and McClintock [98] presented a method based on specific uncertainties in each measurement.

The accuracy of the measurement is denoted by a plus or minus sign in order to designate the associated uncertainty. In the case, where the uncertainty in each measurement has the same odds, the measurements can then be used to calculate the respective results of the experiments. The uncertainties associated with the calculated results would be based on the corresponding uncertainties associated with the primary measurements, where the result R is a function of independent variables denoted by subscripts of x [99].

$$R = R(x_1, x_2, x_3, \dots, x_n) \tag{3.5}$$

$$\sigma_R = \left[\left(\frac{\partial R}{\partial x_1}\sigma_1\right)^2 + \left(\frac{\partial R}{\partial x_2}\sigma_2\right)^2 + \left(\frac{\partial R}{\partial x_3}\sigma_3\right)^2 + \cdots + \left(\frac{\partial R}{\partial x_n}\sigma_n\right)^2\right]^{0.5} \tag{3.6}$$

where $\sigma$ denotes the uncertainty in the results and $\sigma_1$, $\sigma_2$, $\sigma_3$,... ,$\sigma_n$ are the uncertainties in the independent variables. When the uncertainties in these independent variables are all given with the same odds, then the uncertainty in the result having these odds would be given as $\sigma_R$.

In this study, stoichiometric approach for gasification is adopted by using the experimental gas analysis results to calculate the molar inputs of dry, ash free coal and water input to the system, as well as nitrogen output and heat output caused by the reaction. This reaction can be though as a combustion reaction with lack of oxygen. For calculating the oxygen input in mol, the equation below is applied:

$$\alpha = \alpha(O_{ex}, n) \tag{3.7}$$

where $O_{ex}$ is the excess oxygen measured with simultaneous gas analysis device that has an uncertainty of 1%, and n is the oxygen content of the feedstock gasified that is analyzed with GC device with an uncertainty of 0.5%.

$$\alpha = 0.5(1 - n) + O_{ex} \tag{3.8}$$

$$\sigma_\alpha = \left[\left(\frac{\partial\alpha}{\partial n}\sigma_n\right)^2 + \left(\frac{\partial\alpha}{\partial O_{ex}}\sigma_{O_{ex}}\right)^2\right]^{1/2} \tag{3.9}$$

$$\frac{\partial\alpha}{\partial n} = \frac{\partial}{\partial n}(0.5 - 0.5n + O_{ex}) = -0.5$$

$$\frac{\partial\alpha}{\partial O_{ex}} = 1$$

$$\sigma_\alpha = [(-0.5 \times 0.005)^2 + (1 \times 0.01)^2]^{1/2}$$

$$= 0.0103\, mol$$

# Chapter 4: Descriptions of Integrated Systems

In this chapter, the integrated systems are described and their schematic representations are given. For both systems, ORC is integrated to make use of low-grade heat. Due to the importance of the ORC cycles, firstly, three different configurations are considered to obtain the most efficient one for the related temperature levels. Secondly, various working fluids are selected, which are appropriate for the temperature level and calculations are performed to point out the best configuration and the working fluid. After selection, the integrated systems are introduced.

## 4.1 Various Types of ORC Systems

Heat engines can be classified into two main groups as gas power cycles (such as Brayton, Diesel, Ericsson, Otto, Stirling) and vapour power cycles (such as Rankine). Rankine cycles are divided into two sub-groups: steam and non-steam Rankine cycles. Steam Rankine cycle is operational for up to 620°C based on the metallurgical limitations of the present turbine materials [1]. For low-grade heat, however, non-steam Rankine cycles are the most appropriate ones for maximizing the heat recovery. These cycles are ORC and non-organic Rankine cycles (such as ammonia-water, carbon dioxide). The main advantage of utilizing an organic substance (as opposed to water) is the lower boiling point temperature that is more suited to low source and sink temperature profiles. Superheating the working fluid is not necessary to run the cycle; a low-speed expansion device can be employed that is operational at two-phase region.

Renewable sources and waste process heat are not at high temperatures as required for other cycles than non-steam Rankine cyles, which creates a great interest of non-steam Rankine cycles. ORCs are mainly utilized at temperatures up to 400°C and from 1 to 800 kW power output range, whereas ammonia-water cycles are feasible for the temperature range up to 250°C due to ammonia decomposition.

In this section, three different ORC configurations are considered to obtain the best efficiency value both for energy and exergy. Another very important variable is the working fluid that flows through the cycle. Various studies on ORC are presented elsewhere [100, 101].

For ammonia-water, the optimum concentration value was obtained by keeping the other parameters constant, which are the expander isentropic efficiencies of 0.7 and pump isentropic efficiency of 0.7. After determining the optimum ammonia mass fraction that has the most compatibility with the source and sink temperature line, this time expander isentropic efficiency is altered between 0.65 to 0.85 and energy and exergy efficiencies are calculated for each case.

R124, R141b, and n-butane are selected for ORC calculations for each system considering their critical temperature and critical pressure properties. Overall energy and exergy efficiencies are plotted with respect to the expander efficiency.

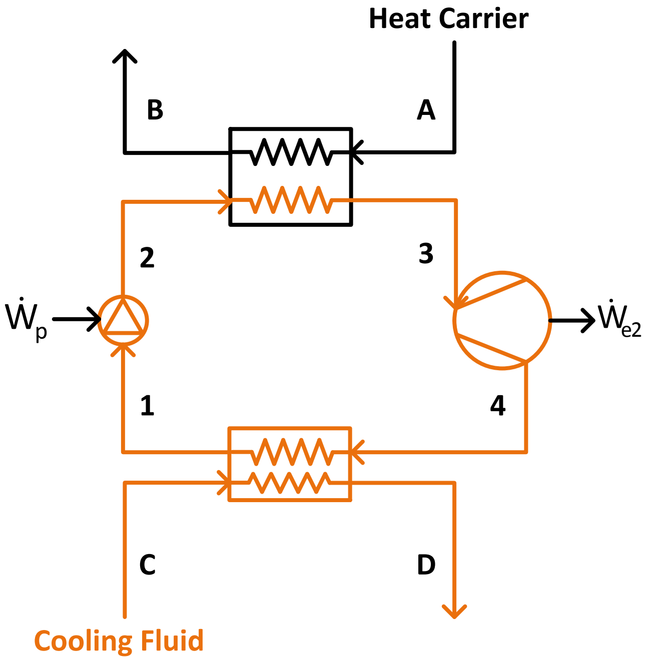

**Figure 4.1** Schematic diagram of TRC.

A trilateral Rankine cycle (TRC) is shown in Figure 4.1, which consists of four components, namely a pump, a heater, an expander, and a resorber. In the calculations, state properties of the cycle are determined as follows:

In state 1, before entering the pump, the liquid is in saturation phase. Then it is pumped to state 2, where it gets heated by the geothermal brine. After the heater, the temperature of the working fluid rises to 180°C (state 3). Once the sub-cooled liquid is heated, it reaches a saturated liquid phase at the corresponding high pressure and is ready for expansion. Between states 3 and 4, a two-phase expander is employed for electric power generation. At state 4, there is a two-phase flow, which loses heat to the environment to complete the cycle at resorber. For state 4 and state 1, since there is no expansion or compression device in between, the pressure remains constant.

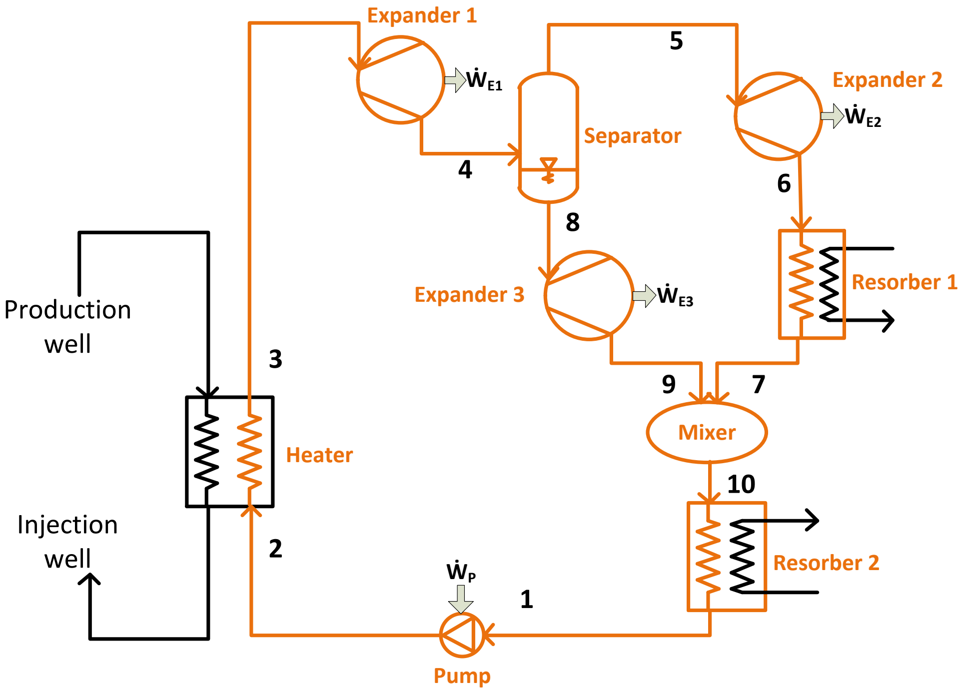

**Figure 4.2** Schematic diagram of DS ORC.

The second system seen in Figure 4.2 comprises of one pump, one heater, three expanders, one separator, two resorbers, and a mixing chamber. With the same approach as trilateral ORC, in this double stage ORC (DS ORC) the working fluid at state 1 has a vapour quality of zero. It is then pressurized by utilizing a pump and the pressure rises up to the pressure at state 3. State 3 has a temperature of 120°C and a vapour quality of zero. After exiting the heater, the fluid enters Expander 1. The expansion results in a two-phase flow at state 4 that gets separated through a separator unit into liquid and vapour phases. Vapour and liquid have the same temperature as state 4; the vapour quality of state 4 is equal to the mass flow rate of state 5 due to the assumption of a total mass flow rate of 1 kg/s. Thus, at state 8, the mass flow rate can be determined by subtracting the vapour mass flow rate from the total mass flow. After the separation, both vapour and liquid phases are directed into separate expanders, which result in two-phase flows. Due to the high vapour quality at the exit of Expander 2, at state 6 the fluid is navigated into a Resorber to obtain the saturated liquid phase. In the meantime, the fluid leaving Expander 3 having a low vapour quality is mixed with the parallel flow in a mixing chamber having an outlet flow of state 10. Again, state 10 is cooled down to saturated liquid before entering the pump. Here, states 7, 9, 10, and 1 have the same pressure.

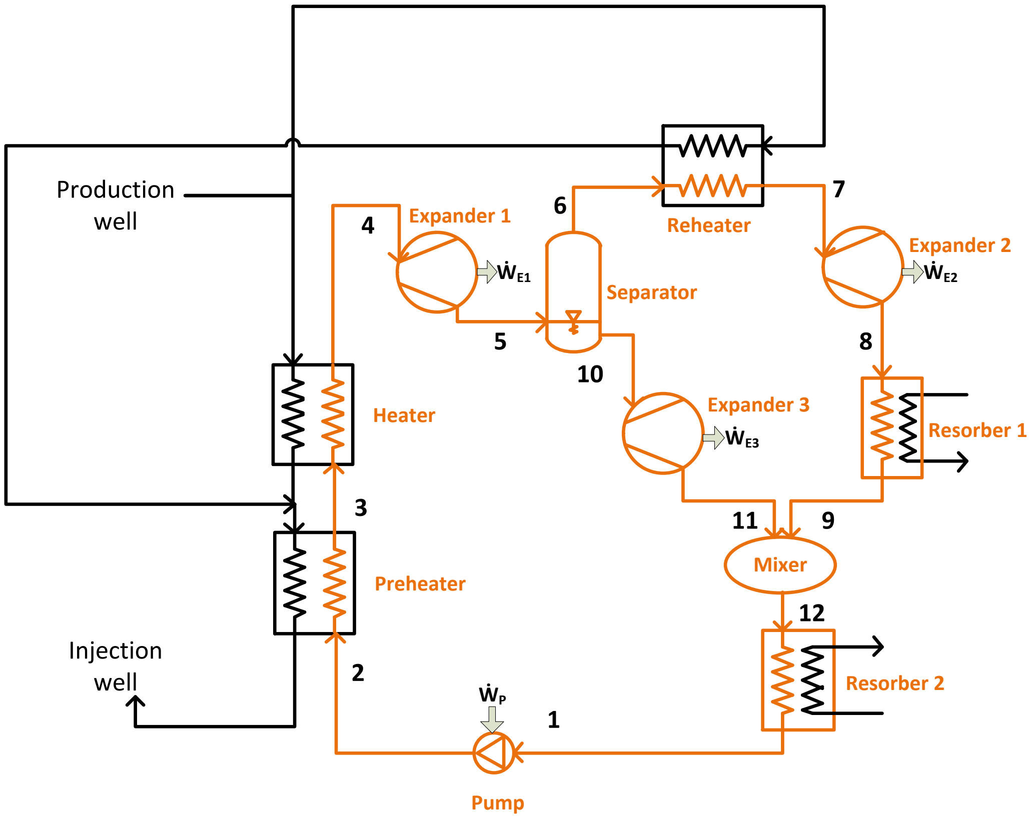

**Figure 4.3** Schematic diagram of DS ORC-R.

A double-stage ORC with reheating (DS ORC) similar to the previous system given in Figure 4.4 is shown in Figure 4.3. The only difference is applying reheating before Expander 2 in DS ORC-R. The achieved lower temperature brine is mixed with a separate brine stream (used in the heater) which gets combined as a single flow and used for preheating the ORC working fluid before entering the heater. This third system consists of a preheater, a heater and a rehetaer as mentioned, along with a pump, three expanders, a separator, and two resorbers. In this system, state one is at saturated liquid phase that is 10°C above the ambient temperature. Between the preheater and heater at state 3, temperature of the fluid is considered the same as state 6 and the pressure is the same as state 4. At state 7, the fluid is heated up to the same temperature as state 4, but this time the vapour has a quality of one, because of the lower pressure compared to state 4. The remaining process is the same as in the second system.

## 4.2 System 1

In the first system, shown in Figure 4.4, solar thermal energy is concentrated in a solar power tower. A steam Rankine cycle, an ORC, and a desalination unit are driven by solar thermal energy to generate various outputs such as mechanical energy, hot water, and desalinated water. Molten salt thermal storage is connected to the solar tower to maintain the temperature, which otherwise would be intermittent. Thermal storage is employed to make use of heat, when the solar irradiation is not sufficient. It is assumed that, 60,000 heliostats with 2.3 $m^2$ surface area each are employed to concentrate solar radiation onto the receiver with an efficiency of 10%.

In the thermal storage tank, molten salt that consists of 60% $NaNO_3$, 40% $KNO_3$ by weight, is pumped from the cold storage tank to the solar receiver, where it is heated up to 580°C. EES internal library (see Appendix) for incompressible substances is used for calculating enthalpy and entropies, which are derived from [102]. The library is capable of calculating results for the molten salt in a temperature range of 260–595°C. The hot molten salt is pumped from the receiver to the hot storage tank, where it is stored and pumped as a continuous flow, which is divided into two separate flows. One of these supplies heat to drive a steam Rankine cycle with two turbines. The other flow supplies heat to a desalination sub-system for preheating saline water before reverse osmosis membrane and for superheating the desalinated water to produce mechanical work through a turbine.

To recover heat more effectively, two turbines are included in the Rankine cycle, where the temperature range is compatible. The rejected heat from the Rankine cycle is transferred to an ORC.

ORC has two expanders and one turbine to generate electricity. Heat rejection to the environment is considered in two different cases: by utilizing heat and by rejecting it directly to the surroundings. Making use of the heat will increase the efficiency where hot water is needed.

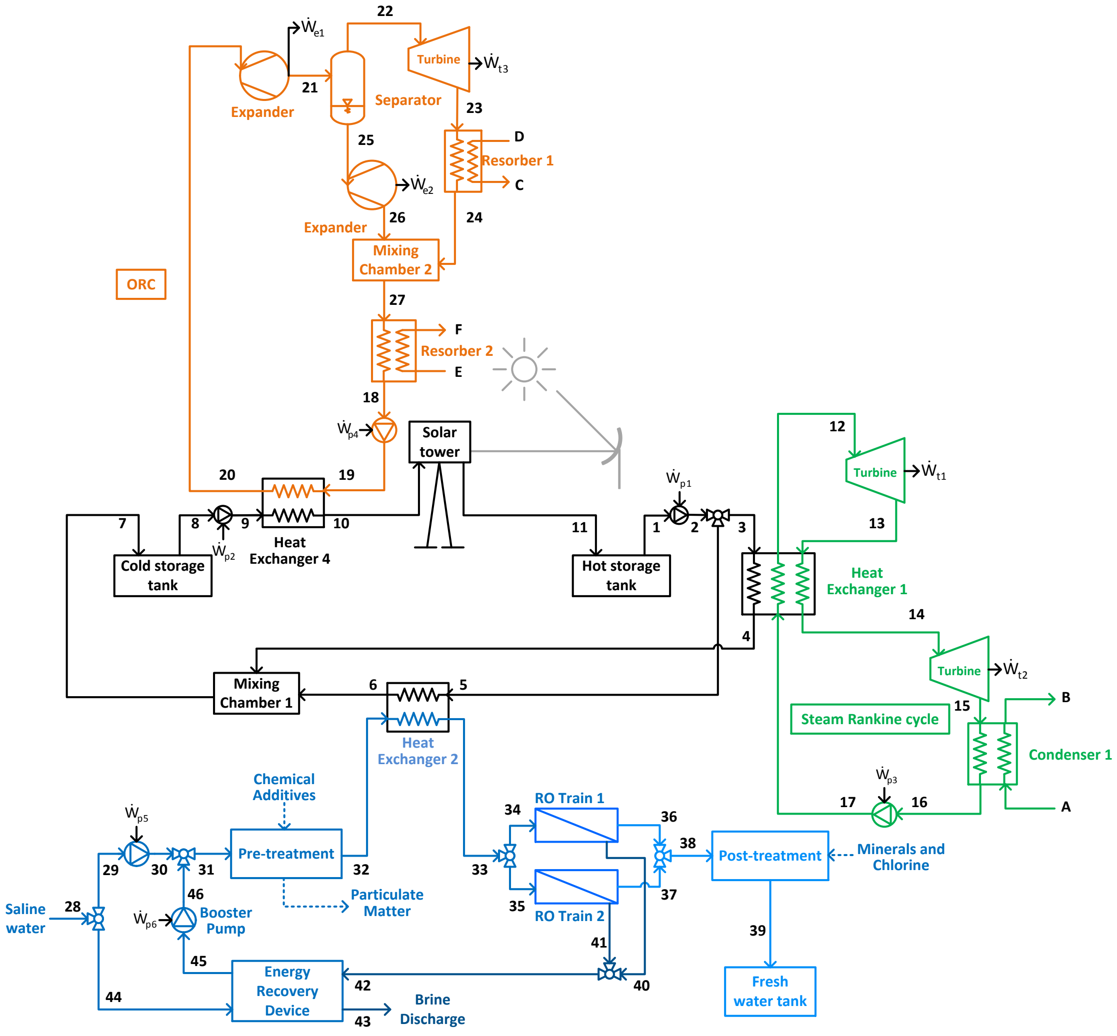

**Figure 4.4** Schematic of System 1.

The desalination system consists of a pump that pressurizes the sea water, a filter to remove the coarse particles, an energy recovery turbine, an osmotic membrane to filter fine particles and salt, a turbine to produce electricity and a fresh water tank to store the drinking water. The energy recovery turbine basically recovers the pressure from the salty condensate rejected by the osmotic membrane. In the system, there is a turbine that produces electricity to power a pump to pressurize the sea water to the required pressure level before entering the osmotic membrane. With the use of an osmotic membrane, the conversion to drinking water can be provided with better quality.

## 4.3 System 2

The second system, shown in Figure 4.5, comprises of five sub-systems: gasification sub-system, Brayton cycle, steam Rankine cycle, an ORC and a Fischer-Tropsch synthesis sub-system. The inputs are considered as coal or biomass and the outputs of this system are power, hot water and fuel.

Gasification sub-system consists of a reactor, a cyclone to remove coarse particles, a compressor to provide the required pressure level for the acid gas removal, and a portion of the resultant synthesis gas is directed to a Fischer Tropsch synthesis sub-system. The acid gas removal unit eliminates the undesirable sulfur compounds in the synthesis gas, mainly caused by the sulfur content of coal.

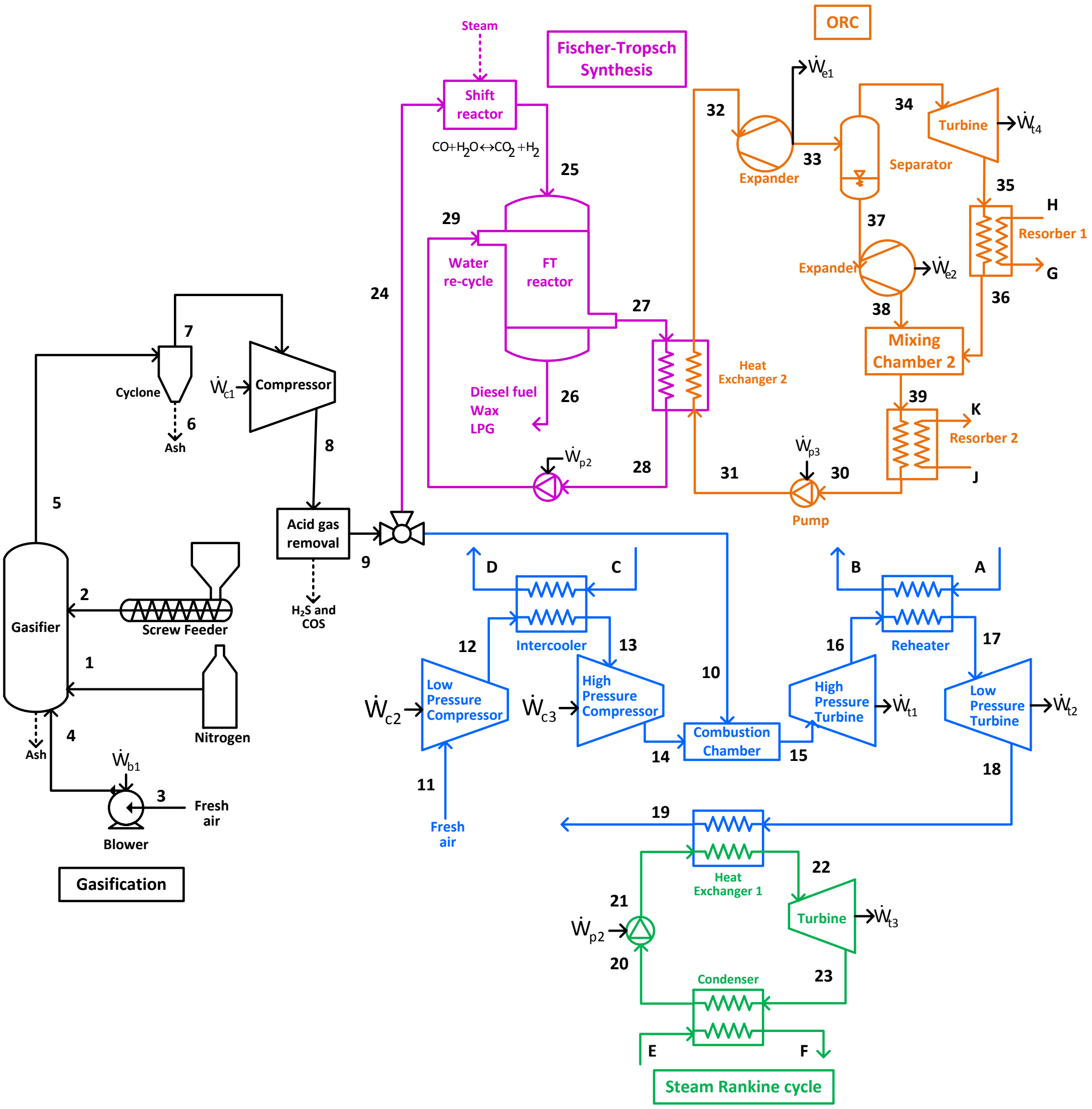

**Figure 4.5** Schematic of System 2.

A T-valve is placed after the acid gas removal unit, which divides the synthesis gas flow into two separate flows. One of these flows is fed into a Fischer-Tropsch synthesis unit to produce liquid and gaseous fuels with addition of an iron based catalyst through exothermic reactions. The resultant heat is balanced with water circulation through the Fischer-Tropsch reactor that can be considered as a heat exchanger. The water continuously gains heat to keep the reactor temperature at constant levels. This heat is then used as a heat source for an attached ORC unit, which is merely a very small unit to make use of the recoverable heat and increase the energy and exergy efficiencies.

The ORC unit is chosen to be DS-ORC due to the energy and exergy calculation results, where ammonia-water mixture is chosen to be as the working fluid of tte ORC.

The other flow exiting the T-valve is burned in a combustor to supply heat for a Brayton cycle with cooling and reheat. There are two compressors and two turbines: low pressure and high pressure. The resultant hot gas exiting the low pressure turbine supplies heat to a steam Rankine cycle. A combined gas-vapour cycle is proposed, again, to increase the thermodynamic efficiencies.

The hot gas exiting the low-pressure turbine is transferred to an integrated Rankine cyxle to make use of this heat to produce power and hot water.

# Chapter 5: Thermodynamic Analyses

This chapter is organized in the following order: First, balance equations are given and then system schemes are presented with explanation of each sub-system. Next, organic fluid is selected for the ORC followed by the illustration of the thermodynamic model of each system. Finally, energy and exergy analyses are presented and optimization is conducted based on various criteria.

In this chapter, two novel tri-generation systems are introduced, as well as an experimental study on biomass and coal gasification. By placing emphasis on renewable sources, various energy sources are considered in this thesis. ORC is included in both systems while keeping in mind that all the systems need to be environmentally benign by employing renewable heat sources, using the energy as efficient as possible. The sub-systems of the introduced systems are given in Table 5.1.

**Table 5.1** Systems and related sub-systems chosen to be analyzed.

| **Experimental System** | **System 1** | **System 2** |
|---|---|---|
| ▪ Fluidized bed gasification | ▪ Solar tower with molten salt thermal storage<br>▪ Steam Rankine cycle<br>▪ ORC<br>▪ Desalination unit | ▪ Gasification plant<br>▪ Brayton cycle<br>▪ Steam Rankine cycle<br>▪ Fischer Tropsch synthesis<br>▪ ORC |

## 5.1 Balance Equations

Exergy analysis is a methodology for the evaluation of the performance of devices and processes, and involves examining the exergy efficiencies at different points in a series of energy conversion steps. Exergy (also called available energy or availability) of a system is the "maximum shaft work that can be done by the composite of the system and a specified reference environment" [103]. In every thermal system, heat transfer within the system, or between the system and surrounding environment, occurs at a finite temperature difference, which is a key contributor to irreversibilities for the system. All real processes, including natural events are irreversible and the system performance degrades as a result of these irreversibilities in each individual thermodynamic process that makes up the system. The work potential is reduced by the irreversibilities and the corresponding amount of energy becomes unusable [104]. Entropy generation measures the effect of these irreversibilities in a system during a process and helps compare each component in the system based on how much they contribute to the operation inefficiencies of the overall system. Therefore, entropy generation associated with each process needs to be evaluated to determine the overall system efficiency. Even though energy analysis is the most commonly used method for examining thermal systems, it is only concerned with the conservation of energy, which neither takes the corresponding environmental conditions into account, nor provides how, where and why the system performance degrades. Consequently, energy analysis only measures the quantity of energy and does not reveal the full efficiencies of the system [105]. Thus, in this research, the analyzed system is examined with respect to exergy to better understand the true efficiencies of the components by determining the irreversibilities in each cycle, as well as the overall system and how nearly the respective performances approach ideal conditions. By analyzing both the quality (usefulness) and the quantity of the energy, the true magnitude of losses, and their causes and locations are identified by investigating the sites of exergy destruction in order to improve the individual components and overall system [103-105].

In this section, general forms of balance equations will be explained to develop a clear understanding of the systematic approach adopted in the case study.

In the most general sense, any balance equation for a quantity in a system can be expressed as the following equation:

$$Input + Generation - Output - Consumption = Accumulation \tag{5.1}$$

This relation is referred to as the quantity balance and can be stated as quantity accumulated in a system during a process is equal to the difference between the net quantity transfer through the system boundary plus the quantity generated and the quantity consumed within the system boundaries.

The conservation of mass is a fundamental principle in analyzing any thermodynamic system. Mass balance equation:

$$\sum \dot{m}_{in} - \sum \dot{m}_{out} = \frac{dm_{cv}}{dt} \tag{5.2}$$

where $m$ and $\dot{m}$ are the mass and mass flow rate and the subscript *cv* indicates the control volume. In steady-state, mass balance equation will become as follows,

$$\sum \dot{m}_{in} = \sum \dot{m}_{out} \tag{5.3}$$

Total energy of a control volume is always conserved within the system according to the first law of thermodynamics. The energy in an isolated system is constant. Energy balance equation:

$$\dot{Q} - \dot{W}_{net} + \sum \dot{m}_{in}\left(h_{in} + \frac{v_{in}^2}{2} + g\, z_{in}\right) - \sum \dot{m}_{out}(h_{out} + \frac{v_{out}^2}{2} + g\, z_{out}) = \frac{dE_{cv}}{dt} \tag{5.4}$$

where $E$ is energy; $\dot{Q}$ is heat transfer rate; $\dot{W}$ is power; $t$ is time; $h$ is specific enthalpy; $V$ is velocity; $g$ is gravitational acceleration; and $z$ is elevation.

The entropy generation rate, $S_{gen}$, for a control volume is defined as entropy balance equation:

$$\dot{S}_{gen} = \sum \dot{m}_{out}s_{out} - \sum \dot{m}_{in}s_{in} - \sum \frac{\dot{Q}_b}{T_b} + \frac{dS_{cv}}{dt} \tag{5.5}$$

where $\dot{S}$ is the entropy flow or generation rate, $S$ is entropy, and $s$ is specific entropy. In actual life, entropy exiting the system is always larger than that of entering the system, where the difference due to internal irreversibility is named as entropy generation. Only in an ideal (reversible) system, the amount of irreversibility is zero, thus there is no entropy generation.

When energy is converted into another less useful form, the rest of the useful part cannot be recovered again, a portion that is not conserved as total energy of the system. The amount of useful work is defined as exergy.

Exergy can be classified in three groups: thermo-mechanical (physical), chemical, and nuclear. Thermo-mechanical exergy can be transferred by heat, work, and mass flow, which cover kinetic and potential exergies that are neglected, since elevation and speed difference are considered negligibly small. The rest of thermo-mechanical exergy remains as flow or non-flow exergy according to the type of the system. Chemical exergy comes into account in presence of fuels, which have a potential of chemical decomposition rather than the reference environment. Finally, nuclear exergy is caused by the instability of nuclear substances and it is not a subject of this study. Exergy balance equation is given below for a fixed volume system:

$$\dot{E}x_{Q,in} + \dot{E}x_{W,in} + \sum \dot{m}_{in} ex_{in} = \dot{E}x_{Q,out} + \dot{E}x_{W,out} + \sum \dot{m}_{out} ex_{out} + \dot{E}x_{dest} \quad (5.6)$$

The following assumptions are made for the analyses:

- Pressure drops and heat losses in piping are negligible.
- The components are well insulated and hence are taken as adiabatic.
- Steady-state, steady-flow operating conditions exist.
- Kinetic and potential energy changes are negligible.
- Dry and ash free portion of the feed-stock is completely reacted in the gasifier.
- Dead state temperature and pressure for the base case scenario is taken as $T_0 = 25°\mathrm{C}$ and $P_0 = 101.3\ kPa$.

In this study, specific thermo-mechanical exergy is calculated through the given equation:

$$ex = h - h_0 - T_0\,(s - s_0) \quad (5.7a)$$

$$\Delta_f S^0 = s^0 - \sum_{elements} v\, s^0_{f,element} \quad (5.7b)$$

$$\Delta_f G^0 = \Delta_f H^0 - T_0 \Delta_f S^0 \quad (5.7c)$$

$$ex^{ch} = \Delta_f G^0 + \sum_{elements} v \times ex^{ch}_{element} \quad (5.7d)$$

where $\Delta_f S^0$is formation entropy (kJ/mol K), $\Delta_f G^0$ is Gibbs free energy of formation, $\Delta_\mathrm{f}\mathrm{H}^0$ is formation enthalpy (kJ/mol), $v$ is the number of moles of the element in chemical equation of formation, $ex^{ch}$ is chemical exergy (kJ/mol), subscript f represents reactants.

The subscripts $W$ and $Q$ denote the work and heat, where the other terms are given in details below:

$$\dot{E}x_Q = (1 - \frac{T_0}{T_b})\dot{Q}_{in} \quad (5.8)$$

$$\dot{E}x_w = \dot{W} \quad (5.9)$$

The general forms of the aforementioned thermodynamic balance equations are given as follows:

Mass $\sum \dot{m}_{in} = \sum \dot{m}_{out}$ (5.10a)
Energy $\sum \dot{m}_{in} h_{in} + \sum \dot{W}_{in} + \sum \dot{Q}_{in} = \sum \dot{m}_{out} h_{out} + \sum \dot{W}_{out} + \sum \dot{Q}_{out}$ (5.10b)
Entropy $\sum \dot{m}_{in} s_{in} + \sum(\dot{Q}_{in}/T_0) + \dot{S}_{gen} = \sum \dot{m}_{out} s_{out} + \sum(\dot{Q}_{out}/T_0)$ (5.10c)
Exergy $\sum \dot{m}_{in} ex_{in} + \sum \dot{W}_{in} + \sum \dot{Ex}_{Q,in} = \sum \dot{m}_{out} ex_{out} + \sum \dot{W}_{out} + \sum \dot{Ex}_{Q,out} + \dot{Ex}_{des}$ (5.10d)

where $T$ is the absolute temperature, $\dot{E}x_Q$ and $\dot{E}x_w$ are the exergy rates associated with heat transfer and work across the boundary of a control volume, respectively. The efficiencies of the systems are as follows:

The energy efficiency for single generation option:

$$\eta = \frac{Energy\ in\ output\ products}{Energy\ in\ inputs} = \frac{\dot{W}_{net}}{\dot{Q}_{in}} \tag{5.11}$$

The energy efficiency for co-generation option:

$$\eta_{cogen,I} = \frac{\dot{W}_{net} + \dot{H}_{fresh\ water}}{\dot{Q}_{in}} \tag{5.11a}$$

$$\eta_{cogen,II} = \frac{\dot{W}_{net} + \dot{Q}_{heating}}{\dot{Q}_{in}} \tag{5.11b}$$

$$\eta_{cogen,III} = \frac{\dot{W}_{net} + HHV_{FT}}{\dot{Q}_{in}} \tag{5.11c}$$

The energy efficiency for tri-generation option:

$$\eta_{trigen,I} = \frac{\dot{W}_{net} + \dot{Q}_{heating} + \dot{H}_{fresh\ water}}{\dot{Q}_{in}} \tag{5.11d}$$

$$\eta_{trigen,II} = \frac{\dot{W}_{net} + \dot{Q}_{heating} + HHV_{FT}}{\dot{Q}_{in}} \tag{5.11e}$$

The exergy efficiency for single generation option:

$$\eta_{ex} = \frac{Exergy\ in\ output\ products}{Exergy\ in\ inputs} = \frac{\dot{W}_{net}}{\dot{Ex}_{Q_{in}}} \tag{5.12}$$

The exergy efficiency for co-generation option:

$$\eta_{ex,cogen,I} = \frac{\dot{W}_{net} + \dot{Ex}_{fresh\ water}}{\dot{Ex}_{in}} \tag{5.12a}$$

$$\eta_{ex,cogen,II} = \frac{\dot{W}_{net} + \dot{Ex}_{heating}}{\dot{Ex}_{in}} \tag{5.12b}$$

$$\eta_{ex,cogen,III} = \frac{\dot{W}_{net} + \dot{Ex}_{FT}^{ch}}{\dot{Ex}_{in}} \tag{5.12c}$$

The exergy efficiency for tri-generation option:

$$\eta_{ex,trigen,I} = \frac{\dot{W}_{net}+\dot{Ex}_{heating}+\dot{Ex}_{fresh\,water}}{\dot{Ex}_{in}} \tag{5.12d}$$

$$\eta_{ex,trigen,II} = \frac{\dot{W}_{net}+\dot{Ex}_{heating}+\dot{Ex}_{FT}^{ch}}{\dot{Ex}_{in}} \tag{5.12e}$$

$$\dot{W}_{net} = \dot{W}_{out} - \dot{W}_{in} \tag{5.13}$$

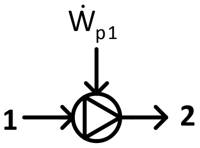

**Figure 5.1** Schematic of Pump 1 of System 1.

The molten salt that consists of 60% $NaNO_3$ and 40%-$KNO_3$ by weight exits at State 1 from the hot storage tank and is pumped to make up for the pressure lost in the tank, where $\dot{W}_{p1}$ amount of power is consumed in the process as shown in Figure 5.1. All the pumps in the system are assumed to have an isentropic efficiency of 0.80. The mass, energy, entropy and exergy balance equations are written for Pump 1 under steady-state, steady-flow conditions, where the molten salt mixture is considered to be saturated liquid at State 1.

Mass $\dot{m}_1 = \dot{m}_2$ (5.14a)
Energy $\dot{m}_1 h_1 + \dot{W}_{p1} = \dot{m}_2 h_2$ (5.14b)
Entropy $\dot{m}_1 s_1 + \dot{S}_{gen,p1} = \dot{m}_2 s_2$ (5.14c)
Exergy $\dot{m}_1 ex_1 + \dot{W}_{p1} = \dot{m}_2 ex_2 + \dot{Ex}_{des,p1}$ (5.14d)

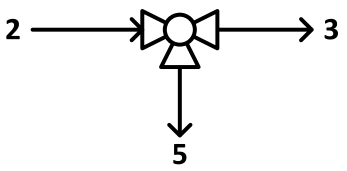

**Figure 5.2** Schematic of 3-way Valve of System 1.

Subsequently, the molten salt mixture (60%$NaNO_3$, 40%$KNO_3$ by wt.) is split to flow through two separate systems using a three-way Valve as shown in Figure 5.2. For the three-way Valve of System 1, the balance equations are provided under steady-state, steady-flow conditions, where the enthalpy and the pressure of the molten-salt mixture remain constant.

Mass $\dot{m}_2 = \dot{m}_3 + \dot{m}_5$ (5.15a)
Energy $\dot{m}_2 h_2 = \dot{m}_3 h_3 + \dot{m}_5 h_5$ (5.15b)
Entropy $\dot{m}_2 s_2 + \dot{S}_{gen,v} = \dot{m}_3 s_3 + \dot{m}_5 s_5$ (5.15c)
Exergy $\dot{m}_2 ex_2 = \dot{m}_3 ex_3 + \dot{m}_5 ex_5 + \dot{E}x_{des,v}$ (5.15d)

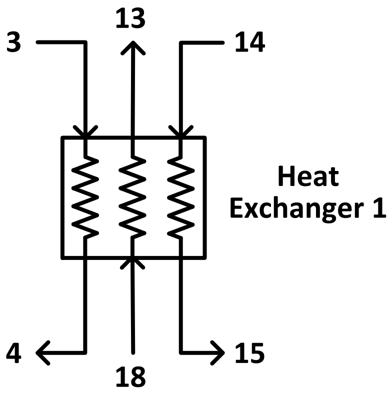

**Figure 5.3** Schematic of Heat Exchanger 1 of System 1.

One portion of the splitted fluid (State 3) passes through Heat Exchanger 1 and goes through a phase change in the process to transfer the latent heat into the Steam Rankine Cycle as shown in Figure 5.3. The mass, energy, entropy and exergy balance equations are written for Heat Exchanger 1 under steady-state, steady-flow conditions, where effectiveness of Heat Exchanger 1 is considered to be 0.85.

Mass $\dot{m}_3 = \dot{m}_4 \quad ; \quad \dot{m}_{13} = \dot{m}_{18} \quad ; \quad \dot{m}_{14} = \dot{m}_{15}$ (5.16a)
Energy $\dot{m}_3 h_3 + \dot{m}_{18} h_{18} + \dot{m}_{14} h_{14} = \dot{m}_4 h_4 + \dot{m}_{13} h_{13} + \dot{m}_{15} h_{15}$ (5.16b)
Entropy $\dot{m}_3 s_3 + \dot{m}_{18} s_{18} + \dot{m}_{14} s_{14} + \dot{S}_{gen,HEx1} = \dot{m}_4 s_4 + \dot{m}_{13} s_{13} + \dot{m}_{15} s_{15}$ (5.16c)
Exergy $\dot{m}_3 ex_3 + \dot{m}_{18} ex_{18} + \dot{m}_{14} ex_{14} = \dot{m}_4 ex_4 + \dot{m}_{13} ex_{13} + \dot{m}_{15} ex_{15} + \dot{E}x_{des,HEx1}$ (5.16d)

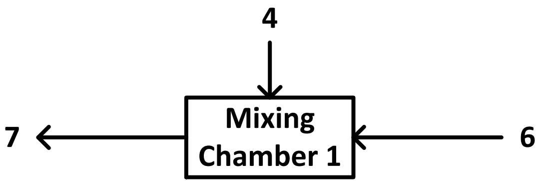

**Figure 5.4** Schematic of Mixing Chamber of System 1.

The fluids exiting from Heat Exchanger 1 (which conducts heat transfer with the Steam Rankine Cycle) and Heat Exchanger 2 (which conducts heat transfer with the desalination unit) are mixed in Mixing Chamber 1 before entering the Cold

Storage Tank as shown in Figure 5.4. The balance equations of Mixing Chamber 1 under steady-state, steady-flow conditions are written as follows:

Mass $\dot{m}_4 + \dot{m}_6 = \dot{m}_7$ (5.17a)

Energy $\dot{m}_4 h_4 + \dot{m}_6 h_6 = \dot{m}_7 h_7$ (5.17b)

Entropy $\dot{m}_4 s_4 + \dot{m}_6 s_6 + \dot{S}_{gen,m1} = \dot{m}_7 s_7$ (5.17c)

Exergy $\dot{m}_4 ex_4 + \dot{m}_6 ex_6 = \dot{m}_7 ex_7 + \dot{E}x_{des,m1}$ (5.17d)

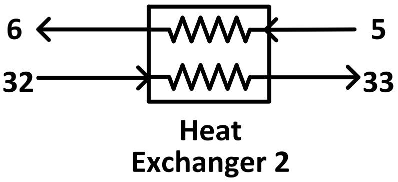

**Figure 5.5** Schematic of Heat Exchanger 2 of System 1.

The other branch of the fluid (State 5) passes through Heat Exchanger 2, where the heat of the fluid exiting from the Osmotic membrane is absorbed as shown in Figure 5.5. The mass, energy, entropy and exergy balance equations are written for Heat Exchanger 2 under steady-state, steady-flow conditions, where effectiveness of Heat Exchanger 2 is considered to be 0.85.

Mass $\dot{m}_5 = \dot{m}_6 \quad ; \quad \dot{m}_{32} = \dot{m}_{33}$ (5.18a)

Energy $\dot{m}_5 h_5 + \dot{m}_{32} h_{32} = \dot{m}_6 h_6 + \dot{m}_{33} h_{33}$ (5.18b)

Entropy $\dot{m}_5 s_5 + \dot{m}_{32} s_{32} + \dot{S}_{gen,HEx2} = \dot{m}_6 s_6 + \dot{m}_{33} s_{33}$ (5.18c)

Exergy $\dot{m}_5 ex_5 + \dot{m}_{32} ex_{32} = \dot{m}_6 ex_6 + \dot{m}_{33} ex_{33} + \dot{E}x_{des,HEx2}$ (5.18d)

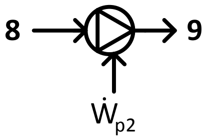

**Figure 5.6** Schematic of Pump 2 of System 1.

Next, the molten salt mixture passes through Pump 2 to compensate for the pressure lost in the Cold Storage Tank, where $\dot{W}_{p2}$ amount of power is consumed in the process as shown in Figure 5.6. The mass, energy, entropy and exergy balance equations are written for Pump 2 under steady-state, steady-flow conditions, where the molten salt mixture is considered to be saturated liquid at State 8.

Mass $\dot{m}_8 = \dot{m}_9$ (5.19a)

Energy $\dot{m}_8 h_8 + \dot{W}_{p2} = \dot{m}_9 h_9$ (5.19b)

Entropy $\dot{m}_8 s_8 + \dot{S}_{gen,p2} = \dot{m}_9 s_9$ (5.19c)

Exergy $\dot{m}_8 ex_8 + \dot{W}_{p2} = \dot{m}_9 ex_9 + \dot{E}x_{des,p2}$ (5.19d)

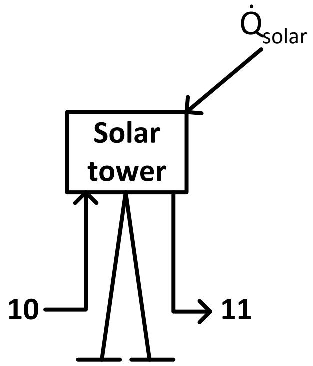

**Figure 5.7** Schematic of Solar Tower of System 1.

The mixture then runs through the Solar Tower, where it absorbs solar radiation and raises the temperature as shown in Figure 5.7. In the system, T$_{st}$ is assumed to be 2541 K as stated as optimum temperature elsewhere [51]. The balance equations of Solar Tower under steady-state, steady-flow conditions are written as follows:

Mass $\dot{m}_{10} = \dot{m}_{11}$ (5.20a)
Energy $\dot{m}_{10}h_{10} + \dot{Q}_{solar} = \dot{m}_{11}h_{11}$ (5.20b)
Entropy $\dot{m}_{10}s_{10} + \dot{Q}_{solar}/T_{st} + \dot{S}_{gen,st} = \dot{m}_{11}s_{11}$ (5.20c)
Exergy $\dot{m}_{10}ex_{10} + \dot{Q}_{solar}(1 - T_0/T_{st}) = \dot{m}_{11}ex_{11} + \dot{E}x_{des,st}$ (5.20d)

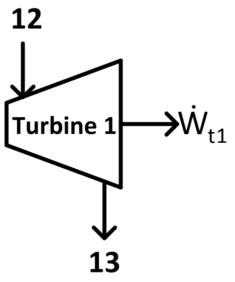

**Figure 5.8** Schematic of Turbine 1 of System 1.

The turbine is used in the Steam Rankine Cycle to generate power in the system as shown in Figure 5.8. All the turbines in the system are assumed to have an isentropic efficiency of 0.80. State 12 is in a superheated phase. Under steady-state, steady-flow conditions, the mass, energy, entropy and exergy balance equations for Turbine 1 are provided below:

Mass $\dot{m}_{12} = \dot{m}_{13}$ (5.21a)
Energy $\dot{m}_{12}h_{12} = \dot{m}_{13}h_{13} + \dot{W}_{t1}$ (5.21b)
Entropy $\dot{m}_{12}s_{12} + \dot{S}_{gen,t1} = \dot{m}_{13}s_{13}$ (5.21c)
Exergy $\dot{m}_{12}ex_{12} = \dot{m}_{13}ex_{13} + \dot{W}_{t1} + \dot{E}x_{des,t1}$ (5.21d)

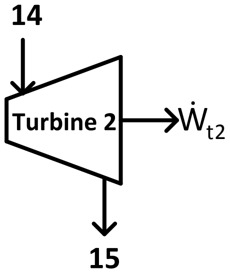

**Figure 5.9** Schematic of Turbine 2 of System 1.

After the first turbine, the water flows through the heat exchanger where it gains heat to run through Turbine 2 to generate additional power in the system as shown in Figure 5.9. Under steady-state, steady-flow conditions, the mass, energy, entropy and exergy balance equations for Turbine 2 are then written below:

Mass $\dot{m}_{14} = \dot{m}_{15}$ (5.22a)
Energy $\dot{m}_{14}h_{14} = \dot{m}_{15}h_{15} + \dot{W}_{t2}$ (5.22b)
Entropy $\dot{m}_{14}s_{14} + \dot{S}_{gen,t2} = \dot{m}_{15}s_{15}$ (5.22c)
Exergy $\dot{m}_{14}ex_{14} = \dot{m}_{15}ex_{15} + \dot{W}_{t2} + \dot{E}x_{des,t2}$ (5.22d)

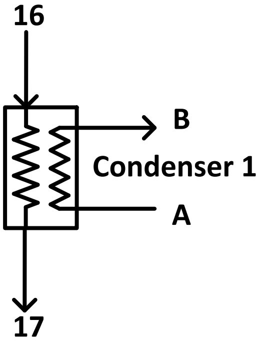

**Figure 5.10** Schematic of Condenser 1 of System 1.

After leaving Turbine 2, the water flows through Condenser 1 to release heat to complete the cycle. This heat is utilized for hot water production. It heats the water enters to the heat exchanger as State A and exits as hot water as State B as shown in Figure 5.10. The mass, energy, entropy and exergy balance equations are written for Condenser 1 under steady-state, steady-flow conditions, where effectiveness of Condenser 1 is considered to be 0.85.

Mass $\dot{m}_{15} = \dot{m}_{16}$ ; $\dot{m}_{A} = \dot{m}_{B}$ (5.23a)
Energy $\dot{m}_{15}h_{15} + \dot{m}_{A}h_{A} = \dot{m}_{16}h_{16} + \dot{m}_{B}h_{B}$ (5.23b)
Entropy $\dot{m}_{15}s_{15} + \dot{m}_{A}s_{A} + \dot{S}_{gen,Con1} = \dot{m}_{16}s_{16} + \dot{m}_{B}s_{B}$ (5.23c)
Exergy $\dot{m}_{15}ex_{15} + \dot{m}_{A}ex_{A} = \dot{m}_{16}ex_{16} + \dot{m}_{B}ex_{B} + \dot{E}x_{des,Con1}$ (5.23d)

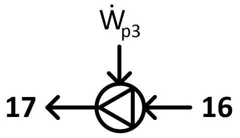

**Figure 5.11** Schematic of Pump 3 of System 1.

Next, the water is pumped through Pump 3 to make up for the pressure losses in the cycle as shown in Figure 5.11. Isentropic efficiency of the pump is taken as 80%. The mass, energy, entropy and exergy balance equations are written for Pump 3 under steady-state, steady-flow conditions, where water is considered to be saturated liquid at State 16.

Mass $\dot{m}_{16} = \dot{m}_{17}$ (5.24a)
Energy $\dot{m}_{16}h_{16} + \dot{W}_{p3} = \dot{m}_{17}h_{17}$ (5.24b)
Entropy $\dot{m}_{16}s_{16} + \dot{S}_{gen,p3} = \dot{m}_{17}s_{17}$ (5.24c)
Exergy $\dot{m}_{16}ex_{16} + \dot{W}_{p3} = \dot{m}_{17}ex_{17} + \dot{E}x_{des,p3}$ (5.24d)

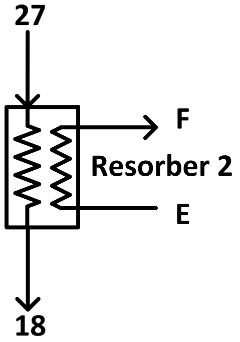

**Figure 5.12** Schematic of Resorber 2 of System 1.

In the Organic Rankine Cycle sub-system, ammonia-water mixture with 23% ammonia mass fraction runs through Resorber 2 as shown in Figure 5.12. The mixture that leaves Resorber two is in liquid phase. The mass, energy, entropy and exergy balance equations are written for Resorber 2 under steady-state, steady-flow conditions, where effectiveness of Resorber 2 is considered to be 0.85.

Mass $\dot{m}_{27} = \dot{m}_{18} \quad ; \quad \dot{m}_E = \dot{m}_F$ (5.25a)
Energy $\dot{m}_{27}h_{27} + \dot{m}_E h_E = \dot{m}_{18}h_{18} + \dot{m}_F h_F$ (5.25b)
Entropy $\dot{m}_{27}s_{27} + \dot{m}_E s_E + \dot{S}_{gen,Res2} = \dot{m}_{18}s_{18} + \dot{m}_F s_F$ (5.25c)
Exergy $\dot{m}_{27}ex_{27} + \dot{m}_E ex_E = \dot{m}_{18}ex_{18} + \dot{m}_F ex_F + \dot{E}x_{des,Res2}$ (5.25d)

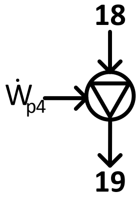

**Figure 5.13** Schematic of Pump 4 of System 1.

The 23% ammonia-water mixture is then runs through the pump before entering Heat Exchanger 4 as shown in Figure 5.13. The mass, energy, entropy and exergy balance equations are written for Pump 4 under steady-state, steady-flow conditions, where the ammonia-water mixture is considered to be saturated liquid at State 18.

Mass $\dot{m}_{18} = \dot{m}_{19}$ (5.26a)
Energy $\dot{m}_{18}h_{18} + \dot{W}_{p4} = \dot{m}_{19}h_{19}$ (5.26b)
Entropy $\dot{m}_{18}s_{18} + \dot{S}_{gen,p4} = \dot{m}_{19}s_{19}$ (5.26c)
Exergy $\dot{m}_{18}ex_{18} + \dot{W}_{p4} = \dot{m}_{19}ex_{19} + \dot{E}x_{des,p4}$ (5.26d)

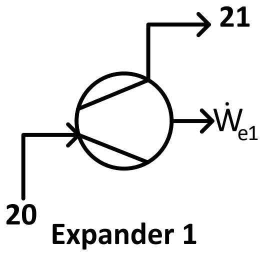

**Figure 5.14** Schematic of Expander 1 of System 1.

After leaving Heat Exchanger 4, the ORC mixture runs through the expander to generate power as shown in Figure 5.14. Under steady-state, steady-flow conditions, the mass, energy, entropy and exergy balance equations for Expander 1 are expressed in the following forms:

Mass $\dot{m}_{20} = \dot{m}_{21}$ (5.27a)
Energy $\dot{m}_{20}h_{20} = \dot{m}_{21}h_{21} + \dot{W}_{e1}$ (5.27b)
Entropy $\dot{m}_{20}s_{20} + \dot{S}_{gen,e1} = \dot{m}_{21}s_{21}$ (5.27c)
Exergy $\dot{m}_{20}ex_{20} = \dot{m}_{21}ex_{21} + \dot{W}_{e1} + \dot{E}x_{des,e1}$ (5.27d)

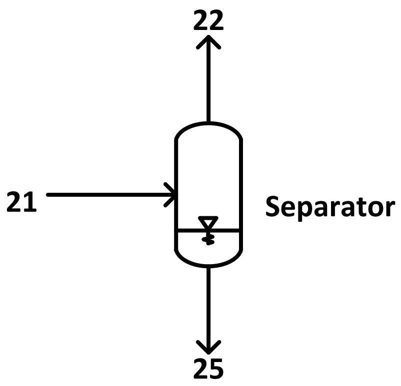

**Figure 5.15** Schematic of Seperator of System 1.

At State 21, ammonia mass fraction in the mixture is 23%. In Seperator, this mixture is separated into vapor (State 22) and liquid (State 25) phases. In the vapor phase, ammonia mass fraction becomes 33%, where it becomes 6% the liquid phase as shown in Figure 5.15. The balance equations of Seperator under steady-state, steady-flow conditions are defined as follows:

Mass $\dot{m}_{21} = \dot{m}_{22} + \dot{m}_{25}$ (5.28a)
Energy $\dot{m}_{21}h_{21} = \dot{m}_{22}h_{22} + \dot{m}_{25}h_{25}$ (5.28b)
Entropy $\dot{m}_{21}s_{21} + \dot{S}_{gen,Sep} = \dot{m}_{22}s_{22} + \dot{m}_{25}s_{25}$ (5.28c)
Exergy $\dot{m}_{21}ex_{21} = \dot{m}_{22}ex_{22} + \dot{m}_{25}ex_{25} + \dot{Ex}_{des,Sep}$ (5.28d)

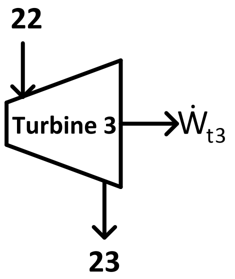

**Figure 5.16** Schematic of Turbine 3 of System 1.

The 33% ammonia contsaining mixture from State 22 runs through Turbine 3 to generate power as shown in Figure 5.16. Under steady-state, steady-flow conditions, the mass, energy, entropy and exergy balance equations for Turbine 3 are written as follows:

Mass $\dot{m}_{22} = \dot{m}_{23}$ (5.29a)
Energy $\dot{m}_{22}h_{22} = \dot{m}_{23}h_{23} + \dot{W}_{t3}$ (5.29b)
Entropy $\dot{m}_{22}s_{22} + \dot{S}_{gen,t3} = \dot{m}_{23}s_{23}$ (5.29c)
Exergy $\dot{m}_{22}ex_{22} = \dot{m}_{23}ex_{23} + \dot{W}_{t3} + \dot{Ex}_{des,t3}$ (5.29d)

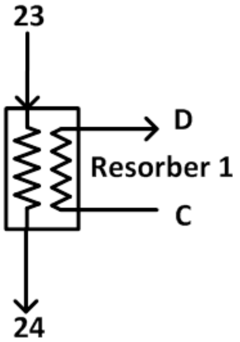

**Figure 5.17** Schematic of Resorber 1 of System 1.

The mixture exiting Turbine 3 enters Resorber 1 and provides heating to water supply as presented in Figure 5.17. The mass, energy, entropy and exergy balance equations are written for Resorber 1 under steady-state, steady-flow conditions, where effectiveness of Resorber 1 is considered to be 0.85.

Mass $\dot{m}_{23} = \dot{m}_{24} \quad ; \quad \dot{m}_C = \dot{m}_D$ (5.30a)
Energy $\dot{m}_{23}h_{23} + \dot{m}_C h_C = \dot{m}_{24}h_{24} + \dot{m}_D h_D$ (5.30b)
Entropy $\dot{m}_{23}s_{23} + \dot{m}_C s_C + \dot{S}_{gen,Res1} = \dot{m}_{24}s_{24} + \dot{m}_D s_D$ (5.30c)
Exergy $\dot{m}_{23}ex_{23} + \dot{m}_C ex_C = \dot{m}_{24}ex_{24} + \dot{m}_D ex_D + \dot{E}x_{des,Res1}$ (5.30d)

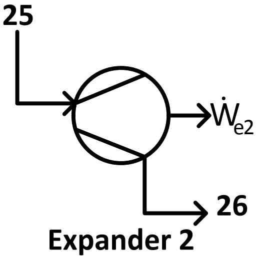

**Figure 5.18** Schematic of Expander 2 of System 1.

The 6% ammonia containing mixture at State 25, on the other hand, enters Expander 2 to generate additional power in the system as shown in Figure 5.18. All the expanders in the system are assumed to have an efficiency of 0.80. Under steady-state, steady-flow conditions, the mass, energy, entropy and exergy balance equations for Expander 2 are written as follows:

Mass $\dot{m}_{25} = \dot{m}_{26}$ (5.31a)
Energy $\dot{m}_{25}h_{25} = \dot{m}_{26}h_{26} + \dot{W}_{e2}$ (5.31b)
Entropy $\dot{m}_{25}s_{25} + \dot{S}_{gen,e2} = \dot{m}_{26}s_{26}$ (5.31c)
Exergy $\dot{m}_{25}ex_{25} = \dot{m}_{26}ex_{26} + \dot{W}_{e2} + \dot{E}x_{des,e2}$ (5.31d)

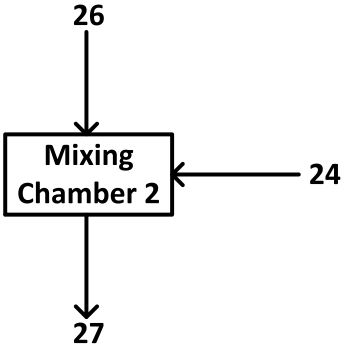

**Figure 5.19** Schematic of Mixing Chamber 2 of System 1.

After exiting Resorber 1 and Expander 2, the two different mixture concentrations that are obtained through the separator are mixed in Mixing Chamber 2 before entering Resesorber 2 in the ORC cycle as shown in Figure 5.19. The balance equations of Mixing Chamber 2 under steady-state, steady-flow conditions are defined as follows:

Mass $\dot{m}_{24} + \dot{m}_{26} = \dot{m}_{27}$ (5.32a)
Energy $\dot{m}_{24}h_{24} + \dot{m}_{26}h_{26} = \dot{m}_{27}h_{27}$ (5.32b)
Entropy $\dot{m}_{24}s_{24} + \dot{m}_{26}s_{26} + \dot{S}_{gen,m2} = \dot{m}_{27}s_{27}$ (5.32c)
Exergy $\dot{m}_{24}ex_{24} + \dot{m}_{26}ex_{26} = \dot{m}_{27}ex_{27} + \dot{E}x_{des,m2}$ (5.32d)

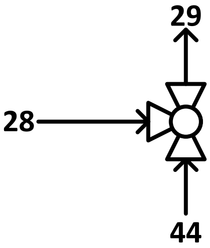

**Figure 5.20** Schematic of 3-way Valve 2 of System 1.

The saline water entering the desalination system is divided into two through the 3-way valve as shown in Figure 5.20, where one portion of the saline water enters the pre-treatment section while the other flows through the energy recovery device. For the 3-way Valve 2 of System 1, the balance equations are provided under steady-state, steady-flow conditions, where the enthalpy and the pressure of the saline water mixture remain constant.

Mass $\dot{m}_{28} + \dot{m}_{44} = \dot{m}_{29}$ (5.33a)
Energy $\dot{m}_{28}h_{28} + \dot{m}_{44}h_{44} = \dot{m}_{29}h_{29}$ (5.33b)
Entropy $\dot{m}_{28}s_{28} + \dot{m}_{44}s_{44} + \dot{S}_{gen,v2} = \dot{m}_{29}s_{29}$ (5.33c)
Exergy $\dot{m}_{28}ex_{28} + \dot{m}_{44}ex_{44} = \dot{m}_{29}ex_{29} + \dot{E}x_{des,v2}$ (5.33d)

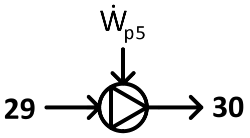

**Figure 5.21** Schematic of Pump 5 of System 1.

The saline water entering the system is pumped by Pump 5 into the Energy Recovery Device as shown in Figure 5.21. The mass, energy, entropy and exergy balance equations are written for Pump 5 under steady-state, steady-flow conditions, where the saline water is considered to be saturated liquid at State 29.

Mass $\dot{m}_{29} = \dot{m}_{30}$ (5.34a)

Energy $\dot{m}_{29}h_{29} + \dot{W}_{p5} = \dot{m}_{30}h_{30}$ (5.34b)

Entropy $\dot{m}_{29}s_{29} + \dot{S}_{gen,p5} = \dot{m}_{30}s_{30}$ (5.34c)

Exergy $\dot{m}_{29}ex_{29} + \dot{W}_{p5} = \dot{m}_{30}ex_{30} + \dot{E}x_{des,p5}$ (5.34d)

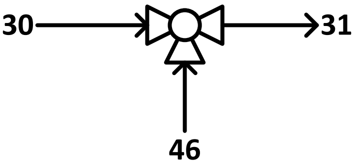

**Figure 5.22** Schematic of 3-way Valve 3 of System 1.

The saline water leaving the Energy Recovery Device is pumped into 3-way Valve 3, where it mixes with the saline water entering the system to get pre-treated as shown in Figure 5.22. For the 3-way Valve 3 of System 1, the balance equations are provided under steady-state, steady-flow conditions, where the enthalpy and the pressure of the saline water mixture remain constant.

Mass $\dot{m}_{30} + \dot{m}_{46} = \dot{m}_{31}$ (5.35a)

Energy $\dot{m}_{30}h_{30} + \dot{m}_{46}h_{46} = \dot{m}_{31}h_{31}$ (5.35b)

Entropy $\dot{m}_{30}s_{30} + \dot{m}_{46}s_{46} + \dot{S}_{gen,v3} = \dot{m}_{31}s_{31}$ (5.35c)

Exergy $\dot{m}_{30}ex_{30} + \dot{m}_{46}ex_{46} = \dot{m}_{31}ex_{31} + \dot{E}x_{des,v3}$ (5.35d)

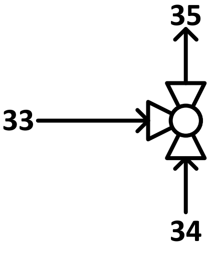

**Figure 5.23** Schematic of 3-way valve 4 of System 1.

After the saline water leaves the pre-treatment and is heated up by Heat Exchanger 2, it splits up at 3-way valve 4 to reduce the mass flow rate of the saline water entering the RO Trains as shown in Figure 5.23. For the 3-way Valve 4 of System 1, the balance equations are provided under steady-state, steady-flow conditions, where the enthalpy and the pressure of the saline water mixture remain constant.

Mass $\dot{m}_{33} + \dot{m}_{34} = \dot{m}_{35}$ (5.36a)
Energy $\dot{m}_{33}h_{33} + \dot{m}_{34}h_{34} = \dot{m}_{35}h_{35}$ (5.36b)
Entropy $\dot{m}_{33}s_{33} + \dot{m}_{34}s_{34} + \dot{S}_{gen,v4} = \dot{m}_{35}s_{35}$ (5.36c)
Exergy $\dot{m}_{33}ex_{33} + \dot{m}_{34}ex_{34} = \dot{m}_{35}ex_{35} + \dot{E}x_{des,v4}$ (5.36d)

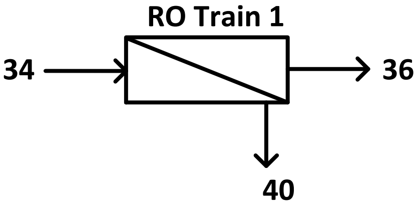

**Figure 5.24** Schematic of RO Train 1 of System 1.

The saline water enters into RO train 1 and 2 where their salinity levels are reduced significantly through the help of the membranes and is split into fresh water and concentrate as shown in Figures 5.24 and 5.25. The balance equations of RO Train 1 under steady-state, steady-flow conditions are given below:

Mass $\dot{m}_{34} = \dot{m}_{36} + \dot{m}_{40}$ (5.37a)
Energy $\dot{m}_{34}h_{34} = \dot{m}_{36}h_{36} + \dot{m}_{40}h_{40}$ (5.37b)
Entropy $\dot{m}_{34}s_{34} + \dot{S}_{gen,RO1} = \dot{m}_{36}s_{36} + \dot{m}_{40}s_{40}$ (5.37c)
Exergy $\dot{m}_{34}ex_{34} = \dot{m}_{36}ex_{36} + \dot{m}_{40}ex_{40} + \dot{E}x_{des,RO1}$ (5.37d)

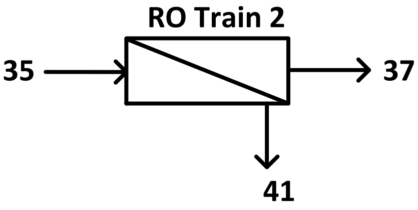

**Figure 5.25** Schematic of RO Train 2 of System 1.

The balance equations of RO Train 2 under steady-state, steady-flow conditions are written as follows:

Mass $\dot{m}_{35} = \dot{m}_{37} + \dot{m}_{41}$ (5.38a)
Energy $\dot{m}_{35}h_{35} = \dot{m}_{37}h_{37} + \dot{m}_{41}h_{41}$ (5.38b)
Entropy $\dot{m}_{35}s_{35} + \dot{S}_{gen,RO2} = \dot{m}_{37}s_{37} + \dot{m}_{41}s_{41}$ (5.38c)
Exergy $\dot{m}_{35}ex_{35} = \dot{m}_{37}ex_{37} + \dot{m}_{41}ex_{41} + \dot{E}x_{des,RO2}$ (5.38d)

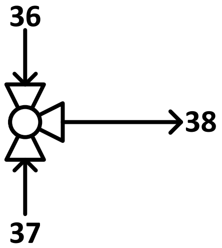

**Figure 5.26** Schematic of 3-way valve 5 of System 1.

The desalinated water that leaves the RO Train 1 and 2 are mixed in 3-way valve 5 as shown in Figure 5.26 to enter the post-treatment stage of the process. For the 3-way Valve 5 of System 1, the balance equations are provided under steady-state, steady-flow conditions, where the enthalpy and the pressure of the fresh water remain constant.

Mass $\dot{m}_{36} + \dot{m}_{37} = \dot{m}_{38}$ (5.39a)
Energy $\dot{m}_{36}h_{36} + \dot{m}_{37}h_{37} = \dot{m}_{38}h_{38}$ (5.39b)
Entropy $\dot{m}_{36}s_{36} + \dot{m}_{37}s_{37} + \dot{S}_{gen,v5} = \dot{m}_{38}s_{38}$ (5.39c)
Exergy $\dot{m}_{36}ex_{36} + \dot{m}_{37}ex_{37} = \dot{m}_{38}ex_{38} + \dot{E}x_{des,v5}$ (5.39d)

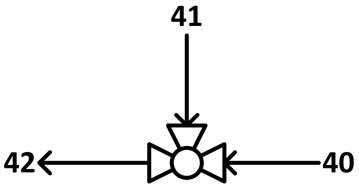

**Figure 5.27** Schematic of 3-way valve 6 of System 1.

Meanwhile, the concentrate portion of the seawater that leaves RO Train 1 and 2 are mixed in 3-way valve 6 as shown in Figure 5.27 before entering the Energy Recovery Device and discharges the system. For the 3-way Valve 6 of System 1, the balance equations are provided under steady-state, steady-flow conditions, where the enthalpy and the pressure of the condensate remain constant.

Mass $\dot{m}_{40} + \dot{m}_{41} = \dot{m}_{42}$ (5.40a)
Energy $\dot{m}_{40}h_{40} + \dot{m}_{41}h_{41} = \dot{m}_{42}h_{42}$ (5.40b)
Entropy $\dot{m}_{40}s_{40} + \dot{m}_{41}s_{41} + \dot{S}_{gen,v6} = \dot{m}_{42}s_{42}$ (5.40c)
Exergy $\dot{m}_{40}ex_{40} + \dot{m}_{41}ex_{41} = \dot{m}_{42}ex_{42} + \dot{E}x_{des,v6}$ (5.40d)

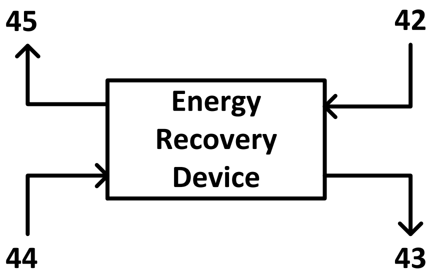

**Figure 5.28** Schematic of Energy Recovery Device of System 1.

The energy recovery device makes use of the energy of pressurized condensate (State 42) by exchanging its pressure with saline water (State 44) as shown in Figure 5.29. The analysis is performed by assuming that the condensate drives a turbine with an isentropic efficiency of 80% that drives a shaft connected to a pump with the same isentropic efficiency. This assumption is made to account for the exergy loss occuring in the device. The balance equations of Energy Recovery Device under steady-state, steady-flow conditions are written as follows:

Mass $\dot{m}_{42} = \dot{m}_{43} \quad ; \quad \dot{m}_{44} = \dot{m}_{45}$ (5.41a)

Energy $\dot{m}_{42}h_{42} + \dot{m}_{44}h_{44} = \dot{m}_{43}h_{43} + \dot{m}_{45}h_{45}$ (5.41b)

Entropy $\dot{m}_{42}s_{42} + \dot{m}_{44}s_{44} + \dot{S}_{gen,ERD} = \dot{m}_{43}s_{43} + \dot{m}_{45}s_{45}$ (5.41c)

Exergy $\dot{m}_{42}ex_{42} + \dot{m}_{44}ex_{44} = \dot{m}_{43}ex_{43} + \dot{m}_{45}ex_{45} + \dot{E}x_{des,ERD}$ (5.41d)

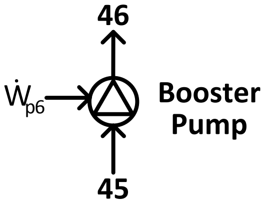

**Figure 5.29** Schematic of Booster Pump of System 1.

The saline water leaving the Energy Recovery Device goes through the Booster Pump as shown in Figure 5.29 to increase the pressure before mixing with the fresh seawater. The mass, energy, entropy and exergy balance equations are written for Booster Pump under steady-state, steady-flow conditions, where the saline water is considered to be saturated liquid at State 45.

Mass $\dot{m}_{45} = \dot{m}_{46}$ (5.42a)

Energy $\dot{m}_{45}h_{45} + \dot{W}_{p6} = \dot{m}_{46}h_{46}$ (5.42b)

Entropy $\dot{m}_{45}s_{45} + \dot{S}_{gen,p6} = \dot{m}_{46}s_{46}$ (5.42c)

Exergy $\dot{m}_{45}ex_{45} + \dot{W}_{p6} = \dot{m}_{46}ex_{46} + \dot{E}x_{des,p6}$ (5.42d)

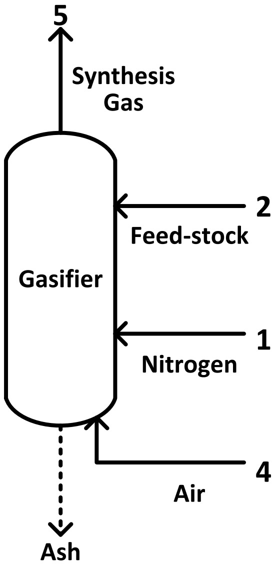

**Figure 5.30** Schematic of Gasifier of System 2.

Gasification is a process that mostly involves chemical reactions in presence of feed-stock and oxygen at high temperatures enough to breake the chemical bonds of the molecules. At the end of the reaction, this chemical bond energy comes out as heat. Therefore, chemical energy and exergy of the feed-stock and the resultant synthesis gas should be taken into account instead of thermo-mechanicacal energy and exergy. The balance equations of Gasifier under steady-state, steady-flow conditions are provided in Equations 5.43a-d.

The chemical properties of coal can be calculated by using the equations given in Section 5.2.1. In the following equations, the chemical exergy calculations for synthesis gas are written accordingly:

Mass $\dot{m}_5 = \dot{m}_1 + \dot{m}_2 + \dot{m}_4$ (5.43a)

Energy $\dot{m}_1 h_1 + \dot{m}_2 h_2 + \dot{m}_4 h_4 = \dot{m}_5 h_5$ (5.43b)

Entropy $\dot{m}_1 s_1 + \dot{m}_2 s_2 + \dot{m}_4 s_4 + \dot{S}_{gen,Gas} = \dot{m}_5 s_5$ (5.43c)

Exergy $\dot{m}_1 ex_1 + \dot{m}_2 ex_2^{ch} + \dot{m}_4 ex_4 = \dot{m}_5 ex_5^{ch} + \dot{E}x_{des,Gas}$ (5.43d)

$$ex_5^{ch} = \rho_{H2} M_{H2}\, \overline{ex}_{H2}^{ch} + \rho_{CO} M_{CO} \overline{ex}_{CO}^{ch} + \rho_{CH4} M_{CH4} \overline{ex}_{CH4}^{ch} \tag{5.43e}$$

$$\overline{ex}_{CO}^{ch} = \bar{h}_{CO}^{0} - (\bar{h}_{C}^{0} + 0.5\, \bar{h}_{O2}^{0}) - T_0\, (\bar{s}_{CO}^{0} - (\bar{s}_{C}^{0} + 0.5\, \bar{s}_{O2}^{0}) + \overline{ex}_{C}^{ch} + 0.5\, \overline{ex}_{O2}^{ch} \tag{5.43f}$$

$$\overline{ex}_{CO2}^{ch} = \bar{h}_{CO2}^{0} - (\bar{h}_{C}^{0} + \bar{h}_{O2}^{0}) - T_0 \left(\bar{s}_{CO}^{0} - (\bar{s}_{C}^{0} + \bar{s}_{O2}^{0}\right) + \overline{ex}_{C}^{ch} + \overline{ex}_{O2}^{ch} \tag{5.43g}$$

$$\overline{ex}_{CH4}^{ch} = \bar{h}_{CH4}^{0} - (\bar{h}_{C}^{0} + 2\, \bar{h}_{H2}^{0}) - T_0 \left(\bar{s}_{CO}^{0} - (\bar{s}_{C}^{0} + 2\bar{s}_{H2}^{0}\right) + \overline{ex}_{C}^{ch} + 2\, \overline{ex}_{H2}^{ch} \tag{5.43h}$$

where $M_{CO}$ is molar mass (kg/kmol) of carbon monoxide, $h^0$ is enthalpy (kJ/kmol), $s^0$ is the entropy (kJ/kmol-K), $ex^{ch}$ is chemical exergy (kJ/kmol) of the corresponding substance at 25°C and 101.3 kPa, the bar accent represents molar basis, ρ is the mass concentration (wt.%) of the substance.

State 2 is considered as a mixture of dry, ash-free feedstock, moisture and ash to model gasification in a molar basis. At State 5, the composition of the synthesis gas that consists of hydrogen, carbon monoxide, carbon dioxide, nitrogen, methane, ash and trace amounts of sulfur compounds is retrived from the gasification experiment results. Tunçbilek-Ömerler coal is chosen for base-case calculations. The amount of ash is calculated such that all of the ash is assumed to come out from the cyclone as State 6 as shown in Figure 5.30.

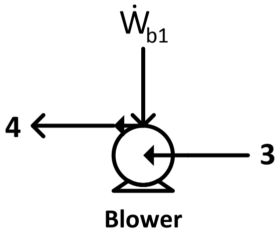

**Figure 5.31** Schematic of Blower of System 2.

In State 1, fresh air enters the system and goes through the blower before reaching the gasifier to force air into the gasifier as shown in Figure 5.31. The mass, energy, entropy and exergy balance equations are written for the blower under steady-state, steady-flow conditions.

Mass $\dot{m}_3 = \dot{m}_4$ (5.44a)

Energy $\dot{m}_3 h_3 + \dot{W}_{b1} = \dot{m}_4 h_4$ (5.44b)

Entropy $\dot{m}_3 s_3 + \dot{S}_{gen,b1} = \dot{m}_4 s_4$ (5.44c)

Exergy $\dot{m}_3 ex_3 + \dot{W}_{b1} = \dot{m}_4 ex_4 + \dot{E}x_{des,b1}$ (5.44d)

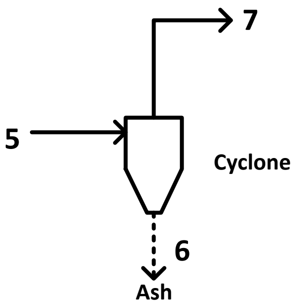

**Figure 5.32** Schematic of Cyclone of System 2.

The synthesis gas leaving the gasifier enters the cyclone, where the ash, with the composition of 62% $SiO_2$, 21% $Al_2O_3$, 11% $Fe_2O_3$, 6% MgO, is disposed from the system as shown in Figure 5.32. As a result the composition in State 7 becomes the same as State 5, but without ash content in the baseline scenario [106]. The balance equations of Cyclone under steady-state, steady-flow conditions are written in the following equstions:

Mass $\dot{m}_5 = \dot{m}_6 + \dot{m}_7$ (5.45a)
Energy $\dot{m}_5 h_5 = \dot{m}_6 h_6 + \dot{m}_7 h_7$ (5.45b)
Entropy $\dot{m}_5 s_5 + \dot{S}_{gen,Cyc} = \dot{m}_6 s_6 + \dot{m}_7 s_7$ (5.45c)
Exergy $\dot{m}_5 ex_5 = \dot{m}_6 ex_6 + \dot{m}_7 ex_7 + \dot{E}x_{des,Cyc}$ (5.45d)

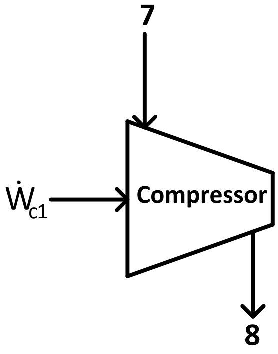

**Figure 5.33** Schematic of Compressor 1 of System 2.

The synthesis gas that leaves the cyclone at State 7 enters the compressor before reaching the acid gas removal stage as shown in Figure 5.33. The mass, energy, entropy and exergy balance equations for Compressor 1 are given under steady-state, steady-flow conditions as follows:

Mass $\dot{m}_7 = \dot{m}_8$ (5.46a)
Energy $\dot{m}_7 h_7 + \dot{W}_{c1} = \dot{m}_8 h_8$ (5.46b)
Entropy $\dot{m}_7 s_7 + \dot{S}_{gen,c1} = \dot{m}_8 s_8$ (5.46c)
Exergy $\dot{m}_7 ex_7 + \dot{W}_{c1} = \dot{m}_8 ex_8 + \dot{E}x_{des,c1}$ (5.46d)

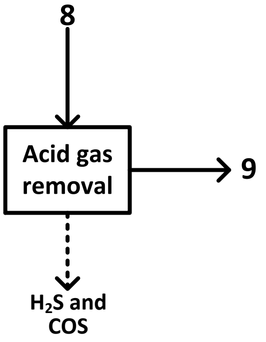

**Figure 5.34** Schematic of Acid Gas Removal of System 2.

$H_2S$ and COS are found in trace amounts in synthesis gas. It is assumed that the mass flow rate does not change between States 8 and 9 (shown in Figure 5.34). On the other hand, a power input is taken into account as 180 kJ/kg as given elsewhere [107]. The balance equations of Acid Gas Removal under steady-state, steady-flow conditions are listed here:

Mass $\dot{m}_8 = \dot{m}_9$ (5.47a)
Energy $h_8 = h_9$ (5.47b)
Entropy $s_8 = s_9$ (5.47c)
Exergy $ex_8 = ex_9$ (5.47d)

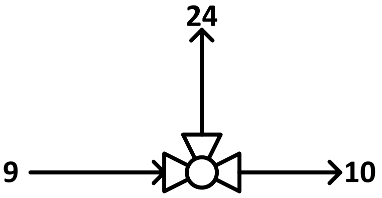

**Figure 5.35** Schematic of 3-way Valve of System 2.

Once the trace amounts of $H_2S$ and COS are removed from the synthesis gas, it is distributed equally among the Fischer-Tropsch Synthesis and Brayton Cycle in States 24 and 10 respectively as shown in Figure 5.35. For the 3-way Valve of System 2, the balance equations are provided under steady-state, steady-flow conditions, where the enthalpy and the pressure of the synthesis gas mixture remain constant.

Mass $\dot{m}_9 = \dot{m}_{10} + \dot{m}_{24}$ (5.48a)
Energy $h_9 = h_{10} + h_{24}$ (5.48b)
Entropy $\dot{m}_9 s_9 + \dot{S}_{gen,v} = \dot{m}_{10} s_{10} + \dot{m}_{24} s_{24}$ (5.48c)
Exergy $\dot{m}_9 ex_9 = \dot{m}_{10} ex_{10} + \dot{m}_{24} ex_{24} + \dot{E}x_{des,v}$ (5.48d)

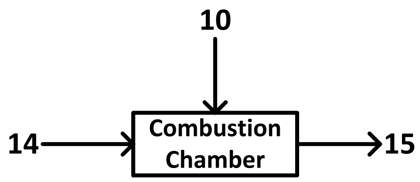

**Figure 5.36** Schematic of Combustion Chamber of System 2.

In the combustion process, the synthesis gas coming from the gasifier is combusted in presence of compressed air shown as State 14. To simplify the calculations, State 15 is assumed to be hot air, whose temperature is raised by the heat of combustion occurring in the combustion chamber. This heat is the higher heating value of the synthesis gas mixture. The balance equations of Combustion Chamber under steady-state, steady-flow conditions are provided in Equations 5.49a-d. Also, in the chemical exergy calculations, the chemical exergy of the synthesis gas is calculated through the Equations 5.49e-h.

Mass $\dot{m}_{10}+\dot{m}_{14} = \dot{m}_{15}$ (5.49a)

Energy $\dot{m}_{10}h_{10} + \dot{m}_{14}h_{14} = \dot{m}_{15}h_{15}$ (5.49b)

Entropy $\dot{m}_{10}s_{10} + \dot{m}_{14}s_{14} + \dot{S}_{gen,cc} = \dot{m}_{15}s_{215}$ (5.49c)

Exergy $\dot{m}_{10}ex_{10}^{ch}+\dot{m}_{14}ex_{14} = \dot{m}_{15}ex_{15} + \dot{E}x_{des,cc}$ (5.49d)

$$ex_{10}^{ch} = \rho_{H2}M_{H2}\,\overline{ex}_{H2}^{ch} + \rho_{CO}M_{CO}\overline{ex}_{CO}^{ch} + \rho_{CH4}M_{CH4}\overline{ex}_{CH4}^{ch} \quad (5.49e)$$

$$\overline{ex}_{CO}^{ch} = \bar{h}_{CO}^{0} - (\bar{h}_{C}^{0} + 0.5\,\bar{h}_{O2}^{0}) - T_0\,(\bar{s}_{CO}^{0} - (\bar{s}_{C}^{0} + 0.5\,\bar{s}_{O2}^{0}) + \overline{ex}_{C}^{ch} + 0.5\,\overline{ex}_{O2}^{ch} \quad (5.49f)$$

$$\overline{ex}_{CO2}^{ch} = \bar{h}_{CO2}^{0} - (\bar{h}_{C}^{0} + \bar{h}_{O2}^{0}) - T_0\left(\bar{s}_{CO}^{0} - (\bar{s}_{C}^{0} + \bar{s}_{O2}^{0}\right) + \overline{ex}_{C}^{ch} + \overline{ex}_{O2}^{ch} \quad (5.49g)$$

$$\overline{ex}_{CH4}^{ch} = \bar{h}_{CH4}^{0} - (\bar{h}_{C}^{0} + 2\,\bar{h}_{H2}^{0}) - T_0\left(\bar{s}_{CO}^{0} - (\bar{s}_{C}^{0} + 2\bar{s}_{H2}^{0}\right) + \overline{ex}_{C}^{ch} + 2\,\overline{ex}_{H2}^{ch} \quad (5.49h)$$

where $M_{CO}$ is molar mass (kg/kmol) of carbon monoxide, $h^0$ is enthalpy (kJ/kmol), $s^0$ is the entropy (kJ/kmol-K), $ex^{ch}$ is chemical exergy (kJ/kmol) of the corresponding substance at 25°C and 101.3 kPa, the bar accent represents molar basis, ρ is the mass concentration (wt.%) of the substance.

The synthesis gas from State 10 enters the combustion chamber along with air leaving the high pressure compressor as shown in Figure 5.36. The amount of oxygen is calculated by chemical reaction balance and it is assumed that 20% more air is provided for better combustion relative to the stoichiometric amount. The efficiency of combustion is taken as 90%.

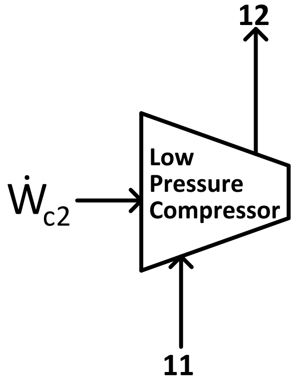

**Figure 5.37** Schematic of Low Pressıre Compressor of System 2.

In the Brayton Cycle, the fresh air initially enters the low pressure compressor before reaching the intercooler as shown in Figure 5.37. The mass, energy, entropy and exergy balance equations for Low Pressure Compressor are given under steady-state, steady-flow conditions in Equations 5.50a-d, where isentropic efficiency is taken as 0.8.

Mass $\dot{m}_{11} = \dot{m}_{12}$ (5.50a)

Energy $\dot{m}_{11}h_{11} + \dot{W}_{c2} = \dot{m}_{12}h_{12}$ (5.50b)

Entropy $\dot{m}_{11}s_{11} + \dot{S}_{gen,c2} = \dot{m}_{12}s_{12}$ (5.50c)

Exergy $\dot{m}_{11}ex_{11} + \dot{W}_{c2} = \dot{m}_{12}ex_{12} + \dot{E}x_{des,c2}$ (5.50d)

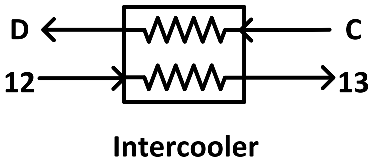

**Figure 5.38** Schematic of Intercooler of System 2.

The intercooler enables heat transfer between the air leaving the low pressure compressor and water to increase the efficiency of the cycle as shown in Figure 5.38. The heat input is taken into account when calculating energy and exergy efficiencies of Brayton cycle and the overall system efficiency. The mass, energy, entropy and exergy balance equations are written for Intercooler under steady-state, steady-flow conditions, where effectiveness of Intercooler is considered to be 0.85.

Mass $\dot{m}_{12} = \dot{m}_{13}$ ; $\dot{m}_C = \dot{m}_D$ (5.51a)

Energy $\dot{m}_{12}h_{12} + \dot{m}_C = \dot{m}_{13}h_{13} + \dot{m}_D h_D$ (5.51b)

Entropy $\dot{m}_{12}s_{12} + \dot{m}_C s_C + \dot{S}_{gen,ic} = \dot{m}_{13}s_{13} + \dot{m}_D s_D$ (5.51c)

Exergy $\dot{m}_{12}ex_{12} + \dot{m}_C ex_C = \dot{m}_{13}ex_{13} + \dot{m}_D ex_D + \dot{E}x_{des,ic}$ (5.51d)

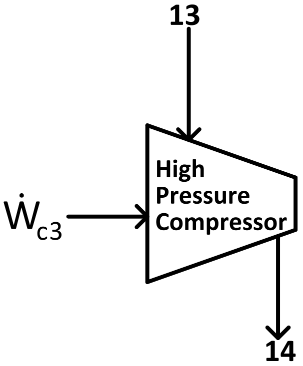

**Figure 5.39** Schematic of High Pressure Compressor of System 2.

The air then enters the high pressure compressor before the combustion chamber as shown in Figure 5.39. The mass, energy, entropy and exergy balance equations for High Pressure Compressor are given under steady-state, steady-flow conditions in Equations 5.52a-d, where isentropic efficiency is taken as 0.8.

Mass $\dot{m}_{13} = \dot{m}_{14}$ (5.52a)
Energy $\dot{m}_{13}h_{13} + \dot{W}_{c3} = \dot{m}_{14}h_{14}$ (5.52b)
Entropy $\dot{m}_{13}s_{13} + \dot{S}_{gen,c3} = \dot{m}_{14}s_{14}$ (5.52c)
Exergy $\dot{m}_{13}ex_{13} + \dot{W}_{c3} = \dot{m}_{14}ex_{14} + \dot{E}x_{des,c3}$ (5.52d)

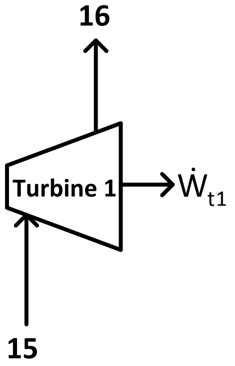

**Figure 5.40** Schematic of Turbine 1 of System 2.

On the other side of the cycle, the air leaving the combustion chamber enters the high pressure turbine as shown in Figure 5.40. The mass, energy, entropy and exergy balance equations for Turbine 1 are given under steady-state, steady-flow conditions in Equations 5.53a-d, where isentropic efficiency is taken as 0.8.

Mass $\dot{m}_{15} = \dot{m}_{16}$ (5.53a)
Energy $\dot{m}_{15}h_{15} = \dot{m}_{16}h_{16} + \dot{W}_{t1}$ (5.53b)
Entropy $\dot{m}_{15}s_{15} + \dot{S}_{gen,t1} = \dot{m}_{16}s_{16}$ (5.53c)
Exergy $\dot{m}_{15}ex_{15} = \dot{m}_{16}ex_{16} + \dot{W}_{t1} + \dot{E}x_{des,t1}$ (5.53d)

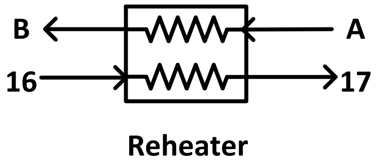

**Figure 5.41** Schematic of Reheater of System 2.

The air then flows through the reheater to provide heat exchange between the water running on the other end to improve the efficiency of the cycle as shown in Figure 5.41. The mass, energy, entropy and exergy balance equations are written for Reheater under steady-state, steady-flow conditions, where effectiveness of Reheater is considered to be 0.85.

Mass $\dot{m}_{16} = \dot{m}_{17}$ ; $\dot{m}_B = \dot{m}_B$ (5.54a)
Energy $\dot{m}_{16}h_{16} + \dot{m}_A h_A = \dot{m}_{17}h_{17} + \dot{m}_B h_B$ (5.54b)
Entropy $\dot{m}_{16}s_{16} + \dot{m}_A s_A + \dot{S}_{gen,rh} = \dot{m}_{17}s_{17} + \dot{m}_B s_B$ (5.54c)
Exergy $\dot{m}_{16}ex_{16} + \dot{m}_A ex_A = \dot{m}_{17}ex_{17} + \dot{m}_B ex_B + \dot{E}x_{des,rh}$ (5.54d)

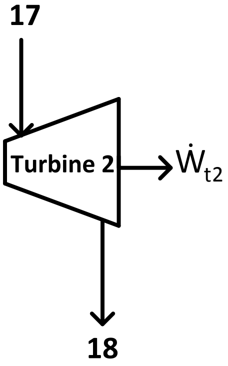

**Figure 5.42** Schematic of Turbine 2 of System 2.

The air then enters the low pressure turbine before reaching Heat Exchanger 1 as shown in Figure 5.42. The mass, energy, entropy and exergy balance equations for Turbine 2 are given under steady-state, steady-flow conditions in Equations 5.55a-d, where isentropic efficiency is assumed as 0.8.

Mass $\dot{m}_{17} = \dot{m}_{18}$ (5.55a)
Energy $\dot{m}_{17}h_{17} = \dot{m}_{18}h_{18} + \dot{W}_{t2}$ (5.55b)
Entropy $\dot{m}_{17}s_{17} + \dot{S}_{gen,t2} = \dot{m}_{18}s_{18}$ (5.55c)
Exergy $\dot{m}_{17}ex_{17} = \dot{m}_{18}ex_{18} + \dot{W}_{t2} + \dot{E}x_{des,t2}$ (5.55d)

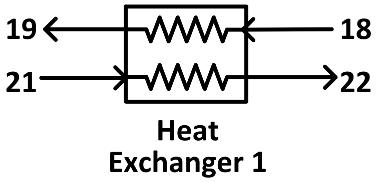

**Figure 5.43** Schematic of Heat Exchanger 1 of System 2.

The air leaving the Brayton cycle then enters Heat Exchanger 1 to heat the water in the Steam Rankine Cycle as shown in Figure 5.43. The mass, energy, entropy and exergy balance equations are written for Heat Exchanger 1 under steady-state, steady-flow conditions with an effectiveness of Heat Exchanger 1 of 0.85.

Mass $\dot{m}_{18} = \dot{m}_{19} \quad ; \quad \dot{m}_{21} = \dot{m}_{22}$ (5.56a)
Energy $\dot{m}_{18}h_{18} + \dot{m}_{21}h_{21} = \dot{m}_{19}h_{19} + \dot{m}_{22}h_{22}$ (5.56b)
Entropy $\dot{m}_{18}s_{18} + \dot{m}_{21}s_{21} + \dot{S}_{gen,HEx1} = \dot{m}_{19}s_{19} + \dot{m}_{22}s_{22}$ (5.56c)
Exergy $\dot{m}_{18}ex_{18} + \dot{m}_{21}ex_{21} = \dot{m}_{19}ex_{19} + \dot{m}_{22}ex_{22} + \dot{E}x_{dest,HEx1}$ (5.56d)

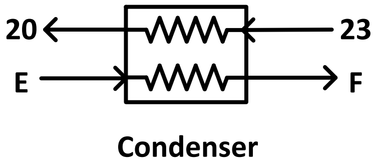

**Figure 5.44** Schematic of Condenser of System 2.

The water in the condenser is utilized to provide heating to the water in State E as shown in Figure 5.44. The mass, energy, entropy and exergy balance equations are written for Condenser under steady-state, steady-flow conditions, where effectiveness of Condenser is considered to be 0.85.

Mass $\dot{m}_{20} = \dot{m}_{23} \quad ; \quad \dot{m}_E = \dot{m}_F$ (5.57a)
Energy $\dot{m}_{20}h_{20} + \dot{m}_E h_E = \dot{m}_{23}h_{23} + \dot{m}_F h_F$ (5.57b)
Entropy $\dot{m}_{20}s_{20} + \dot{m}_E s_E + \dot{S}_{gen,Con} = \dot{m}_{23}s_{23} + \dot{m}_F s_F$ (5.57c)
Exergy $\dot{m}_{20}ex_{20} + \dot{m}_E ex_E = \dot{m}_{23}ex_{23} + \dot{m}_F ex_F + \dot{E}x_{des,Con}$ (5.57d)

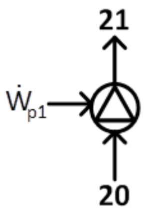

**Figure 5.45** Schematic of Pump of System 2.

The water goes through a pump before entering Heat Exchanger 1 to make up for the pressure losses in between as shown in Figure 5.45. The mass, energy, entropy and exergy balance equations are written for Pump 1 under steady-state, steady-flow conditions, where water is considered to be saturated liquid at State 20.

Mass $\dot{m}_{20} = \dot{m}_{21}$ (5.58a)
Energy $\dot{m}_{20}h_{20} + \dot{W}_{p1} = \dot{m}_{21}h_{21}$ (5.58b)
Entropy $\dot{m}_{20}s_{20} + \dot{S}_{gen,p1} = \dot{m}_{21}s_{21}$ (5.58c)
Exergy $\dot{m}_{20}ex_{20} + \dot{W}_{p1} = \dot{m}_{21}ex_{21} + \dot{Ex}_{des,p1}$ (5.58d)

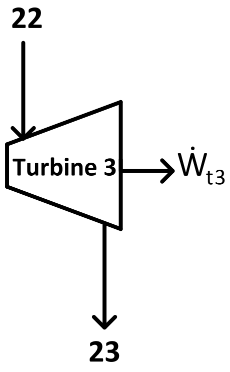

**Figure 5.46** Schematic of Turbine 3 of System 2.

Turbine 3 is utilized in the Steam Rankine Cycle to produce additional power from the system as shown in Figure 5.46. The mass, energy, entropy and exergy balance equations for Turbine 3 are given under steady-state, steady-flow conditions in Equations 5.59a-d, where isentropic efficiency is assumed as 0.8.

Mass $\dot{m}_{22} = \dot{m}_{23}$ (5.59a)
Energy $\dot{m}_{22}h_{22} = \dot{m}_{23}h_{23} + \dot{W}_{t3}$ (5.59b)
Entropy $\dot{m}_{22}s_{22} + \dot{S}_{gen,t3} = \dot{m}_{23}s_{23}$ (5.59c)
Exergy $\dot{m}_{22}ex_{22} = \dot{m}_{23}ex_{23} + \dot{W}_{t3} + \dot{Ex}_{des,t3}$ (5.59d)

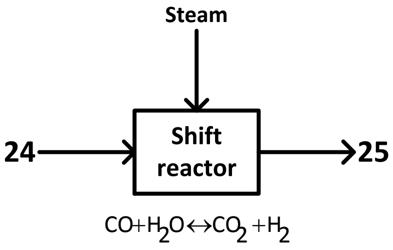

**Figure 5.47** Schematic of Shift Reactor of System 2.

Meanwhile, the remaining synthesis gas (half of the total synthesis gas) that does not enter the combustion chamber reaches the shift reactor (shown in Figure 5.47) to increase its $H_2$/CO ratio to 2 before entering the FT reactor. The temperature of the shift reactor, $T_{sr}$, is taken as same as $T_{24}$. $\dot{Q}_{steam}$ is the heat rate required to heat the water from the dead state temperature to $T_{24}$. The balance equations of Shift Reactor under steady-state, steady-flow conditions are written as

Mass $\dot{m}_{24} = \dot{m}_{25}$ (5.60a)

Energy $\dot{m}_{24}h_{24} + \dot{Q}_{steam} = \dot{m}_{25}h_{25}$ (5.60b)

Entropy $\dot{m}_{24}s_{24} + \dot{Q}_{steam}/T_{sr} + \dot{S}_{gen,sr} = \dot{m}_{25}s_{25}$ (5.60c)

Exergy $\dot{m}_{24}ex_{24} + \dot{Q}_{steam}(1 - T_0/T_{sr}) = \dot{m}_{25}ex_{25} + \dot{Ex}_{des,sr}$ (5.60d)

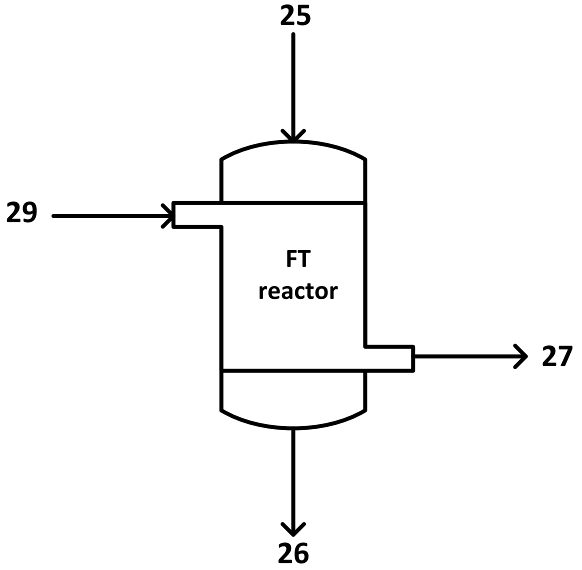

**Figure 5.48** Schematic of FT Reactor of System 2.

In the FT reactor, it is assumed that iron-based catalyst is used, while this catalyst enters and exits the reaction with the same amount and only accelerates the reaction. Since the reactions are exothermic, the heat is transferred to a water cycle through a heat exchanger, which is heated up to a sufficient temperature level to drive the ORC in the process shown in Figure 5.48. State 25 is sulfur-free synthesis gas, which enters the FT reactor. State 26 is a mixture of hydrocarbons, mainly olefins and paraffins, which can be introduced to chemical cracking to obtain gasoline and diesel fuel. The balance equations of FT reactor under steady-state, steady-flow conditions are written as follows:

Mass $\dot{m}_{25} = \dot{m}_{26} \quad ; \quad \dot{m}_{27} = \dot{m}_{29}$ (5.61a)

Energy $\dot{m}_{25}h_{25} + \dot{m}_{29}h_{29} = \dot{m}_{26}h_{26} - \dot{m}_{27}h_{27}$ (5.61b)

Entropy $\dot{m}_{25}s_{25} + \dot{m}_{29}s_{29} + \dot{S}_{gen,FT} = \dot{m}_{26}s_{26} + \dot{m}_{27}s_{27}$ (5.61c)

Exergy $\dot{m}_{25}ex_{25}^{ch} + \dot{m}_{29}ex_{29} = \dot{m}_{26}ex_{26}^{ch} + \dot{m}_{27}ex_{27} + \dot{Ex}_{des,FT}$ (5.61d)

$ex_{25}^{ch} = \rho_{H2}M_{H2}\,\overline{ex}_{H2}^{ch} + \rho_{CO}M_{CO}\overline{ex}_{CO}^{ch} + \rho_{CH4}M_{CH4}\overline{ex}_{CH4}^{ch}$ (5.61e)

$$\overline{ex}_{CO}^{ch} = \bar{h}_{CO}^{0} - (\bar{h}_{C}^{0} + 0.5\,\bar{h}_{O2}^{0}) - T_0\,(\bar{s}_{CO}^{0} - (\bar{s}_{C}^{0} + 0.5\,\bar{s}_{O2}^{0}) + \overline{ex}_{C}^{ch} + 0.5\overline{ex}_{O2}^{ch} \quad (5.61f)$$

$$\overline{ex}_{CO2}^{ch} = \overline{h}_{CO2}^{0} - (\overline{h}_{C}^{0} + \overline{h}_{O2}^{0}) - T_0\left(\bar{s}_{CO}^{0} - (\bar{s}_{C}^{0} + \bar{s}_{O2}^{0}\right) + \overline{ex}_{C}^{ch} + \overline{ex}_{O2}^{ch} \quad (5.61g)$$

$$\overline{ex}_{CH4}^{ch} = \overline{h}_{CH4}^{0} - (\overline{h}_{C}^{0} + 2\,\overline{h}_{H2}^{0}) - T_0\left(\bar{s}_{CO}^{0} - (\bar{s}_{C}^{0} + 2\bar{s}_{H2}^{0}\right) + \overline{ex}_{C}^{ch} + 2\,\overline{ex}_{H2}^{ch} \quad (5.61h)$$

The chemical exergy of State 25 is calculated through Equations 5.61e-h. The chhamical exergy of State 26 is very complicated due to the number of hydrocarbons involved. The heating values and chemical exergies of these hydrocarbons are calculated and plotted in Chapter 6.

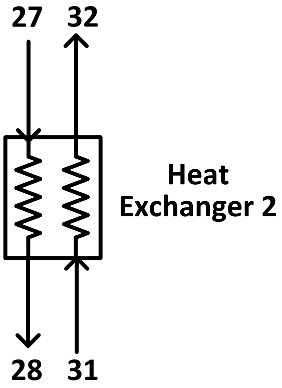

**Figure 5.49** Schematic of Heat Exchanger 2 of System 2.

The water disposed from the FT reactor enters Heat Exchanger 2, where the latent heat of water is used to heat the Organic Rankine Cycle as shown in Figure 5.49. The mass, energy, entropy and exergy balance equations are written for Heat Exchanger 2 under steady-state, steady-flow conditions, where effectiveness of Heat Exchanger 2 is considered to be 0.85.

Mass $\dot{m}_{27} = \dot{m}_{28}$ ; $\dot{m}_{31} = \dot{m}_{32}$ (5.62a)

Energy $\dot{m}_{27}h_{27} + \dot{m}_{31}h_{31} = \dot{m}_{28}h_{28} + \dot{m}_{32}h_{32}$ (5.62b)

Entropy $\dot{m}_{27}s_{27} + \dot{m}_{31}s_{31} + \dot{S}_{gen,HEx2} = \dot{m}_{28}s_{28} + \dot{m}_{32}s_{32}$ (5.62c)

Exergy $\dot{m}_{27}ex_{27} + \dot{m}_{31}ex_{31} = \dot{m}_{28}ex_{28} + \dot{m}_{32}ex_{32} + \dot{Ex}_{dest,HEx2}$ (5.62d)

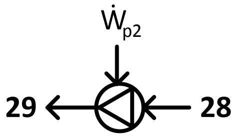

**Figure 5.50** Schematic of Pump of System 2.

The water leaving Heat Exchanger 1 then enters the pump before being recycled in the FT reactor as shown in Figure 5.50. The mass, energy, entropy and exergy balance equations are written for Pump 2 under steady-state, steady-flow conditions, where water is considered to be saturated liquid at State 28.

Mass $\dot{m}_{28} = \dot{m}_{29}$ (5.63a)
Energy $\dot{m}_{28} h_{28} + \dot{W}_{p2} = \dot{m}_{29} h_{29}$ (5.63b)
Entropy $\dot{m}_{28} s_{28} + \dot{S}_{gen,p2} = \dot{m}_{29} s_{29}$ (5.63c)
Exergy $\dot{m}_{28} ex_{28} + \dot{W}_{p2} = \dot{m}_{29} ex_{29} + \dot{E}x_{des,p2}$ (5.63d)

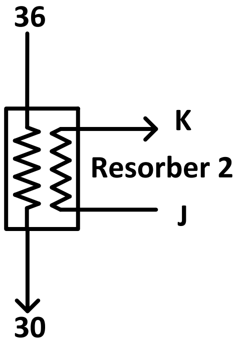

**Figure 5.51** Schematic of Resorber 2 of System 2.

State 36, which has 23% ammonia mass fraction, passes through Resorber 2 to provide heating to the industrial water supply as shown in Figure 5.51. The mass, energy, entropy and exergy balance equations are written for Resorber under steady-state, steady-flow conditions, where effectiveness of Resorber is considered to be 0.85.

Mass $\dot{m}_{36} = \dot{m}_{30} \quad ; \quad \dot{m}_C = \dot{m}_D$ (5.64a)
Energy $\dot{m}_{36} h_{36} + \dot{m}_J h_J = \dot{m}_{30} h_{30} + \dot{m}_K h_K$ (5.64b)
Entropy $\dot{m}_{36} s_{36} + \dot{m}_J s_J + \dot{S}_{gen,Res2} = \dot{m}_{30} s_{30} + \dot{m}_K s_K$ (5.64c)
Exergy $\dot{m}_{36} ex_{36} + \dot{m}_J ex_J = \dot{m}_{30} ex_{30} + \dot{m}_K ex_K + \dot{E}x_{des,Res2}$ (5.64d)

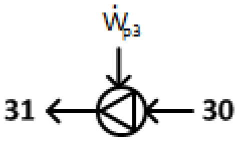

**Figure 5.52** Schematic of Pump of System 2.

The mixture then passes through the pump before entering Heat Exchanger 1 as shown in Figure 5.52. The mass, energy, entropy and exergy balance equations are written for Pump 3 under steady-state, steady-flow conditions, where ammonia-water mixture is considered to be saturated liquid at State 30.

Mass $\dot{m}_{30} = \dot{m}_{31}$ (5.65a)

Energy $\dot{m}_{30}h_{30} + \dot{W}_{p3} = \dot{m}_{31}h_{31}$ (5.65b)

Entropy $\dot{m}_{30}s_{30} + \dot{S}_{gen,p3} = \dot{m}_{31}s_{31}$ (5.65c)

Exergy $\dot{m}_{30}ex_{30} + \dot{W}_{p3} = \dot{m}_{31}ex_{31} + \dot{E}x_{des,p3}$ (5.65d)

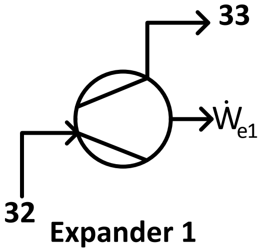

**Figure 5.53** Schematic of Expander 1of System 2.

The mixture enters Expander 1 to generate additional power as shown in Figure 5.53. The mass, energy, entropy and exergy balance equations for Expander 1 are given under steady-state, steady-flow conditions in Equations 5.66a-d, where isentropic efficiency is assumed as 0.8.

Mass $\dot{m}_{32} = \dot{m}_{33}$ (5.66a)

Energy $\dot{m}_{32}h_{32} = \dot{m}_{33}h_{33} + \dot{W}_{e1}$ (5.66b)

Entropy $\dot{m}_{32}s_{32} + \dot{S}_{gen,e1} = \dot{m}_{33}s_{33}$ (5.66c)

Exergy $\dot{m}_{32}ex_{32} = \dot{m}_{33}ex_{33} + \dot{W}_{e1} + \dot{E}x_{des,e1}$ (5.66d)

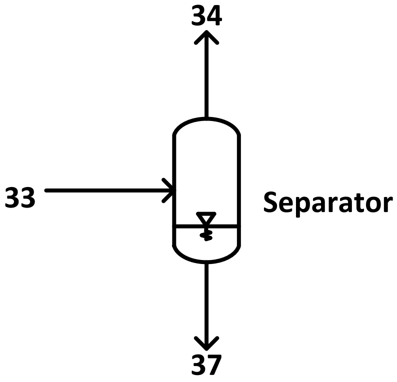

**Figure 5.54** Schematic of Seperator of System 2.

The mixture leaving the expander enters the separator, where it is divided into State 34 (with an ammonia mass fraction of 56%) and State 37 (with an ammonia mass fraction of 13%) as shown in Figure 5.54. The balance equations of Separator under steady-state, steady-flow conditions are given below:

Mass $\dot{m}_{33} = \dot{m}_{34} + \dot{m}_{37}$ (5.67a)
Energy $\dot{m}_{33}h_{33} = \dot{m}_{34}h_{34} + \dot{m}_{37}h_{37}$ (5.67b)
Entropy $\dot{m}_{33}s_{33} + \dot{S}_{gen,Sep} = \dot{m}_{34}s_{34} + \dot{m}_{37}s_{37}$ (5.67c)
Exergy $\dot{m}_{33}ex_{33} = \dot{m}_{34}ex_{34} + \dot{m}_{37}ex_{37} + \dot{E}x_{des,Sep}$ (5.67d)

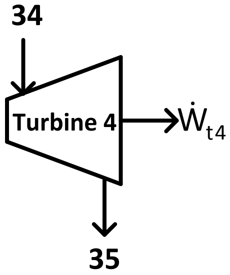

**Figure 5.55** Schematic of Turbine 4 of System 2.

The mixture leaving State 34 enters the turbine to produce additional power as shown in Figure 5.55. The mass, energy, entropy and exergy balance equations for Turbine 4 are given under steady-state, steady-flow conditions in Equations 5.68a-d, where isentropic efficiency is assumed as 0.8.

Mass $\dot{m}_{34} = \dot{m}_{35}$ (5.68a)
Energy $\dot{m}_{34}h_{34} = \dot{m}_{35}h_{35} + \dot{W}_{t4}$ (5.68b)
Entropy $\dot{m}_{34}s_{34} + \dot{S}_{gen,t4} = \dot{m}_{35}s_{35}$ (5.68c)
Exergy $\dot{m}_{34}ex_{34} = \dot{m}_{35}ex_{35} + \dot{W}_{t4} + \dot{E}x_{des,t4}$ (5.68d)

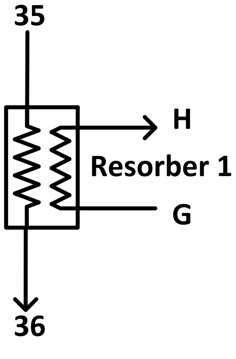

**Figure 5.56** Schematic of Resorber 1 of System 2.

The ammonia-water mixture leaving the turbine enters Resorber 1, where it provides useful heat to the water supply as shown in Figure 5.56. The mass, energy, entropy and exergy balance equations are written for Resorber 1 under steady-state, steady-flow conditions, where effectiveness of Resorber 1 is considered to be 0.85.

Mass $\dot{m}_{35} = \dot{m}_{36} \quad ; \quad \dot{m}_G = \dot{m}_H$ (5.69a)

Energy $\dot{m}_{35}h_{35} + \dot{m}_G h_G = \dot{m}_{36}h_{36} + \dot{m}_H h_H$ (5.69b)

Entropy $\dot{m}_{35}s_{35} + \dot{m}_G s_G + \dot{S}_{gen,Res1} = \dot{m}_{36}s_{36} + \dot{m}_H s_H$ (5.69c)

Exergy $\dot{m}_{35}ex_{35} + \dot{m}_G ex_G = \dot{m}_{36}ex_{36} + \dot{m}_H ex_H + \dot{E}x_{des,Res1}$ (5.69d)

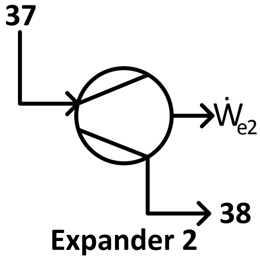

**Figure 5.57** Schematic of Expander 2 of System 2.

Meanwhile, the remaining mixture enters Expander 2 to generate additional power as shown in Figure 5.57. The mass, energy, entropy and exergy balance equations for Expander 2 are given under steady-state, steady-flow conditions in Equations 5.70a-d, where isentropic efficiency is assumed as 0.8.

Mass $\dot{m}_{37} = \dot{m}_{38}$ (5.70a)

Energy $\dot{m}_{37}h_{37} = \dot{m}_{38}h_{38} + \dot{W}_{e2}$ (5.70b)

Entropy $\dot{m}_{37}s_{37} + \dot{S}_{gen,e2} = \dot{m}_{38}s_{38}$ (5.70c)

Exergy $\dot{m}_{37}ex_{37} = \dot{m}_{38}ex_{38} + \dot{W}_{e2} + \dot{E}x_{des,e2}$ (5.70d)

## 5.2 Thermodynamic Properties

In this section, mostly chemical processes are investigated in detail. For the theoretical analysis, the properties of inputs and outputs are calculated for chemical substances such as coal, biomass, synthesis gas, and Fischer-Tropsch synthesis products. Without calculating the chemical energy and exergy of these substances, overall energy and exergy efficiencies cannot be determined.

### 5.2.1 Determination of Coal Properties

Gross calorific value (GCV), net calorific value (NCV), entropy and chemical exergy are calculated for Orhaneli–Gümüşpınar lignite. The formula based on weight percentages of main coal components [86] which estimates of the gross calorific value of coal is given below:

$$\mathrm{GCV} = 326 \times [0.198(\%\mathrm{C}) + 0.6203(\%\mathrm{H}) + 0.0809(\%S) + 0.04495(\%\mathrm{A}) - 5.153] \tag{5.71}$$

For a dry, ash-free basis GCV calculation, the formula is as follows [108], where *c*, *h*, *o*, *n*, *s* are the molar concentrations of carbon, hydrogen, oxygen, nitrogen and sulfur in kg of DAF coal basis respectively. GCV and $\mathrm{GCV_{DAF}}$ are given in MJ/kg.

$$\mathrm{GCV_{DAF}} = (151.19 \times \mathrm{h} + 98.767) \times ((\mathrm{c}/3) + \mathrm{h} - (\mathrm{o} - \mathrm{s})/8) \tag{5.72}$$

It is useful to express the net calorific value (NCV) on original basis; this can be done with the equation presented in Van Loo and Koppejan [109]:

$$\mathrm{NCV} = \mathrm{GCV}(1 - w_{\mathrm{w}}) - 2.444 w_{\mathrm{w}} - 21.839 w_{\mathrm{H}}(1 - w_{\mathrm{w}}) \tag{5.73}$$

where $w_{\mathrm{w}}$ is the moisture content by weight. The moisture content of the coals used are taken from the proximate analysis results given in Tables 3.3 and 3.4, on original basis.

The estimation of coal entropy and chemical exergy is of outmost importance for exergy analysis of energy systems involving coal combustion. For the specific exergy content of dry and ash-free coal, Mancarella and Chicco [28] give the following regression formula, based on the concentration of main elements expressed in kmol per kg dry and ash-free coal:

$$s_{\mathrm{DAF}} = c\left[37.1653 - 31.4767 \exp\left(-0.564682 \frac{h}{c+n}\right) + 20.1145 \frac{o}{c+n} + 54.3111 \frac{n}{c+n} + 44.6712 \frac{s}{c+n}\right] \tag{5.74}$$

where subscript DAF stands for dry and ash-free basis, and the entropy unit is kJ/kg-K.

The chemical exergy of coal, dry and ash-free basis can be calculated with the formula obtained by Kaygusuz as given below [110].

$$ex_{\mathrm{DAF}}^{\mathrm{ch}} = \mathrm{GCV_{DAF}} - T_0\left[s_{\mathrm{DAF}} + \left(c + \frac{1}{4}h + s - \frac{1}{2}o\right)s_{\mathrm{O_2}} - c \times s_{\mathrm{CO_2}} - \frac{1}{2}h \times s_{\mathrm{H_2O}} - s \times s_{\mathrm{SO_2}} - \frac{1}{2}n \times s_{\mathrm{N_2}}\right] + c \times ex_{\mathrm{CO_2}}^{\mathrm{ch}} + \frac{1}{2}h \times ex_{\mathrm{H_2O}}^{\mathrm{ch}} + s \times ex_{\mathrm{SO_2}}^{\mathrm{ch}} + \frac{1}{2}n \times ex_{\mathrm{N_2}}^{\mathrm{ch}} - \left(c + \frac{1}{4}h + s - \frac{1}{2}o\right)ex_{\mathrm{O_2}}^{\mathrm{ch}} \tag{5.75}$$

where the exergy value results in MJ/kg for dry coal in ash-free basis. The chemical exergy of high fixed carbon containing coals varies between 7–8.2 MJ per kg dry ash-free basis. The specific chemical exergy of coal, wet basis can be estimated with neglecting the ash content, because the contribution of ash to chemical exergy is negligible [11].

$$ex^{\mathrm{ch}} = (\%coal_{\mathrm{DAF}}) \times ex^{\mathrm{ch}}_{\mathrm{DAF}} + \frac{(\%H_2O)}{MW_{\mathrm{H_2O}}} \times ex^{\mathrm{ch}}_{\mathrm{H_2O}} \tag{5.76}$$

where $(\%coal_{\mathrm{DAF}})$ is the wt. percent of dry ash-free coal; $(\%H_2O)$ is the wt. percent of water; $MW_{H2O}$ is molecular mass of water.

### 5.2.2 Gasification

Coal, a solid fuel, is less convenient for storage and transportation than petroleum and natural gas, and usually holds undesirable compounds such as S, N and various others. Gasification converts coal into $H_2$, CO, and $CH_4$ by the reacting with gasifying agents such as $O_2$ and $H_2O$. There are three types of commercialized processes:

1. Fixed bed gasifier; lump coal is gasified in a shaft reactor at approximately 900-1000℃
2. Fluidized bed gasifier; crashed coal is gasified in a fluidized reactor at around 900℃
3. Entrained bed gasifier; pulverized coal is gasified by burner system at 1350~1600℃.

The coal supplied to the gasifier is generally decomposed thermally to produce gases such as $H_2$, CO, $CO_2$, $H_2O$, and $CH_4$, tar, and char. Tar and char react with $O_2$ and $H_2O$ supplied to form $H_2$, CO, $CO_2$ and $CH_4$. However, it is quite difficult to understand gasification mechanism only based on the aforementioned reaction kinetics [111].

A gasification reaction is composed of various kinds of chemical processes such as pyrolysis of coal, decomposition of tar, oxidation of char, combustion of gas, shift reaction, and formation of various organic compounds. To elucidate the reaction process, the method to delve into the composition of gas for information on the reaction state in the reactor needs to be established.

Coal scientists imagine coal to be a complex of heterogeneous macromolecular compounds composed of aromatic rings, aliphatic chains, and various kinds of functional groups containing heteroatoms such as O, N, and S. One of the problems to express the reaction formula of gasification is how to express the molecular formula of coal. Even if a relatively accurate reaction formula could be obtained, it would not be available for investigation of practical analysis. Since the molecular structure of most of product is very simple, the chemical process may be discussed sufficiently based on the $CH_mO_n$ regardless of the detailed structure of coal molecule.

On the other hand, biomass can range from very clean wood chips at 50% moisture, to urban wood residues that are dry but contaminated with ferrous and other materials, to agricultural residues, to animal residues, sludge, and the organic component of municipal solid waste. The process of gasification can convert these materials into carbon- and hydrogen-rich fuel gases that can be more easily utilized, often with a gain in efficiency and environmental performance compared to direct combustion of the biomass [112].

Biomass is a complex mixture of organic compounds and polymers. Biomass such as wood typically has low ash, nitrogen, and sulfur contents. However, some agricultural materials such as straws and grasses have substantially higher amounts. In order to estimate yields during gasification, the complex material must be reduced to a simplified chemical formula, such as $CH_mO_n$. In this analysis, elements such as sulfur and nitrogen are considered to be present in very small amounts and have negligible contribution to the products [112].

### 5.2.3 Stoichiometric Approach to Gasification Process

An equilibrium constant is often used to understand the composition of gasification products. It is, however, only available to the stable state, and therefore inapplicable to the analysis of transient composition of gases in operation, which is constantly fluctuating.

As mentioned above, the chemical process in a large-scale gasifier cannot be completely explained by kinetics and equilibrium. The composition of gases produced by gasification is a very clear indicator of the chemical state in the gasifier.

In this analysis, a stoichiometric method is adopted to analyze the reaction process of coal gasification. Consequently, a hypothetical chemical formula is developed based on the ultimate analysis results of the feedstock. Experiments are carried out for two different types of coal and one type of biomass. The experimental gas analysis results are obtained, and then going backwards, the oxygen and water inputs are calculated by knowing the chemical contents of the feedstock adopting the stoichiometric approach.

The gasification reaction is expressed by formula (Equation 5.77), where $CH_mO_n$ and $CH_{m'}O_{n'}$ is coal and tar respectively [111]:

$$CH_mO_n + \alpha O_2 + \beta H_2O \rightarrow \gamma H_2 + \delta CO + \varepsilon CO_2 + \kappa CH_4 + \zeta C_2H_4 + \theta C_2H_6 + \lambda CH_{m'}O_{n'} \quad (5.77)$$

Equations concerning elemental balance for C, H and O for Equation 5.77 are described as (5.78), (5.79) and (5.80) respectively.

$$1 = \delta + \varepsilon + \kappa + 2\zeta + 2\theta + \lambda \quad (5.78)$$

$$m + 2\beta = 2\gamma + 4\kappa + 4\zeta + 6\theta + m'\lambda \quad (5.79)$$

$$n + 2\alpha + \beta = \delta + 2\varepsilon + n'\lambda \quad (5.80)$$

Let the total moles of product gases in Equation 5.77 are equal to Φ.

$$\Phi = \gamma + \delta + \varepsilon + \kappa + \zeta + \theta \quad (5.81)$$

When the concentrations of $H_2$, CO, $CO_2$, $CH_4$, $C_2H_4$, and $C_2H_6$ (dry and $N_2$ free) are represented by p, q, r, s, t, and u respectively, the mole numbers of all gases are described as follows:

$H_2$ ; $\gamma = p\Phi$ (5.82a)

CO ; $\delta = q\Phi$ (5.82b)

$CO_2$ ; $\varepsilon = r\Phi$ (5.82c)

$CH_4$ ; $\kappa = s\Phi$ (5.82d)

$C_2H_4$ ; $\zeta = t\Phi$ (5.82e)

$C_2H_6$ ; $\theta = u\Phi$ (5.82f)

$\lambda = v\Phi$ (5.82g)

A reference standard should be necessary to elucidate the reaction process concealed in Equation 5.77.

$$CH_mO_n + 0.5(1-n)O_2 \rightarrow 0.5mH_2 + CO \quad (5.83)$$

$$\alpha = 0.5(1-n) + O_{ex} \quad (5.83)$$

In the $O_{ex} > 0$ case when z mole of $CH_4$ is formed, the formula becomes

$$\begin{aligned} CH_mO_n + \{0.5(1-n) + O_{ex}\}O_2 + (y-x-z)H_2O \\ \rightarrow (0.5m + y - x - 3z)H_2 + (1 - 2O_{ex} - y + x - z)CO \\ + (2O_{ex} + y - x)CO_2 + zCH_4 \end{aligned} \tag{5.84}$$

In the $O_{ex} < 0$ case, the formula obtained is below:

$$\begin{aligned} CH_mO_n + \{0.5(1-n) + O_{ex}\}O_2 + (-2O_{ex} + y - z)H_2O \\ \rightarrow (0.5m - 2O_{ex} + y - 3z)H_2 + (1 - y - z)CO + yCO_2 \\ + zCH_4 \end{aligned} \tag{5.85}$$

From the two formulae obtained above, the previously defined coefficients of each component can be expressed numerically as given in Table 5.2.

**Table 5.2** Coefficients of each component in terms of $O_{ex}$ value.

| | $\mathbf{O_{ex} \geq 0}$ | $\mathbf{O_{ex} \leq 0}$ |
|---|---|---|
| α | $0.5(1-n) + O_{ex}$ | $0.5(1-n) + O_{ex}$ |
| β | $y - x - z - 2w - 2u - (1 - n')v$ | $-2O_{ex} + y - z - 2w - 2u - (1 - n')v$ |
| γ | $0.5m + y - x - 3z - 4w - 5u - \{(1 - n') + 0.5m'\}v$ | $0.5m - 2O_{ex} + y - 4w - 5u - \{(1 - n') + 0.5m'\}v$ |
| δ | $1 - 2O_{ex} - y + x - z - 2w - 2u - v$ | $1 - y - z - 2w - 2u - v$ |
| ε | $2O_{ex} + y - x$ | Y |
| κ | Z | z |
| ζ | w | w |
| θ | u | u |
| λ | v | v |

Heat of reaction of gasification, $h_r$ (kcal/mol-coal) is calculated by

$$h_r = \gamma h_{H_2} + \delta h_{CO} + y h_{CO_2} + \kappa h_{CH_4} - h_{Coal} \tag{5.86}$$

## 5.3 Optimization

In this section, optimization using a genetic algorithm is conducted with respect to these aforementioned analyses and is utilized to compensate for the shortcomings of traditional objective approaches by allowing a larger perspective and determining a more complete spectrum of solutions.

### 5.3.1 Objective Functions

In this study, the objective functions considered are the exergy efficiency (to be maximized) and total electricity generation (to be maximized). Even though each objective function varies in terms of the objective it is optimizing, they all have the same underlying parameters which are affected by the changes in the selected decision variables.

$$\eta_{ex} = \frac{\dot{W}_{t,ORC}+\dot{W}_{R,t1}+\dot{W}_{R,t2}+\dot{W}_{D,t}+\dot{W}_{ORC,e1}+\dot{W}_{ORC,e2}-\dot{W}_{P,Total}}{\dot{Ex}_{\dot{Q}_{solar}}} \quad (5.87)$$

In the above system, the inputs are the exergy of heat provided from the solar tower and the total work of the pumps and expanders and the output is the total electricity provided from the turbines.

### 5.3.2 Decision Variables and Constraints

In this study, the following seven decision variables are chosen for the system for the analysis:

- The ambient temperature ($T_0$),
- The salinity of the sea water ($s_w$)
- The feedstock type
- The turbine isentropic efficiency ($\eta_{turb}$).

In engineering applications of optimization problems, there are usually constraints on the trade-off decision variables that arise from appropriate feasibility, commercial availability, and engineering constraints [113, 114]. The limitations on the minimum and maximum ranges of decision variables are given in Table 5.3.

As can be seen from the table, the range for the ambient temperature is taken to be between 20 and 30°C. In addition, the FT reactor temperature of 220°C is considered. Moreover, the salinity range of the seawater fed into the system is limited between 35 g/kg and 70 g/kg, which is the salinity range of the oceans around the world. Finally, heat exchanger effectiveness and turbine efficiencies are considered between 0.8–0.9 and 0.7–0.85 respectively.

**Table 5.3** Constraints associated with the decision variables selected for the TMS.

| **Constraints** |
|---|
| $20℃ \leq T_0 \leq 30℃$ |
| $35\ g/L \leq s_w \leq 70\ g/L$ |
| $0.2\ \leq ammonia - water\ conc. \leq 0.3$ |
| $0.8\ \leq\ \eta_{HEX} \leq 0.9$ |
| $0.7\ \leq\ \eta_{turb} \leq 0.85$ |

### 5.3.3 Genetic Algorithm

Currently, there are many search techniques that are used to deal with optimization problems. These include, but are not limited to, generic algorithm, simulated annealing, tabu and scatter search, ant system, particle swarm, and fuzzy programing. Among these, there is no technique that provides the optimum results for all problems and thus the best method should be selected with respect to the current system. In this research, a genetic algorithm is used since it requires no initial conditions, works with multiple design variables, finds global optima (as opposed to local optima), utilizes populations (as opposed to individuals) and uses objective function formation (as opposed to derivatives).

In the last decades, genetic algorithms (GAs) have been extensively used as search and optimization tools in various problem domains due to their broad applicability, ease of use and global perspective [115]. The concept of GAs was first conceived by Holland in 1970s [116] in order to simulate growth and decay of living organisms in a natural environment and various improvements were conducted ever since. GAs today apply an iterative and stochastic search strategy to drive its search towards an optimal solution by mimicking nature`s evolutionary principles and have received increasing attention by the research community as well as the industry to be used in optimization procedures.

Based on the inspired evolutionary process, weak and unfit species are faced with extinction while strong ones have greater opportunity to pass their genes to future generation via reproduction. Throughout this process, given long enough time lines, the species carrying the suitable combination in their genes become the dominant population.

In the analysis, the GA terminology adopted by [117] is used. Based on this terminology, a solution vector is called an individual or a *chromosome*, which consists of discrete units called *genes*. Each gene controls one or more features of the chromosome, which corresponds to a unique solution in the solution space. Moreover, the collection of these chromosomes are called a *population*, which are initialized randomly at first and includes solutions with increasing fitness as the search evolves until converging to a single solution. Furthermore, operators called *crossover* and *mutation* are used to generate new solutions from existing ones. Crossover is one of the key operators where two chromosomes, called *parents*, are combined together to form new chromosomes called *offspring*. As fitness is the preferred feauture, these offspring inherit good genes from the parents and through the iterative process. The good genes are expected to appear more frequently in the population, where they eventually converge to an overall good solution.

The mutation operator on the other hand introduces random changes into the characteristics of the chromosomes at the gene level. Usually the mutation rate (probability of changing properties of a gene) is very small and therefore the new chromosome produced will not be very different than the original one. The key here is that while crossover leads the population to converge (by making the chromosome in the population alike), mutation reintroduces genetic diversity and assists escape from local optima [117].

Reproduction involves selection of chromosomes for the next generation, where the fitness of an individual usually determines the probability of its survival. The selection procedures can vary depending on how the fitness values are used (such as proportional selection, ranking and tournament). The basic schematic for the evolutionary algorithm for the case used in the study is given in Figure 5.58.

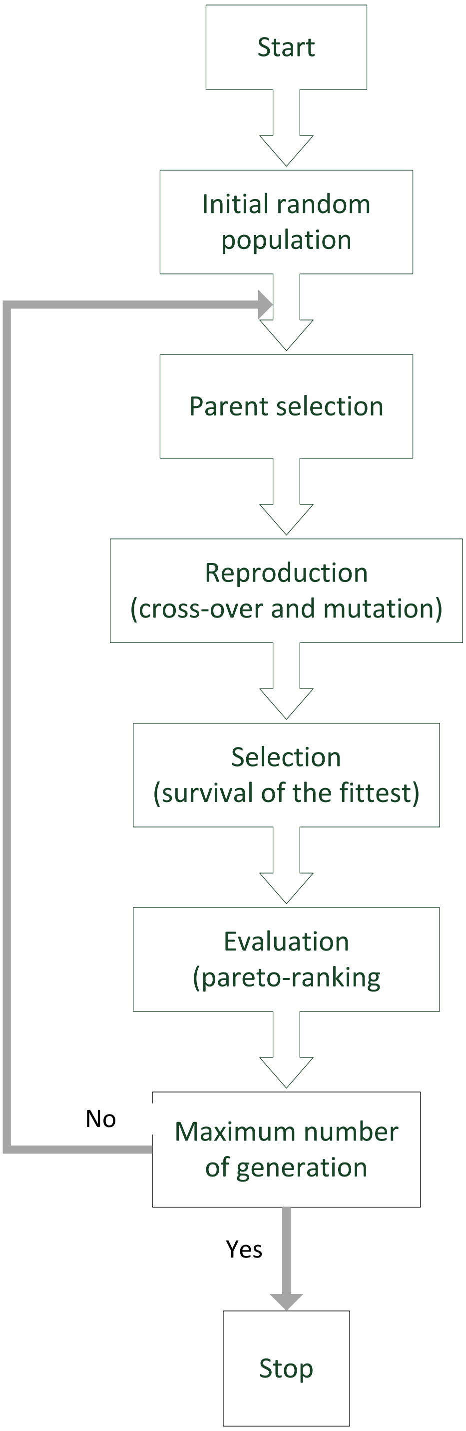

**Figure 5.58** Sample schematic for the evolutionary algorithm used (modified from [114]).

# Chapter 6: Results and Discussion

In this chapter, different output key parameters are investigated. These parameters are experimental results and theoretical analysis, which consists of selection of ORC configuration and working fluid, System 1 results and System results in terms of energy and exergy efficiencies, electrical power, exergy destruction rate, optimization, cost analysis and environmental impact. The results obtained from the experiments are considered as inputs for theoretical analysis of System 2 for more realistic results.

## 6.1 Experimental Results

Gasification is a complex process which involves drying, pyrolysis, and gasification reactions. Devolatization takes place in the pyrolysis step: larger hydrocarbons break down into smaller ones and biomass thermally decomposes into char and gas products. These char and gas products react with oxygen to form CO, $CO_2$, $CH_4$, and $H_2$ gases in the gasification step. Since the molecular structure of the gas and char is reformed through a series of reactions such as carbon, Boudouard, water gas, and CO shift or methanation, the effect of agent is mostly observed in the gasification step [85].

The effects of equivalence ratio (ER) on CO, $CH_4$, and $H_2$ concentrations, as well as LHV values of the product gases are presented in Figures 6.1–6.8. In addition to hazelnut shell, cotton stalk, and straw data, Tunçbilek–Ömerler, Konya–Ilgın, and Kale-1 results are shown in these figures.

Figures 6.1 and 6.2 show the effects of ER on the CO concentrations of the product gases. It should be noted that as oxygen decreases with decreasing ER, carbon mainly converts to CO instead of $CO_2$. Therefore, there is an inverse relationship between ER and the product gas CO concentration.

Figure 6.1 shows the effects of ER on CO concentration of the product gas for hazelnut shell, cotton stalk, and straw. The shell and cotton stalk cases are studied by [85]. The results show that CO concentration slightly changes with decreasing ER for cotton stalk, this change is within 5%. However, for hazelnut shell, the effect of ER on

CO concentration is more significant, which is over 15%. In this PhD study, it is found that the effects of ER on CO concentration are much smaller compared to the results previously listed in the literature.

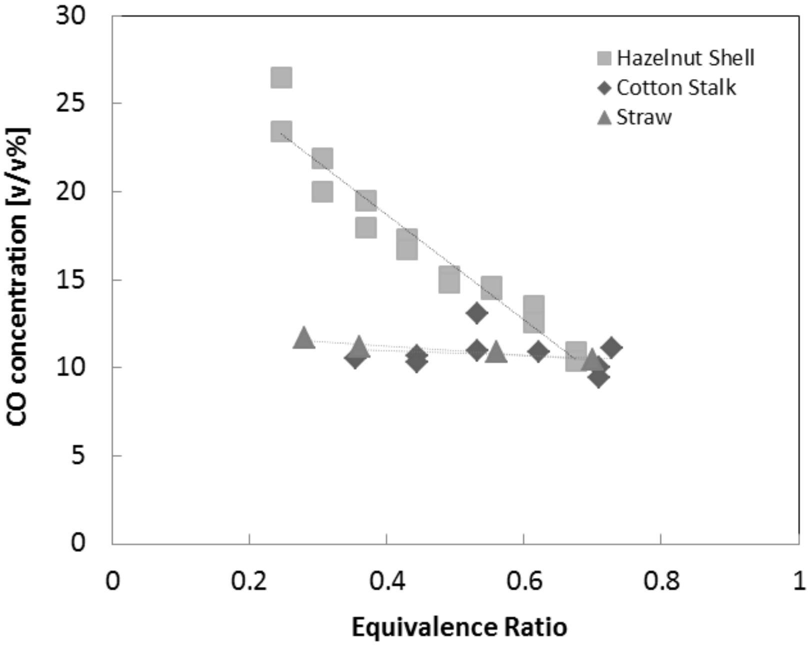

**Figure 6.1** Effects of ER on the CO concentration of the product gas for hazelnut shell, cotton stalk, and straw.

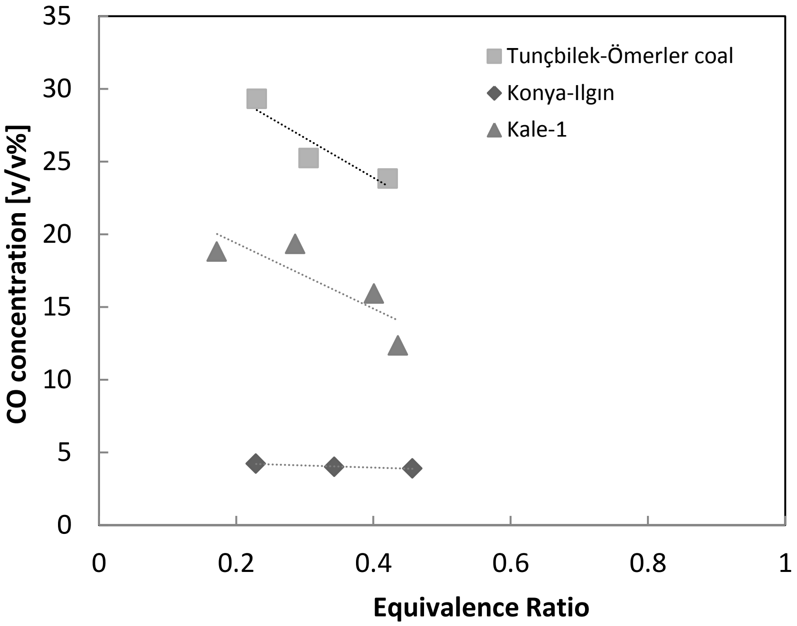

**Figure 6.2** Effects of ER on the CO concentration of the product gas for Tunçbilek–Ömerler, Konya-Ilgın, and Kale-1.

In case of Tunçbilek-Ömerler and Kale-1, three test results are presented; Konya-Ilgın study has four test result points. The CO concentration of the product gas with respect to change in ER for Tunçbilek-Ömerler, Konya-Ilgın, and Kale-1 is shown in Figure 6.2. In all three cases, the CO concentration decreases with increasing ER. Although this change is not very significant (around 1%) for Konya-Ilgın, Tunçbilek-Ömerler and Kale-1 product gas CO concentration decrease between 7–10% with increasing ER.

Figures 6.3 and 6.4 show the effects of ER on the $CH_4$ concentration of the product gas. As mentioned earlier, product gas CO concentration is decreasing with increasing ER; less $CH_4$ is formed through methanation and shift reactions as ER increases. Therefore, the trends of Figures 6.3 and 6.4 are similar to Figures 6.1 and 6.2.

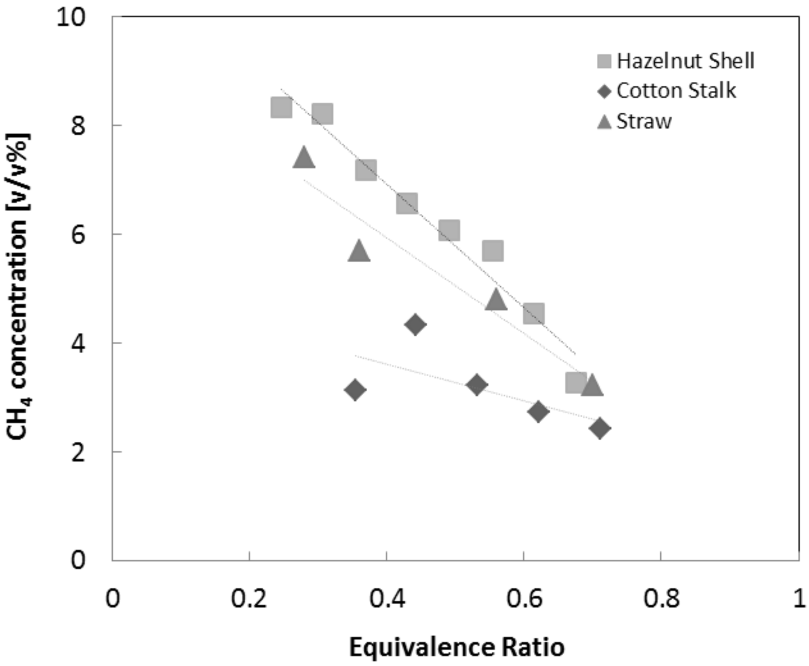

**Figure 6.3** Effect of ER on the $CH_4$ concentration of the product gas for hazelnut shell, cotton stalk, and straw.

According to Figure 6.3, with increasing ER, the $CH_4$ concentrations of the hazelnut shell, cotton stalk, and straw’s product gases have a tendency to decrease. This change is mostly visible when hazelnut shell is used around 7%. Straw product gas $CH_4$ concentration decreases by about 4% when ER is increased from 0.3 to 1. Cotton stalk; on the other hand, show a much smaller decrease, less than 1%, within the same ER interval.

Figure 6.4 shows that the $CH_4$ concentration of the product gas generally decreases with increasing ER. However, this change is not very obvious compared to Figure 6.3.

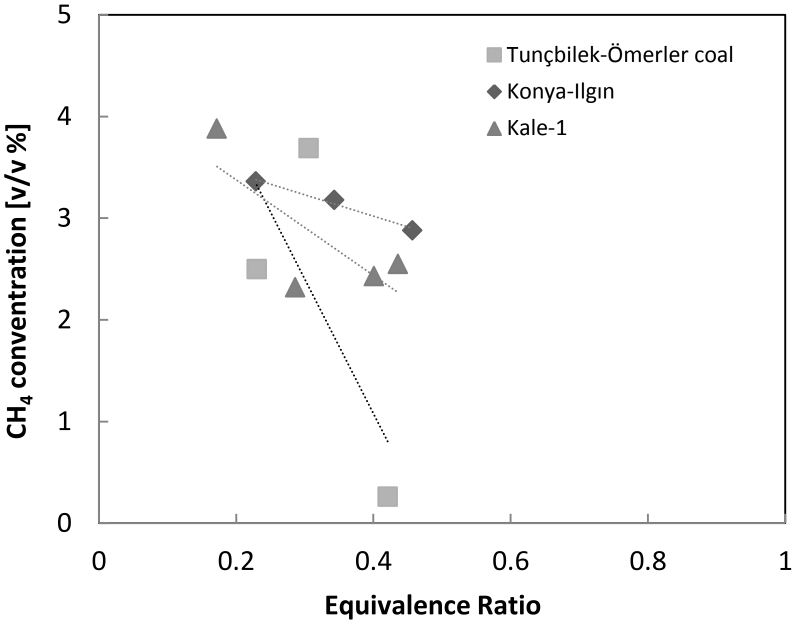

**Figure 6.4** Effect of ER on the $CH_4$ concentration of the product gas for Tunçbilek–Ömerler, Konya–Ilgın, and Kale-1.

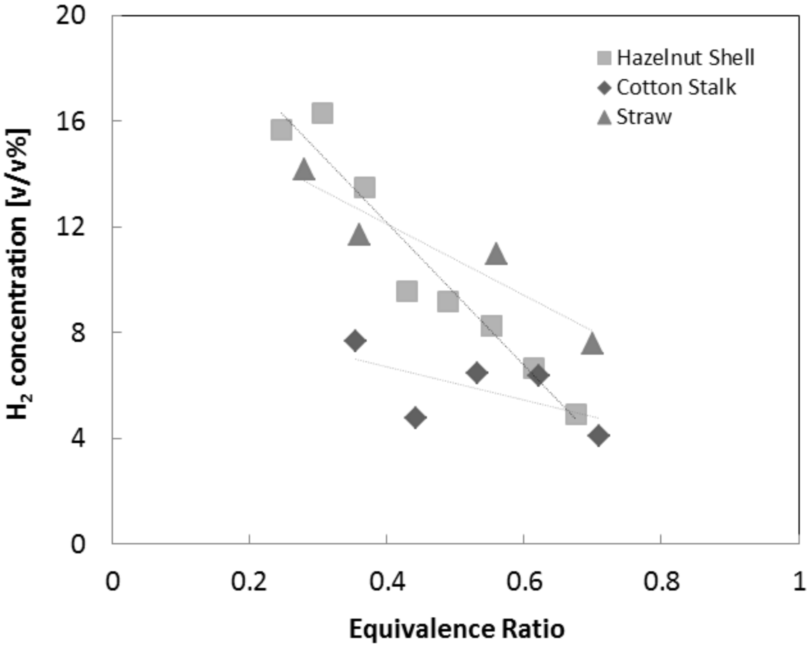

**Figure 6.5** Effect of ER on the $H_2$ concentration of the product gas for hazelnut shell, cotton stalk, and straw.

The effects of ER on the $H_2$ concentrations of the product gases are shown in Figures 6.5 and 6.6. Similar to the $CH_4$ case, product gas CO concentration decrease with increasing ER causes less $H_2$ formation through methanation and shift reactions. Therefore, the trends of Figure 6.5 and 6.6 are pretty similar to Figures 6.1-6.4.

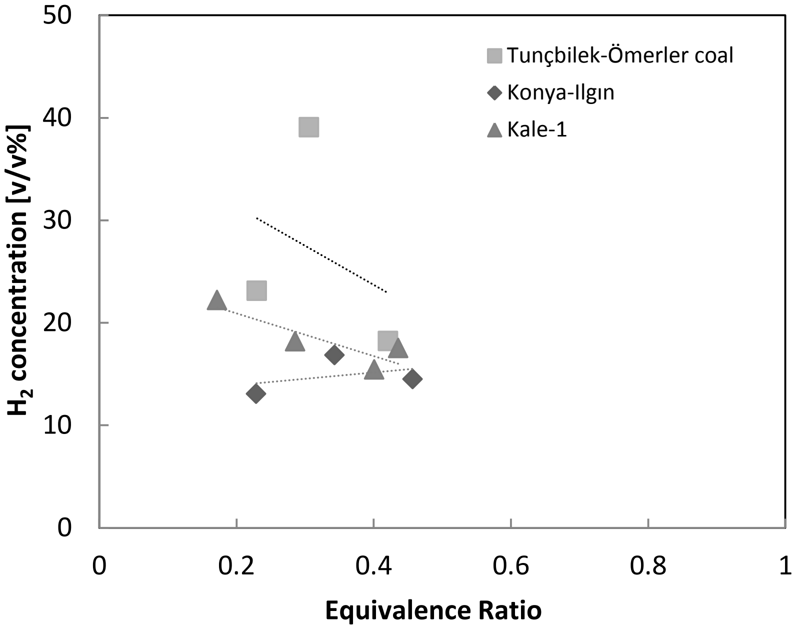

**Figure 6.6** Effect of ER on the $H_2$ concentration of the product gas for Tunçbilek-Ömerler, Konya-Ilgın, and Kale-1.

Figure 6.5 shows that product gas $H_2$ concentration decreases with increasing ER. This trend is very similar to carbon monoxide versus ER graph using hazelnut shell, cotton stalk, and straw as feedstock However; the change is most visible when hazelnut shell is used around 12%. Straw product gas $H_2$ concentration decreases by about 8% when ER increases from 0.3 to 1. Cotton stalk, on the other hand, shows a much smaller decrease, less than 5%, within the same ER interval.

The $H_2$ concentration of the product gas with respect to change in ER for Tunçbilek-Ömerler, Konya-Ilgın, and Kale-1 is shown in Figure 6.6. In all three cases, the $H_2$ concentration decreases with increasing ER. Although this change is not very significant (less than 5%) for Konya-Ilgın and Kale-1, Tunçbilek-Ömerler's product gas $H_2$ concentration decreases by about 25% with increasing ER.

The effects of ER on the LHV of the product gases are shown in Figures 6.7 and 6.8. When ER is equal to 1, it means that combustion conditions exist. LHV of the synthesis gas will be approximately equal to zero when feed-stock is completely combusted, then carbon monoxide and water vapor will be the resultant combustion gases, which have no significant chemical energy and exergy content.

Figure 6.7 show that decreasing oxygen, therefore ER, has a much greater influence on the components and LHV of product gas of hazelnut shell. Straw is also moderately affected by the change in ER. Compared to hazelnut shell and straw, cotton stalk is less affected by the variation in ER. Figure 6.7 shows that LHV follows the same trends with CO, $CH_4$, and $H_2$ concentrations.

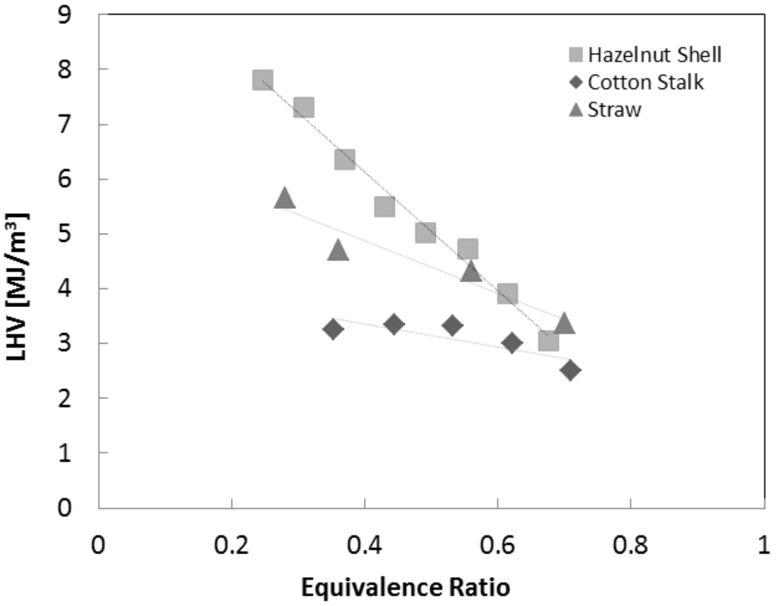

**Figure 6.7** Effect of ER on the LHV of the product gas for hazelnut shell, cotton stalk, and straw.

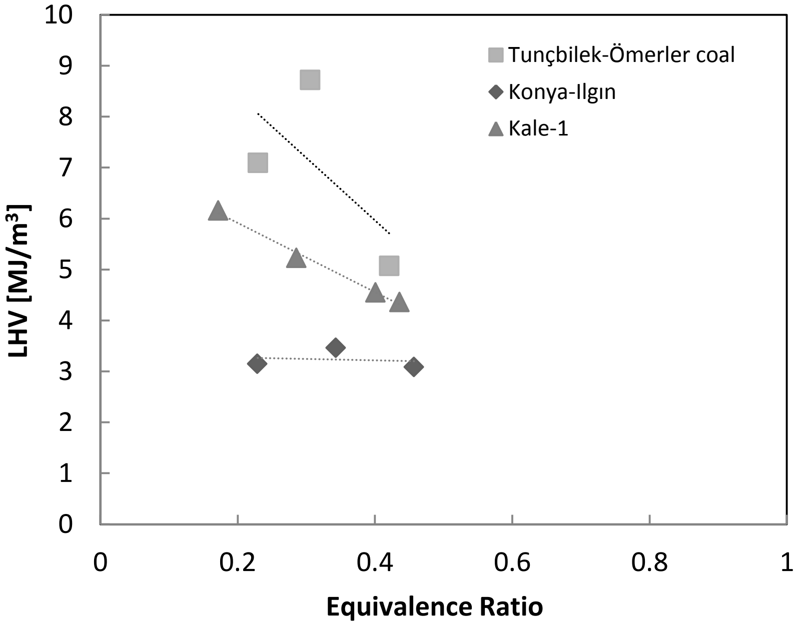

**Figure 6.8** Effect of ER on the LHV of the product gas for Tunçbilek–Ömerler, Konya–Ilgın, and Kale-1.

Figure 6.8 also gives similar results to Figures 6.1, 6.3, and 6.5. Increasing ER decreases the LHV of the product gases for Tunçbilek-Ömerler, Konya-Ilgın, and Kale-1 by 0.5-2 kJ/kg. These results agree with the literature, as LHV is expected to have an inverse relationship with ER.

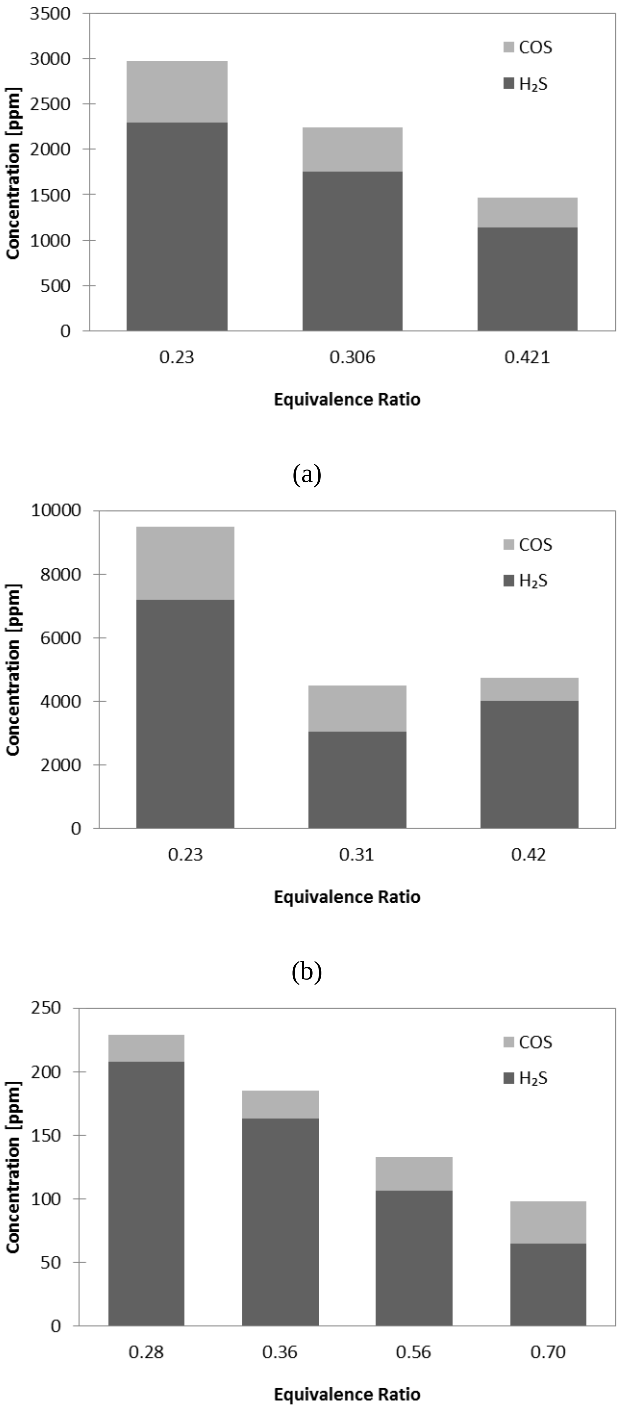

(a)

(b)

(c)

**Figure 6.9** Experimentally obtained $H_2S$ and COS concentrations measured in the synthesis gas for a) Tunçbilek-Ömerler coal, b) Konya Ilgın coal, c) Straw

The sulfur compounds in the synthesis gas are measured in the GC device. The results are given in Figure 6.9 as bar charts for each feedstock. The unit of concentration is ppm (parts per million). It can be seen that, as expected, straw gasification results in very low sulfur concentrations, where Konya-Ilgın coal gasification results are approximately fourty-fold of the results of straw. Moreover, Tunçbilek-Ömerler coal gives three times lower yields compared to Konya-Ilgın coal.

## 6.2 Selection of ORC Configuration and Working Fluid

Today's environmental and economic challenges in the world necessitate the use of energy as efficiently as possible. To make use of low-grade heat sources such as industrial waste heat and sustainable sources like geothermal, solar or biomass combustion, there are several thermodynamic cycle options. Many researchers pay substantial attention and interest to ORC for small-scale heat recovery. The choice of the working fluid for ORC is very important. This study aims to provide a comparison of the results obtained from ORC based on exergy efficiencies. For the same source temperature of 180°C, the cycles are optimized to extract the greatest amount of heat from the source for electricity and hot water production.

For the calculations of thermodynamic properties of ammonia-water mixtures in sub-cooled, saturated, and superheated conditions, the $NH_3H_2O$ procedure of Engineering Equation Software (EES) [87] is adopted. This routine is based on entering three independent parameters out of eight pre-defined parameters and obtaining the remaining five. The correlations that are embedded in the procedure are taken from a study of Ibrahim and Klein [118]. The parameters in this procedure are: T (temperature in K), P (pressure in bar), x (ammonia mass fraction), h (specific enthalpy in kJ/kg), s (specific entropy in kJ/kg K), u (specific internal energy in kJ/kg), v (specific volume in $m^3$/kg), and q (vapour quality). It should be kept in mind that 'x' generally represents the vapour quality in thermodynamics notation, but in this routine, it represents ammonia mass fraction, where vapour mass fraction is shown as 'q' (see Appendix).

The parametric study is conducted with respect to four parameters: isentropic efficiency of expander, ammonia mass fraction for ammonia-water solution and three different organic working fluids namely R124, R141b, n-butane and temperature of surroundings.

Energy and exergy efficiencies versus ammonia fraction for organic TRC, DS ORC, and DS ORC-R are given in Figure 6.9. As can be observed from these results, there is an optimal ammonia concentration that maximizes exergy and energy efficiencies in DS ORC, and DS ORC-R. However, in the TRC cycle, there is no such distinctive path both for energy and exergy efficiencies. In Figure 6.9 (b) and (c), the highest efficiencies are found for the ammonia mass fraction of 23%. This value is in good agreement with a previous study of Zamfirescu and Dincer [48].

In DS ORC-R, the highest energy and exergy efficiency values are obtained due to reheating. These values are slightly higher than those of DS ORC. Reheating increases the vapour temperature entering Expander 2. This causes an enlargement of the area of the closed loop representing the net work output in the T-s diagram. However, after the peak point, the efficiencies gradually decrease with an increase in ammonia mass fraction until 30%, which is a promising result since high ammonia concentrations cause abrasion.

Figure 6.10 shows the exergy consumption rate and net power output versus ammonia fraction for organic TRC, DS ORC, and DS ORC-R. The highest work output is obtained from DS ORC-R compared to the others. Furthermore, it is worth mentioning that the difference between work outputs of DS ORC and DS ORC-R is less than 1%. For both of the DS ORC and DS ORC-R, the exergy consumption rate increases gradually in the direction of increasing ammonia mass fraction. On the other hand, work output of TRC does not get affected by the ammonia mass fraction significantly and remains relatively constant, unlike the other two systems.

Energy efficiency variations with expander efficiency for different ammonia fractions for organic TRC, DS ORC, and DS ORC-R are given in Figure 6.11. Five different ammonia mass fractions (0.10, 0.15, 0.20, 0.25, and 0.30) are considered and shown on the x-axis. Supporting the previous results for efficiencies, the highest efficiencies are obtained for ammonia mass fraction of 30%, where the increment gets smaller after reaching the point of 23% ammonia fraction.

23% ammonia mass fraction is chosen to be utilized in the base case scenarios for both systems.

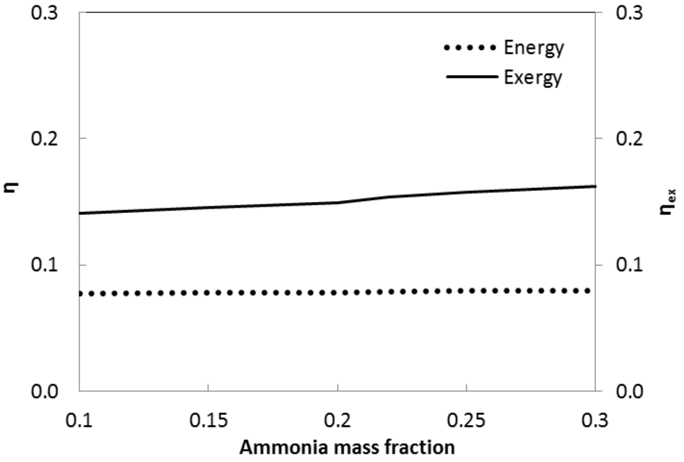

(a)

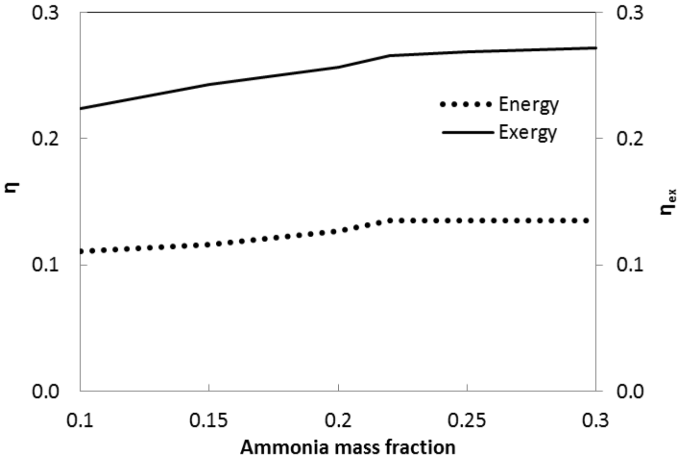

(b)

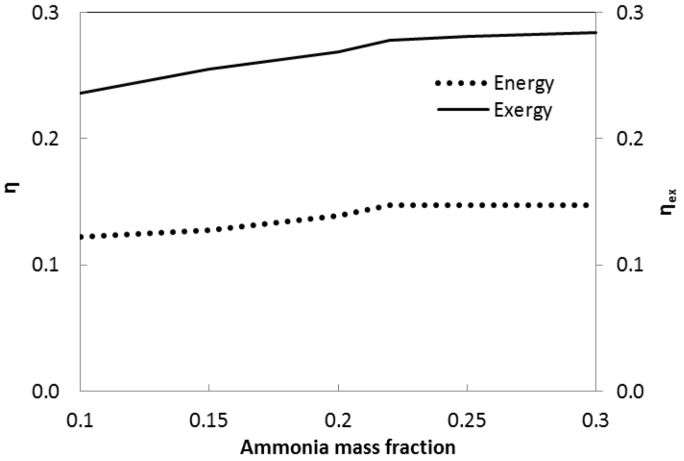

(c)

**Figure 6.10** Energy and exergy efficiencies versus ammonia fraction for (a) organic TRC, (b) organic DS ORC, and (c) organic DS ORC-R.

In the plots, it can be seen that, DS ORC and DS ORC-R have similar tendencies of efficiency increase, where DS ORC-R has a higher efficiency compared to that of DS ORC for higher ammonia concentrations. Although organic TRC has four components and looks straightforward compared to the other systems, the same energy efficiency can be obtained with an ammonia concentration of 0.23. Again, it should be noted that organic TRC has a limited response to ammonia concentration difference.

Figure 6.11 shows exergy efficiency variations with expander efficiency for different ammonia fractions for organic TRC, DS ORC, and DS ORC-R. DS ORC and DS ORC-R show very similar exergy efficiency trend. On the other hand, TRC has lower efficiencies compared to other two systems. The lowest exergy efficiency is observed for DS ORC and DS ORC-R, where ammonia mass concentration equals to 0.1.

Exergy efficiency versus expander efficiency for different organic fluids for organic TRC, DS ORC, and DS ORC-R can be seen in Figure 6.11. This time, the highest exergy efficiency is obtained as 24% by employing R124 for DS ORC-R whereas the lowest one is observed for R-124 with 14.4% for organic TRC.

The exergy efficiency versus dead state temperature for different fluids for organic TRC, DS ORC, and DS ORC-R is shown in Figure 6.12. The temperature of the cooling media is taken as a dependent variable that has been defined at the default ambient temperature of 25°C. As expected, exergy efficiencies decrease with an increase in the dead-state temperature. A fixed ammonia concentration is taken for the comparison with the organic working fluids. 30% is chosen as the ammonia concentration, which results in the highest energy and exergy efficiencies. Organic fluids show the same tendency in all systems with around 30-34% exergy efficiency. The variable that has the most significant impact is the ammonia-water mixture that gives exergetic efficiency around 20-30% for DS ORC and DS ORC-R, where TRC gives around 10-25% exergetic efficiency.

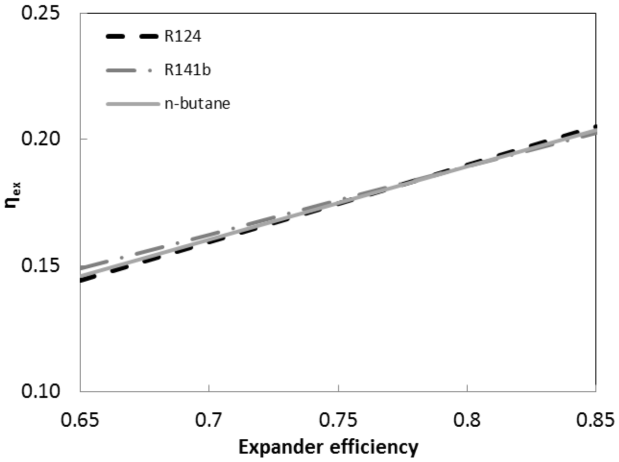

(a)

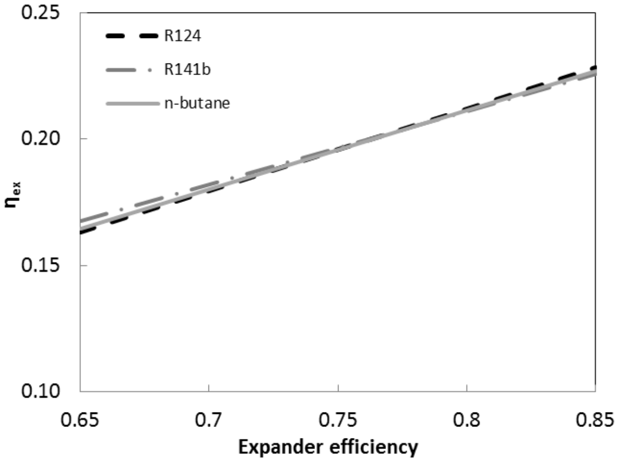

(b)

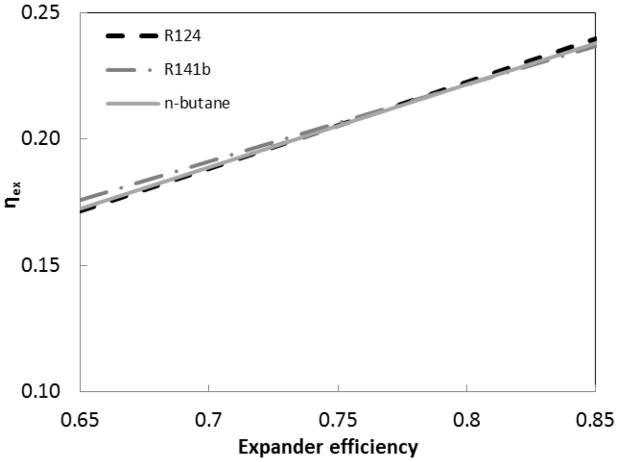

(c)

**Figure 6.11** Exergy efficiency versus expander efficiency for different organic fluids for (a) organic TRC, (b) DS ORC, and (c) DS ORC-R.

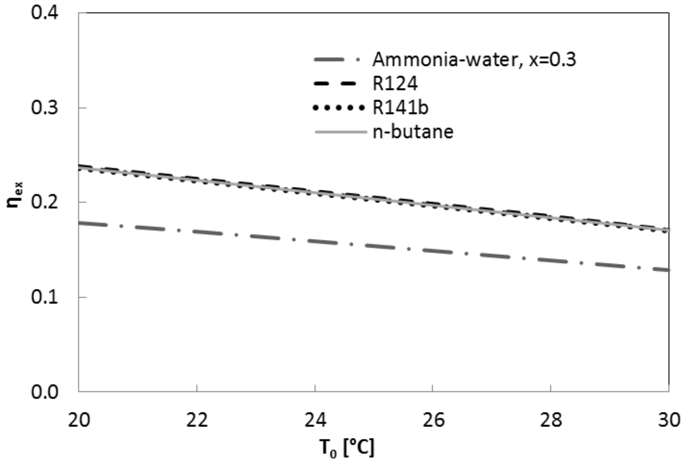

(a)

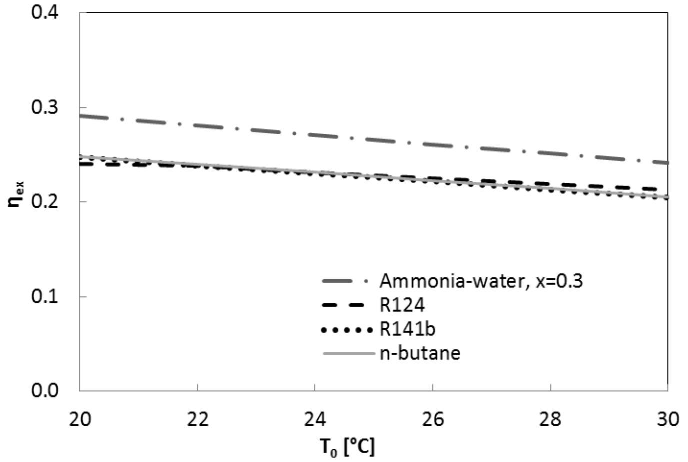

(b)

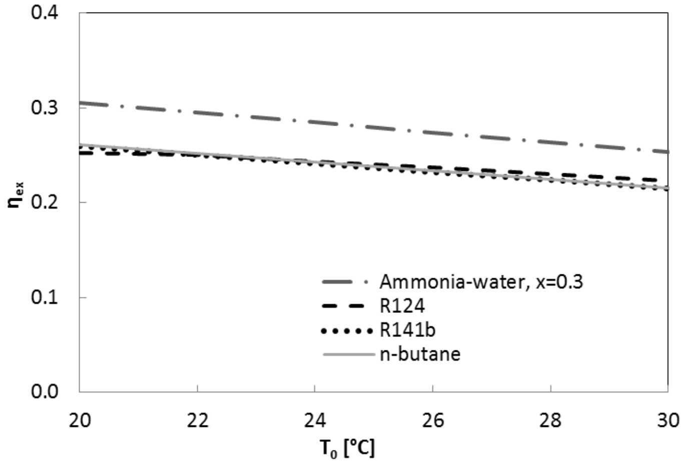

(c)

**Figure 6.12** Exergy efficiency versus dead state temperature for different fluids for (a) organic TRC, (b) DS ORC, and (c) DS ORC-R.

## 6.3 System 1 Results

To calculate the energy and exergy efficiencies and exergy destructions associated with each component, as well as the overall system, a software code in Engineering Equation Solver (EES) is written and used to analyze a baseline model (see Appendix), with respect to the balance equations and system parameters provided in the aforementioned sections. The thermodynamic properties and mass flow rate of each state point are calculated as shown in Table 6.1.

To calculate the properties of saline water, an external library of EES is used. The library accepts two parameters as inputs: salinity in the unit of g/kg, and temperature in °C. To take pressure into account, first the internal energy values are calculated (see Appendix). Then, pressure is multiplied with specific volume and the sum of internal energy and multiplied by the enthalpy of the related state point.

A parametric study is conducted to analyze the variation of energy and exergy efficiencies of each sub-system along with the overall integrated system. When the T-s diagrams of the systems are drawn, it can be seen that a decrease in the ambient temperature will increase the area between the low temperature and high temperature lines. It can be noted that the working fluid of the ORC systems is selected as ammonia-water mixture, where an ammonia concentration change occurs after the separator that cannot be shown in a standard T-s diagram.

Some energy and exergy values depend on the intensive properties of the dead state, such as temperature and pressure. Thus, energy and exergy analyses results generally are sensitive to variations in these properties. In this study, it is seen that dead-state pressure has a very limited effect on energy and exergy values. On the other hand, dead-state temperature has a significant effect on both efficiencies, especially on exergy efficiency of the system. The overall energy efficiency decreases around 1% with an increase in the dead-state temperature from 20°C to 30°C, where exergy efficiency decreases around 4%. The energy and exergy efficiency variations with respect to the ambient temperatures for overall system and the sub-systems are shown in Figures 6.13 and 6.14.

**Table 6.1** Thermodynamic properties associated with each state point for System 1.

| **State** | **h [kJ/kg]** | **$\dot{m}$ [kg/s]** | **P [kPa]** | **s [kJ/kg K]** | **T [°C]** | **ex [kJ/kg]** | **Composition (wt%)** |
|---|---|---|---|---|---|---|---|
| 1 | 484.70 | 20.0 | 1342 | 578.4 | 1111.0 | 0.71 | $NaNO_3$ (60%), $KNO_3$ (40%) |
| 2 | 489.00 | 13.3 | 2012 | 580.9 | 1115.0 | 0.72 | $NaNO_3$ (60%), $KNO_3$ (40%) |
| 3 | 152.60 | 13.3 | 2012 | 360.9 | 790.2 | 0.26 | $NaNO_3$ (60%), $KNO_3$ (40%) |
| 4 | 485.10 | 6.7 | 2012 | 578.4 | 1111.0 | 0.71 | $NaNO_3$ (60%), $KNO_3$ (40%) |
| 5 | 485.10 | 6.7 | 2012 | 578.4 | 1111.0 | 0.71 | $NaNO_3$ (60%), $KNO_3$ (40%) |
| 6 | 209.30 | 6.7 | 2012 | 398.4 | 844.8 | 0.35 | $NaNO_3$ (60%), $KNO_3$ (40%) |
| 7 | 156.30 | 20.0 | 2012 | 363.4 | 793.8 | 0.27 | $NaNO_3$ (60%), $KNO_3$ (40%) |
| 8 | 81.00 | 20.0 | 2012 | 313.4 | 721.6 | 0.14 | $NaNO_3$ (60%), $KNO_3$ (40%) |
| 9 | 84.39 | 20.0 | 1342 | 315.9 | 724.8 | 0.15 | $NaNO_3$ (60%), $KNO_3$ (40%) |
| 10 | 32.70 | 20.0 | 1342 | 281.4 | 675.4 | 0.06 | $NaNO_3$ (60%), $KNO_3$ (40%) |
| 11 | 515.70 | 20.0 | 1342 | 598.4 | 1141.0 | 0.75 | $NaNO_3$ (60%), $KNO_3$ (40%) |
| 12 | 3117.00 | 1.3 | 6475 | 380.9 | 1208.0 | 6.42 | Water |
| 13 | 2978.00 | 1.3 | 3238 | 297.3 | 1051.0 | 6.48 | Water |
| 14 | 3182.00 | 1.3 | 3238 | 380.9 | 1155.0 | 6.81 | Water |
| 15 | 2492.00 | 1.3 | 35 | 72.7 | 316.1 | 7.31 | Water |
| 16 | 283.20 | 1.3 | 35 | 67.7 | 11.6 | 0.93 | Water |
| 17 | 291.40 | 1.3 | 6475 | 68.4 | 18.4 | 0.93 | Water |
| 18 | 201.80 | 1.3 | 4 | 83.0 | 21.7 | 1.10 | Ammonia (23%), water (77%) |
| 19 | 203.40 | 1.3 | 5 | 83.2 | 23.1 | 1.10 | Ammonia (23%), water (77%) |
| 20 | 1783.00 | 1.3 | 5 | 181.2 | 507.3 | 4.78 | Ammonia (23%), water (77%) |
| 21 | 1717.00 | 1.3 | 8 | 153.2 | 429.5 | 4.81 | Ammonia (23%), water (77%) |
| 22 | 2363.00 | 0.8 | 8 | 153.2 | 602.1 | 6.51 | Ammonia (33%), water (67%) |
| 23 | 2264.00 | 0.8 | 4 | 128.6 | 484.7 | 6.57 | Ammonia (33%), water (67%) |
| 24 | 62.68 | 0.8 | 4 | 61.3 | 9.2 | 0.78 | Ammonia (33%), water (67%) |
| 25 | 612.10 | 0.5 | 8 | 153.2 | 92.7 | 1.92 | Ammonia (6%), water (94%) |
| 26 | 525.20 | 0.5 | 4 | 127.5 | 67.6 | 1.72 | Ammonia (6%), water (94%) |
| 27 | 233.40 | 1.3 | 4 | 85.0 | 27.1 | 1.19 | Ammonia (23%), water (77%) |
| 28 | 99.77 | 2.25 | 101 | 25.0 | 0.0 | 0.35 | NaCl (3.4%), water (96.6%) |
| 29 | 104.84 | 1.35 | 101 | 0.37 | 25 | 0 | NaCl (3.4%), water (96.6%) |
| 30 | 102.1 | 1.35 | 5796 | 0.36 | 25.6 | 0 | NaCl (3.4%), water (96.6%) |
| 31 | 101.3 | 2.25 | 5796 | 0.35 | 25.4 | 0 | NaCl (3.4%), water (96.6%) |
| 32 | 110.1 | 2.25 | 5796 | 0.38 | 27.6 | -0.01 | NaCl (3.4%), water (96.6%) |
| 33 | 245.2 | 2.25 | 5796 | 0.81 | 61.3 | 8.13 | NaCl (3.4%), water (96.6%) |
| 34 | 245.2 | 1.13 | 5796 | 0.81 | 61.3 | 8.13 | NaCl (3.4%), water (96.6%) |
| 35 | 245.2 | 1.13 | 5796 | 0.81 | 61.3 | 8.13 | NaCl (3.4%), water (96.6%) |
| 36 | 127.3 | 0.45 | 101 | 0.44 | 30.37 | 0.20 | Water |
| 37 | 127.3 | 0.45 | 101 | 0.44 | 30.37 | 0.20 | Water |
| 38 | 104.84 | 0.9 | 101 | 0.37 | 25 | 0 | Water |
| 39 | 104.84 | 0.9 | 101 | 0.37 | 25 | 0 | Water |
| 40 | 118.2 | 0.68 | 4796 | 0.39 | 29.5 | 4.62 | NaCl (5.7%), water (94.3%) |
| 41 | 118.2 | 0.68 | 4796 | 0.39 | 29.5 | 4.62 | NaCl (5.7%), water (94.3%) |
| 42 | 118.2 | 1.35 | 4796 | 0.39 | 29.5 | 4.62 | NaCl (5.7%), water (94.3%) |
| 43 | 104.84 | 1.35 | 101.3 | 0.37 | 25 | 0 | NaCl (5.7%), water (94.3%) |
| 44 | 104.84 | 1.35 | 101.3 | 0.37 | 25 | 0 | NaCl (3.4%), water (96.6%) |
| 45 | 106.5 | 1.35 | 4566 | 0.36 | 25.6 | 4.36 | NaCl (3.4%), water (96.6%) |
| 46 | 108.5 | 1.35 | 5796 | 0.36 | 25.8 | 5.57 | NaCl (3.4%), water (96.6%) |

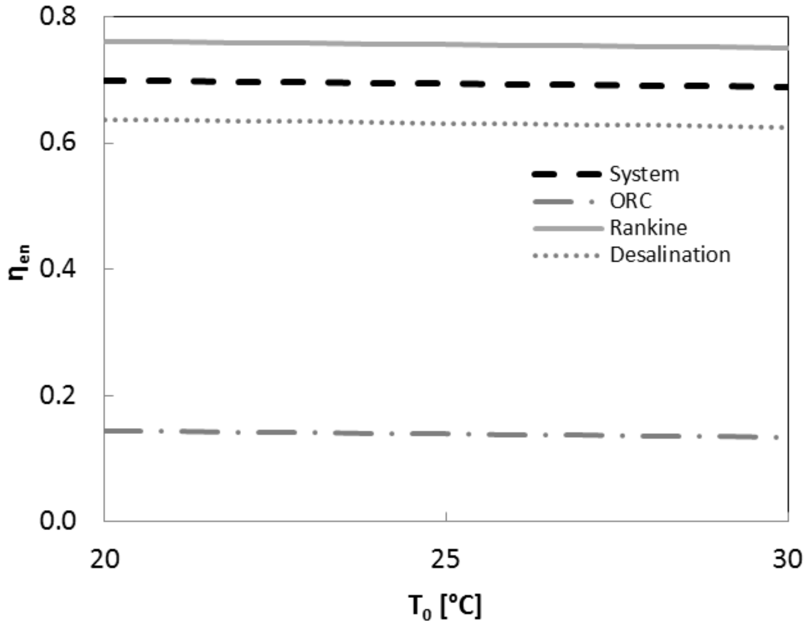

**Figure 6.13** Variation of System 1 energy efficiency with respect to the ambient temperature.

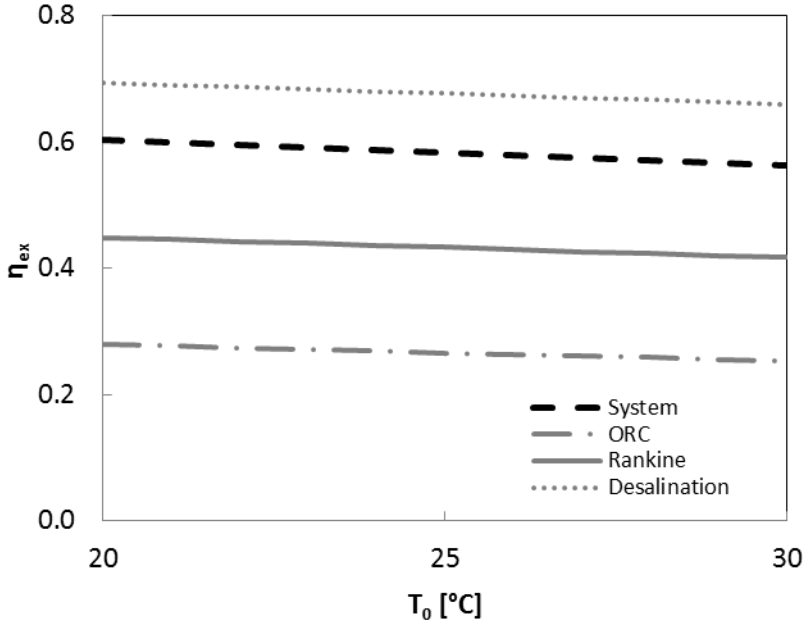

**Figure 6.14** Variation of System 1 exergy efficiency with respect to the ambient temperature.

The salinity of the water that enters the desalination unit to obtain fresh water has an impact on deslination efficiency as well as the overall system efficiency. With increasing salinity, the pressure that needs to be supplied to evercome the osmotic pressure of reverse osmosis membrane increases. The amount of salinity is varied between 35-70 g/kg, which can be considered to be valid for all seas and oceans around the globe. The salinity level has a major effect on the pressure before the osmotic membrane; when salinity increases, it is necessary to pressurize the seawater more to remove the salt content. A parametric study is conducted to calculate the energy and exergy efficiencies of the desalination plant and the overall integrated system to see how the salinity level affects them. It is seen from Figure 6.15 that by increasing salinity, as expected, the desalination plant efficiency decreases and the overall efficiencies (Figure 6.16) drop as well with a smaller increment.

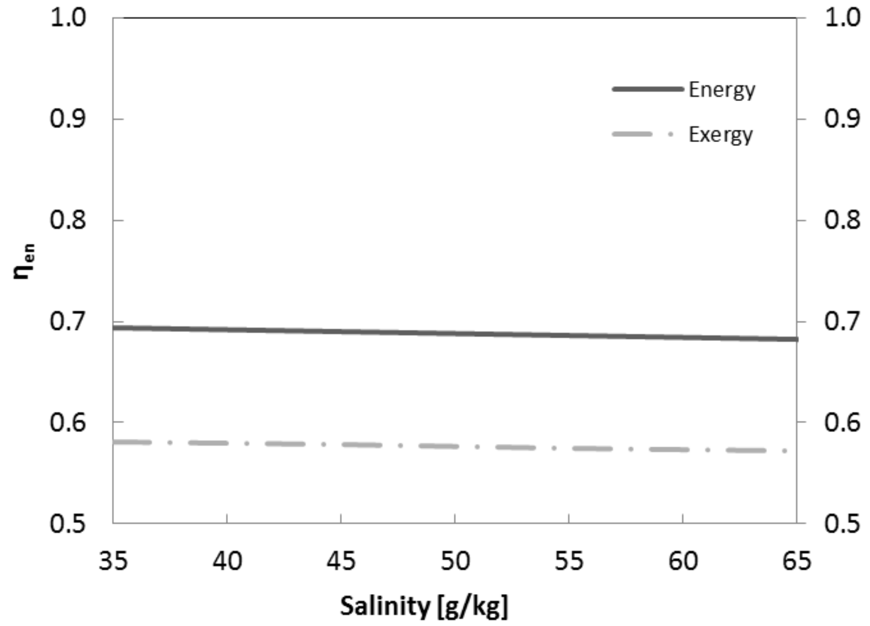

**Figure 6.15** Variation of energy and exergy efficiencies of desalination sub-system with respect to salinity.

The ammonia fraction of the working fluid that flows through the ORC is an important parameter that affects the energy and exergy efficiencies. The ammonia mass fraction of the ORC is varied to observe its effect on the ORC system efficiency, as well as the integrated system efficiency. As seen from Figure 6.17, the overall system efficiency is not affected considerably by the ammonia mass fraction of the ORC sub-system due to the relative mass flow rate of the ORC sub-system.

From Figure 6.18, it can be interpreted that increasing ammonia fraction in the ammonia-water mixture running through the ORC system decreases the energy and exergy efficiencies. This result can be considered advantageous due to the high corrosive tendency of ammonia. It is required to utilize stainless steel or aluminum components to avoid the possible corrosion effect of ammonia. The utilization of ammonia is advantageous due to its adaptability to source temperature deviations. The temperature of the fluid increases gradually despite the linear temperature increase of pure substances. This allows for a tolerance in source temperature changes.

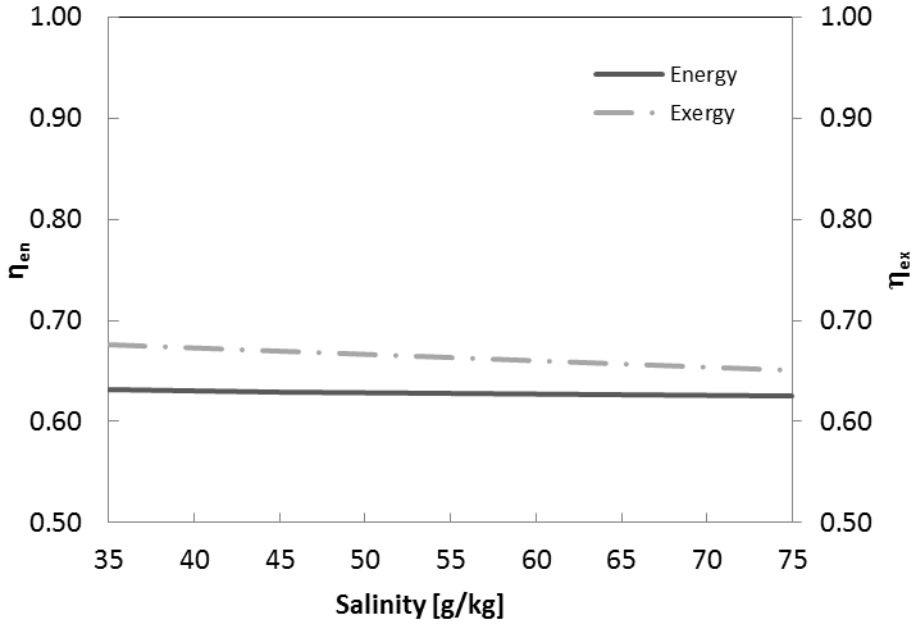

**Figure 6.16** Variation of energy and exergy efficiencies of System 1 with respect to salinity.

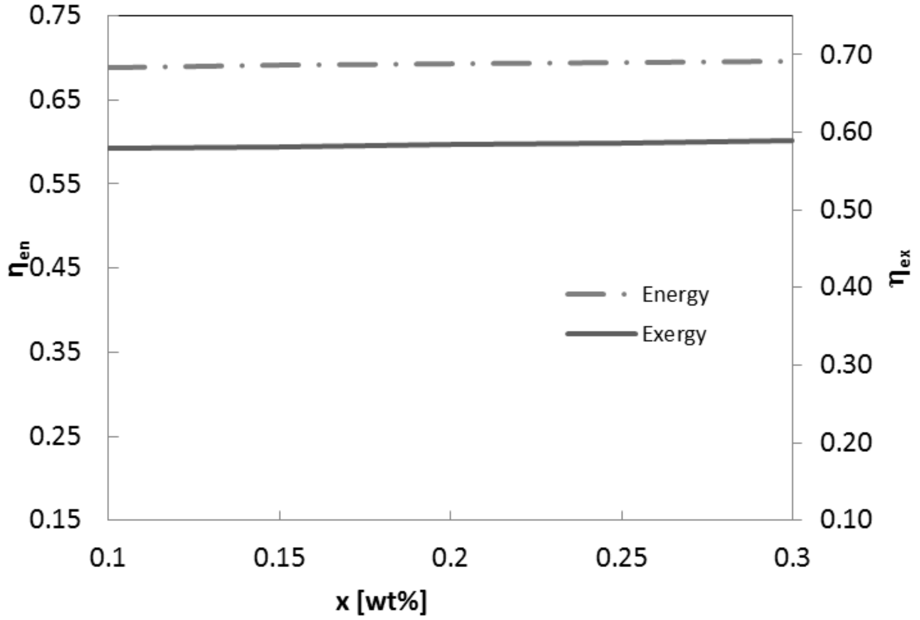

**Figure 6.17** Variation of energy and exergy efficiencies of System 1 with respect to ammonia fraction.

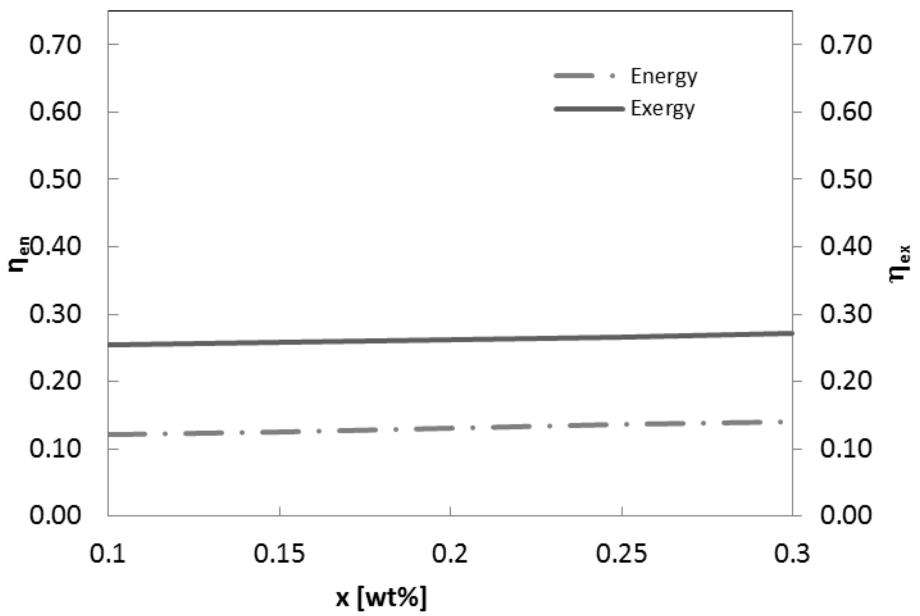

**Figure 6.18** Variation of energy and exergy efficiencies of ORC sub-system with respect to ammonia fraction.

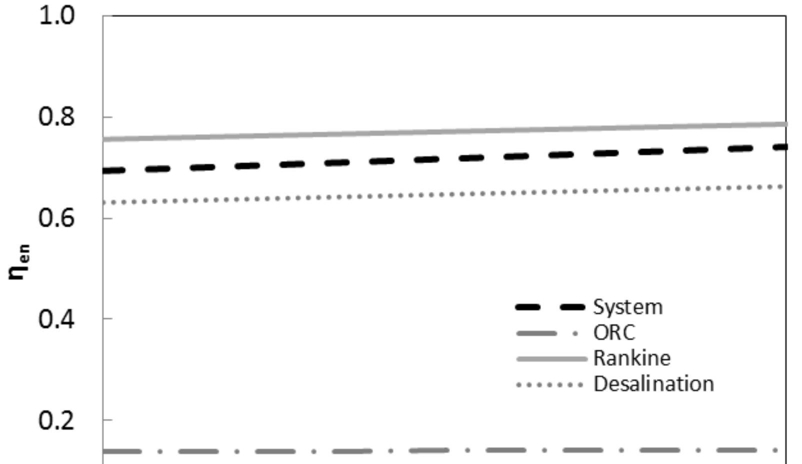

**Figure 6.19** Variation of energy efficiencies of System 1 with respect to solar irradiation.

Solar irradiance is altered in Figure 6.19 and 6.20 in the range of 0.7-1 kW/m$^2$, which has a very significant effect on the system efficiencies due to the large area of the heliostats. The heliostats concentrate the solar radiation on to the surface of the receiver. The molten salt running through the pipes under the receiver gets hot and reaches a temperature of 590°C. The molten salt is in liquid phase at that temperature.

Increasing solar irradiation from 0.7 kW/m$^2$ to 1 kW/m$^2$ results in an energy efficiency increase of 4% and exergy efficiency of 3.5%. This determines the most important parameter to be the location of the plant. If the plant is located somewhere near the equator, the useful work and heat outputs are larger than those located farther from the equator. The largest electricity output is provided by the Rankine cycle, whose source temperature is mainly affected by the temperature of the molten salt. As explained earlier, the ORC efficiencies are not affected significantly by temperature changes. The desalination system efficiency is mainly influenced by the pressure change, which results in larger pump pressures, thus larger electricity inputs along with a smaller output in net work. Temperature change of the molten salt mixture does not affect the desalination efficiencies, since the turbine work produced is small and does not have a major impact on the desalination efficiency.

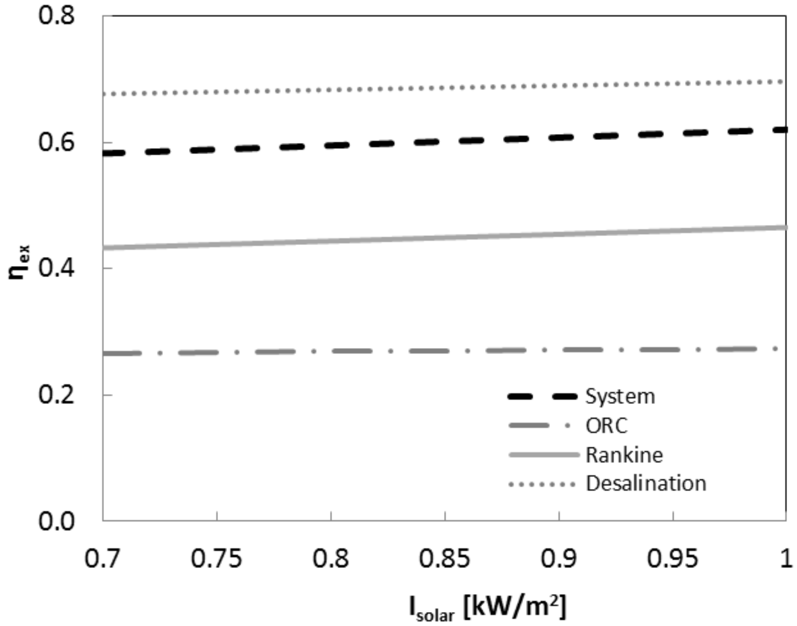

**Figure 6.20** Variation of exergy efficiencies of System 1 with respect to solar irradiation.

Throughout the exergy analysis, the exergy efficiencies and exergy destruction rates are calculated for the system and the exergy destruction rate percentages of some key system components are presented in Figure 6.21, where the solar collector has the largest portion of exergy destruction followed by heat exchangers, turbines, condensers and pumps. The components that have high-grade heat interaction result in higher exergy destruction rates.

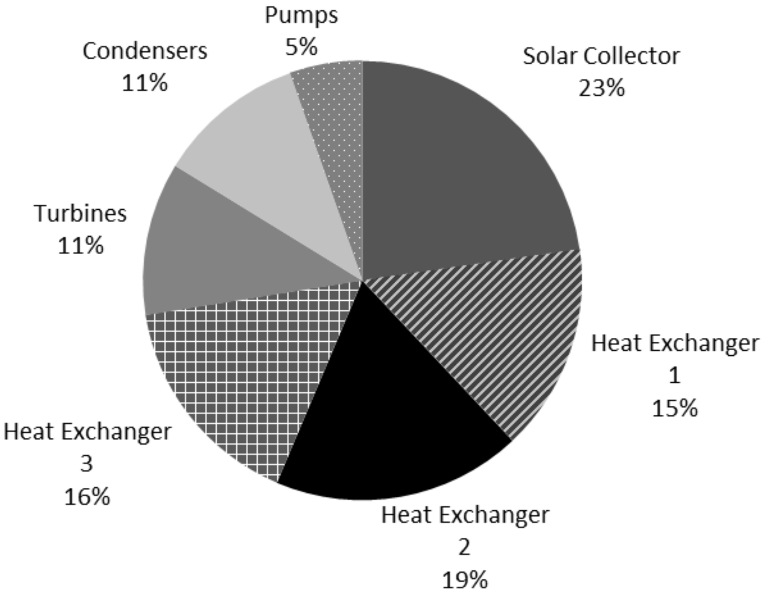

**Figure 6.21** Exergy destruction rates associated for each component of System 1.

**Table 6.2** The energy and exergy efficiency associated with System 1 sub-components.

| **System** | **Energy Efficiency** | **Exergy Efficiency** |
|---|---|---|
| Organic Rankine Cycle | 0.144 | 0.279 |
| Rankine Cycle | 0.761 | 0.449 |
| Desalination Unit | 0.637 | 0.694 |
| Overall System | 0.699 | 0.602 |

The energy and exergy efficiencies of System 1 are given in Table 6.2 with sub-system efficiencies. The efficiency values for tri-generation are higher than co-generation and single-generation, which can be seen from Figure 6.22. Figure 6.22 shows energy and exergy efficiency variations of System 1 for the same input by changing the useful outputs. First, a conventional power plant that generates only mechanical work is considered. Next fresh water is added to the outputs (co-generation 1), followed by heat (co-generation 2), and finally power. Fresh water and heating outputs are considered together (tri-generation). As expected, deriving more outputs from the same input increases both energy and exergy efficiencies, which makes the tri-generation systems superior in this respect. Fresh water comes out at the surrounding temperature, which does not change the exergy efficiency between Conventional and Cogeneration-1, as well as Co-generation-2 and Tri-generation.

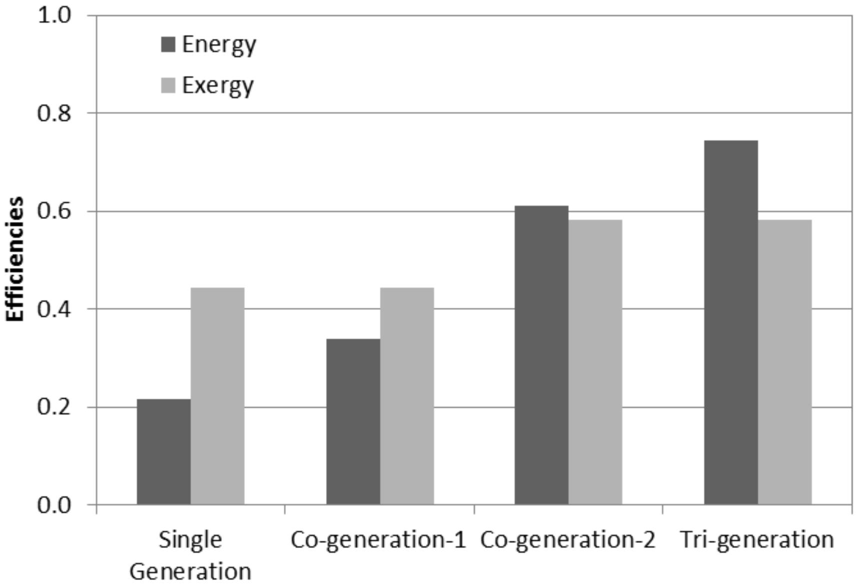

**Figure 6.22** Variation of energy and exergy efficiencies of System 1 for conventional, co-generation and tri-generation power plants.

### 6.4 System 2 Results

In this section, results obtained for System 2 are given in terms of energy and exergy efficiencies. First, experimental results for gasification are presented and compared with results in the literature. In System 2, gasification supplies heat to produce power, and hot water, as well as input for the Fischer-Tropsch sub-system, whose useful outputs are liquid and gaseous fuels. Three different feedstocks are analyzed theoretically as inputs to the gasification sub-system, namely Tunçbilek-Ömerler coal, Konya-Ilgın coal and wheat straw. A parametric study is carried out to evaluate the effects of dead-state temperature, higher heating value of feedstock, and ammonia mass fraction in the ORC working fluid.

### 6.4.1 Gasification

It is generally accepted that gasification consists of more than five chemical processes such as pyrolysis, partial oxidation of char, further decomposition of tar, secondary reaction, and combustion of char or gas. It is cumbersome to simulate actual coal gasification precisely by applying reliable scientific analysis of fundamental experiments. Since coal gasification is very complicated both from experimental and theorethical points of view, its chemical process cannot be completely understood merely by the accumulation of kinetic data.

The method adopted here can be based on the stoichiometry using gas composition obtained at a practical gasification plant. Since this method is constructed based on the stoichiometry of the reaction formula without any arbitrary assumptions and approximations, it is applicable to any gasification process regardless of the type of gasifier or rank of coal used. The feature of gasification in this analysis is to elucidate gasification mathematically based on a material balance of coal gasification reactions, which is traditionally used to calculate carbon conversion and cold gas efficiency. The mathematical reaction formula applied in this study estimates practical reactions that occur in a gasifier more precisely and it shoud help to attain optimum operation condition in practical gasification plant.

In this analysis, tar, $C_2H_4$, and $C_2H_6$ are not considered as outputs and gas analysis results are only available for $CH_4$, $CO_2$, CO, $H_2$, and $N_2$. The results of the experiments conducted under air temperature for straw can be seen in Figures 6.23–6.27, where the effect of ER on CO, $CH_4$ and $H_2$ concentrations and the LHV of the product gas are shown respectively.

The analysis results of the data for Tunçbilek-Ömerler and Konya-Ilgın coals, as well as straw are compared with the results provided in the literature [68, 111]. Average composition of gases produced in this work and the literature are listed in Table 6.3.

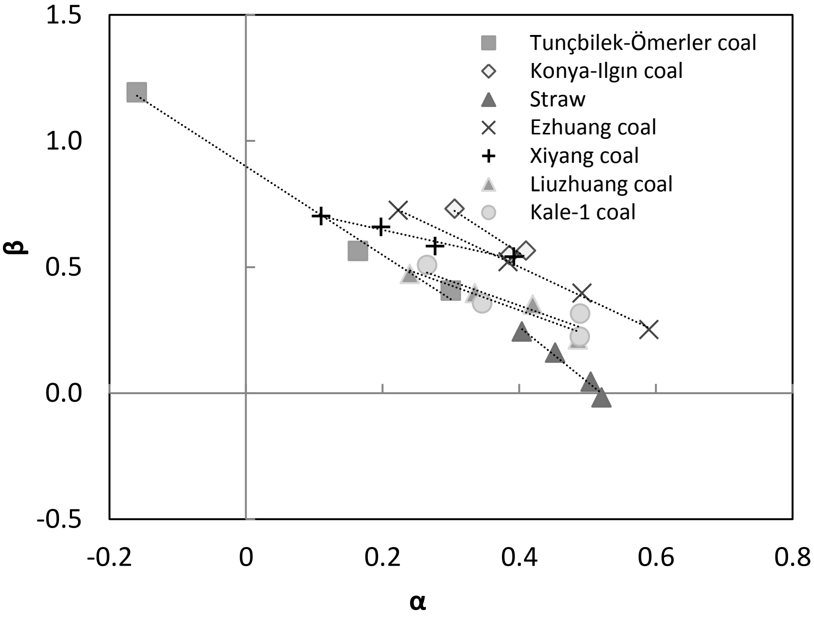

**Figure 6.23** Mole of $H_2O$ input (β) with respect to mole of $O_2$ input (α) in gasification reaction per mole of feedstock

The plot of α vs. β provides a straight line in all coal mines. $O_{ex}$ is almost zero or negative as shown in Figure 6.23. In the case of negative $O_{ex}$, $-2O_{ex}H_2O$ is consumed in water gas reaction to compensate the lack of $O_2$. Thus, the amount of reacted water increases in proportion to the reduction of the reacted oxygen. Moreover, the progress of the shift reaction of formation of $CH_4$ has an influence on the slope of each straight line.

The relationship between α and β is given in Figure 6.23. These are the major coefficients affecting the stoichiometric reaction. Employing the synthesis gas composition measurements enables derivation of these coefficients to calculate the mole numbers of oxygen and steam/moisture input to the gasifier by taking the molar composition of the feedstock into account. The relationship between these coefficients show a linear trend for coal samples, as well as the straw sample, which confirms the results obtained in the relevant literature.

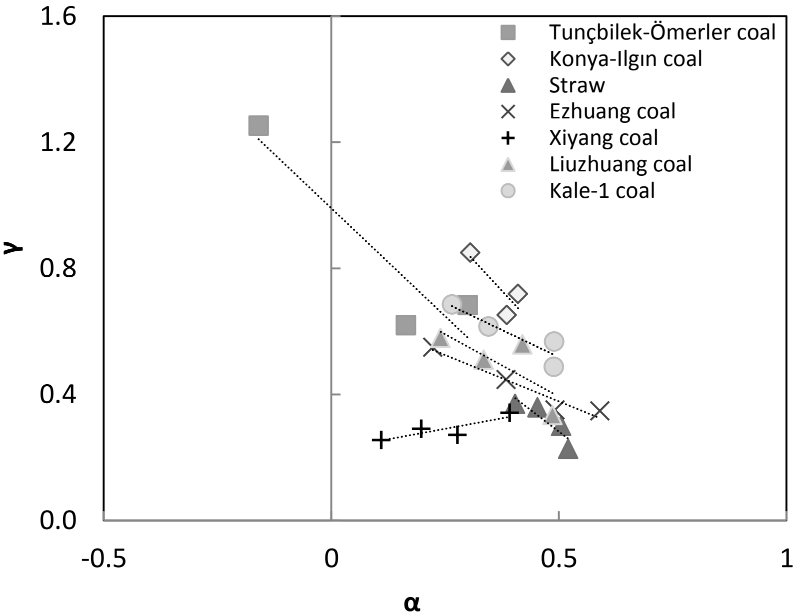

**Figure 6.24** Mole of $H_2$ output (γ) with respect to mole of $O_2$ input (α) in gasification reaction per mole of feedstock

The relationships between α and γ, δ and α, and **ε** and α are provided in Figures 6.23–6.27. A graph of α versus γ is plotted in Figure 6.24. The molar coefficient of hydrogen varies in the range of 0.23-1.25. Tunçbilek-Ömerler samples show a high hydrogen output, whereas all others remain under 0.85 moles per unit mole of coal. All the samples including straw follow a linear decreasing γ trend with an increase in α, except for Xiyang coal samples, which could be explained by the high humidity of the air at the day the data were taken.

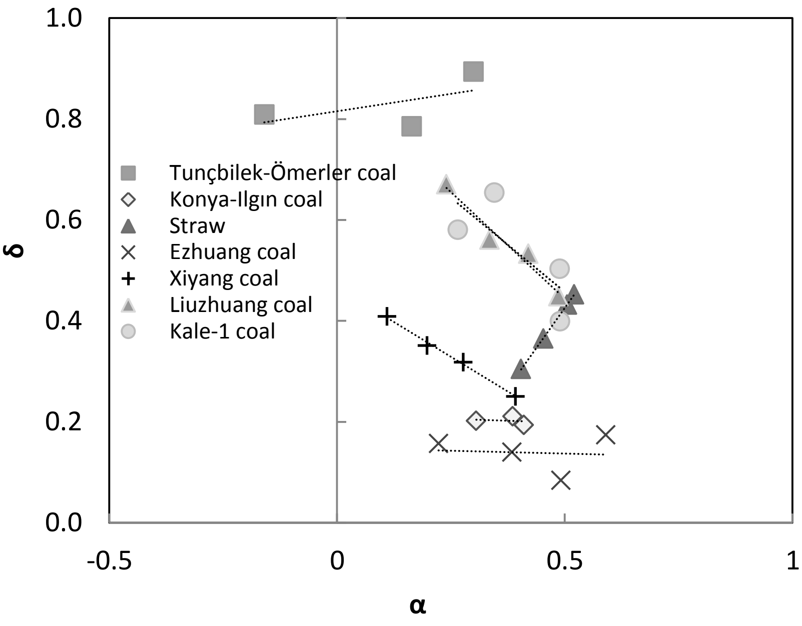

**Figure 6.25** Mole of CO output (δ) with respect to mole of $O_2$ input (α) in gasification reaction per mole of feedstock.

The relationship between α and δ is shown in Figure 6.25. Although the relationship follows a linear trend in each case, δ increases with increasing α for Tunçbilek-Ömerler coal and straw, whereas Ezhuang and Konya-Ilgın, one remains constant in the range 0.2-0.6 of α. The others follow a decreasing pattern. The ratio of $H_2$/CO (γ/δ) is a key parameter, which affects the Fischer-Tropsch synthesis product distribution.

The variation of ε versus α can be seen in Figure 6.26. ε represents the number of moles of carbon dioxide, which is not an environmentally benign output and needs to be kept to a minimum. In this regard, the Tunçbilek-Ömerler coal sample gives the smallest value for carbon dioxide output. On the other hand, Xiyang and Konya-Ilgın samples exhibit a very high content of carbon dioxide. This is not desirable due to the fact that it creates a major environmental concern. Although a solution can be offered by integrating a carbon dioxide sequestration unit to the gasification reactor, it will increase the initial and operational costs of the process.

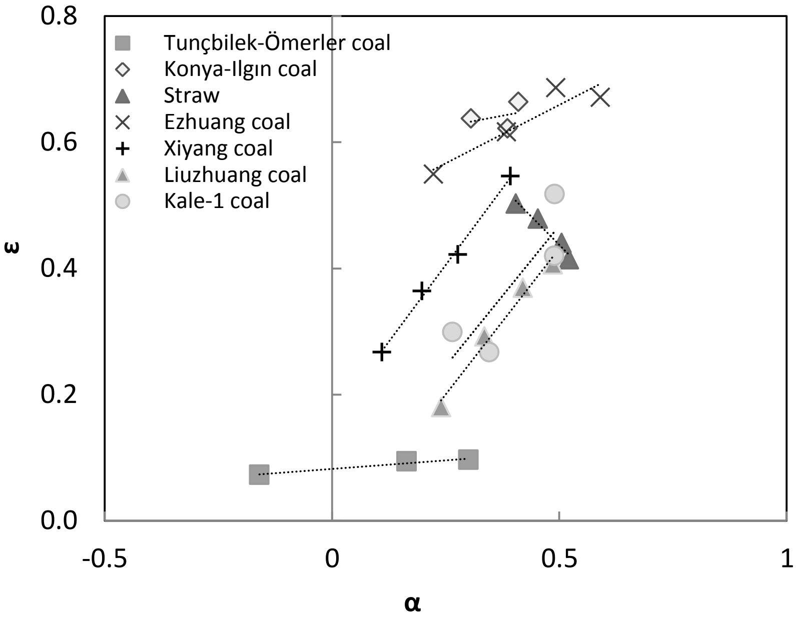

**Figure 6.26** Mole of $CO_2$ output (ε) with respect to mole of $O_2$ input (α) in gasification reaction per mole of feedstock.

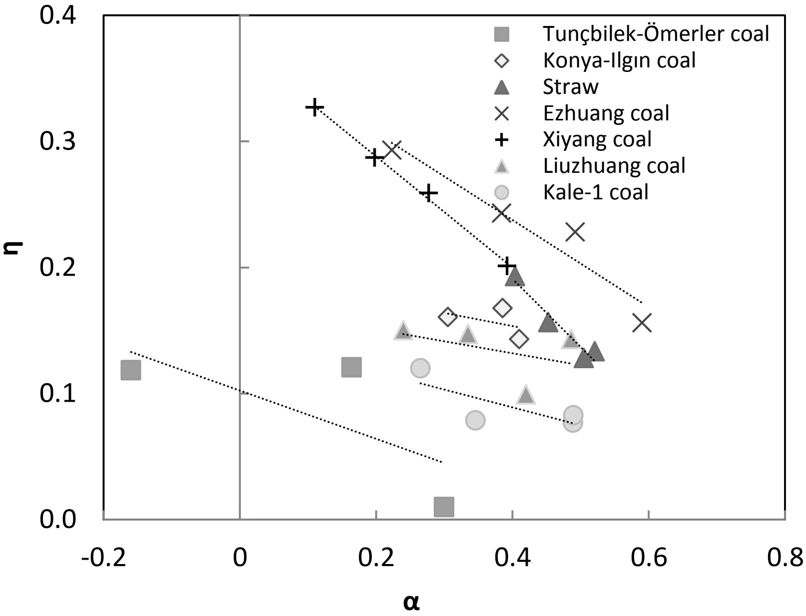

**Figure 6.27** Mole of $CH_4$ output (η) with respect to mole of $O_2$ input (α) in gasification reaction per mole of feedstock.

A relatively linear relationship is found to exist between η and α, as shown in Figure 6.27, indicating an inverse proportion between the two. This is a result of thermal effect on the stability of $CH_4$ determined by the chemical equilibrium. Average η of Xiyang mine is found to be 0.281 mol/mol, which is much larger than those of the other mines as shown in Table 6.3. As the carbon content of Xiyang coal is 92.34%, it should be classified as anthracite. It is generally accepted that most of the H atoms in the molecular structure of anthracite are combined with the existing C hydrocarbon chains. This means that $CH_4$ is produced by hydrogenation or synthesis only with high pressure $H_2$. Therefore, it is considered that $CH_4$ is mainly produced by a synthetic route in the case of this coal.

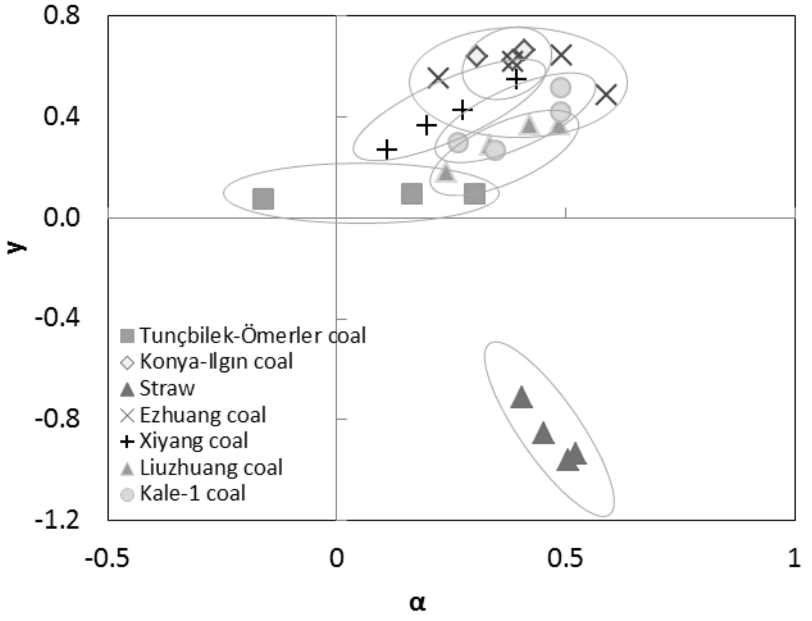

**Figure 6.28** Mole of $H_2O$ input reqired to convert CO into $CO_2$ (y) with respect to mole of $O_2$ input (α) in gasification reaction per mole of feedstock.

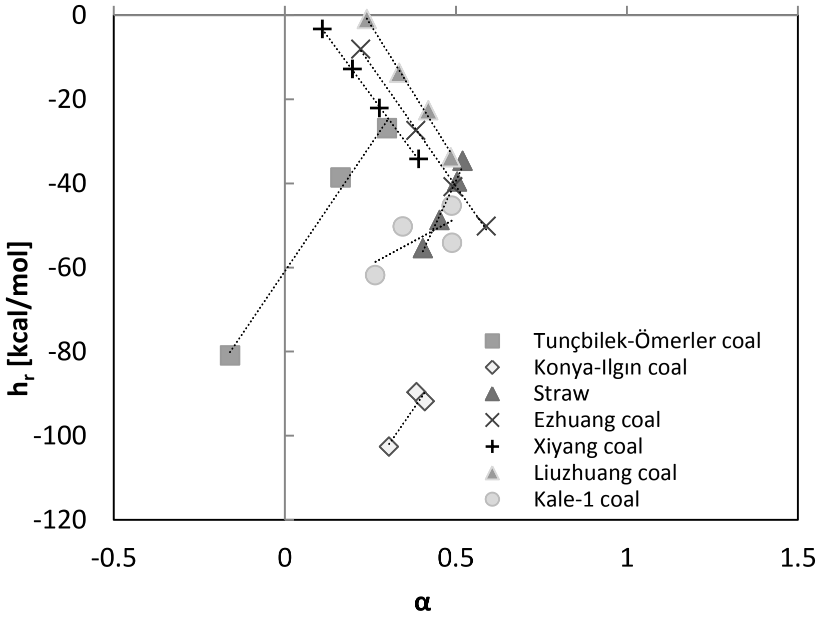

**Figure 6.29** Heat of reaction of gasification ($h_r$) with respect to mole of $O_2$ input (α) in gasification reaction per mole of feedstock.

For the relationship between $\alpha$ and y shown in Figure 6.28, the plots scattered in the range indicated by the ellipse demonstrate that linearity is hardly found. It is considered that the shift reaction is not affected by partial oxidation.

The relationship between $h_r$ and $\alpha$ is shown in Figure 6.29 below. As the plots in the region of positive $h_r$ stays constant for each coal mine, it expresses that positive $h_r$ values are not accidentally obtained. This value is attributed to excessive water-gas reaction promoted by the heat accumulated at the wall of the gasifier. The periodic fluctuations of h may indicate an essential feature of actual reactions.

**Table 6.3** The mean value of each coefficient of reaction formula and indicators of gasification

| Feedstock | $\alpha$ | $\beta$ | $\gamma$ | $\delta$ | $\varepsilon$ | $\eta$ | $O_{ex}$ | Y |
|---|---|---|---|---|---|---|---|---|
| Fuxin[1] | 0.347 | 0.247 | 0.287 | 0.573 | 0.745 | 0.182 | -0.093 | 0.244 |
| Xinghe[1] | 0.333 | 0.688 | 0.882 | 0.348 | 0.545 | 0.108 | -0.126 | 0.520 |
| Liuzhuang[1] | 0.376 | 0.399 | 0.537 | 0.499 | 0.365 | 0.135 | -0.084 | 0.319 |
| Ezhuang[1] | 0.477 | 0.397 | 0.375 | 0.133 | 0.650 | 0.217 | 0.019 | 0.583 |
| Xiyang[1] | 0.171 | 0.717 | 0.363 | 0.359 | 0.359 | 0.281 | -0.319 | 0.354 |
| Wilputte[2] | 0.337 | 0.316 | 0.315 | 0.705 | 0.183 | 0.112 | -0.177 | 0.183 |
| Riley-Morgan[2] | 0.428 | 0.370 | 0.517 | 0.707 | 0.284 | 0.009 | -0.048 | 0.284 |
| Riley-Morgan[2] | 0.407 | 0.256 | 0.560 | 0.658 | 0.279 | 0.062 | -0.020 | 0.279 |
| Riley-Morgan[2] | 0.433 | 0.715 | 0.503 | 0.723 | 0.224 | 0.053 | -0.079 | 0.224 |
| Lurgi[2] | 0.331 | 0.224 | 0.623 | 0.466 | 0.396 | 0.136 | 0.018 | 0.018 |
| Tunçbilek-Ömerler[3] | 0.101 | 0.721 | 0.852 | 0.829 | 0.088 | 0.083 | -0.358 | 0.088 |
| Konya-Ilgın[3] | 0.367 | 0.614 | 0.740 | 0.202 | 0.641 | 0.157 | -0.050 | 0.641 |
| Straw[3] | 0.471 | 0.108 | 0.314 | 0.389 | 0.459 | 0.153 | 0.099 | -0.865 |

[1] Data taken from [111]
[2] Data taken from [119]
[3] Results of this study

The relatively small $\alpha$ of Xiyang coal with respect to its different chemical composition and heating value is shown in Table 6.3. The partial oxidation process is considered to be practically governed by the value $O_{ex.}$ On the other hand, the secondary reaction proceeded more actively compared to the surface fixed bed gasification.

A software code in Engineering Equation Solver [87] is also written and used (see Appendix) for System 2 to analyze its corresponding baseline model using the same methods described earlier. The thermodynamic properties and mass flow rate of each state point are shown in Table 6.4.

**Table 6.4** Thermodynamic properties associated with each state point for System 2.

| State | h [kJ/kg] | m[kg/s] | P [kPa] | s[kJ/kg K] | T[°C] | ex[kJ/kg] |
|---|---|---|---|---|---|---|
| 1 | 309.2 | 1.11 | 151.3 | 6.716 | 25 | -48.05 |
| 2 | 35705 | 1.93 | 151.3 | 9.027 | 25 | 26026 |
| 3 | 298.4 | 1.623 | 101.3 | 6.86 | 25 | 0 |
| 4 | 343.9 | 1.623 | 151.3 | 6.887 | 70.21 | 37.47 |
| 5 | 513.9 | 4.663 | 151.3 | 7.506 | 150 | 30654 |
| 6 | 3527 | 0.2 | 101.3 | 15.63 | 150 | 11.83 |
| 7 | 378.9 | 4.463 | 151.3 | 7.142 | 50 | 30666 |
| 8 | 1007 | 4.463 | 2250 | 7.339 | 500.1 | 31294 |
| 9 | 1007 | 4.463 | 2250 | 7.339 | 500.1 | 31294 |
| 10 | 1007 | 2.232 | 2250 | 7.339 | 100 | 31294 |
| 11 | 298.4 | 4.665 | 138.6 | 6.77 | 25 | 26.83 |
| 12 | 668.8 | 4.665 | 1540 | 6.889 | 384.5 | 361.8 |
| 13 | 295.2 | 4.665 | 1540 | 6.069 | 25 | 232.6 |
| 14 | 675.7 | 4.665 | 17116 | 6.191 | 386.7 | 576.9 |
| 15 | 1145 | 6.896 | 17116 | 6.74 | 800 | 882.1 |
| 16 | 690.7 | 6.896 | 1540 | 6.922 | 405 | 373.9 |
| 17 | 1132 | 6.896 | 1540 | 7.433 | 800 | 662.7 |
| 18 | 688.2 | 6.896 | 138.6 | 7.611 | 402.9 | 165.9 |
| 19 | 478.9 | 6.896 | 138.6 | 7.245 | 202.9 | 65.89 |
| 20 | 283.2 | 0.2 | 75 | 0.9261 | 67.65 | 11.63 |
| 21 | 286.9 | 0.2 | 3000 | 0.9283 | 67.97 | 14.71 |
| 22 | 3896 | 0.2 | 3000 | 7.741 | 693.3 | 1593 |
| 23 | 2999 | 0.2 | 75 | 8.212 | 262.1 | 555 |
| 24 | 1007 | 2.232 | 2250 | 7.339 | 500.1 | 31294 |
| 25 | 576.9 | 2.437 | 2250 | 5.666 | 210 | 31294 |
| 26 | 576.1 | 2.437 | 101.3 | 5.731 | 298.2 | 31246 |
| 27 | 2781 | 0.001414 | 6236 | 5.87 | 278.2 | 1036 |
| 28 | 1253 | 0.001414 | 6236 | 3.096 | 283.2 | 334.1 |
| 29 | 1254 | 0.001414 | 7483 | 3.096 | 283.5 | 335.2 |
| 30 | 248.6 | 0.004096 | 9 | 1.135 | 83 | 21.93 |
| 31 | 251.1 | 0.004096 | 27 | 1.137 | 83.28 | 24 |
| 32 | 673.4 | 0.004096 | 27 | 2.185 | 178 | 133.7 |
| 33 | 671.6 | 0.004096 | 15.59 | 2.186 | 164.9 | 131.6 |
| 34 | 2085 | 0.0001453 | 15.59 | 5.893 | 164.9 | 559.8 |
| 35 | 2002 | 0.0001453 | 9 | 5.941 | 142.9 | 462.8 |
| 36 | -12.91 | 0.0001453 | 9 | 0.562 | 48.25 | 51.46 |
| 37 | 619.6 | 0.00395 | 15.59 | 2.05 | 164.9 | 111.8 |
| 38 | 610.3 | 0.00395 | 9 | 2.035 | 144.9 | 107 |
| 39 | 588.2 | 0.004096 | 9 | 2.002 | 21.38 | 103 |

**Table 6.5** Energy and exergy efficiencies of the System 2 sub-components

| System | Energy Efficiency | Exergy Efficiency |
|---|---|---|
| FT | 0.84 | 0.85 |
| Organic Rankine Cycle | 0.52 | 0.35 |
| Brayton Cycle | 0.41 | 0.48 |
| Rankine Cycle | 0.75 | 0.54 |
| Overall System | 0.71 | 0.73 |

Energy and exergy efficiencies for sub-systems and the overall system are presented in Table 6.5. It can be seen that the efficiency values are greater than those of single generation and co-generation systems as presented in the literature [1]. It should be noted that hot water production contributes more to energy efficiency, where its exergy content is smaller and contributes less to the exergy efficiency. Thus, it can be more meaningful to present both energy and exergy efficiency results.

### 6.4.2 Fischer-Tropsch Synthesis

In this section, the Fischer-Tropsch synthesis unit is analyzed, where complex chemical reactions occur and synthesis gas is converted into liquid fuel and hydrocarbons such as methane, ethane and propane. These chemical reactions are complicated to such a degree that theoretical analysis can result in significant errors. Thus, experimental data presented in the literature are integrated with experimental synthesis gas composition data to obtain practical results to be used in overall system efficiency calculations for System 2.

#### 6.4.2.1 Determination of Anderson–Schulz–Flory Coefficients

The Anderson–Schulz–Flory (ASF) equation gives the mole fractions of hydrocarbons formed via stepwise addition of intermediates containing one carbon atom as a function of the carbon number i and the chain growth probability $\alpha$ [122].

$$x_n = (1-\alpha)\alpha^{n-1} \tag{6.2}$$

where $x_n$ is the mole fraction of a hydrocarbon with chain length $n$ and $\alpha$ is the chain growth probability factor independent of $n$. The chain growth probability factor $\alpha$ determines the total carbon number distribution of the FT products.

In this study, the method proposed by Satterfield [123] is used to characterize the carbon number distribution of Fischer–Tropsch synthesis where two independent ASF distributions with different chain growth probabilities are superimposed [124]. There are two separate lines that intersect at point named ξ. A linear line is drawn starting from ξ to the x-axis to find the corresponding carbon number.

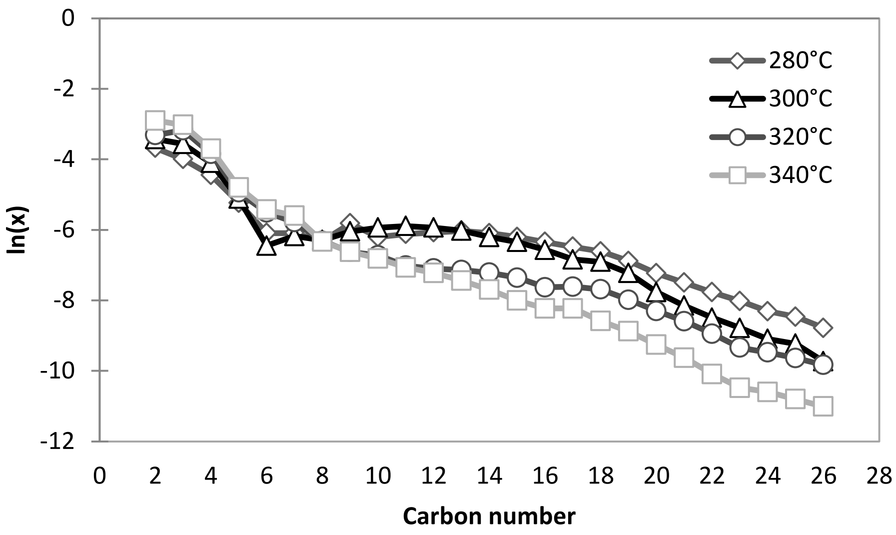

**Figure 6.30** Influence of temperature on the alkene distribution for $H_2/CO = 1.97$ at 2.25MPa (data from [125]).

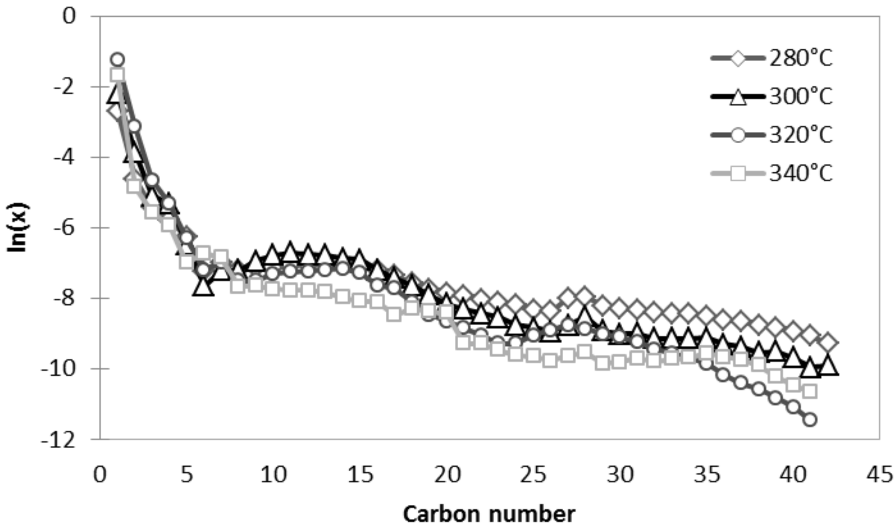

**Figure 6.31** Influence of temperature on the alkane distribution for $H_2/CO = 1.97$ at 2.25MPa (data from [125]).

Alkane (paraffin) and alkene (olefin) are hydrocarbon products of Fischer-Tropsch synthesis reactions. The general chemical formula of alkanes is $C_nH_{2n+2}$, where the general formula of alkenes is $C_nH_{2n}$. Since the mass fractions of the hydrocarbons are very small numbers, usually logarithmic plotes are used to show the product distributions. In Figures 6.30 and 6.31, product distributions for different reactor temperatures are shown. It can be seen that at lower temperatures, high carbon number product fraction becomes larger. High carbon number hydrocarbons are necessary products that can be cracked to gasoline and diesel fuel.

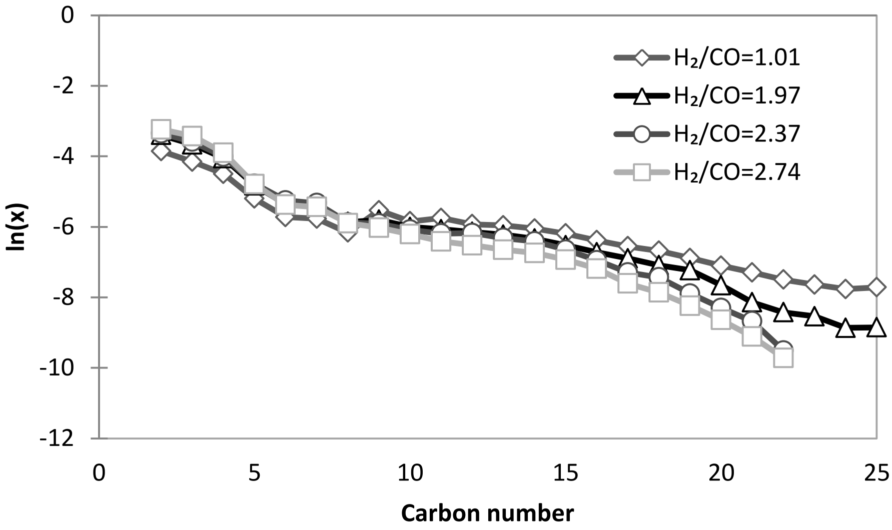

**Figure 6.32** Influence of $H_2$/CO ratio in feed on the alkene (olefin) distribution at 573 K and 2.25MPa (data from [124]).

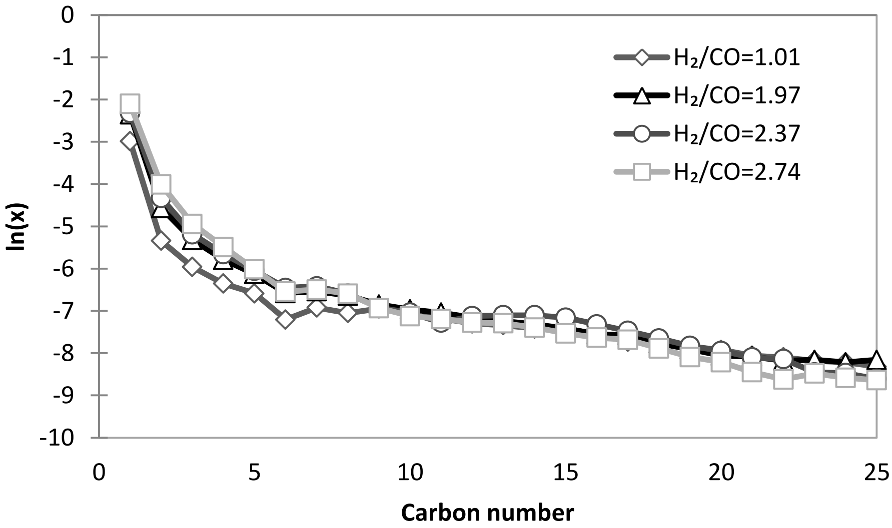

**Figure 6.33** Influence of $H_2$/CO ratio in feed on the alkane (paraffin) distribution at 573 K and 2.25MPa (data from [124]).

The fraction of methane does not work in the ASF equation due to the several routes of formation [126]. The determination of growth probabilities $\alpha_1$ and $\alpha_2$ of the bimodal ASF distribution is based on hydrocarbons with carbon numbers $i > 2$.

The slopes of the two superimposed distributions are given by ln $\alpha_1$ and ln $\alpha_2$ (as shown by the logarithmic plot in Figures 6.30–6.33. The bimodal distribution is characterized by these two growth probabilities and the point of intersection $\xi$ of both ASF distributions. The mathematical procedure given by Donelly et al. [123] arrives at the equation below, where $\mu_1$ represents the total mole fraction of hydrocarbons formed with the growth probability [124].

$$\mu_1 = \frac{(1-\alpha_2)}{(1-\alpha_1)} \alpha_1^2 \left[ \frac{(1-\alpha_2)}{(1-\alpha_1)} \alpha_1^2 + \left( \frac{\alpha_1}{\alpha_2} \right)^{\varepsilon-1} \alpha_2^2 \right]^{-1} \tag{6. 3}$$

Since two independent ASF distributions are superimposed the fraction of hydrocarbons formed with a chain growth probability $\alpha_2$ equals:

$$\mu_2 = 1 - \mu_1 \tag{6. 4}$$

The growth probabilities $\alpha_1$ and $\alpha_2$ as well as the fraction $\mu_1$ depend on reaction conditions. Chain length distributions provided for constant hydrogen pressure and varied $P_{CO}$ as well as for constant carbon monoxide pressure and varied $P_{H_2}$ are provided in Figures 6.33–6.34 respectively, which show that the average carbon number of products is raised with increasing carbon monoxide pressure and is reduced with increasing hydrogen pressure.

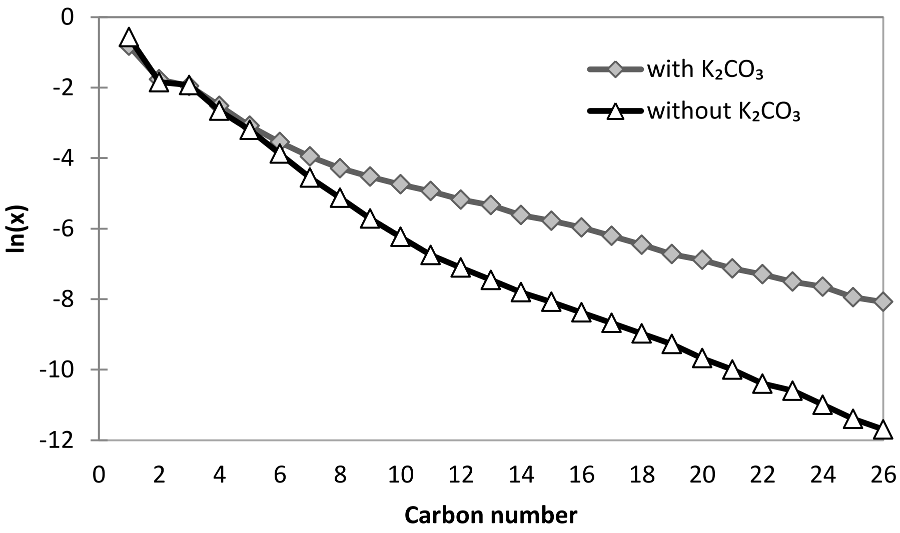

**Figure 6.34** Chain length distributions of alkali promoted and unpromoted precipitated iron catalysts (data from [124]).

The experiments conducted by [124] are carried out by keeping various parameters constant: hydrogen partial pressure at 500 kPa, carbon monoxide partial pressure at 250 kPa, reactor temperature at 220°C. For the experimental results obtained with addition of alkali promoted catalyst $\alpha_1$ value is smaller than that of unpromoted, where $\alpha_2$ becomes larger (Figure 6.34). This indicates that chain length increases with alkali promoted catalyst. To obtain low carbon number species, unpromoted catalysts are preffered. On the other hand, to produce a larger portion of diesel and gasoline, promoted catalysts are preferable.

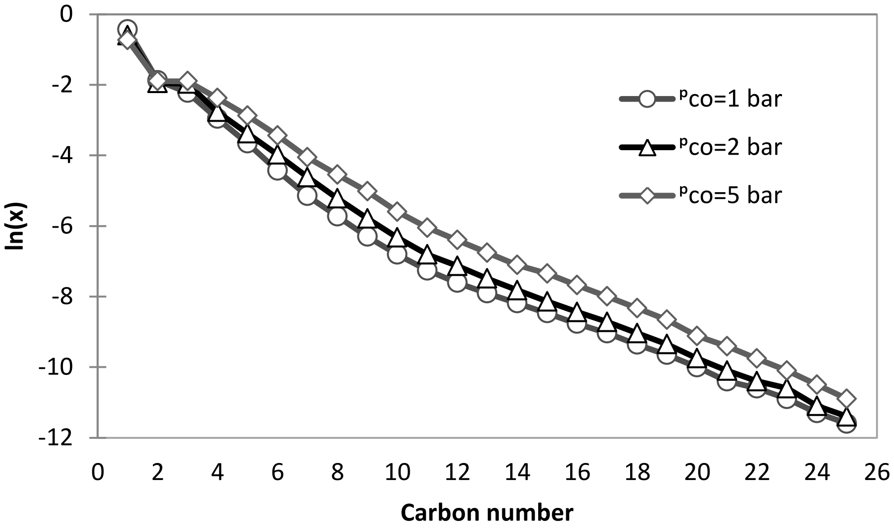

**Figure 6.35** Chain length distributions with respect to partial pressure of carbon monoxide (data from [124]).

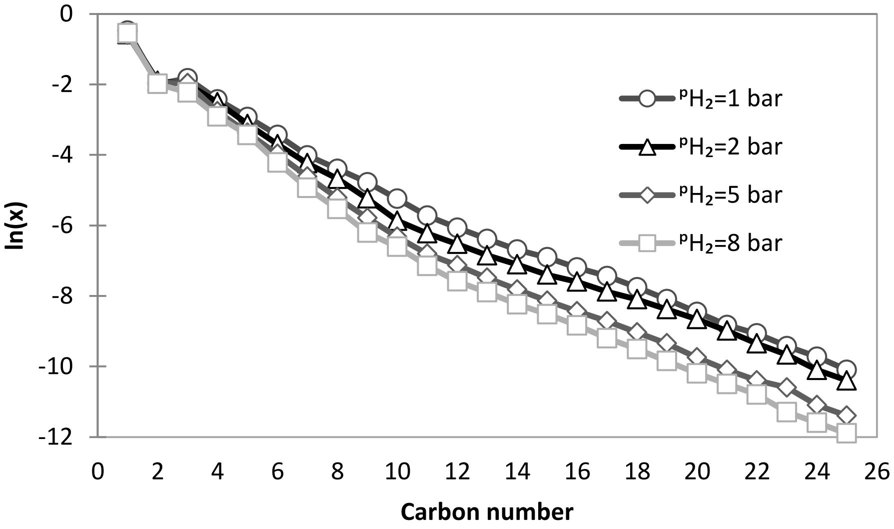

**Figure 6.36** Chain length distributions with respect to partial pressure of hydrogen (data from [124]).

Figures 6.35 and 6.36 show that the partial pressures of carbon monoxide and hydrogen do not have a significant effect on product distribution. The changes in the partial pressures of carbon monoxide and hydrogen have a more dominant effect on producing high carbon number products, which are heavy waxes and not desirable outputs. The partial pressures of hydrogen and carbon monoxide do not play a major role in product distribution, where the reactor temperature has a significant effect on the product distribution.

Alkanes (paraffins) that are represented with a general chemical formula of $C_nH_{2n+2}$ includes gases such as $CH_4$, $C_2H_6$, $C_3H_8$, and $C_4H_{10}$ compose approximately 15% of the overall products. For products starting with $C_{5-11}$ range, it is considered that liquid gasoline is present, and diesel fuel is produced in the range of $C_{12-18}$. Table 6.6 shows the chemical exergy values presented by [48]. The enthalpy of formation, Gibbs free energy, formation entropy, and chemical exergy values of gaseous species are calculated based on NASA external library of EES (see Appendix).

**Table 6.6** Dependence of growth probabilities $\alpha_1$ and $\alpha_2$ and fraction $\mu_1$ on partial pressures $P_{H_2}$ and $P_{CO}$.

| No | T [°C] | $P_{CO}$ [kPa] | $P_{H_2}$ [kPa] | $\alpha_1$ | $\alpha_2$ | $\mu_1$ |
|---|---|---|---|---|---|---|
| 1* | 220 | 110 | 500 | 0.42 | 0.73 | 0.85 |
| 2* | 220 | 230 | 500 | 0.46 | 0.73 | 0.83 |
| 3* | 220 | 490 | 500 | 0.49 | 0.71 | 0.68 |
| 4* | 220 | 200 | 100 | 0.49 | 0.72 | 0.70 |
| 5* | 220 | 200 | 190 | 0.49 | 0.73 | 0.77 |
| 6* | 220 | 200 | 490 | 0.46 | 0.73 | 0.83 |
| 7* | 220 | 200 | 800 | 0.46 | 0.72 | 0.87 |
| 8** | 280 | 750 | 1500 | 0.64 | 0.86 | 0.40 |
| 9** | 300 | 750 | 1500 | 0.61 | 0.87 | 0.46 |
| 10** | 320 | 750 | 1500 | 0.61 | 0.88 | 0.54 |
| 11** | 340 | 750 | 1500 | 0.59 | 0.89 | 0.64 |
| 12** | 300 | 1130 | 1130 | 0.52 | 0.84 | 0.80 |
| 13** | 300 | 750 | 1500 | 0.46 | 0.82 | 0.55 |
| 14** | 300 | 660 | 1600 | 0.48 | 0.81 | 0.65 |
| 15** | 300 | 600 | 1650 | 0.48 | 0.83 | 0.77 |

* Data taken from [124]
** As calculated with experimental data from [125]

The characterizing growth probabilities $\alpha_1$, $\alpha_2$ and the fraction $\mu_1$ of these distributions are listed in Table 6.6. Both probabilities are nearly independent of hydrogen pressure. $\alpha_1$ is slightly increased as the carbon monoxide pressure is raised. A similar result has been obtained by Bub and Baerns for Fe-Mn-oxide catalysts [127]. The fraction $\mu_1$ is raised with increasing hydrogen pressure and decreases with increasing carbon monoxide pressure. In Table 6.6, the results found in the literature are presented with the findings of this study. Reaction temperature has a significant effect on product distribution. A reaction temperature of 280°C is chosen for the calculations to obtain low carbon number products so that more liquid fuels can be obtained after cracking the hydrocarbons.

### 6.4.2.2 Product Distribution

Over the years, many seemingly different mechanisms have been proposed for product distribution. The main commonality among them has been the concept of involving a stepwise chain growth process. This assumption is strongly supported by the fact that the carbon number product distributions calculated solely on probabilities of chain growth were matched by the experimentally observed results obtained in different reactor types and sizes over widely varying process conditions and with different catalysts. Regardless of the catalyst type or feed gas composition, the researchers conclude that, as the temperature is increased, the $CH_4$ selectivity rises, or, put in another way, the probability of chain growth drops.

This work assumes that the Fischer–Tropsch reaction can be described by a stepwise chain-growth reaction for the formation of paraffins as shown below:

$$CO + 2H_2 + [-CH_2-]_{n-1} \leftrightarrow [-CH_2-]_n + H_2O \tag{6.5}$$

The chain growth probability is dependent on the intercept of the Gibbs free energy of reaction/formation ($G_0$) versus carbon number. Gibbs free energy of paraffins varies linearly with carbon number. If a fixed moles of carbon were to be converted to hydrocarbons, a formula that connects total number of moles of hydrocarbons to the the amount of CO converted can be obtained.

$$\frac{\partial G}{\partial \alpha} = -G_0 + R_u\, T[ln\alpha - \ln(1-\alpha)] \tag{6.6}$$

where, $R_u$ is the universal gas constant, $T$ is the temperature of the reaction.

After finding the Gibbs free energy requirement, to convert the hydrocarbons plus mixing, $G_0$ can be minimized by taking the derivative:

$$\frac{\partial G}{\partial \alpha} = 0 \tag{6.7}$$

Then $G_0$ is minimized for the paraffins by the formula below, which is obtained by [128].

$$ln\left(\frac{\alpha}{1-\alpha}\right) = \frac{G_0}{R_u\, T} \tag{6.8}$$

If the enthalpy of reaction is assumed to stay constant with respect to temperature, then the Gibbs–Helmholtz equation can be used to determine the change of the Gibbs free energy of reaction with temperature. The integrated form of the Gibbs–Helmholtz equation is given by:

$$\frac{G_B}{T_B} = H\left(\frac{1}{T_B} - \frac{1}{T_A}\right) + \frac{G_A}{T_A} \tag{6.9}$$

where $G_B$ is the Gibbs free energy of reaction at temperature $T_B$, $H$ is the enthalpy of reaction, and $G_A$ is the Gibbs free energy of reaction at temperature $T_A$.

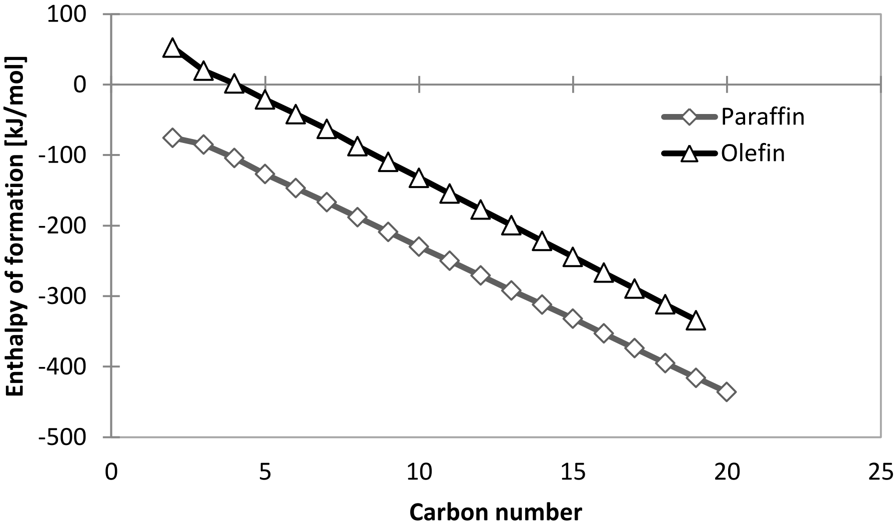

**Figure 6.37** Change of enthalpies of formation with carbon number for paraffins and olefins (modified from [79]).

It can be seen from Figure 6.36 that the enthalpies and Gibbs free energies of formation vary linearly with carbon number for both olefins and paraffins.

Olefins are extensively proposed [79] to be the primary products for the FT reaction and were therefore considered as primary products. Paraffins start with carbon number one. However, olefins start with carbon number two. Therefore, to work out the minimum Gibbs free energy for olefins the derivation has to begin with carbon-number two.

At minimum value of G:

$$\frac{\partial G}{\partial \alpha} = 0 \tag{6.10}$$

Therefore:

$$R_u\, T \frac{1}{(2-a)^2} ln\left(\frac{\alpha^2}{1-\alpha}\right) = \frac{1}{(2-a)^2} \tag{6.11}$$

If one is to assume that the enthalpy of reaction does not change much with temperature then the Gibbs–Helmholtz equation, Equation 6.12, can be used to work out the change of the Gibbs free energy of reaction with temperature as before [128].

$$ln\left(\frac{\alpha^2}{1-\alpha}\right) = \frac{G_0}{R_u\, T} \tag{6.12}$$

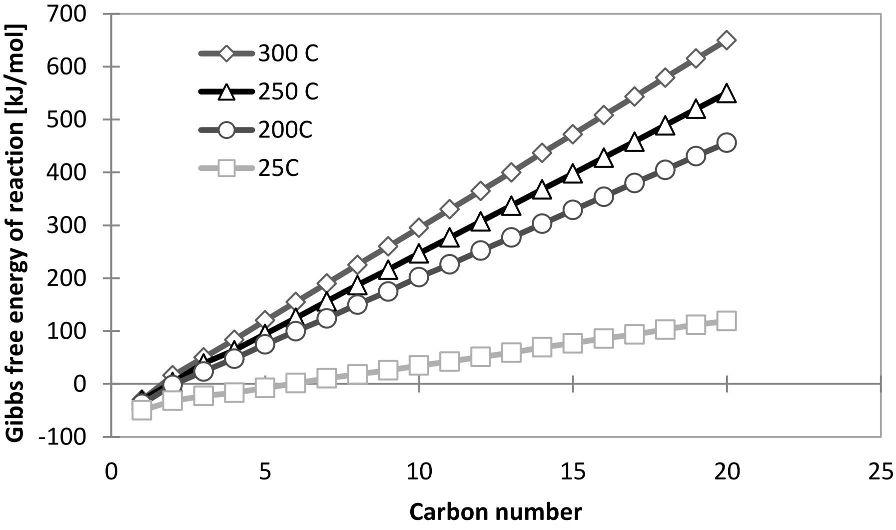

**Figure 6.38** Change of Gibbs free energies of reaction with carbon number and temperature for paraffins (modified from [79]).

It can be interpreted from the above formulae that alpha decreases with increasing temperature. The chain growth probability is dependent on the intercept of the Gibbs free energy of reaction/formation ($G_0$) versus carbon number. Gibbs free energy of reactions of paraffins are extrapolated for relevant temperatures and carbon numbers for paraffins in Figure 6.38 and olefins in Figure 6.39. Relevant data are obtained from [79].

The net change in Gibbs free energy at constant T and P is expressed as [120]:

$$\Delta G = -T\, dS + \Delta H \tag{6.13}$$

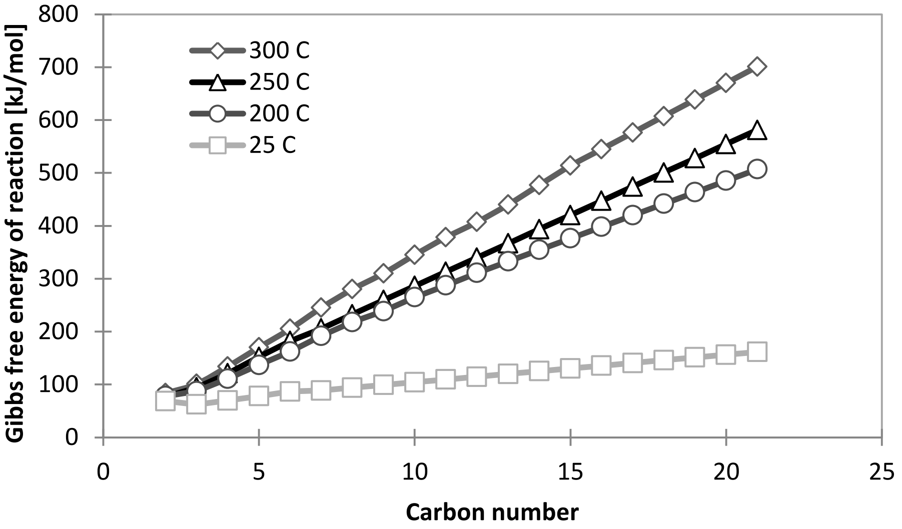

**Figure 6.39** Change of Gibbs free energies of reaction with carbon number and temperature for olefins (modified and extended from [79]).

To calculate the Gibbs free energy and chemical exergy of products, enthalpy and entropy values of EES-NASA external library is employed (see Appendix). The enthalpy value is referenced to 0 for elements at 298.15 K. The reference state for specific entropy is determined by the third law of thermodynamics applied to a pressure of 1.0 bar. Reference chemical exergy values are obtained from [121]. Chemical energy values for alkenes are presented in Table 6.7, where chemical exergy values of alkanes are presented in Table 6.8.

Chemical exergy values are calculated for hydrocarbon products with respect to their carbon number as given in Tables 6.7 and 6.8. In addition to chemical exergies of the hydrocarbon products, their lower heating values and higher heating values are also calculated and presented in Figures 6.40-45. All values are presented both in molar basis and mass basis. For the calculations, chemical exergy values and higher heating values of the products are taken into consideration to calculate the thermodynamic properties of the product. Using the product distribution and higher heating value of the related product, the overall energy of the fuel is calculated. 91% of the fuel consists of these hydrocarbons, where the rest is not taken into consideration. These hydrocarbons can be cracked to obtain liquid fuels such as gasoline and diesel. The higher heating value of the product is utilized in the overall energy efficiency calculation, where chemical exergy is utilized for overall exergy efficiency calculation.

**Table 6.7** Formation enthalpy, entropy, Gibbs energy, and chemical exergy calculated for the alkenes yielded from Fischer Tropsch system.

| **Carbon Number** | **Substance Name** | **Chemical Formula** | **M** | $\Delta_f \boldsymbol{H}^0$ | $\Delta_f \boldsymbol{S}^0$ | $\Delta_f \boldsymbol{G}^0$ | $\boldsymbol{ex}^{ch}$ |
|---|---|---|---|---|---|---|---|
| 2 | acetylene | $C_2H_4$ | 28 | 40.538 | 226 | 54.656 | 1348 |
| 3 | propylene | $C_3H_6$ | 42 | 19.999 | 267 | 62.506 | 2002 |
| 4 | 1-butene | $C_4H_8$ | 56 | -0.540 | 308 | 70.356 | 2656 |
| 5 | 1-pentene | $C_5H_{10}$ | 70 | -21.279 | 347 | 78.585 | 3311 |
| 6 | 1-hexene | $C_6H_{12}$ | 84 | -41.947 | 386 | 86.887 | 3965 |
| 7 | 1-heptene | $C_7H_{14}$ | 98 | -62.756 | 426 | 95.046 | 4620 |
| 8 | 1-octene | $C_8H_{16}$ | 112 | -83.585 | 465 | 103.189 | 5274 |
| 9 | 1-nonene | $C_9H_{18}$ | 126 | -104.401 | 504 | 111.332 | 5928 |
| 10 | 1-decene | $C_{10}H_{20}$ | 140 | -125.220 | 543 | 119.475 | 6582 |
| 11 | 1-undecene | $C_{11}H_{22}$ | 154 | -146.039 | 583 | 127.618 | 7236 |
| 12 | 1-dodecene | $C_{12}H_{24}$ | 168 | -166.858 | 622 | 135.761 | 7890 |
| 13 | 1-tridecene | $C_{13}H_{26}$ | 182 | -187.677 | 661 | 143.904 | 8544 |
| 14 | 1-tetradecene | $C_{14}H_{28}$ | 196 | -208.496 | 700 | 152.047 | 9198 |
| 15 | 1-pentadecene | $C_{15}H_{30}$ | 210 | -229.315 | 740 | 160.190 | 9852 |
| 16 | 1-hexadecene | $C_{16}H_{31}$ | 224 | -250.134 | 779 | 168.333 | 10506 |
| 17 | 1-heptadecene | $C_{17}H_{34}$ | 238 | -270.953 | 818 | 176.476 | 11160 |
| 18 | 1-octadecene | $C_{18}H_{36}$ | 252 | -291.772 | 857 | 184.619 | 11814 |
| 19 | 1-nonadecene | $C_{19}H_{38}$ | 266 | -312.591 | 897 | 192.762 | 12468 |
| 20 | 1-eicosene | $C_{20}H_{40}$ | 280 | -333.410 | 936 | 200.905 | 13122 |
| 21 | 1-henicosene | $C_{21}H_{42}$ | 294 | -354.229 | 975 | 209.048 | 13776 |
| 22 | 1-docosene | $C_{22}H_{44}$ | 308 | -375.048 | 1014 | 217.191 | 14430 |
| 23 | 1-tricosene | $C_{23}H_{46}$ | 322 | -395.867 | 1054 | 225.334 | 15084 |
| 24 | 1-tetracosene | $C_{24}H_{48}$ | 336 | -416.686 | 1093 | 233.477 | 15738 |
| 25 | 1-pentacosene | $C_{25}H_{50}$ | 350 | -437.505 | 1132 | 241.620 | 16392 |
| 26 | 1-hexacosene | $C_{26}H_{52}$ | 364 | -458.324 | 1171 | 249.763 | 17046 |

M molecular mass (kg/kmol)
$\Delta_f H^0$ formation enthalpy (kJ/mol)
Formation entropy: $\Delta_f S^0 = s^0 - \sum_{elements} v s^0_{f,element}$ (J/mol K), where $v$ is the number of moles of the element in chemical equation of formation of the substance
Gibbs free energy of formation: $\Delta_f G^0 = \Delta_f H^0 - T_0 \Delta_f S^0$ (kJ/mol)
Chemical exergy: $ex^{ch} = \Delta_f G^0 + \Sigma_{elements}\, v \times ex^{ch}_{element}$ (kJ/mol)
Reference temperature: $T_0$=298.15 K
Reference pressure: $P_0$=1 bar; superscript 0 in above notations refers to standard pressure

The lower and higher heating values are calculated using formation enthalpies of water and cabon dioxide, since oxidation of hydrocarbons results in water and carbon dioxide. The only difference in the calculations is the latent heat of water; when the product water is in gas phase, then formation enthalpy of water vapor is taken as -241.818 [79], which yields in higher heating value. When the product water is in liquid phase, then formation enthalpy of water vapor is taken as -285.813 [79], which yields in lower heating value.

**Table 6.8** Formation enthalpy, entropy, Gibbs energy, and chemical exergy calculated for the alkanes yielded from Fischer Tropsch system.

| Carbon Number | Substance Name | Chemical Formula | M | $\Delta_f H^0$ | $\Delta_f S^0$ | $\Delta_f G^0$ | $ex^{ch}$ |
|---|---|---|---|---|---|---|---|
| 1 | methane | $CH_4$ | 16 | -74.595 | 186 | -50.529 | 832 |
| 2 | ethane | $C_2H_6$ | 30 | -83.846 | 229 | -31.885 | 1497 |
| 3 | propane | $C_3H_8$ | 44 | -104.674 | 270 | -24.294 | 2151 |
| 4 | n-butane | $C_4H_{10}$ | 58 | -125.782 | 310 | -16.529 | 2805 |
| 5 | n-pentane | $C_5H_{12}$ | 72 | -146.751 | 350 | -8.658 | 3459 |
| 6 | n-hexane | $C_6H_{14}$ | 86 | -166.910 | 389 | 0.140 | 4115 |
| 7 | n-heptane | $C_7H_{16}$ | 100 | -187.768 | 428 | 8.252 | 4769 |
| 8 | n-octane | $C_8H_{18}$ | 114 | -208.737 | 423 | 14.184 | 5421 |
| 9 | n-nonane | $C_9H_{20}$ | 128 | -229.632 | 448 | 22.639 | 6076 |
| 10 | n-decane | $C_{10}H_{22}$ | 142 | -250.546 | 465 | 30.303 | 6730 |
| 11 | n-undecane | $C_{11}H_{24}$ | 156 | -271.459 | 482 | 37.967 | 7384 |
| 12 | n-dodecane | $C_{12}H_{26}$ | 170 | -292.373 | 499 | 45.630 | 8038 |
| 13 | n-tridecane | $C_{13}H_{28}$ | 184 | -313.286 | 516 | 53.294 | 8692 |
| 14 | n-tetradecane | $C_{14}H_{30}$ | 198 | -334.200 | 533 | 60.958 | 9346 |
| 15 | n-pentadecane | $C_{15}H_{32}$ | 212 | -355.113 | 551 | 68.622 | 10000 |
| 16 | n-hexadecane | $C_{16}H_{34}$ | 226 | -376.027 | 568 | 76.286 | 10654 |
| 17 | n-heptadecane | $C_{17}H_{36}$ | 240 | -396.940 | 585 | 83.950 | 11308 |
| 18 | n-octadecane | $C_{18}H_{38}$ | 254 | -417.854 | 602 | 91.613 | 11962 |
| 19 | n-nonadecane | $C_{19}H_{40}$ | 268 | -438.767 | 619 | 99.277 | 12616 |
| 20 | n-eicosane | $C_{20}H_{42}$ | 282 | -459.681 | 636 | 106.941 | 13270 |
| 21 | n-henicosane | $C_{21}H_{44}$ | 296 | -480.594 | 653 | 114.605 | 13924 |
| 22 | n-docosane | $C_{22}H_{46}$ | 310 | -501.508 | 671 | 122.269 | 14578 |
| 23 | n-tricosane | $C_{23}H_{48}$ | 324 | -522.421 | 688 | 129.933 | 15232 |
| 24 | n-tetracosane | $C_{24}H_{50}$ | 338 | -543.335 | 705 | 137.596 | 15886 |
| 25 | n-pentacosane | $C_{25}H_{52}$ | 352 | -564.248 | 722 | 145.260 | 16540 |
| 26 | n-hexacosane | $C_{26}H_{54}$ | 366 | -585.162 | 739 | 152.924 | 17194 |

Same footnotes are valid as Table 6.7.

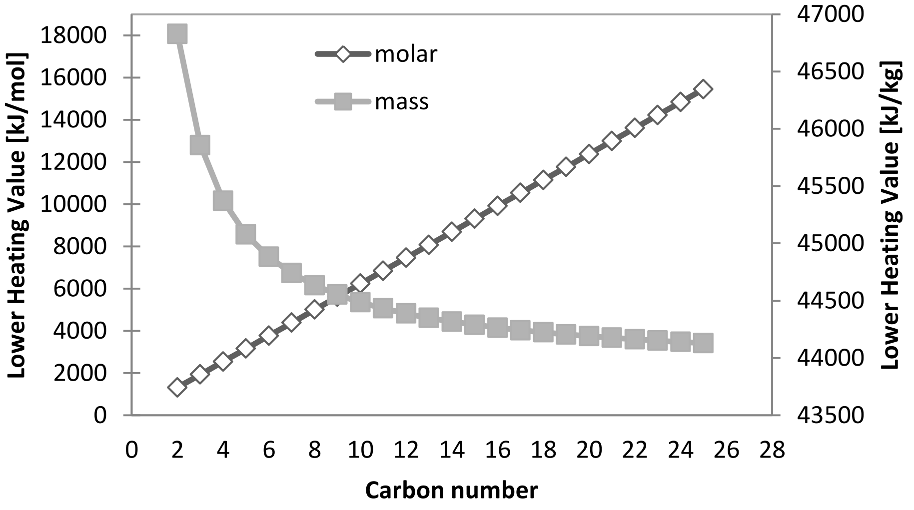

**Figure 6.40** Change of lower heating values with carbon number and for olefins

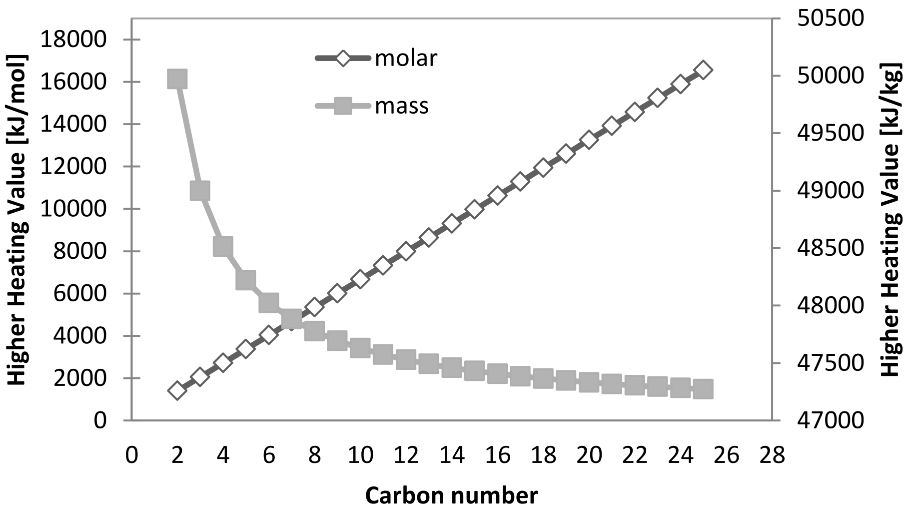

**Figure 6.41** Change of higher heating values with carbon number and for olefins

The chemical exergy values with respect to carbon number of the hydrocarbon products show that molar chemical exergy values generate a linear line, which is not exemplified before according to the author's knowledge. Long-chain molecules have more energy per mole, but since their molar mass is higher, their heating values in mass basis get lower.

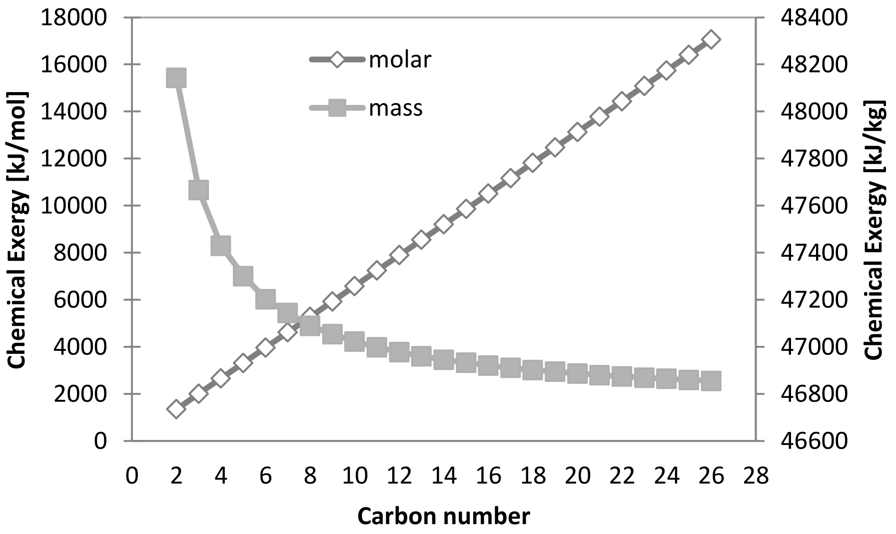

**Figure 6.42** Change of chemical exergy values with carbon number and for olefins

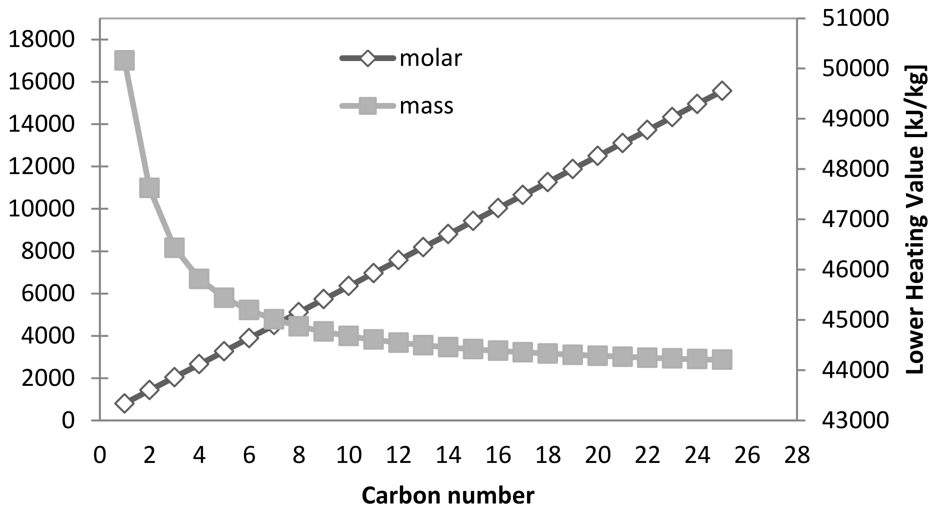

**Figure 6.43** Change of lower heating values with carbon number and for paraffins

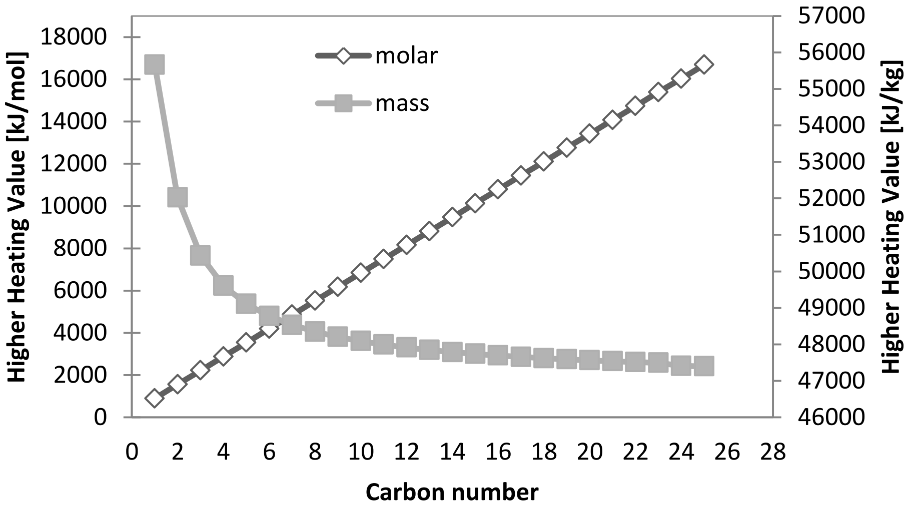

**Figure 6.44** Change of higher heating values with carbon number and for paraffins

It can be seen that heating values of paraffins are higher than those of olefins for the same carbon number due to higher hydrogen content of paraffins. The logarithmic values used in the product distribution graphs are converted into weight fractions. Chemical exergy and heating values are first calculated in molar basis and then converted into mass basis to equalize the units with the product distribution data. To be able to produce more wax, thus more liquid fuels, 280°C is selected as FT reaction temperature.

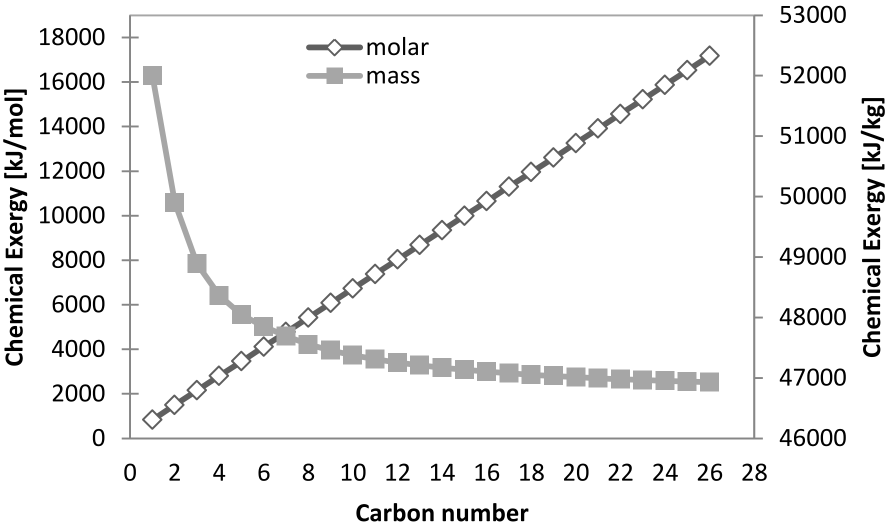

**Figure 6.45** Change of chemical exergy values with carbon number and for paraffins

The heat released during exothermic reactions should be taken into account to calculate the heat transfer to the water cycle, which provides heat for the ORC sub-system. It can be seen from Figure 6.46 that there are two slopes in this graph: from 280°C to 310°C, there is a smaller slope, whereas from 315°C to 310°C, there is a larger slope. For this study, the base case for FT reactor is chosen to be 280°C to minimize heat dissipation.

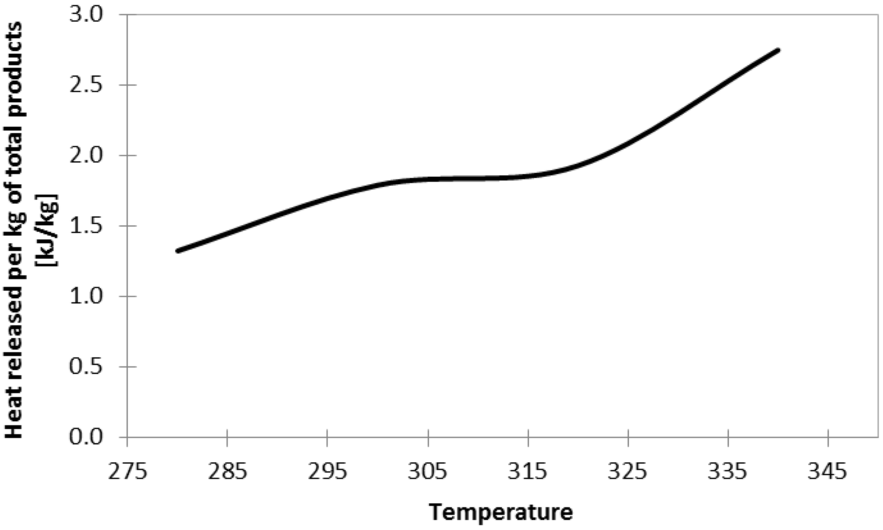

**Figure 6.46** Variation of heat released per unit mass of total products with respect to Fischer-Tropsch reactor temperature.

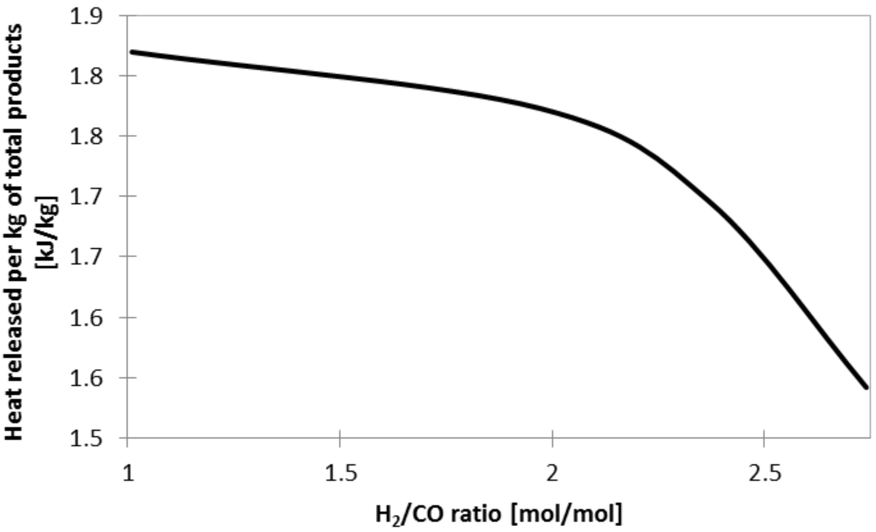

**Figure 6.47** Variation of heat released per unit mass of total products with respect to $H_2$/CO ratio at the inlet of Fischer-Tropsch reactor.

The variation of heat released per unit mass of total products with respect to $H_2$/CO molar ratio is plotted in Figure 6.47. As can be seen from the figure, if the $H_2$/CO molar ratio is from 1 to 2, the amount of heat released does not change significantly, where it drops incrementally after $H_2$/CO molar ratio of 2. Achieving greater $H_2$/CO molar ratio requires additional steam input, which increases the energy input to the system.

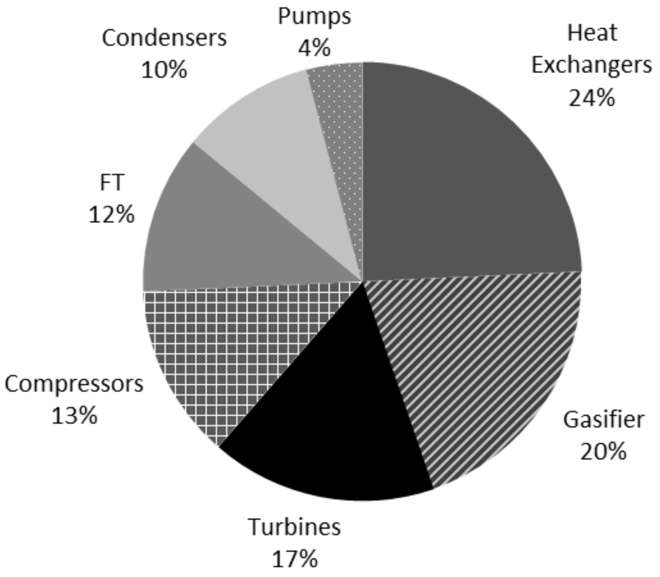

**Figure 6.48** Exergy destruction rates associated for each component of System 2.

### 6.4.3 Parametric Study Results

Various parametric studies are carried out to present the effects of variations in dead state temperature, salinity, ammonia fraction, type of feed-stock and equivalence ratio on energy and exergy efficiencies of System 2. In this section, the results of these aforementioned parametric studies are plotted along with their corresponding explanations.

In Figure 6.49, variation of efficiency of System 2 and its sub-systems are given with respect to ambient temperature. In this thesis, the base case ambient temperature is taken as 25°C and the dead-state temperature is varied between 20°C and 30°C. It is observed that the ambient temperature does not have a significant impact on energy efficiencies. Rankine cycle is the most affected sub-system. Overall system efficiency is decreased approximately 0.5 % with 10°C change in the ambient temperature.

Figure 6.50 shows that the exergy efficiencies are more affected by the ambient temperature, as expected. There is around 1-3% of change in each system, where Rankine cycle shows the largest decrease as a response to increasing ambient temperature. Overall system efficiency decreases around one percent. This result can be interpreted as the colder areas have larger exergy efficiency, where seasonal temperature changes also can affect the exergy efficiency.

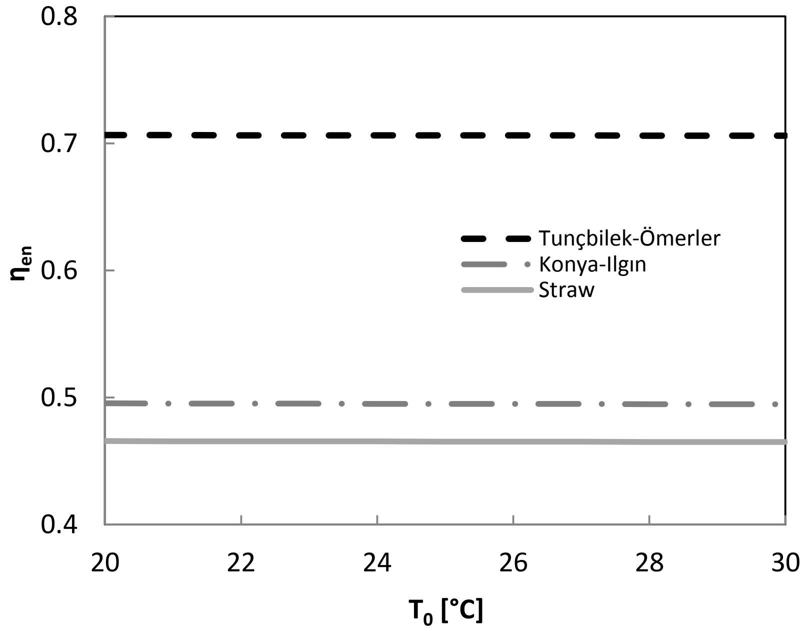

**Figure 6.49** Variation of energy efficiencies of System 2 with respect to ambient temperature.

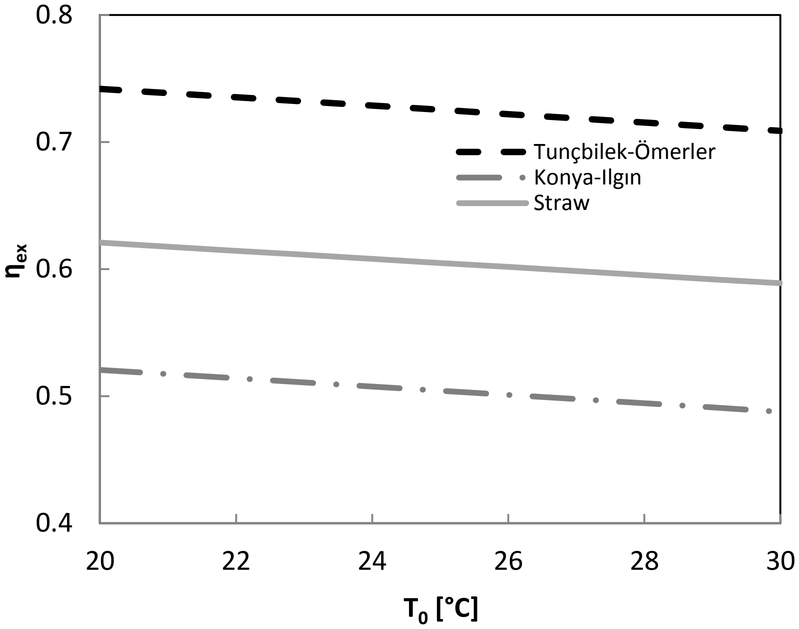

**Figure 6.50** Variation of exergy efficiencies of System 2 with respect to ambient temperature.

The energy efficiency change with respect to dead state temperature can be attributed to temperature difference between the lowest temperature and the highest temperature of the system. When this difference gets larger, the maximum possible work output increases due to Carnot efficiency rule. By keeping the high temperature constant, lowering the low temperature will increase the energy efficiency.

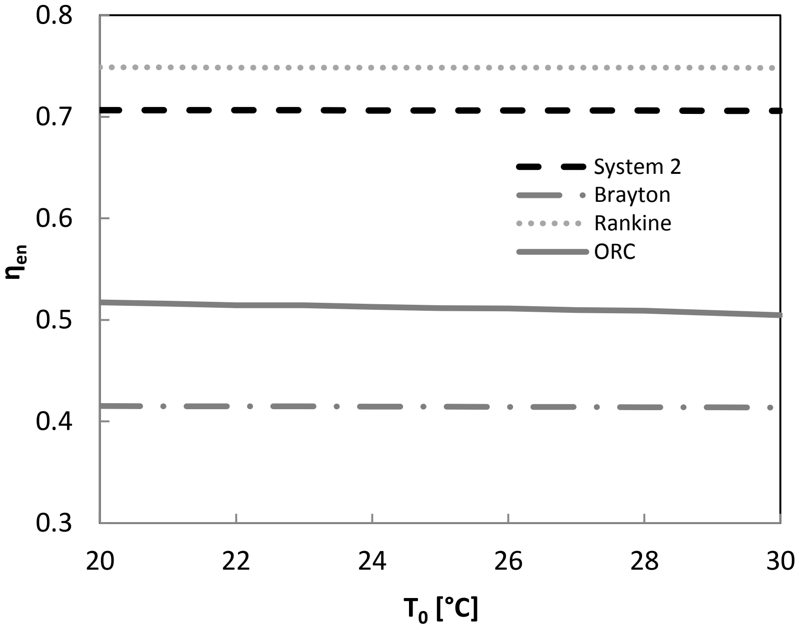

**Figure 6.51** Variation of energy efficiencies of System 2 and its sub-systems with respect to ambient temperature.

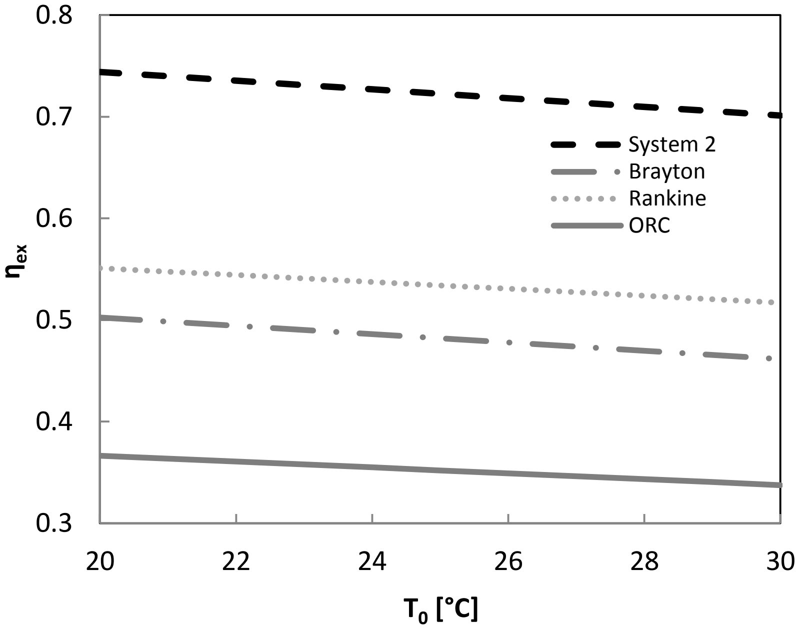

**Figure 6.52** Variation of energy efficiencies of System 2 and its sub-systems with respect to ambient temperature.

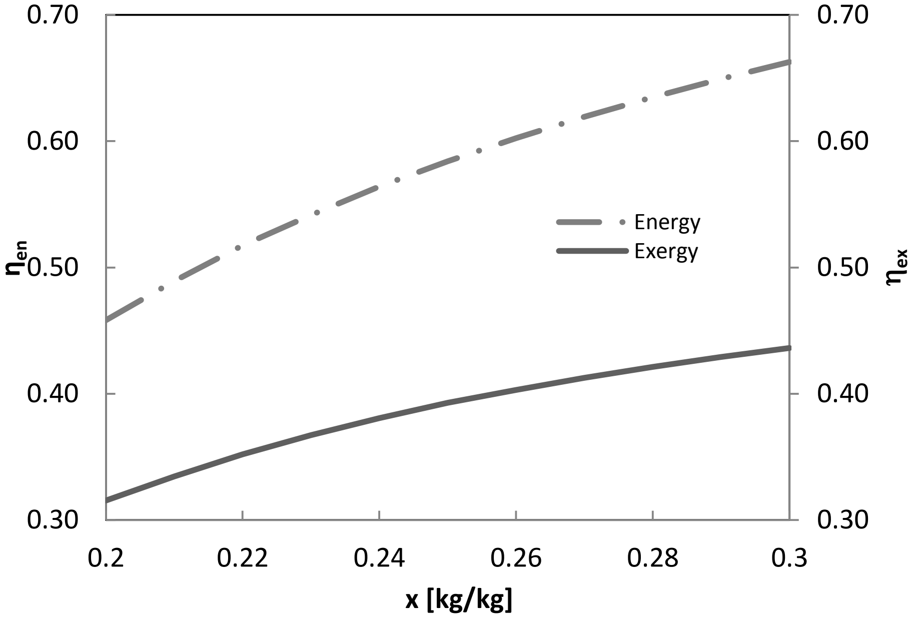

**Figure 6.53** Variation of energy and exergy efficiencies of ORC system with respect to ammonia mass fraction.

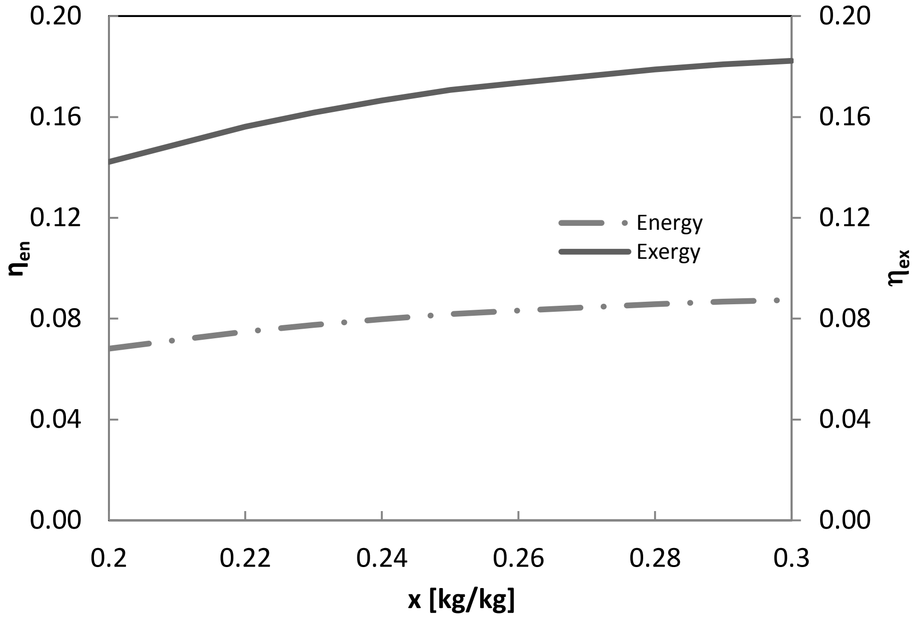

**Figure 6.54** Variation of energy and exergy efficiencies of ORC system with respect to ammonia mass fraction without hot water production.

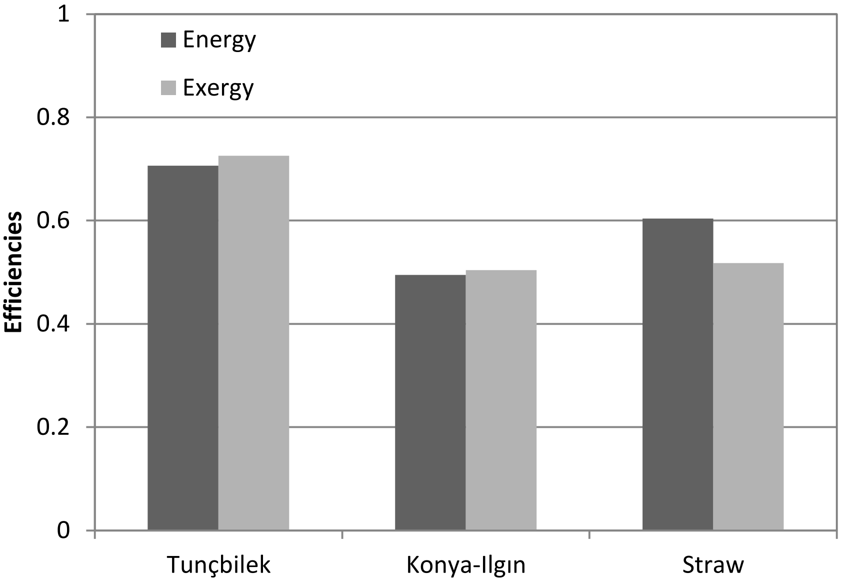

**Figure 6.55** Variation of energy and exergy efficiencies of System 2 with respect to the feedstock.

The exergy efficiencies of the overall system, as well as sub-systems are affected significantly by change in the dead state temperature. Exergy efficiency of System 2 decreases approximately 3.5% by an increase in the dead state temperature from 20°C to 30°C, where the lowest affected sub-system is the ORC. The ORC is highly affected by ammonia concentration of the working fluid. Energy efficiency of the cycle increases approximately 2%, exergy efficiency of the cycle increases 4% with 10% increase in the ammonia mass fraction starting from 20%.

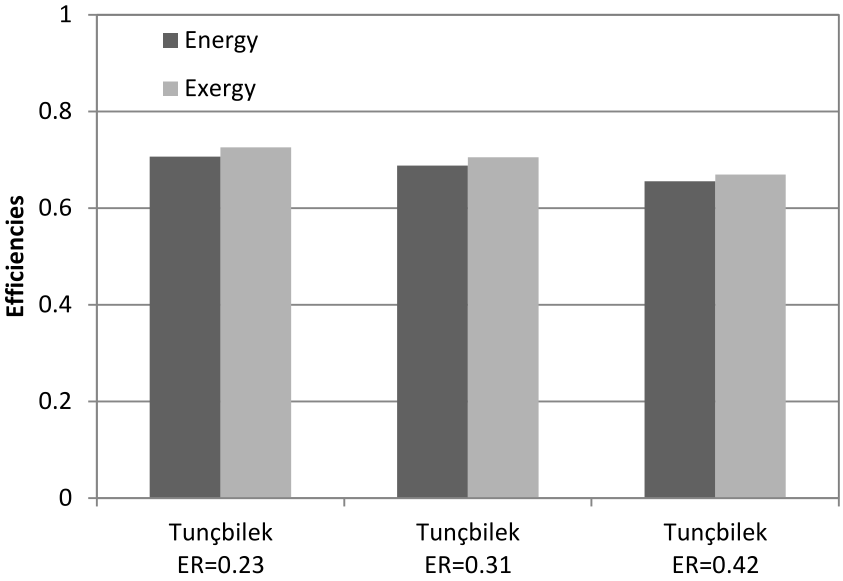

**Figure 6.56** Variation of energy and exergy efficiencies of System 2 with respect to air ratio for Tunçbilek coal.

It can be seen from Figure 6.56 that lower equivalence ratios result in a higher energy and exergy efficiency. It should be noted that there is a minimum fluidization velocity that must be provided to obtain fluidization, which increases the efficiency of the reaction by enabling a better mixing of air and feedstock. Also, if the equivalence ratio becomes zero, pyrolysis reactions take place that result in liquid products, which is also not desirable for a gasification system.

Figure 6.57 shows energy and exergy efficiency variations for System 2 for the same input by changing the useful outputs. First, a conventional power plant that generates power alone (Single-Generation), second heating is added to the outputs (Co-generation), and finally power, heating and FT fuel outputs are considered together (Tri-generation). Once again, as found in the first system, tri-generation is superior among all. Heating output affects the overall efficiencies more than that of FT fuels. Although co-generation results in better efficiencies, it is worth mentioning that liquid fuels can be more desirable where gaseous and liquid fossil fuel resources are limited.

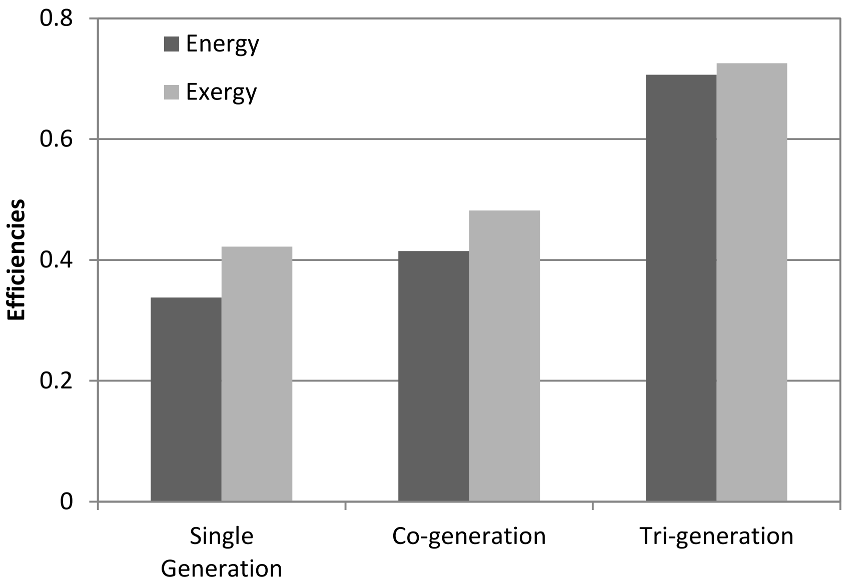

**Figure 6.57** Variation of energy and exergy efficiencies of System 2 for conventional, co-generation and tri-generation power plants.

## 6.5 Optimization

Optimization using the aforementioned objective function (Equation 5.34), constraints (Table 5.3) and decision variables are performed with the help of genetic algorithms. In the analysis, optimization scenarios with the objective functions of exergy efficiency with and without waste water utilization and electricity production are performed. The corresponding optimization scenarios can be seen in Figures 6.57–59 respectively.

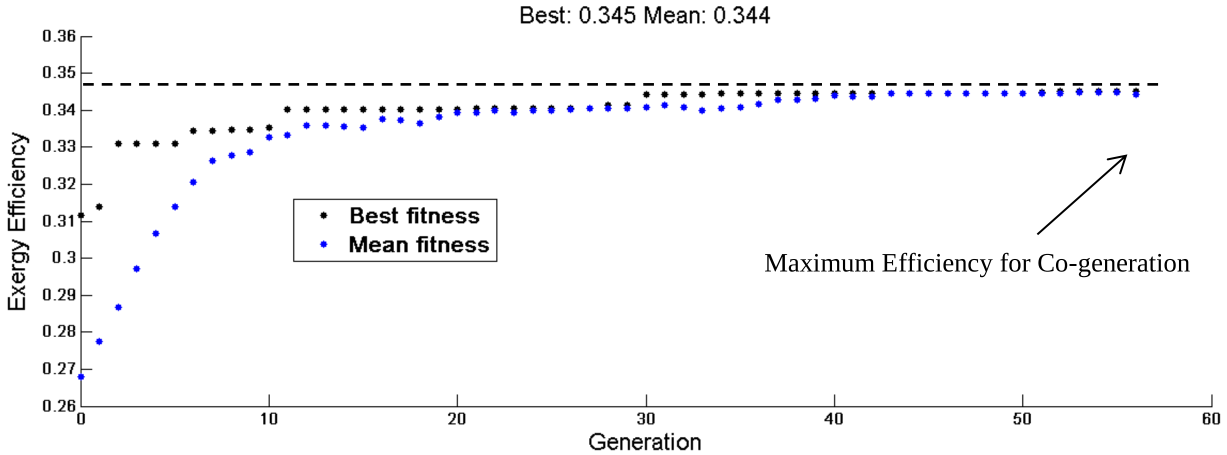

Maximum Efficiency for Co-generation

**Figure 6.58** Optimization of the system over generations with respect to exergy efficiency.

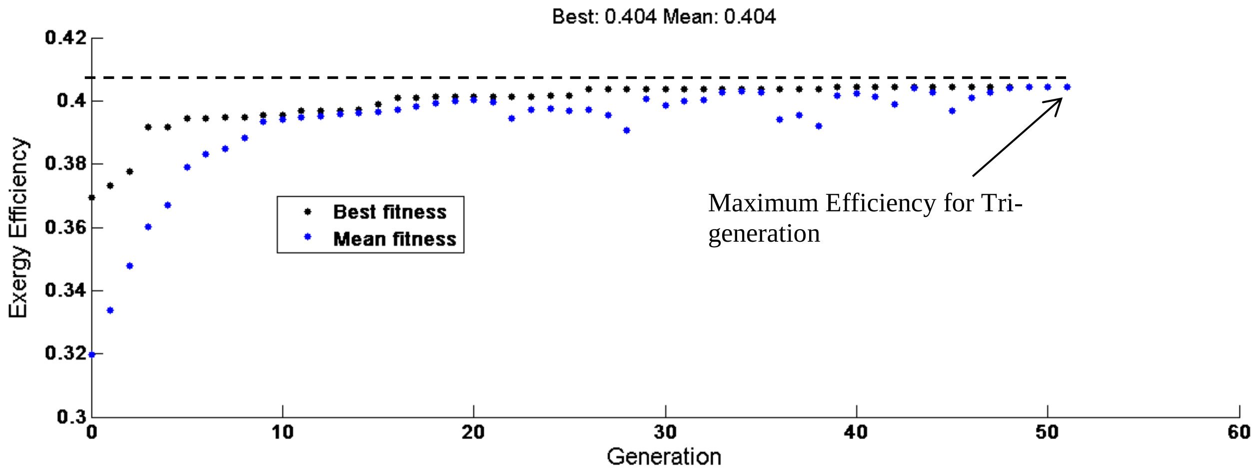

Maximum Efficiency for Tri-generation

**Figure 6.59** Optimization of the system over generations with respect to exergy efficiency with the utilization of hot water.

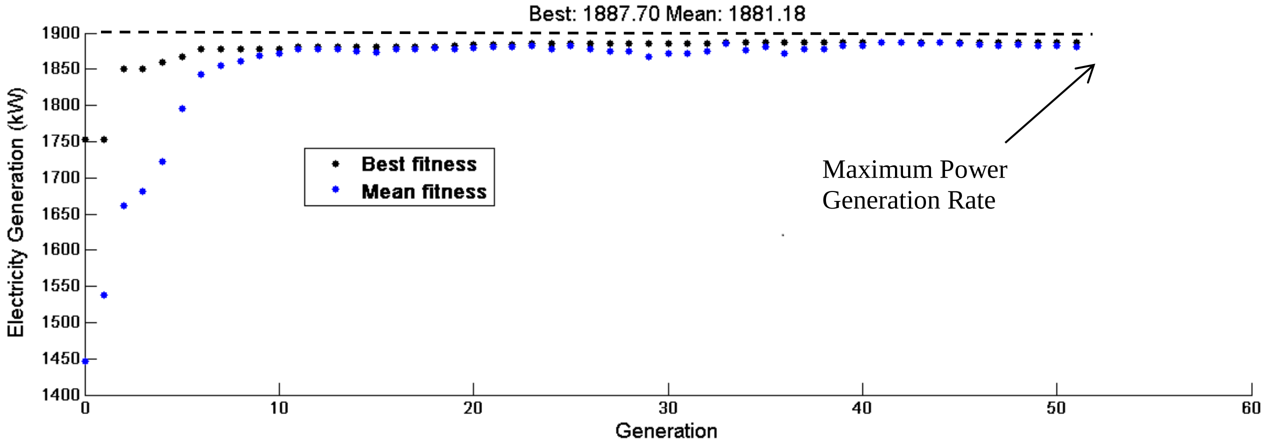

Maximum Power Generation Rate

**Figure 6.60** Optimization of the system over generations with respect to electricity generated in the turbines.

Table 6.60 shows the values for the decision variables in the base case design along with different optimization criteria. In addition, the results of analyses for each optimization criteria are also shown in the table. It should be noted that the values for the decision variables are considered to be continuous over the determined constraints for the optimization problem. However, usually parameters associated with some of these variables are only available in discrete units. Therefore, in a case where the determined parameter values are not available, the closest available values should be utilized in the system for most optimal results.

**Table 6.9** Decision variables for the base case design under various optimization criteria for the systems.

| Decision Variable | Base Case Design | Exergy Efficiency (co-generation) | Exergy Efficiency (tri-generation) | Power Production |
|---|---|---|---|---|
| $\boldsymbol{T_0}$ [°C] | 25 | 22.34 | 29.96 | 20.02 |
| $\boldsymbol{I_{solar}}$ [kW/m$^2$-°C] | 0.7 | 1 | 1 | 1 |
| $\boldsymbol{salinity}$ | 35 | 35 | 35 | 35 |
| $\boldsymbol{x}$ | 0.15 | 0.25 | 0.25 | 0.23 |
| $\boldsymbol{\eta_{turb}}$ | 0.8 | 0.89 | 0.80 | 0.90 |
| $\boldsymbol{\eta_{HEX}}$ | 0.85 | 0.9 | 0.90 | 0.90 |

As shown above, the analyzed system is optimized with respect to a genetic algorithm using total electricity production and exergy efficiency. The optimization is performed to maximize the energy efficiency and electricity production. Ambient temperature, solar intensity, water salinity, ammonia-water concentration and heat exchanger and turbine efficiency are selected as the decision variables and various constraints are applied based on appropriate feasibility and engineering constraints. The decision variables along with efficiencies for each component are compared under each optimization approach.

In a multi-objective optimization scenario however, these objectives are considered simultaneously, which provides optimized solutions with values in between the extremes yielded by the single-objective approaches as a result of the trade-offs made between the solutions of the two different objectives.

The Pareto frontier associated with the multi-optimization scenario is shown in Figure 6.61 below. It should be noted that all of the points on the Pareto frontier yield optimum solutions for the system. However, the slope of the Pareto curve shows that around exergy efficiency values of 0.47, the impact of the exergy efficiency is significantly higher than that of the power generation and therefore, a solution before this point on the curve should be selected for the optimized value.

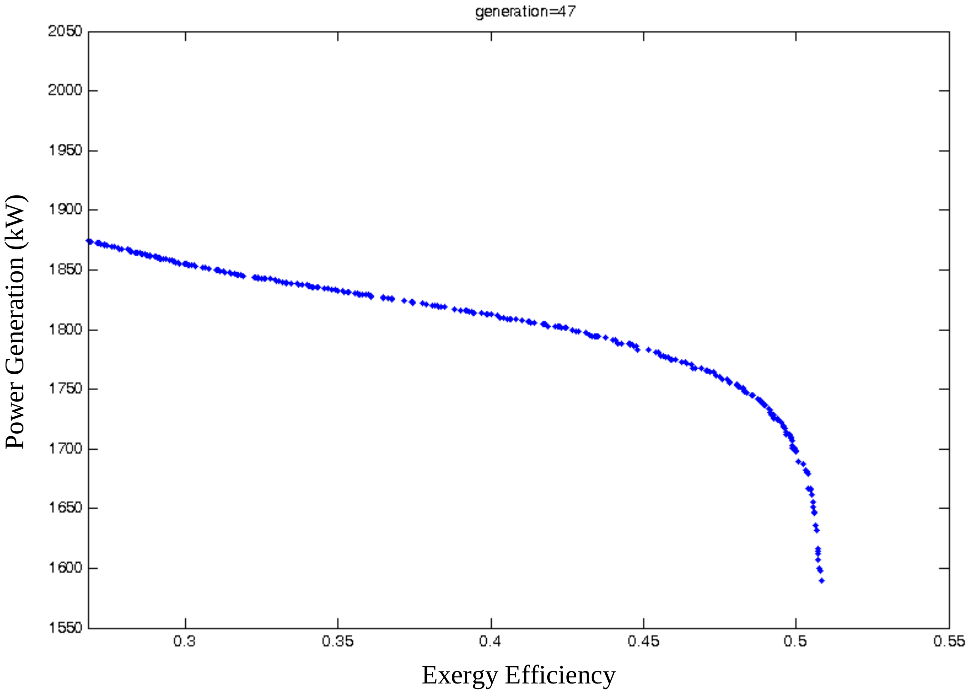

**Figure 6.61** Multi-objective optimization of the system with respect to exergy efficiency and power generation.

In summary, the system is optimized using a multi-objective genetic algorithm using total electricity production and power generation objectives. The optimization is performed to maximize the electricity production (based on turbine work) and maximize the product yield (based on the FT reactor). Ambient temperature, solar intensity, water salinity, ammonia-water concentration and heat exchanger and turbine efficiency are selected as the decision variables for the systems, and various constraints are applied based on appropriate feasibility and engineering constraints. The decision variables along with efficiencies for each component are compared under each optimization approach. In the multi-objective optimization, a Pareto frontier is obtained and a group of desirable optimal solutions are selected based on the slope of the curve. The corresponding solutions are compared against each single-objective optimization results. Even though the single-objective approaches provided optimal solutions for their objectives, they provided very poor solutions for the remaining objectives. Thus, the multi-objective optimization approach provides a solution set within the extremes of the single-objective results by evaluating two objectives simultaneously and providing trade-offs between them to obtain desirable solution sets.

## 6.6 Cost Analysis

Even though the thermodynamic analyses (especially exergy analysis) can be used to improve the efficiencies and performance of the systems, the feasibility of applying these improvements is generally constrained by the limitation of financial resources. Moreover, in many cases, the approaches taken by purely scientific motivation may not always be cost effective. Thus, to conduct a complete analysis, economic aspects of the systems should also be examined thoroughly.

For the economic aspect of the analysis, the capital investment rates are calculated with respect to the purchase cost of equipment and capital recovery as well as maintenance factor over the number of operation hours per year [129] as given below:

$$\dot{Z}_k = \frac{Z_k \cdot CRF \cdot \varphi}{N}$$

where $N$ is the annual number of operation hours for the unit and $\varphi$ is the maintenance factor, generally taken as 1.06 [130]. *CRF* is the capital recovery factor which depends on the interest rate *(i)* and equipment life-time in years *(n)* as:

$$CRF = \frac{i \times (1+i)^n}{(1+i)^n - 1}$$

For the conducted studies, an interest rate of 10% and depreciation period of 15 years are used. Here, $Z_k$ is the purchase equipment cost of the system components that should be written in terms of design parameters. For the heat exchangers, since the component cost mainly depends on the heat exchanger area, initial calculations are done to determine the heat exchange area for each component. Thus, temperature differences are determined based on the log mean temperature difference method (LMTD) for heat exchangers as given below:

$$LMTD = \frac{\left(T_{H,i} - T_{L,o}\right) - \left(T_{H,o} - T_{L,i}\right)}{\ln\left(\frac{T_{H,i} - T_{L,o}}{T_{H,o} - T_{L,i}}\right)}$$

where the subscripts $H$ and $L$ represent high and low temperature sides and $i$ and $o$ refer to “in” and “out”, respectively. The heat load on the system is calculated with respect to the mass flow rate, temperature differences and specific heat of the fluid, and the corresponding heat transfer area of the heat exchanger is calculated accordingly as shown below:

$$\dot{Q} = \dot{m}_{ref} C_p \Delta T_{LMTD}$$

$$A = \dot{Q}/U\Delta T_{LMTD}$$

Once the heat exchange area is determined, the associated cost correlations developed by Turton et al. [131] are used as shown below:

$$log_{10}(Z_k) = K_1 + K_2 log_{10}(A) + K_3[log_{10}(A)]^2$$

where $A$ is the capacity or size parameter for the equipment. The values for constants $K_1$, $K_2$, $K_3$ are 4.3247, -0.3030 and 0.1634, respectively. Moreover, the pumps used in both systems are calculated with respect to the pumping power as shown below [132]:

$$Z_{pump} = 308.9\dot{W}_{pump}^{C_{pump}}$$

$C_{pump}$ = 0.25 for 0.02 kW < $\dot{W}_{pump}$ < 0.3 kW

$C_{pump}$ = 0.45 for 0.3 kW < $\dot{W}_{pump}$ < 20 kW

$C_{pump}$ = 0.84 for 20 kW < $\dot{W}_{pump}$ < 200 kW

Here, $\dot{W}_{pump}$ is the pumping power in kW and $C_{pump}$ is the pump coefficient with respect to the corresponding pumping power ranges.

For the solar tower, cost correlations are developed by using the data obtained by [133], where the characteristics and costs of solar increment are provided for various solar tower models and configurations. For a collector size of 13,800 $m^2$ and receiver power of 1.45 $MW_{th}$, the costs associated with heliostats, receiver/tower and thermal storage are calculated to be \$1.01M, \$0.30M and \$0.37M respectively.

For the desalination plant, since the overall cost of the system is highly dependent on the plant capacity, the cost is determined with respect to the cost database found in the literature. The analyzed desalination system uses seawater reverse osmosis with a capacity of 15.8 $m^3$/day. The correlation shown below is utilized for the analyzed plant size [73]. In addition, a membrane replacement cost of 5% of the overall plant cost is accounted for in the cost calculations.

The sizes of the systems are selected such that they both generate 5 MW power.

$$Z_{desalination} = 7100 \times C^{0.85}$$

The component costs associated with the gasification and Fischer-Tropsch synthesis processes are calculated with respect to cost correlations used from the available data in the literature [134]. Specific costs of most system components are affected mostly by their capacity. Thus, the general equation given below is used.

$$Costs_{system}/Costs_{base} = (Size_{system}/Size_{base})^{R}$$

where R is the scaling factor. For the most of the components, the value of R usually lies between 0.6 and 0.8. The maximum size for each unit is taken into consideration for each component, above which increasing scale is no longer economically attractive. Overall scale factors are used for making cost estimated for the capacities used in the study compared to the base capacity of 367 $MW_{th}$ (shown in Table 6.10 below).

**Table 6.10** Basic costs for all units used with their maximum size (based costs are in relation to base scales). All costs are expressed in MUS$.

| **Component** | **Base Cost** | **Scale Factor** | **Base scale** | **Unit Maximum Size** |
|---|---|---|---|---|
| Compressors[1] | 12.0 | 0.85 | 13.2 $MW_e$ | - |
| Turbines[1] | 7.7 | 0.7 | 25 $MW_e$ | - |
| Feeding System[1] | 0.38 | 1 | 69.54 $MW_{th}$ LHV | 367 |
| Gasifier[2] | 13 | 0.7 | 400 $MW_{th}$ HHV | 200 |
| Cyclones[1] | 2.57 | 0.7 | 69.54 $MW_{th}$ LHV | 367 |
| Gas Turbine[1] | 7.7 | 0.7 | 25 $MW_e$ | - |
| Shift Reactor | 0.45 | 0.6 | 2400 kmol/h | - |
| FT Reactor[3] | 16.7 | 1 | 100 MW FT-liquid | - |

[1] Cost figures based on first generation BIG/CC installations, taken from [135]
[2] Cost figures taken from [134].
[3] Calculated for fixed bed reactor since no reliable cost data are found in the literature for fluidized bed reactors. Main factor used in the amount of CO converted to FT-liquids (in MW, HHV based)

The cost of the blower is determined with respect to the cost correlations provided by Loh et al. [136] based on the actual capacity of the component. In addition, the cost of electronics and piping are considered to be 7% and 4% of the total hardware costs, respectively. The cost associated with each component for the systems are listed below in Table 6.11.

From Table 6.11, it can be seen that the overall costs for 5 MW power generation for both Systems 1 and 2, System 2 has a lower investment cost. On the other hand, operational cost of System 2 will be higher than System 1 due to feed-stock costs. Solar power generation has a higher investment cost, whereas it has less operational cost.

**Table 6.11** The cost of each components for Systems 1 and System 2 under baseline configurations and conditions.

| **Component** | **Cost ($M)** | |
|---|---|---|
| | **System 1** | **System 2** |
| Solar Tower System | 5.69 | -- |
| Desalination System | 19.28 | -- |
| Osmotic Membrane | 0.96 | -- |
| Blower | -- | <0.01 |
| Feeding System | -- | 0.19 |
| Gasifier | -- | 2.03 |
| Cyclone | -- | 1.60 |
| Shift Reactor | -- | 0.12 |
| FT Reactor | -- | 14.65 |
| Compressors | -- | 4.40 |
| Pumps | <0.01 | <0.01 |
| Expanders | <0.01 | <0.01 |
| Turbines | 3.31 | 3.8 |
| Heat Exchangers | 0.14 | 0.12 |
| Electronics | 1.35 | 2.08 |
| Piping | 0.77 | 1.19 |
| Total Cost | 32.52 | 30.09 |

## 6.7 Environmental Impact Assessment

The solar tower power plant with the nominal capacity of 2 MW and heliostat area of 13,800 $m^2$ are analyzed with respect to the associated environmental impact. The required materials for the solar tower utilized in the system along with the energy used in the production of 1 ton of each material and its distribution are correlated from the data provided in [137] and are shown in Table 6.12.

**Table 6.12** Required materials and associated energy consumption for construction of the studied solar power tower sub-system (data taken from [137])

| **Material** | **Weight [ton]** | **Energy Consumption** | | | **Total [MJ/ton]** |
|---|---|---|---|---|---|
| | | **Coal [MJ/ton]** | **Crude Oil [MJ/ton]** | **Natural Gas [MJ/ton]** | |
| Aluminum | 64 | 3960 | 4 | 18410 | 22374 |
| Concrete | 3700 | 720 | 1 | 1266 | 1987 |
| Copper | 14100 | 27828 | 56 | 40530 | 68414 |
| Chromium | 2750 | 102960 | 133 | 85400 | 188493 |
| Glass | 136 | 0 | 135 | 309 | 444 |
| Plastic | 23 | 15192 | 91 | 5320 | 20603 |
| Steel | 1090 | 67680 | 47 | 23520 | 91247 |
| Insulation | 55 | 10928 | 79860 | 144960 | 235748 |

Thus, the associated energy consumption for the raw material production is provided in Figure 6.62. The aforementioned materials and the associated energy consumption are analyzed with respect to various impact categories to determine the corresponding impacts to the environment. These impacts are calculated adopting the Eco-indicator method [138]. The standard Eco-indicator values are dimensionless and named as Eco-indicator point (Pt). The absolute value of the points does not provide a tangible quantity, whereas it provides a chance of comparison between components. Standard Eco-indicator values are available for materials, production process, transport process, energy generation process and disposal scenarios. The impact assessment with respect to several impact categories are shown below in Table 6.13.

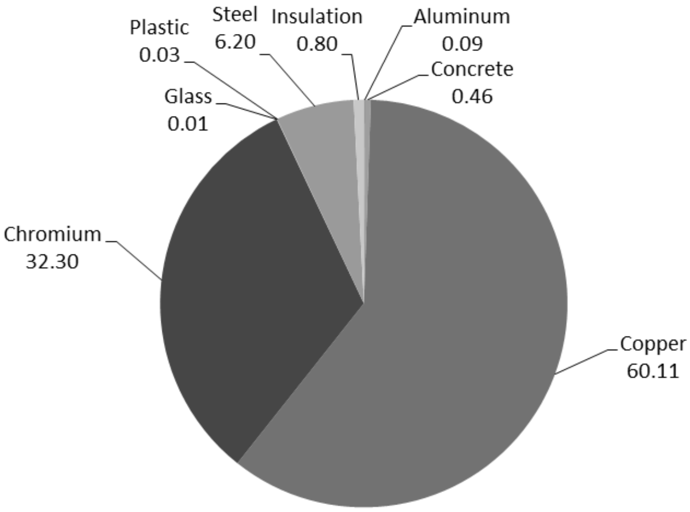

**Figure 6.62** Energy consumption for the raw material production of the solar power tower sub-system

**Table 6.13** Emissions associated with raw-material production and energy consumption for each impact[1]

| **Impact Category** | **Value [millipoints]** |
|---|---|
| Greenhouse Effect | 1.01E+03 |
| Acidification | 1.51E+02 |
| Eutrophication (air) | 7.46E+01 |
| Eutrophication (water) | 6.04E-02 |
| Stratospheric Ozone Depletion | 6.36E-02 |
| Carcinogenesis | 1.02E+01 |
| Winter Smog | 1.79E+01 |
| Summer Smog | 1.85E+00 |
| Solid Waste | 0.00E+00 |
| Heavy Metals (air) | 2.04E+01 |
| Heavy Metals (water) | 3.78E+00 |

[1] Data taken from [137]

In addition, there are also environmental impacts associated with the integrated seawater reverse osmosis desalination system. The energy requirements of this desalination system are satisfied only with the solar tower in the system. Thus, the environmental impact associated with the operation stage is taken to be virtually zero to not double count this impact. However, the plant still has environmental impact based on its assembly stage, which accounts for the extraction of the materials used in the production, transportation and assembly. In seawater reverse osmosis desalination plants, this generally accounts for 1.5% of the total environmental impact. Moreover, since the membranes are assumed to be changed every 5 years, this also accounts for the 0.9% of the total environmental impact [139]. Based on the data gathered from the literature, the environmental impact value associated with the studied plant with respect to Eco-indicator 99 is determined to be 847.5 points.

# Chapter 7: Conclusions and Recommendations

In this chapter two main sections are presented as conclusions where there is a summary of the work and its main findings and recommnedations where some recommendations are made for future studies to guide researchers who want to perform further works.

## 7.1 Conclusions

Tri-generation systems offer a promising alternative to traditional single and co-generation systems. In this study, an experimental investigation of gasification is presented and two integrated tri-generation systems are proposed. In the first system, (System 1) solar thermal energy is utilizied to obtain power, hot water and desalinated water. In the second system, (System 2) coal and biomass are gasified to obtain power, hot water and fuel through Fischer-Tropsch synthesis. The new experimental data offers essential insights into the gasification reactions and provides a more realistic approach for calculating the overall energy and exergy efficiencies of System 2. The following concluding remarks are drawn from this thesis study:

- If coal is combusted in a conventional power plant, it creates challenges due to sulfur compounds and carbon dioxide emissions. Straw's sulfur content is about 40 times less than Konya-Ilgın coal.
- If tri-generation is adopted instead of implementing single generation of power in System 1, the overall energy efficiency increases from 21.72% to 69.38%, where the overall exergy efficiency will increase from 33.76% to 70.64%. System 1 requires a larger physical area due to the large size of the heliostats. On the other hand, solar energy is widely available and has no additional costs such as fossil fuels. Seawater containing less salt is preferable for desalinattion due to lower energy needs for pressurizing the seawater to overcome the osmotic pressure requirements of the reverse osmosis membrane. An increase in solar irradiation from 0.7 kW/m$^2$ to 1 kW/m$^2$ increases the overall system energy efficiency by 4% and exergy efficiency by 3.5%. Also, when the dead-

state temperature decreases from 30°C to 20°C, the overall energy efficiency increases by 1% and the overall exergy efficiency inceases by approximately 4%. This means that low-temperature and high solar irradiation receiving places will exhibit larger exergy efficiencies.

- System 1 has the advantage of being operational in countries with no coal reserves. Naturally, if the local solar irradiation is greater, more power can be generated. For a country that has low-grade and high-sulfur content coals, gasification can be considered as a more environmentally benign method of utilizing its chemical energy.
- By implementing tri-generation in place of single generation of power in System 2, the overall energy efficiency increases from 33.76% to 70.64%, whereas the overall exergy efficiency increases from 42.21% to 72.54%. A smaller equivalence ratio in the gasification reaction results in higher heating values but decreasing the amount of air will result in pyrolysis, which harms the gasification reactor. Also, when the dead-state temperature decreases from 30°C to 20°C, the overall energy efficiency increases by 1% and the overall exergy efficiency inceases by approximately 2%.
- Energy and exergy efficiencies of System 2 for different feedstocks show that staw provides higher energy and exergy efficiencies (60.41% and 71.78%, respectively) compared to Konya-Ilgın coal (49.50% and 50.54%, respectively), where Tunçbilek coal holds the highest energy and exergy efficiencies (70.64% and 72.54%, respectively). Although as a feedstock straw has a lower cost, it would get stuck in the screw feeder during experiments due to its fiber content. This results in longer time spans for labour and maintenance, which also suspends the operation.
- The cost of System 1 is 2.5 million dollars higher than the 30 million dollar cost of System 2 for 5 MW of power generation. Furthermore, one of the outcomes of System 2 is a liquid fuel, which is more advantageous for residential areas with high transportation density and high fuel prices.

## 7.2 Recommendations

Further research is recommended to improve understanding of the scientific and engineering characteristics of tri-generation systems and to help develop various aspects relating to the performance and implementation of these systems. The results obtained from this thesis research also suggest several areas for future studies, as summarized below:

- In System 2, the efficiency results show that straw follows a different trend compared to coal samples analyzed and the other biomass samples presented in the literature. Different kinds of biomass samples should be investigated to provide a better understanding of the synthesis gas composition to compare the effects of feedstocks on overall energy and exergy efficiencies.
- Additional outputs such as cooling, hydrogen production, drying, and ammonia production can be integrated to both systems to further increase the energy and exergy efficiencies of the systems together with a cost analysis.
- Molten salt thermal storage in System 1 should be analyzed in a more detailed manner as it is a key component of the system.
- As a future experimental study, coal and biomass should be mixed and fed into the gasification plant together to reduce the coal input, cost and environmental impact. The results can then be used as part of a theoretical analysis.
- The first integrated system, driven by solar radiation, has a better efficiency when the solar irradiation increases. A cooling system should be integrated into this system to meet domestic cooling requirements.
- Carbon-containing wastes are promising candidates to be analyzed through various additional experiments in terms of gasification and Fischer-Tropsch synthesis.

# References

[1] Y. A. Cengel, M. A. Boles, *Thermodynamics: an engineering approach*, 6th ed. New York: McGraw-Hill, 2008.

[2] “2012 Key World Energy Energy Statistics,” Int. Energy Agency, Paris, France: Soregraph, 2012, p. 6.

[3] T.A. Boden, G. Marland, R.J. Andres, “Global, regional, and national fossil-fuel CO2 emissions,” U.S. Dept. Energy, Oak Ridge, TN, Rep., 2010.

[4] J. Conti, "International Energy Outlook 2013 with projections to 2040," US. Energy Information Administration, Washington DC, July 2013, pp. 9-12, 292.

[5] F. Birol, "Coal: A bet that could go either way?," World Energy Insight, World Energy Council, London, UK: First, pp. 20-21, 2012.

[6] L. Fauchon, "Water, energy: The same shock, the same battle," World Energy Insight, World Energy Council, London, UK: First, pp. 24-25, 2012.

[7] "World Health Statistics," World Health Org., 2013, Geneva, Switzerland, WA 900.1, pp. 108-16.

[8] C. de Albuquerque, “On the right track: good practices in realising the rights to water and sanitation,” Lisbon, Portugal, United Nations, Rep. 340 098/12, Feb. 2012.

[9] “Pre-2020 ambition: energy transformation, including scaling-up renewable energy, enhancing energy efficiency and consideration of carbon capture and storage,” Bonn, Germany, United Nations Framework Conv. Climate Change, Summary Rep., June 7, 2013, Part 2.

[10] K. Goldewijk, A. Beusen, M. de Vos, G. van Drecht “The HYDE 3.1 spatially explicit database of human induced land use change over the past 12,000 years,” *Global Ecology and Biogeography,* vol. 20, np. 1, pp. 73-86, 2011.

[11] M. Sudiro, A. Bertucco, “Production of synthetic gasoline and diesel fuel by alternative processes using natural gas and coal: Process simulation and optimization,” *Energy*, vol. 34, no. 12, pp. 2206–14, Dec. 2009.

[12] M. Asif, T. Muneer, “Energy supply, its demand and security issues for developed and emerging economies,” *Renewable and Sustainable Energy Reviews,* vol. 11, no. 7, pp. 1388-1413, Sep. 2007.

[13] M. A. Rosen, “Energy sustainability: A pragmatic approach and illustrations,” *Sustainability,* vol. 1, no: 1, pp. 55-80, Mar. 2009.

[14] Richard E. Smalley, "Future Global Energy Prosperity: The Terawatt Challenge," *Material Matters Bulletin,* vol. 30, June 2005.

[15] The promotion of cogeneration based on a useful heat demand in the internal energy market and amending Directive 92/42/EEC, European Parliament, Directive 2004/8/EC., Brussels, Belgium, Feb 11, 2004.

[16] W. B. Buescher, *Trigeneration: principles, feasibility, and energy price sensitivity*, Raleigh: North Carolina State Univ., 2011.

[17] Q. A. Acton, *Issues in engineering research and application*, 2013 ed. Atlanta, GA: Scholarly Editions, 2013.

[18] A. Thumann, *Plant engineers and managers guide to energy conservation*, Lilburn, GA: The Fairmont Press, 2010.

[19] A. Zię̨bik, K. Hoinka, *Energy systems of complex buildings: green energy and technology*, London, UK: Springer-Verlag, 2012.

[20] M. M. El-Halwagi, *Sustainable design through process integration: fundamentals and applications to industrial pollution prevention, resource conservation, and profitability enhancement*, Oxford, UK: Elsevier, 2011.

[21] S. de Oliveira, Jr., *Exergy: production, cost and renewability*, London, UK: Springer-Verlag, 2012.

[22] J. C. Sabonnadière, *Low emission power generation technologies and energy management*, London, UK: John Wiley and Sons, 2013.

[23] U. Gehmacher. (2010, Nov 2). *Coca-Cola Hellenic showcases $CO_2$ reduction success at leading European sustainability conference* [Online]. Available: http://www.coca-colahellenic.com/investorrelations/2010-11-02.

[24] F. A. Al-Sulaiman, “Thermodynamic modeling and thermoeconomic optimization of integrated trigeneration plants using organic Rankine cycles,” Ph.D. dissertation, Dept. of Mech. Eng., Univ. of Waterloo, Waterloo, ON, 2010.

[25] D. Berger, J. Sinai, L. Y. Bronicki, “Multi-heat source power plant,” U.S. Patent 2010 0242474 A1, Sep. 30, 2010.

[26] M. Carvalho, M. A. Lozano, L. M. Serra, “Multicriteria synthesis of trigeneration systems considering economic and environmental aspects,” *Appl. Energy*, vol. 91, no. 1, pp. 245-54, Mar. 2012.

[27] I. Dincer, C. Zamfirescu, *Sustainable energy systems and applications*, New York, NY: Springer, 2011.

[28] P. Mancarella, G. Chicco, “Assessment of the greenhouse gas emissions from cogeneration and trigeneration systems. Part II: Analysis techniques and application cases,” *Energy*, vol. 33, no. 3, pp. 418-30, Mar. 2008.

[29] K. J. Chua, W. M. Yang, T. Z. Wong, C. A. Ho, “Integrating renewable energy technologies to support building trigeneration-A multi-criteria analysis,” *Renewable Energy*, vol. 41, pp. 358–67, May 2012.

[30] Y. Huang, Y. D. Wang, S. Rezvani, D. R. McIlveen-Wright, M. Anderson, N. J. Hewitt, “Biomass fuelled trigeneration system in selected buildings,” *Energy Conversion and Manage.*, vol. 52, no. 6, pp. 2448-54, June 2011.

[31] Y. Dai, J. Wang, L. Gao, “Parametric optimization and comparative study of organic Rankine cycle (ORC) for low grade waste heat recovery,” *Energy Conversion and Manage.*, vol. 50, no. 3, pp. 576-82, Mar. 2009.

[32] A. Schuster, S. Karellas, E. Kakaras, H. Spliethoff, “Energetic and economic investigation of organic Rankine cycle applications,” *Appl. Thermal Eng.*, vol. 29, no.s 8-9, pp. 1809-17, June 2009.

[33] A. Schuster, S. Karellas, R. Aumann, “Efficiency optimization potential in supercritical organic Rankine cycles,” *Energy*, vol. 35, no. 2, pp. 1033-9, Feb. 2010.

[34] B. F. Tchanche, G. Lambrinos, A. Frangoudakis, G. Papadakis, “Exergy analysis of micro-organic Rankine power cycles for a small scale solar driven reverse osmosis desalination system,” *Appl. Energy*, vol. 87, no. 4, pp. 1295-1306, Apr. 2010.

[35] J. P. Roy, M. K. Mishra, A. Misra, “Parametric optimization and performance analysis of a waste heat recovery system using organic Rankine cycle,” *Energy*, vol. 35, no. 12, pp. 5049-62, Dec. 2010.

[36] R. Rayegan, Y. X. Tao, “A procedure to select working fluids for solar organic Rankine cycles (ORCs),” *Renewable Energy*, vol. 36, no. 2, pp. 659-70, Feb. 2011.

[37] E. H. Wang, H. G. Zhang, B. Y. Fan, M. G. Ouyang, Y. Zhao, Q. H. Mu, “Study of working fluid selection of organic Rankine cycle (ORC) for engine waste heat recovery,” *Energy*, vol. 36, no. 5, pp. 3406-18, May 2011.

[38] S. Quoilin, R. Aumann, A. Grill, A. Schuster, V. Lemort, H. Spliethoff, “Dynamic modeling and optimal control strategy of waste heat recovery organic Rankine cycles,” *Appl. Energy*, vol. 88, no. 6, pp. 2183-90, June 2011.

[39] J. Sun, W. Li, “Operation optimization of an organic Rankine cycle (ORC) heat recovery power plant,” *Appl. Thermal Eng.*, vol. 31, no.s 11-12, pp. 2032-41, Aug. 2011.

[40] Z. Shengjun, W. Huaixin, G. Tao, “Performance comparison and parametric optimization of sub-critical organic Rankine cycle (ORC) and transcritical power cycle system for low-temperature geothermal power generation,” *Appl. Energy*, vol. 88, no. 8, pp. 2740-54, Aug. 2011.

[41] S. Quoilin, S. Declaye, B. F. Tchanche, V. Lemort, “Thermo-economic optimization of waste heat recovery organic Rankine cycles,” *Appl. Thermal Eng.*, vol. 31, no.s 14-15, pp. 2885-93, Oct. 2011.

[42] B. F. Tchanche, G. Lambrinos, A. Frangoudakis, G. Papadakis, “Low-grade heat conversion into power using organic Rankine cycles-A review of various applications,” *Renewable and Sustainable Energy Reviews*, vol. 15, no. 8, pp. 3963-79, Oct. 2011.

[43] M. Kanoglu, A. Bolatturk, “Performance and parametric investigation of a binary geothermal power plant by exergy,” *Renewable Energy*, vol. 33, no. 11, pp. 2366-74, Nov. 2008.

[44] R. DiPippo, “Second law assessment of binary plants generating power from low-temperature geothermal fluids,” *Geothermics*, vol. 33, no. 5, pp. 565-86, Oct. 2004.

[45] J. T. McMullan, “Refrigeration and the environment-issues and strategies for the future,” *Int. J. Refrigeration*, vol. 25, no. 1, Pages 89-99, Jan. 2002.

[46] D. Y. Goswami, “Solar thermal power: Status of technologies and opportunities for research,” Proc. of 2nd ASME-ISHMT Heat and Mass Transfer Conf., McGraw Hill: New Delhi India, pp. 57-60, Dec. 1995.

[47] H .A. Ingley, R. Reed, D. Y. Goswami, “Optimization of a scroll expander applied to an ammonia/water combined cycle system for hydrogen production,” *Proc. of the ISES Solar World Congr.*, Orlando, FL, Aug. 2005.

[48] C. Zamfirescu, I. Dincer, “Thermodynamic analysis of a novel ammonia-water trilateral Rankine cycle,” *Thermochimica Acta,* vol. 477, no.s 1-2, pp. 7-15, Oct. 2008.

[49] W. R. Wagar, C. Zamfirescu, I. Dincer, “Thermodynamic performance assessment of an ammonia–water Rankine cycle for power and heat production,” *Energy Conversion and Manage.*, vol. 51, no. 12, pp. 2501-2509, Dec. 2010.

[50] K. H. Kim, C. H. Han, K. Kim, “Effects of ammonia concentration on the thermodynamic performances of ammonia–water based power cycles,” *Thermochimica Acta,* vol. 530, pp. 7-16, Feb. 2012.

[51] C. Zamfirescu, I. Dincer, “How much exergy one can obtain from incident solar radiation?,” *J. of Appl. Physics*, vol. 105, no. 4, pp. 44911-5, Feb. 2009.

[52] R. Petela, “Exergy of undiluted thermal radiation,” *Solar Energy,* vol. 74, no. 6, pp. 469-88, June 2003.

[53] A. Hepbasli, “A key review on exergetic analysis and assessment of renewable energy resources for a sustainable future,” *Renewable and Sustainable Energy Reviews,* vol. 12, no. 3, pp. 593-661, Apr. 2008.

[54] S. A. Kalogirou, “Solar thermal collectors and applications,” *Progress in Energy and Combustion Science,* vol. 30, no. 3, pp. 231-95, May 2004.

[55] A. Bejan, “Unification of three different theories concerning the ideal conversion of enclosed radiation,” *J. Solar Energy Eng.*, vol. 109, no. 1, pp. 46-51, Feb. 1987.

[56] A. Bejan, *Advanced Engineering Thermodynamics,* New York: Wiley, 2006, p. 880.

[57] P. Würfel, *Physics of Solar Cells,* Weinheim: Wiley-VCH, 2005, p. 186.

[58] A. de Vos, H. Pauwels, “Comment on a controversy between M. Castañs and S. Jeter” *Solar Energy,* vol. 33, no. 1, pp. 91-2, July 1984.

[59] C. Xu, Z. Wang, X. Li, F. Sun, “Energy and exergy analysis of solar power tower plants,” *Appl. Thermal Eng.*, vol. 31, pp. 3904-13, Dec. 2011.

[60] X. Yang, X. Yang, J. Dingc, Y. Shao Y, H. Fan, “Numerical simulation study on the heat transfer characteristics of the tube receiver of the solar thermal power tower,” *Energy,* vol. 90, no: 1, pp. 142-7, Feb. 2012.

[61] F. J. Collado, J. Guallar, “A review of optimized design layouts for solar power tower plants with campo code,” *Renewable and Sustainable Energy Reviews,* vol. 20, pp. 142-54, Apr. 2013.

[62] D. P. Cap, A. V. von Arx, “Solar desalinization plant,” U.S. Patent 2011 0048921 A1, Mar. 3, 2011.

[63] C. Fritzmann, J. Löwenberg, T. Wintgens, T. Melin, “State-of-the-art of reverse osmosis desalination,” *Desalination*, vol. 216, no.s 1-3, pp. 1-76, Oct. 2007.

[64] I. C. Karagiannis, P. G. Soldatos, “Water desalination cost literature: review and assessment,” *Desalination*, vol. 223, no.s 1-3, pp. 448-56, Mar. 2008.

[65] E. Mathioulakis, V. Belessiotis, E. Delyannis, “Desalination by using alternative energy: review and state-of-the-art,” *Desalination*, vol. 203, no.s 1-3, pp. 346-65, Feb. 2007.

[66] F. Trieb, “Concentrating solar power for seawater desalination,” in "AQUA-CSP: Executive Summary," German Aerospace Center Inst. of Tech. Thermodynamics, Stuttgart, Germany, Final Rep., Nov. 12, 2007.

[67] C. Fernández-López, A. Viedma, R. Herrero, A. S. Kaiser, “Seawater integrated desalination plant without brine discharge and powered by renewable energy systems,” *Desalination*, vol. 235, no.s 1-3, pp. 179-98, Jan. 2009.

[68] M. H. Sharqawy, J. H. Lienhard, V. S. M. Zubair, “On exergy calculations of seawater with applications in desalination systems,” *Int. J. Thermal Sciences*, vol. 50, no. 2, 187-96, Feb. 2011.

[69] B. Peñate, L. García-Rodríguez, “Current trends and future prospects in the design of seawater reverse osmosis desalination technology,” *Desalination*, vol. 284, pp. 1-8, Jan. 2012.

[70] R. Saidur, G. BoroumandJazi, S. Mekhilef, H. A. Mohammed, “A review on exergy analysis of biomass based fuels,” *Renewable and Sustainable Energy Reviews*, vol. 16, no. 2, pp. 1217-22, Feb. 2012.

[71] M. J. Prins, K. J. Ptasinski, F. J. J. G. Janssen, “From coal to biomass gasification: Comparison of thermodynamic efficiency,” *Energy*, vol. 32, no. 7, pp. 1248-59, July 2007.

[72] W. de Jong, J. Andries, K. R. G. Hein, “Coal/biomass co-gasification in a pressurized fluidized bed reactor,” *Renewable Energy*, vol. 16, no.s 1-4, pp. 1110-3, Jan.-Apr. 1999.

[73] F. Miccio, G. Ruoppolo, S. Kalisz, L. Andersen, T. J. Morgan, D. Baxter, “Combined gasification of coal and biomass in internal circulating fluidized bed,” *Fuel Process. Tech.*, vol. 95, pp. 45-54, Mar. 2012.

[74] N. Howaniec, A. Smoliński, K. Stańczyk, M. Pichlak, “Steam co-gasification of coal and biomass derived chars with synergy effect as an innovative way of hydrogen-rich gas production,” *Int. J. Hydrogen Energy*, vol. 36, no. 22, pp. 14455-63, Nov. 2011.

[75] J. F. Vélez, F. Chejne, C. F. Valdés, E. J. Emery, C. A. Londoño, “Co-gasification of Colombian coal and biomass in fluidized bed: An experimental study,” *Fuel*, vol. 88, no. 3, pp. 424-30, Mar. 2009.

[76] H. Karatas, H. Olgun, F. Akgun, “Coal and coal and calcined dolomite gasification experiments in a bubbling fluidized bed gasifier under air atmosphere,” *Fuel Process. Tech.*, vol. 106, pp. 666-72, Feb. 2013.

[77] A. Wagner, D. Becker, B. Dicke, S. Ebert, A. Regab, “International Fuel Prices 2010/2011,” Federal Ministry of Economic Cooperation and Develop. Secretariat, 7th ed., Rep., Aug. 2011.

[78] C. M. Masuku, D. Hildebrandt, D. Glasser, "The role of vapor–liquid equilibrium in Fischer–Tropsch product distribution," *Chemical Eng. Sci.*, vol. 66, no.1, pp. 6254-63, Jan. 2011.

[79] C. M. Masuku, "Interaction between reaction and phase equilibria in the Fischer–Tropsch reaction," PhD dissertation, School of Chemical and Metallurgical Eng., Univ. of the Witwatersrand, Johannesburg, South Africa, 2011.

[80] E. Iglesia, S. C. Reyes, R. J. Madon, "Transport-enhanced α-olefin readsorption pathways in Ru-catalyzed hydrocarbon synthesis," *J. Catalysis*, vol. 129, no. 1, pp. 238-56, May 1991.

[81] T. Komaya, A. T. Bell, "Estimates of rate coefficients for elementary processes occurring during Fischer–Tropsch synthesis over $Ru/TiO_2$," *J. Catalysis*, vol. 146, no. 1, pp. 237-248, Mar. 1994.

[82] X. Zhan, B. H. Davis, "Assessment of internal diffusion limitation on Fischer–Tropsch product distribution," *Appl. Catalysis A: General*, vol. 236, no.s 1-2, pp. 149-61, Sep. 2002.

[83] H. Karatas, H. Olgun, F. Akgun, F. "Experimental results of gasification of waste tire with air&$CO_2$, air&steam and steam in a bubbling fluidized bed gasifier," *Fuel Process. Tech.*, vol. 102, pp. 166-74, Oct. 2012.

[84] H. Karatas, H. Olgun, B. Engin, F. Akgun, F. "Experimental results of gasification of waste tire with air in a bubbling fluidized bed gasifier," *Fuel*, vol. 105, pp. 566-71, Mar. 2013.

[85] H. Karatas, H. Olgun F. Akgun, "Experimental results of gasification of cotton stalk and hazelnut shell in a bubbling fluidized bed gasifier under air and steam atmospheres," *Fuel*, vol. 112, pp. 494-501, Oct. 2013.

[86] D. Kunii, O. Levenspiel, *Fluidization engineering,* 2nd ed. Newton, MA: Butterworth-Heinemann, 1991.

[87] S. A. Klein, Engineering Equation Solver, F-Chart Software, version 8.904, 2011.

[88] R. Muncaster, *A-level physics,* 4th ed. Cheltenham, UK: Nelson Thornes, 1993.

[89] P. Basu, *Combustion and gasification in fluidized beds,* London, UK: Taylor and Francis, 2006.

[90] P. Hofmann, K. D. Panopoulos, L. E. Fryda, A. Schweiger, J. P. Ouweltjes, J. Karl, "Integrating biomass gasification with solid oxide fuel cells: Effect of real product gas tars, fluctuations and particulates on Ni-GDC anode," *Int. J. Hydrogen Energy,* vol. 33, no. 11, pp. 2834-44, June 2008.

[91] S. Arvelakis, H. Gehrmann, M. Beckmann, E. G. Koukios, "Agglomeration problems during fluidized bed gasification of olive-oil residue: evaluation of fractionation and leaching as pre-treatments," *Fuel,* vol. 82, no. 10, pp. 1261-70, July 2003.

[92] P. Lahijani, Z. A. Zainal, "Gasification of palm empty fruit bunch in a bubbling fluidized bed: a performance and agglomeration study," *Bioresource Tech.*, vol. 102, no. 2, pp. 2068-76, Jan. 2011.

[93] M. Bartels, W. Lin, J. Nijenhuis, F. Kapteijn, J. R. van Ommen "Agglomeration in fluidized beds at high temperatures: mechanisms, detection and prevention," *Progress in Energy and Combustion Sci.*, vol. 34, no. 5, pp. 633-66, Oct. 2008.

[94] J. Kuo, C. Lin, M. Wey, "Effect of agglomeration/defluidization on hydrogen generation during fluidized bed air gasification of modified biomass," *Int. J. Hydrogen Energy*, vol. 37, no. 2, pp. 1409-17, Jan. 2012.

[95] R. S. Dahlin, P.WanWang, N.Matt, V. Pannalal, L. Guohai, "Formation and prevention of agglomerated deposits during the gasification of high-sodium lignite," *Energy and Fuels*, vol. 20, no. 6, pp. 2465-70, Oct. 2006.

[96] A. Kosminski, D.P. Ross, J.B. Agnew, "Reactions between sodium and kaolin during gasification of a low-rank coal," *Fuel Process. Tech.*, vol. 87, no. 12, pp. 1051-62, Dec. 2006.

[97] R. S. Dahlin, J. R. Dorminey, W. W. Peng, R. F. Leonard, P. Vimalchand, "Preventing ash agglomeration during gasification of high-sodium lignite," *Energy and Fuels*, vol. 23, no. 2, pp. 785-93, Nov. 2009.

[98] S. J. Kline, F. A. McClintock, "Describing uncertainties in single-sample experiments," *Mech. Eng.*, vol. 75, no. 1, pp. 3-8, Jan. 1953.

[99] J. P. Holman, *Experimental methods for engineers*, 7th ed., New York: McGraw-Hill, 2001.

[100] E. Cetinkaya, I. Dincer, C. Zamfirescu, "Exergy analysis of three ORC systems for a low-temperature geothermal brine," Graduate Student Research Conf., Oshawa, ON, Apr. 2012.

[101] E. Cetinkaya, I. Dincer, C. Zamfirescu, "A comparative performance assessment of Kalina cycle and organic Rankine cycle (ORC)," 6th Int. Ege Energy Symp. and Exhibition, Izmir, Turkey, June 28-30, 2012.

[102] J. E. Pacheco, *Results of molten salt panel and component experiments for solar central receivers: cold fill, freeze/thaw, thermal cycling and shock, and instrumentation tests,* Albuquerque, NM: Sandia National Laboratory, 1995.

[103] I. Dincer, M. A. Rosen, Exergy: *energy, environment and sustainable development*, Oxford, UK: Elsevier, 2007.

[104] E. Arcaklıoğlu, A. Çavuşoğlu, A. Erişen, "An algorithmic approach towards finding better refrigerant substitutes of CFCs in terms of the second law of thermodynamics," *Energy Conversion and Manage.*, vol. 46, no.s 9-10, pp. 1595-1611, June 2005.

[105] R. Yumrutas, M. Kunduz, M. Kanoglu, "Exergy analysis of vapor compression refrigeration systems," *Exergy, an Int. J.*, vol. 2, no. 4. pp. 266-72, May 2002.

[106] A. Baba, A. Kaya, "Leaching characteristics of fly ash from thermal power plants of Soma and Tunçbilek, Turkey," *Environmental Monitoring and Assessment*, vol. 91, no.s 1-3, pp. 171-81, February 2004.

[107] K. Lampert, A. Ziebik, "Comparative analysis of energy requirements of $CO_2$ removal from metallurgical fuel gases," *Energy*, vol. 32, no. 4, pp. 521-7, Apr. 2007.

[108] D. Mason, “Formulas for calculating the calorific value of coal and coal chars: development, tests, and uses,” *Fuel Proces. Tech.*, vol. 7, no. 1, pp. 11-22, Jan. 1983.

[109] S. Van Loo, J. Koppejan, *The handbook of biomass combustion and co-firing*, London, UK: Earthscan, 2008.

[110] K. Kaygusuz, “Chemical exergies of some coals in Turkey,” *Energy Sources*, vol. 31, no. 4, pp. 299-307, Jan. 2009.

[111] M. Kaiho O. Yamada, “Stoichiometric Approach to the Analysis of Coal Gasification Process,” *Stoichiometry and materials science-when numbers matter,* New York: In Tech, 2012, ch. 16.

[112] R. Bain, “United States Country Report IEA Bioenergy Task 33,” U.S. Dept. of Energy, Golden, CO, DE-AC36-08GO28308, Tech. Rep., Aug. 2011.

[113] H. Sayyaadi, M. Nejatolahi, “Multi-objective optimization of a cooling tower assisted vapor compression refrigeration system,” *Int. J. Refrigeration*, vol. 34, no. 1, pp. 243-56, Jan. 2011.

[114] H. S. Hamut, “Exergy and Exergoeconomic Analyses and Optimization of Thermal Management Systems in Electric and Hybrid Electric Vehicles,” PhD disserttion, Dept. Mech. Eng., Univ. Ontario Inst. Tech., Oshawa, 2013.

[115] D. M. Goldenberg, “Future role of radiolabeled monoclonal antibodies in oncological diagnosis and therapy,” *Seminars in Nuclear Medicine*, vol. 19, no. 4, pp. 332-9, Oct. 1989.

[116] J. Holland, *Adaptation in natural and artificial systems: An introductory analysis with applications to biology, control, and artificial intelligence*, Oxford, England: Univ. Michigan Press, 1975.

[117] A. Konak, D. W. Coit, A. E. Smith, “Multi-objective optimization using genetic algorithms: a tutorial,” *Reliability Eng. and System Safety*, vol. 91, no. 9, pp. 992-1007, Sep. 2006.

[118] O. M. Ibrahim, S. A. Klein, “Thermodynamic properties of ammonia-water mixtures,” *ASHRAE Transactions*, vol. 99, no. 1, pp. 1495-1502, 1993.

[119] M. A. Eliott, *Chemistry of coal utilization*, New York City, NY: Wiley, 1981, p. 1615.

[120] R. K. Niven, “Minimization of a free-energy-like potential for non-equilibrium flow systems at steady state,” *Philosoph. Trans.Roy. Soc. B: Biological Sci.*, vol. 365, no. 1545, pp. 1323-31, May 2010.

[121] R. Rivero, M. Garfias, “Standard chemical exergy of elements updated,” *Energy*, vol. 31, no. 15, pp. 3310-26, Dec. 2006.

[122] P. J. Flory, “Molecular size distribution in linear condensation polymers,” *J. Amer. Chemical Soc.*, vol. 58, pp. 1877-85, Oct. 1936.

[123] T. J. Donnelly, I. C. Yates, C. N. Satterfield, “Analysis and prediction of product distributions of the Fischer–Tropsch synthesis,” *Energy Fuels*, vol. 2, no. 6, pp. 734-9, June 1988.

[124] J. Patzlaff, Y. Liu, C. Graffmann, J. Gaube, “Studies on product distributions of iron and cobalt catalyzed Fischer–Tropsch synthesis,” *Appl. Catalysis A: General*, vol. 186, no. 1-2, pp. 109-19, Oct. 1999.

[125] Y. Y. Ji, H. W. Xiang, J. L. Yang, Y. Y. Xu, Y. W. Li, B. Zhong, “Effect of reaction conditions on the product distribution during Fischer-Tropsch synthesis over an industrial Fe-Mn catalyst,” *Applied Catalysis A: General*, vol. 214, no. 1, pp. 77-86, June 2001.

[126] H. Kölbel, H. Roberg, "Heats of chemisorption of simultaneous adsorption on Fe catalysts for the Fischer-Tropsch synthesis. Pt. 11. reaction mechanism for the Fischer-Tropsch synthesis," (in German), *Berichte der Bunsengesellschaft für Physikalische Chemie*, vol. 81, no. 7, pp. 634-8, July 1977.

[127] V. Ponec, “Some Aspects of the Mechanism of Methanation and Fischer-Tropsch Synthesis,” *Catalysis, Reviews, Sci., and Eng.*, vol. 18, no. 1, pp. 151-71, 1978.

[128] P. A. Jacobs, D. V. Wouwe, “Selective synthesis of hydrocarbons via heterogeneous Fischer-Tropsch chemistry,” *J. Molecular Catalysis*, vol. 17, no.s 2-3, pp. 145-60, Nov.-Dec. 1982.

[129] A. Valero, “CGAM problem: definition and conventional solution”, *Energy*, vol. 19, no. 3, pp. 268-79, Mar. 1994.

[130] A. Bejan, *Entropy generation minimization: the method of thermodynamic optimization of finite-size systems and finite-time processes*, Boca Raton, FL: CRC Press, 1996.

[131] R. Turton, R. C. Bailie, W. B. Whiting, J. A. Shaeiwitz, D. Bhattacharyya, *Analysis, synthesis, and design of chemical processes*, 4th ed. Upper Saddle River, NJ: Prentice Hall, 2012.

[132] S. Sanaye, B. Niroomand, “Thermal-economic modeling and optimization of vertical ground-coupled heat pump,” *Energy Conversion and Manage.*, vol. 50, no. 4, pp. 1136-47, Apr. 2009.

[133] G. J. Kolb, “Economic evaluation of solar-only and hybrid power towers using molten-salt technology,” *Solar Energy*, vol. 62, no. 1, pp. 51-61, Jan. 1998.

[134] M. J. A. Tijmensen, A. P. C. Faaij, C. N. Hamelinck, M. R. M. Hardeveld, “Exploration of the possibilities for production of Fischer Tropsh liquids and power via biomass gasification,” *Biomass and Bioenergy*, vol. 23, no. 2, pp. 129-52, Aug. 2002.

[135] A. Faaij, R. van Ree, B. Meuleman, *Long term perspectives of biomass integrated gasification with combined cycle technology: costs efficiency and a comparison with combustion*, Utrecht: The Netherlands Agency for Energy and the Environment, 1998.

[136] H. P. Loh, J. Lyons, C. W. White, III, “Process Equipment Cost Estimation,” Nat. Energy Tech. Laboratory, U.S Dept. of Energy, Pittsburgh, PA, Final Rep., DOE/NETL-2002/1169, Jan 1, 2002.

[137] C. J. Koroneos, S. A. Piperodos, C. A. Tatatzikidis, D. C. Rovas, “Life cycle assessment of a solar thermal concentrating system,” *World Scientific and Eng. Academy and Soc.* Conf., Cantabria, Spain. Sept. 2008.

[138] M. Goedkoop, R. Spriensma, ‘The Eco-indicator 99: a damage oriented method for life cycle impact assessment,” PRé Consultants, Amersfoort, The Netherlands, Rep. June 2001, 3rd ed.

[139] R. G. Raluy, L. Serra, J. Uche, A. Valero, “Life-cycle assessment of desalination technologies integrated with energy production systems,” *Desalination*, vol. 167, pp. 445-58, Aug. 2004.

# Appendix

EES Code Written and Used for Calculating Stoichiometric Coefficients of Gasification Reaction

```
//Verification of  O_ex<=0 Fuxin Coal
epsilon=r*sigma
epsilon=y
eta=z
eta=s*sigma
delta=q*sigma
delta=1-y-z
gamma=p*sigma
gamma=0.5*m-2*O_ex+y-3*z
alpha=0.5*(1-n)+O_ex
beta=-2*O_ex+y-z
h_r=gamma*(-68.32)-delta*67.64-epsilon*94.05-eta*212.80-h_feedstock
//TUNCBILEK-OMERLER O_ex<=0
//ER=0.23
m=0.593
n=0.081
h_feedstock=-91.37
p=23.1
q=29.3
r=3.5
s=4.5

{//TUNCBILEK-OMERLER O_ex<=0
//ER=0.23
m=0.593
n=0.081
h_feedstock=-91.37
p=23.1
q=29.3
r=3.5
s=2.5
//TUNCBILEK-OMERLER O_ex<=0
//ER=0.306
m=0.593
n=0.081
h_feedstock=-91.37
p=39.06
q=25.22
r=2.27
```

```
s=3.69
//TUNCBILEK-OMERLER O_ex<=0
//ER=0.421
m=0.593
n=0.081
h_feedstock=-91.37
p=18.21
q=23.83
r=2.57
s=0.26
//TUNCBILEK-OMERLER O_ex>=0
//ER=0.46
m=0.593
n=0.081
h_feedstock=-91.37
p=14.49
q=23.9
r=13.38
s=2.88
//KONYA-ILGIN O_ex<=0
//ER=0.229
m=0.880
n=0.136
h_feedstock=-63.21
p=13.07
q=4.23
r=12.47
s=3.36
//KONYA-ILGIN O_ex<=0
//ER=0.343
m=0.880
n=0.136
h_feedstock=-63.21
p=16.84
q=4.00
r=12.64
s=3.18
//KONYA-ILGIN O_ex>=0
//ER=0.457
m=0.880
n=0.136
h_feedstock=-63.21
p=14.49
q=3.90
r=13.38
s=2.88
//BRISK-Saman O_ex>=0
//ER=0.28
m=1.022
n=0.257
```

```
h_feedstock=-78.77
p=14.2
q=11.7
r=19.3
s=7.41
//BRISK-Saman O_ex>=0
//ER=0.56
m=1.022
n=0.257
h_feedstock=-78.77
p=11
q=11.2
r=14.7
s=4.8
//BRISK-Saman O_ex>=0
//ER=0.70
m=1.022
n=0.257
h_feedstock=-78.77
p=7.57
q=10.9
r=11.1
s=3.23
//BRISK-Saman O_ex>=0
//ER=0.98
m=1.022
n=0.257
h_feedstock=-78.77
p=5.27
q=10.5
r=9.61
s=3.09
//KALE-1 O_ex<=0
//ER=0.17
m=0.836
n=0.142
h_feedstock=-77.93
p=22.2
q=18.81
r=9.69
s=3.88
//KALE-1 O_ex<=0
//ER=0.29
m=0.836
n=0.142
h_feedstock=-77.93
p=18.18
q=19.32
r=7.88
s=2.32
```

```
//KALE-1 O_ex>=0
//ER=0.4
m=0.836
n=0.142
h_feedstock=-77.93
p=15.43
q=15.91
r=13.28
s=2.43
//KALE-1 O_ex>=0
//ER=0.44
m=0.836
n=0.142
h_feedstock=-77.93
p=17.53
q=12.34
r=16
s=2.55
//Verification of  O_ex>=0 Ezhuang Coal
epsilon=r*sigma
epsilon=2*O_ex+y-x
eta=z
eta=s*sigma
delta=q*sigma
delta=1-2*O_ex-y+x-z
gamma=p*sigma
gamma=0.5*m+y-x-3*z
sigma=0.5*m-4*z+y+1
alpha=0.5*(1-n)+O_ex
beta=y-x-z
h_r=gamma*(-68.32)-delta*67.64-epsilon*94.05-eta*212.80-h_feedstock
m=0.822
n=0.083
h_feedstock=-119.02
p=16.42
q=5.83
r=28.47
s=9.48}
```

## EES Code Written and Used for Calculating Thermodynamic Properties of System 1

```
PROCEDURE molten(T0,P0,P,T:h,s,ex_molten)
h0 :=Enthalpy('Salt(60NaNO3_40KNO3)', T=T0-273.15, P=P0)
s0 :=Entropy('Salt(60NaNO3_40KNO3)', T=T0-273.15)
h := Enthalpy('Salt(60NaNO3_40KNO3)', T=T, P=P)
s := Entropy('Salt(60NaNO3_40KNO3)', T=T)
ex_molten := (h-h0)-T0*(s-s0)
END
FUNCTION ex(T0,P0,h,s)
h0 := Enthalpy(Water,T=T0-273.15,P=P0)
s0 := Entropy(Water,T=T0-273.15,P=P0)
ex := (h-h0)-T0*(s-s0)
END
FUNCTION ex_saline(T0,P0,P,T,slnty)
h0 := 0.001*SW_IntEnergy(T0-273.15,slnty)+P0*SW_Volume(T0-273.15,slnty)
s0 := 0.001*SW_Entropy(T0-273.15,slnty)
h := 0.001*SW_IntEnergy(T,slnty)+P*SW_Volume(T,slnty)
s := 0.001*SW_Entropy(T,slnty)
ex_saline := (h-h0)-T0*(s-s0)
END
To= 273.15+25
I_solar=0.70 [kW/m2]
eta_Hex=0.85
salinity=35
x=0.15
eta_pt=0.8
Po= 101.325
A_heliostat=60000*2.3*0.1
"60000 heliostats with an efficiency of 10% that have a
2.3 m2 surface area"
q_insolar=I_solar*A_heliostat
m[10]=20
T[10]=I_solar*402
"260 C is the lowest allowable limit for the EES library
function"
P[10]=P[11]
h_10=Enthalpy('Salt(60NaNO3_40KNO3)', T=T[10], P=P[10])
m[11]=m[10]
m[10]*h_10+q_insolar=m[11]*h_11
rho_salt=Density('Salt(60NaNO3_40KNO3)', T=T[11])
g=9.81
h_tower=40
P[11]=2*rho_salt*g*h_tower*0.001
"*0.001 to convert Pa into kPa"
h_11=Enthalpy('Salt(60NaNO3_40KNO3)', T=T[11], P=P[11])
P[1]=P[11]
P[2]=P[1]+670
"Alan B. Schwartz, Hamilton Sundstrand Rocketdyne &
```

```
Pratt & Whitney Rocketdyne: Molten Salt Pump Overview-Phase I, DE-FC36-
08GO18031, Program Review
Meeting with DOE, February 9 -11, 2010"
P[3]=P[2]
P[4]=P[2]
P[5]=P[2]
P[6]=P[2]
P[7]=P[2]
P[8]=P[2]
P[9]=P[11]
T[1]=T[11]-20
T[2]=T[1]+2.5
T[3]=T[2]-220
"Exit temperature of Rankine cycle boiler - will affect
mass flow rate of rankine cycle"
T[4]=T[1]
T[5]=T[4]
T[6]=T[5]-180
T_6_7=T[6]-30
T[7]*m[7]=m[6]*T_6_7+m[3]*T[3]
T[8]=T[7]-50
T[9]=T[8]+2.5
m[5]=m[4]
m[4]=m[2]*0.5
m[1]=m[11]
m[3]=m[2]
m[6]=m[4]
m[7]=m[6]+m[3]
m[8]=m[7]
m[8]=m[9]
m[8]=m[10]
CALL molten(To-273.15,Po,P[1],T[1]:h[1],s[1],ex[1])
CALL molten(To-273.15,Po,P[2],T[2]:h[2],s[2],ex[2])
CALL molten(To-273.15,Po,P[3],T[3]:h[3],s[3],ex[3])
CALL molten(To-273.15,Po,P[4],T[4]:h[4],s[4],ex[4])
CALL molten(To-273.15,Po,P[5],T[5]:h[5],s[5],ex[5])
CALL molten(To-273.15,Po,P[6],T[6]:h[6],s[6],ex[6])
CALL molten(To-273.15,Po,P[6],T_6_7:h_6_7,s_6_7,ex_6_7)
CALL molten(To-273.15,Po,P[7],T[7]:h[7],s[7],ex[7])
CALL molten(To-273.15,Po,P[8],T[8]:h[8],s[8],ex[8])
CALL molten(To-273.15,Po,P[9],T[9]:h[9],s[9],ex[9])
CALL molten(To-273.15,Po,P[10],T[10]:h[10],s[10],ex[10])
CALL molten(To-273.15,Po,P[11],T[11]:h[11],s[11],ex[11])
W_solar=m[2]*h[2]+m[4]*h[4]-m[1]*h[1]+m[9]*(h[9]-h[8])
//Steam Rankine Cycle
//m[2]*(h[2]-h[3])*eta_Hex=m[17]*(h[12]-h[17]+h[14]-h[13])
m[16]=1.257
m[16]=m[12]
m[16]=m[13]
m[16]=m[14]
```

```
m[16]=m[15]
m[16]=m[17]
T[12]=T[2]-200
P[12]=P[17]
h[12]=Enthalpy(Water,T=T[12],P=P[12])
s[12]=Entropy(Water,T=T[12],P=P[12])
P[13]*2=P[12]
h13s=Enthalpy(Water,s=s[12],P=P[13])
h[13]=Enthalpy(Water,T=T[13],P=P[13])
"T[13]"
s[13]=Entropy(Water,T=T[13],P=P[13])
m[16]*h[12]=m[16]*h[13]+W_t1a
m[16]*h[12]=m[16]*h13s+W_t1s
W_t1s*eta_pt=W_t1a
T[14]=T[12]
P[14]=P[13]
h[14]=Enthalpy(Water,T=T[14],P=P[14])
s[14]=Entropy(Water,T=T[14],P=P[14])
x16=0
"x16=0 @To=25 C and Po=101.3 kPa."
P[16]=P[15]
//T[16]=T_sat(Water,P=P[16])
T[16]=To-230.5
h[16]=Enthalpy(Water,P=P[16],T=T[16])
s[16]=Entropy(Water,P=P[16],T=T[16])
P[17]=185*P[16]
h17s=Enthalpy(Water,s=s[16],P=P[17])
h[17]=Enthalpy(Water,T=T[17],P=P[17])
"T[17]"
s[17]=Entropy(Water,T=T[17],P=P[17])
m[16]*h[16]+W_p1s=m[16]*h17s
m[16]*h[16]+W_p1a=m[16]*h[17]
W_p1a*eta_pt=W_p1s
P[15]=35
"x15=0.89 at standard dead state conditions."
h15s=Enthalpy(Water,s=s[14],P=P[15])
T[15]=T_sat(Water,P=P[15])
"T[15]"
s[15]=Entropy(Water,h=h[15],P=P[15])
m[14]*h[14]=m[15]*h[15]+W_t2a
m[14]*h[14]=m[15]*h15s+W_t2s
W_t2s*eta_pt=W_t2a
ex(To,Po,h[12],s[12])=ex[12]
ex(To,Po,h[13],s[13])=ex[13]
ex(To,Po,h[14],s[14])=ex[14]
ex(To,Po,h[15],s[15])=ex[15]
ex(To,Po,h[16],s[16])=ex[16]
ex(To,Po,h[17],s[17])=ex[17]
W_R=W_t1a+W_t2a-W_p1a
Q_R=m[2]*(h[2]-h[3])
```

```
eta_R*Q_R=W_R+m[15]*eta_Hex*(h[15]-h[16])
T_QR=T[3]+273.15
S_genR=m[15]*(s[15]-s[16])-Q_R/T_QR
Ex_dR=S_genR*To
//Ex_inR=(1-To/T_QR)*Q_R
Ex_inR=m[2]*(ex[2]-ex[3])
eta_exR*Ex_inR=W_R+(1-eta_HEx)*m[15]*(ex[15]-ex[16])
//Desalination
T[28]=To-273.15
P[28]=Po
h[28]=0.001*SW_IntEnergy(T[28],salinity)+P[28]*SW_Volume(T[28],salinity)
"To
take pressure into account, u+Pv is used for calculating enthalpy values for seawater."
s[28]=0.001*SW_Entropy(T[28],salinity)
rho_sea = SW_Density(T[28],salinity)
"rho = density   [kg/m^3]"
c=salinity/58.443*0.001*rho_sea
"Reference-desalination word file, c is in mole/L."
P_sea=c*8.314*(T[28]+273.15)
"Osmotic pressure Ps is given by van't Hoff equation as
Ps=c R T, where Ps is osmotic pressure in bar, c is ionic salt concentration of seawater
in mole / liter, R = 0.082 (
liter bar / degree mole) is the gas constant"
P[29]=2*P_sea+8.75*salinity
"delta_P is taken as 2 bars in the membrane+2 bars in
the filter"
T[29]=T[28]+0.6
h[29]=0.001*SW_IntEnergy(T[29],salinity)+P[29]*SW_Volume(T[29],salinity)
s[29]=0.001*SW_Entropy(T[29],salinity)
"Pump"
W_psln=m[28]*(h[29]-h[28])
T[30]=T[29]+2
P[30]=P[29]*0.9
"The pressure drop through the filter is assumed to be
200 kPa."
h[30]=0.001*SW_IntEnergy(T[30],salinity)+P[30]*SW_Volume(T[30],salinity)
s[30]=0.001*SW_Entropy(T[30],salinity)
P[31]=P[30]*salinity*0.055
"taken from the paper of Baltasar Penate et al."
T[31]=T[30]+2.77
"assumed that expansion results in 2.5 C cooling"
h[31]=0.001*SW_IntEnergy(T[31],salinity)+P[31]*SW_Volume(T[31],salinity)
s[31]=0.001*SW_Entropy(T[31],salinity)
m[30]*h[30]+W_ppex=m[31]*h[31]
m_total=m_saline+m_fresh
m_saline=0.8079
m_fresh=0.55
m[28]=m_total
m[29]=m_total
m[30]=m_total
```

```
m[31]=m_total
m[32]=m_total
m[33]=m_fresh
m[34]=m_fresh
m[35]=m_fresh
m[36]=m_fresh
m[37]=m_saline
m[38]=m_saline
"The calculations are made based on the assumption that the energy of pressurized
saline water is conducted to
the sea water to boost the pump. It is assumed that there is a turbine in the high
pressure side, which produces
mechanical power to rotate the pump that pressures the sea water.Pump is between
States 30-31 and turbine is
between states 37-38."
T[32]=T_6_7-293.5
P[32]=P[31]
h[32]=0.001*SW_IntEnergy(T[32],salinity)+P[32]*SW_Volume(T[32],salinity)
s[32]=0.001*SW_Entropy(T[32],salinity)
Q_slr_Hex1=m[5]*(h[5]-h[6])
Q_slr_Hex2=m[6]*(h[6]-h_6_7)
//Q_slr_Hex2*eta_Hex=m_total*(h[32]-h[31])
T[37]=T[28]+4.5
P[37]=P[31]-200
h[37]=0.001*SW_IntEnergy(T[37],salinity/0.6)+P[37]*SW_Volume(T[37],salinity/0.
6)
s[37]=0.001*SW_Entropy(T[37],salinity/0.6)
P[38]=Po
T[38]=T[37]-4.5
h[38]=0.001*SW_IntEnergy(T[38],salinity/0.6)+P[38]*SW_Volume(T[38],salinity/0.
6)
s[38]=0.001*SW_Entropy(T[38],salinity/0.6)
m[37]*h[37]=m[38]*h[38]+W_tpex
T[33]=T[31]
P[33]=Po
h[33]=Enthalpy(Water,T=T[33],P=P[33])
s[33]=Entropy(Water,T=T[33],P=P[33])
T[35]=T[6]-60
P[35]*3=P_sat(Water,T=T[35])
h[35]=Enthalpy(Water,T=T[35],P=P[35])
s[35]=Entropy(Water,T=T[35],P=P[35])
//Turbine
T[36]=T[28]
h36s=Enthalpy(Water,s=s[35],T=T[36])
h[35]=h36s+W_tds
h[35]=h[36]+W_tda
W_tds*eta_pt=W_tda
P[36]=Pressure(Water,h=h[36],T=T[36])
s[36]=Entropy(Water,h=h[36],T=T[36])
x36=Quality(Water,T=T[36],h=h[36])
```

```
//Pump
P[35]=P[34]
h34s=Enthalpy(Water,s=s[33],P=P[34])
h[33]+W_pda*0.7=h34s
h[33]+W_pda=h[34]
T[34]=Temperature(Water,h=h[34],P=P[34])
s[34]=Entropy(Water,h=h[34],P=P[34])
ex_saline(To,Po,P[28],T[28],salinity)=ex[28]
ex_saline(To,Po,P[29],T[29],salinity)=ex[29]
ex_saline(To,Po,P[30],T[30],salinity)=ex[30]
ex_saline(To,Po,P[31],T[31],salinity)=ex[31]
ex_saline(To,Po,P[32],T[32],salinity)=ex[32]
ex(To,Po,h[33],s[33])=ex[33]
ex(To,Po,h[34],s[34])=ex[34]
ex(To,Po,h[35],s[35])=ex[35]
ex(To,Po,h[36],s[36])=ex[36]
ex_saline(To,Po,P[37],T[37],salinity/0.6)=ex[37]
ex_saline(To,Po,P[38],T[38],salinity/0.6)=ex[38]
W_sln=W_tda-W_pda-W_psln+W_tpex-W_ppex
eta_sln*(Q_slr_Hex1+Q_slr_Hex2+m[28]*h[28])=(W_sln+m[36]*h[36])
S_dot_gensln=m[36]*s[36]+m[38]*s[38]-m[28]*s[28]-Q_slr_Hex1/(T[6]+273.15)-
Q_slr_Hex2/(T_6_7+273.15)
Ex_dot_dsln=S_dot_gensln*To
Ex_dot_insln=(1-To/(T[6]+273.15))*Q_slr_Hex1+(1-
To/(T_6_7+273.15))*Q_slr_Hex2
eta_exsln*Ex_dot_insln=(W_sln+m[36]*ex[36])
//Q_slr_Hex1*eta_Hex=m_fresh*(h[35]-h[34])
//ORC
CALL NH3H2O(138,To+58,x,0: T[18]+273.15,P[18],x18,h[18],s[18],u18,v18,q18)
//m[9]*(h[9]-h[10])*eta_Hex=m[19]*(h[20]-h[19])
m[18]=1.3
m[18]=m[19]
m[18]=m[20]
m[18]=m[21]
m[18]=m[27]
"Pump"
CALL NH3H2O(235,P[20],x,s[18]:
T19s+273.15,P19s,x19s,h19s,s19s,u19s,v19s,q19s)
m[18]*h[18]+W_p=m[19]*h[19]
m[18]*h[18]+W_ps=m[19]*h19s
W_ps=eta_pt*W_p
CALL NH3H2O(234,P[20],x,h[19]: T[19]+273.15,P[19],x19,h19,s[19],u19,v19,q19)
"Expander 1"
CALL NH3H2O(123,T[10]-100+273,15,x:
T[20]+273.15,P[20],x[20],h[20],s[20],u[20],v[20],q[20])
P[21]=(P[18]*P[20])^0.5
CALL NH3H2O(235,P[21],x,s[20]:
T21s+273.15,P21s,x21s,h21s,s21s,u21s,v21s,q21s)
m[20]*h[20]=m[21]*h[21]+W_e1
m[20]*h[20]=m[21]*h21s+W_e1s
```

```
eta_pt*W_e1s=W_e1
CALL NH3H2O(234,P[21],x,h[21]:
T[21]+273.15,P21,x[21],h21,s[21],u[21],v[21],q[21])
"Separator"
x[21]=(1-q[21])*x[25]+q[21]*x[22]
"At the separator, temperature and pressure of liquid and
vapor phase are assumed to be equal to that of State 21"
m[22]*x[22]+m[25]*x[25]=m[21]*x[21]
m[21]=m[25]+m[22]
CALL NH3H2O(128,T[21]+273.15,P[21],1:
T[22]+273.15,P[22],x22,h[22],s[22],u[22],v[22],q[22])
CALL NH3H2O(128,T[21]+273.15,P[21],0:
T[25]+273.15,P[25],x[25],h[25],s[25],u[25],v[25],q[25])
"Expander 2"
m[25]=m[26]
m[25]*h[25]=m[26]*h[26]+W_e2
m[25]*h[25]=m[26]*h26s+W_e2s
eta_pt*W_e2s=W_e2
CALL NH3H2O(235,P[18],x,s[25]:
T26s+273.15,P26s,x26s,h26s,s26s,u26s,v26s,q26s)
CALL NH3H2O(234,P[18],x[25],h[26]:
T[26]+273.15,P[26],x[26],h26,s[26],u[26],v[26],q[26])
m[22]=m[23]
m[22]=m[24]
"Turbine"
CALL NH3H2O(235,P[18],x[22],s[22]:
T23s+273.15,P23s,x23s,h23s,s23s,u23s,v23s,q23s)
m[22]*h[22]=m[23]*h[23]+W_tORC
m[22]*h[22]=m[23]*h23s+W_tsORC
eta_pt*W_tsORC=W_tORC
CALL NH3H2O(234,P[18],x[22],h[23]:
T[23]+273.15,P[23],x[23],h23,s[23],u[23],v[23],q[23])
CALL NH3H2O(238,P[23],x[23],0:
T[24]+273.15,P[24],x[24],h[24],s[24],u[24],v[24],q[24])
"Mixing chamber"
m[24]*h[24]+m[26]*h[26]=m[27]*h[27]
CALL NH3H2O(234,P[18],x,h[27]:
T[27]+273.15,P[27],x[27],h27,s[27],u[27],v[27],q[27])
CALL NH3H2O(123,To,Po*0.01,x:
T0main,P0main,x0main,h0main,s0main,u0main,v0main,q0main)
CALL NH3H2O(123,To,Po*0.01,x[22]:
T0top,P0top,x0top,h0top,s0top,u0top,v0top,q0top)
CALL NH3H2O(123,To,Po*0.01,x[25]:
T0btm,P0btm,x0btm,h0btm,s0btm,u0btm,v0btm,q0btm)
ex[18]=(h[18]-h0main)-To*(s[18]-s0main)
ex[19]=(h[19]-h0main)-To*(s[19]-s0main)
ex[20]=(h[20]-h0main)-To*(s[20]-s0main)
ex[21]=(h[21]-h0main)-To*(s[21]-s0main)
ex[27]=(h[27]-h0main)-To*(s[27]-s0main)
ex[22]=(h[22]-h0top)-To*(s[22]-s0top)
```

```
ex[23]=(h[23]-h0top)-To*(s[23]-s0top)
ex[24]=(h[24]-h0top)-To*(s[24]-s0top)
ex[25]=(h[25]-h0btm)-To*(s[25]-s0btm)
ex[26]=(h[26]-h0btm)-To*(s[26]-s0btm)
W_ORC=W_tORC+W_e1+W_e2-W_p
Q_ORC=m[18]*(h[20]-h[19])
eta_ORC*Q_ORC=W_ORC
Tb=T[10]+273
S_genORC=m[22]*(s[23]-s[24])+m[18]*(s[27]-s[18])-Q_ORC/Tb
Ex_dORC=S_genORC*To
Ex_inORC=m[9]*(ex[9]-ex[10])
eta_exORC*Ex_inORC=W_ORC+m[22]*eta_HEx*(ex[23]-ex[24])
//Overall
W=W_R+W_ORC+W_sln-W_solar
eta*q_insolar=W+m[36]*h[36]+eta_HEx*m[23]*(h[23]-h[24])
T_slr=2541
S_gen=m[22]*(s[23]-s[24])+m[18]*(s[27]-
s[18])+m[36]*s[36]+m[38]*s[38]+m[15]*(s[15]-s[16])-q_insolar/T_slr-m[28]*
s[28]
Ex_in=(1-To/T_slr)*q_insolar
```

EES Code Written and Used for Calculating Thermodynamic Properties of System 2

```
FUNCTION ex(T0,P0,h,s)
h0 := Enthalpy(Water,T=T0-273.15,P=P0)
s0 := Entropy(Water,T=T0-273.15,P=P0)
ex := (h-h0)-T0*(s-s0)
END
FUNCTION ex_air(T0,P0,h,s)
h0 := Enthalpy(Air_ha,T=T0-273.15,P=P0)
s0 := Entropy(Air_ha,T=T0-273.15,P=P0)
ex_air := (h-h0)-T0*(s-s0)
END
//Variable
mr_10_7=0.5
eta_Hexg=0.85
To=298.15
Po=101.3
eta_pt=0.8
eta_HEx=0.85
x=0.15
r_H2CO=1.97
m[1]=1.11
T[1]=To-273.15
P[1]=Po+50
h[1]=Enthalpy(Nitrogen,T=T[1],P=P[1])
s[1]=Entropy(Nitrogen,T=T[1],P=P[1])
ex[1]=h[1]-Enthalpy(Nitrogen,T=To,P=Po)-To*(s[1]-Entropy(Nitrogen,T=To,P=Po))
m[2]=1.73+m[6]
T[2]=To-273.15
P[2]=Po+50
h[2]=GCV_daf+Enthalpy(Water,T=T[2],P=P[2])
s[2]=s_daf+Entropy(Water,T=T[2],P=P[2])
ex[2]=ex_ch
P[3]=Po
T[3]=To-273.15
h[3]=Enthalpy(Air_ha,T=T[3],P=P[3])
s[3]=Entropy(Air_ha,T=T[3],P=P[3])
m[3]=1.623
m[4]=m[3]
P[4]=P[1]
h4s=Enthalpy(Air_ha,s=s[3],P=P[4])
m[3]*h[3]+W_bs=m[4]*h4s
m[3]*h[3]+W_ba=m[4]*h[4]
W_ba*eta_pt=W_bs
s[4]=Entropy(Air_ha,h=h[4],P=P[4])
T[4]=Temperature(Air_ha,h=h[4],P=P[4])
//Coal Properties
//s_daf in kJ/kg K
```

```
s_daf=c*(37.1653-31.4767*exp(-
0.564682*h/AA)+20.1145*o/AA+54.3111*n/AA+44.6712*s/AA)
AA=c+n
coal_daf=0.7882
moisture=0.0565
c=0.884
h=0.0437
o=0.0223
n=0.033
s=0.0170
//GCV in kJ/kg
GCV_daf=1000*(152.19*h+98.767)*(c/3+h-(o-s)/8)
//entopies in kJ/kmol converted into kJ/mol
s_O2*1000=Entropy(O2,T=To-273,P=Po)
s_CO2*1000=Entropy(CO2,T=To-273,P=Po)
s_H2O*1000=Entropy(H2O,T=To-273,P=Po)
s_SO2*1000=Entropy(SO2,T=To-273,P=Po)
s_N2*1000=Entropy(N2,T=To-273,P=Po)
//kJ/mol
ex_CO2=19.84
ex_H2O=0.956
ex_SO2=313.15
ex_N2=0.67
ex_O2=3.92
//kJ/kg
ex_ch_daf=GCV_daf-298.15*(s_daf+B*s_O2-c/12*s_CO2-0.5*h/1*s_H2O-
s/32*s_SO2-0.5*n/14*s_N2)+c/12*
ex_CO2+0.5*h/1*ex_H2O+s/32*ex_SO2+0.5*n/14*ex_N2-B*ex_H2O
B=c/12+0.25*h/1+s/32-0.5*o/16
//kJ/kg
ex_ch=coal_daf*ex_ch_daf+moisture/18*0.956
//MolarMass in kg/mol
MolarMass_coal=0.01388
ex_ch_molar=ex_ch*MolarMass_coal
T[5]=150
P[5]=P[4]
m[5]=4.463+m[6]
h[5]*(m[5]-
m[6])=0.09*Enthalpy(Hydrogen,T=T[5],P=P[5])+1.58*Enthalpy(CarbonMonoxide,T
=T[5],P=P[5])+0.3*
Enthalpy(CarbonDioxide,T=T[5],P=P[5])+0.14*Enthalpy(Methane,T=T[5],P=P[5])+2
.36*Enthalpy(Nitrogen,T=T[5],
P=P[5])
s[5]*(m[5]-
m[6])=0.09*Entropy(Hydrogen,T=T[5],P=P[5])+1.58*Entropy(CarbonMonoxide,T=
T[5],P=P[5])+0.3*
Entropy(CarbonDioxide,T=T[5],P=P[5])+0.14*Entropy(Methane,T=T[5],P=P[5])+2.3
6*Entropy(Nitrogen,T=T[5],P=
P[5])
m[6]=0.2
```

```
P[6]=Po
T[6]=T[5]
m[5]*h[5]-m[6]*h[6]=m[7]*h[7]
m[5]*s[5]-m[6]*s[6]=m[7]*s[7]
"Ash composition is approximated as 62%SiO2, 21% Al2O3, 11% Fe2O3, 6% MgO
[Alper Baba, Abidin Kaya, '
Leaching Characteristics of Fly Ash from Thermal Power Plants of Soma and
Tunçbilek, Turkey' Environmental
Monitoring and Assessment, February 2004, Volume 91, Issue 1-3, pp 171-181]."
T[7]=50
P[7]=P[5]
m[7]=m[5]-m[6]
h[7]*m[7]=0.09*Enthalpy(Hydrogen,T=T[7],P=P[7])+1.58*Enthalpy(CarbonMonoxi
de,T=T[7],P=P[7])+0.3*Enthalpy(
CarbonDioxide,T=T[7],P=P[7])+0.14*Enthalpy(Methane,T=T[7],P=P[7])+2.36*Enth
alpy(Nitrogen,T=T[7],P=P[7])
s[7]*m[7]=0.09*Entropy(Hydrogen,T=T[7],P=P[7])+1.58*Entropy(CarbonMonoxide,
T=T[7],P=P[7])+0.3*Entropy(
CarbonDioxide,T=T[7],P=P[7])+0.14*Entropy(Methane,T=T[7],P=P[7])+2.36*Entro
py(Nitrogen,T=T[7],P=P[7])
m[8]=m[7]
P[8]=2250
h7=Enthalpy(Air_ha,T=T[7],P=P[7])
s7=Entropy(Air_ha,T=T[7],P=P[7])
h8=Enthalpy(Air_ha,T=T[8],P=P[8])
h8s=Enthalpy(Air_ha,s=s7,P=P[8])
m[7]*h7+W_compa=m[8]*h8
m[7]*h7+W_comps=m[8]*h8s
W_comps=W_compa*eta_pt
h[8]*m[8]=0.09*Enthalpy(Hydrogen,T=T[8],P=P[8])+1.58*Enthalpy(CarbonMonoxi
de,T=T[8],P=P[8])+0.3*Enthalpy(
CarbonDioxide,T=T[8],P=P[8])+0.14*Enthalpy(Methane,T=T[8],P=P[8])+2.36*Enth
alpy(Nitrogen,T=T[8],P=P[8])
s[8]*m[8]=0.09*Entropy(Hydrogen,T=T[8],P=P[8])+1.58*Entropy(CarbonMonoxide,
T=T[8],P=P[8])+0.3*Entropy(
CarbonDioxide,T=T[8],P=P[8])+0.14*Entropy(Methane,T=T[8],P=P[8])+2.36*Entro
py(Nitrogen,T=T[8],P=P[8])
m[9]=m[8]
T[9]=T[8]
P[9]=P[8]
h[9]*m[9]=0.09*Enthalpy(Hydrogen,T=T[9],P=P[9])+1.58*Enthalpy(CarbonMonoxi
de,T=T[9],P=P[9])+0.3*Enthalpy(
CarbonDioxide,T=T[9],P=P[9])+0.14*Enthalpy(Methane,T=T[9],P=P[9])+2.36*Enth
alpy(Nitrogen,T=T[9],P=P[9])
s[9]*m[9]=0.09*Entropy(Hydrogen,T=T[9],P=P[9])+1.58*Entropy(CarbonMonoxide,
T=T[9],P=P[9])+0.3*Entropy(
CarbonDioxide,T=T[9],P=P[9])+0.14*Entropy(Methane,T=T[9],P=P[9])+2.36*Entro
py(Nitrogen,T=T[9],P=P[9])
n_O2need=0.5*(44.59*mr_10_7)+0.5*(56.56*mr_10_7)+2*(8.68*mr_10_7)
m_O2need=32*n_O2need
```

```
m_N2air=n_O2need*79/21*28
m[11]*1000=m_O2need+m_N2air
//Brayton Cycle
P[10]=P[9]
T[10]=100
m[10]=m[7]*mr_10_7
h[10]=h[9]
s[10]=s[9]
m[15]=m[11]+m[10]
m[11]=m[12]
m[11]=m[13]
m[11]=m[14]
m[15]=m[16]
m[15]=m[17]
m[15]=m[18]
m[15]=m[19]
T[15]=To+501.85
T[17]=T[15]
P[11]=138.6
T[11]=To-273.15
h[11]=Enthalpy(Air_ha,T=T[11],P=P[11])
s[11]=Entropy(Air_ha,T=T[11],P=P[11])
rp=((T[15]+273.15)/(T[11]+273.15))^(k/(2*(k-1)))
cp*2=Cp(Air,T=T[11])+Cp(Air,T=T[15])
cv*2=Cv(Air,T=T[11])+Cv(Air,T=T[15])
k=cp/cv
P[12]=P[11]*rp
h12s=Enthalpy(Air_ha,s=s[11],P=P[12])
m[11]*h[11]+W_c1s=m[12]*h12s
m[11]*h[11]+W_c1a=m[12]*h[12]
W_c1a*eta_pt=W_c1s
T[12]=Temperature(Air_ha,h=h[12],P=P[12])
s[12]=Entropy(Air_ha,h=h[12],P=P[12])
P[13]=P[12]
T[13]=T[11]
h[13]=Enthalpy(Air_ha,T=T[13],P=P[13])
s[13]=Entropy(Air_ha,T=T[13],P=P[13])
P[14]=P[13]*rp
h14s=Enthalpy(Air_ha,s=s[13],P=P[14])
m[13]*h[13]+W_c2s=m[14]*h14s
m[13]*h[13]+W_c2a=m[14]*h[14]
W_c2a*eta_pt=W_c2s
T[14]=Temperature(Air_ha,h=h[14],P=P[14])
s[14]=Entropy(Air_ha,h=h[14],P=P[14])
P[15]=P[14]
h[15]=Enthalpy(Air_ha,T=T[15],P=P[15])
s[15]=Entropy(Air_ha,T=T[15],P=P[15])
P[16]*rp=P[15]
h16s=Enthalpy(Air_ha,s=s[15],P=P[16])
m[15]*h[15]=m[16]*h16s+W_t1s
```

```
m[15]*h[15]=m[16]*h[16]+W_t1a
W_t1s*eta_pt=W_t1a
T[16]=Temperature(Air_ha,h=h[16],P=P[16])
s[16]=Entropy(Air_ha,h=h[16],P=P[16])
P[17]=P[16]
h[17]=Enthalpy(Air_ha,T=T[17],P=P[17])
s[17]=Entropy(Air_ha,T=T[17],P=P[17])
P[18]*rp=P[17]
h18s=Enthalpy(Air_ha,s=s[17],P=P[18])
m[17]*h[17]=m[18]*h18s+W_t2s
m[17]*h[17]=m[18]*h[18]+W_t2a
W_t2s*eta_pt=W_t2a
T[18]=Temperature(Air_ha,h=h[18],P=P[18])
s[18]=Entropy(Air_ha,h=h[18],P=P[18])
P[19]=P[18]
T[19]=T[18]-200
h[19]=Enthalpy(Air_ha,T=T[19],P=P[19])
s[19]=Entropy(Air_ha,h=h[19],P=P[19])
W_B=W_t1a+W_t2a-W_c1a-W_c2a
W_B=eta_B*(m[10]*LHV_syn+m[16]*(h[17]-h[16]))
T_B=T[15]+273
W_B=eta_exB*((m[10]*LHV_syn*(1-To/T_B))+m[16]*(h[17]-h[16])*(1-
To/(T[18]+273)))
//Steam Rankine Cycle
m[20]=0.20
m[20]=m[21]
m[20]=m[22]
m[20]=m[23]
//T[20]=T_sat(Water,P=P[20])
P[20]=75
T[20]=To-230.5
h[20]=Enthalpy(Water,P=P[20],T=T[20])
s[20]=Entropy(Water,P=P[20],T=T[20])
P[21]=3000
h21s=Enthalpy(Water,s=s[20],P=P[21])
T[21]=Temperature(Water,h=h[21],P=P[21])
s[21]=Entropy(Water,T=T[21],P=P[21])
m[20]*h[20]+W_p1s=m[21]*h21s
m[20]*h[20]+W_p1a=m[21]*h[21]
W_p1a*eta_pt=W_p1s
m[18]*(h[18]-h[19])*eta_Hexg=m[20]*(h[22]-h[21])
P[22]=P[21]
h[22]=Enthalpy(Water,P=P[22],T=T[22])
s[22]=Entropy(Water,P=P[22],T=T[22])
P[23]=P[20]
h23s=Enthalpy(Water,P=P[23],s=s[22])
m[22]*h[22]=m[23]*h23s+W_tr1s
m[22]*h[22]=m[23]*h[23]+W_tr1a
W_tr1a=W_tr1s*eta_pt
T[23]=Temperature(Water,P=P[23],h=h[23])
```

```
s[23]=Entropy(Water,P=P[23],h=h[23])
W_R=W_tr1a-W_p1a
Q_R=m[18]*(h[18]-h[19])
eta_R*Q_R=W_R
T_BR=T[22]+273
eta_exR*Q_R*(1-To/T_BR)=W_R
//Molar Calculation
H2_in=44.59*(1-mr_10_7)
CO_in=56.56*(1-mr_10_7)
CO2_in=6.76*(1-mr_10_7)
CH4=8.68*(1-mr_10_7)
N2=84.14*(1-mr_10_7)
H2_out=H2_in+H2_rxn
CO_out=CO_in-CO_rxn
H2_rxn=CO_rxn
H2_out=r_H2CO*CO_out
h[24]=h[9]
s[24]=s[9]
m[24]=m[9]*(1-mr_10_7)
P[24]=P[9]
T[24]=T[9]
//25
m_H2=0.001*MolarMass(H2)*H2_out
m_CO=0.001*MolarMass(CO)*CO_out
CO2_out=CO2_in+CO_rxn
m_CO2=0.001*MolarMass(CO2)*CO2_out
m_CH4=0.001*MolarMass(CH4)*CH4
m_N2=0.001*MolarMass(N2)*N2
m[25]=m_H2+m_CO+m_CO2+m_CH4+m_N2
CO_rxn=H2O
h[25]*m[25]=m_H2*Enthalpy(Hydrogen,T=T[25],P=P[25])+m_CO*Enthalpy(Carbo
nMonoxide,T=T[25],P=P[25])+
m_CO2*Enthalpy(CarbonDioxide,T=T[25],P=P[25])+m_CH4*Enthalpy(Methane,T=
T[25],P=P[25])+m_N2*Enthalpy(
Nitrogen,T=T[25],P=P[25])
s[25]*m[25]=m_H2*Entropy(Hydrogen,T=T[25],P=P[25])+m_CO*Entropy(Carbon
Monoxide,T=T[25],P=P[25])+m_CO2*Entropy(CarbonDioxide,T=T[25],P=P[25])+m
_CH4*Entropy(Methane,T=T[25],P=P[25])+m_N2*Entropy(Nitrogen,T=T[25],P=P[2
5])
T[25]=210
P[25]=2250
m_H2O=0.001*MolarMass(H2O)*H2O
delta_h=Enthalpy(Water,T=T[25],P=P[25])-Enthalpy(Water,T=To-273.15,P=P[25])
m[25]*h[25]-m[26]*1.773*eta_Hexg=m[26]*h[26]
"Q_steam is in kJ"
Q_steam=m_H2O*delta_h
m[26]=m[25]
T[26]=To
P[26]=Po
m[26]*1.773*eta_Hexg=m[27]*(h[27]-h[29])
```

```
T[27]=T[26]-20
x[27]=1
h[27]=Enthalpy(Water,x=x[27],T=T[27])
s[27]=Entropy(Water,x=x[27],T=T[27])
P[27]=P_sat(Water,T=T[27])
ex[26]=1273
h[25]*ex[26]=h[26]*ex[25]
ex[24]=ex[25]-Q_steam/To
ex[24]=ex[8]
ex[24]=ex[9]
ex[24]=ex[10]
ex[7]=ex[8]-(h[8]-h[7])
ex[5]=ex[7]-ex[6]
ex[6]=h[6]/To
T[28]=T[26]-15
x[28]=0
h[28]=Enthalpy(Water,x=x[28],T=T[28])
s[28]=Entropy(Water,x=x[28],T=T[28])
P[28]=P[27]
m[28]=m[27]
m[28]=m[29]
P[29]=P[28]*1.2
h29s=Enthalpy(Water,P=P[29],s=s[28])
T[29]=Temperature(Water,P=P[29],h=h[29])
s[29]=Entropy(Water,h=h[29],P=P[29])
m[28]*h[28]+W_lps=m[29]*h29s
m[28]*h[28]+W_lpa=m[29]*h[29]
W_lpa*eta_pt=W_lps
LHV_syn=5500
eta_FT*(m[24]*LHV_syn)=m[26]*h[26]
eta_exFT*(m[24]*LHV_syn)*(1-To/(T[24]+273))=m[26]*ex[26]
{Enthalpy [kJ/kg product]
r_H2CO=1.011.819561777
r_H2CO=1.971.773077514
r_H2CO=2.371.695898647
r_H2CO=2.741.542081966}
//ORC
CALL NH3H2O(123,To+58,9,x: T[30]+273.15,P[30],x30,h[30],s[30],u30,v30,q30)
//m[30]=1.3"to be changed"
m[30]=m[31]
m[30]=m[32]
m[30]=m[33]
m[30]=m[39]
"Expander 1"
CALL NH3H2O(123,T[27]-100+273,27,x:
T[32]+273.15,P[32],x[32],h[32],s[32],u[32],v[32],q[32])
P[33]=(P[30]*P[32])^0.5
CALL NH3H2O(235,P[33],x,s[32]:
T33s+273.15,P33s,x33s,h33s,s33s,u33s,v33s,q33s)
m[32]*h[32]=m[33]*h[33]+W_e1
```

```
m[32]*h[32]=m[33]*h33s+W_e1s
eta_pt*W_e1s=W_e1
CALL NH3H2O(234,P[33],x,h[33]:
T[33]+273.15,P33,x[33],h33,s[33],u[33],v[33],q[33])
"Pump"
CALL NH3H2O(235,P[32],x,s[30]:
T31s+273.15,P31s,x31s,h31s,s31s,u31s,v31s,q31s)
m[30]*h[30]+W_ps=m[31]*h31s
W_ps=eta_pt*W_p
m[30]*h[30]+W_p=m[31]*h[31]
CALL NH3H2O(234,P[32],x,h[31]: T[31]+273.15,P[31],x31,h31,s[31],u31,v31,q31)
m[27]*(h[27]-h[28])*eta_Hex=m[31]*(h[32]-h[31])
"Separator"
x[33]=(1-q[33])*x[37]+q[33]*x[34]
"At the separator, temperature and pressure of liquid and
vapor phase are assumed to be equal to that of State 33"
m[34]*x[34]+m[37]*x[37]=m[33]*x[33]
m[33]=m[37]+m[34]
CALL NH3H2O(128,T[33]+273.15,P[33],1:
T[34]+273.15,P[34],x34,h[34],s[34],u[34],v[34],q[34])
CALL NH3H2O(128,T[33]+273.15,P[33],0:
T[37]+273.15,P[37],x[37],h[37],s[37],u[37],v[37],q[37])
"Expander 2"
m[37]=m[38]
m[37]*h[37]=m[38]*h[38]+W_e2
m[37]*h[37]=m[38]*h38s+W_e2s
eta_pt*W_e2s=W_e2
CALL NH3H2O(235,P[30],x,s[37]:
T38s+273.15,P38s,x38s,h38s,s38s,u38s,v38s,q38s)
CALL NH3H2O(234,P[30],x[37],h[38]:
T[38]+273.15,P[38],x[38],h38,s[38],u[38],v[38],q[38])
m[34]=m[35]
m[34]=m[36]
"Turbine"
CALL NH3H2O(235,P[30],x[34],s[34]:
T35s+273.15,P35s,x35s,h35s,s35s,u35s,v35s,q35s)
m[34]*h[34]=m[35]*h[35]+W_tORC
m[34]*h[34]=m[35]*h35s+W_tsORC
eta_pt*W_tsORC=W_tORC
CALL NH3H2O(234,P[30],x[34],h[35]:
T[35]+273.15,P[35],x[35],h35,s[35],u[35],v[35],q[35])
CALL NH3H2O(238,P[35],x[35],0:
T[36]+273.15,P[36],x[36],h[36],s[36],u[36],v[36],q[36])
"Mixing chamber"
m[36]*h[36]+m[38]*h[38]=m[39]*h[39]
CALL NH3H2O(234,P[30],x,h[39]:
T[39]+393.15,P[39],x[39],h39,s[39],u[39],v[39],q[39])
CALL NH3H2O(123,To,Po*0.01,x:
T0main,P0main,x0main,h0main,s0main,u0main,v0main,q0main)
```

```
CALL NH3H2O(123,To,Po*0.01,x[34]:
T0top,P0top,x0top,h0top,s0top,u0top,v0top,q0top)
CALL NH3H2O(123,To,Po*0.01,x[37]:
T0btm,P0btm,x0btm,h0btm,s0btm,u0btm,v0btm,q0btm)
ex[30]=(h[30]-h0main)-To*(s[30]-s0main)
ex[31]=(h[31]-h0main)-To*(s[31]-s0main)
ex[32]=(h[32]-h0main)-To*(s[32]-s0main)
ex[33]=(h[33]-h0main)-To*(s[33]-s0main)
ex[39]=(h[39]-h0main)-To*(s[39]-s0main)
ex[34]=(h[34]-h0top)-To*(s[34]-s0top)
ex[35]=(h[35]-h0top)-To*(s[35]-s0top)
ex[36]=(h[36]-h0top)-To*(s[36]-s0top)
ex[37]=(h[37]-h0btm)-To*(s[37]-s0btm)
ex[38]=(h[38]-h0btm)-To*(s[38]-s0btm)
W_ORC=W_tORC+W_e1+W_e2-W_p
Q_ORC=m[30]*(h[32]-h[31])
eta_ORC*Q_ORC=W_ORC
Tb=T[27]+273
S_genORC=m[35]*(s[35]-s[36])+m[30]*(s[39]-s[30])-Q_ORC/Tb
Ex_dORC=S_genORC*To
Ex_inORC=m[27]*(ex[27]-ex[28])
eta_exORC*Ex_inORC=W_ORC+m[35]*eta_HEx*(ex[35]-ex[36])
ex(To,Po,h[20],s[20])=ex[20]
ex(To,Po,h[21],s[21])=ex[21]
ex(To,Po,h[22],s[22])=ex[22]
ex(To,Po,h[23],s[23])=ex[23]
ex(To,Po,h[27],s[27])=ex[27]
ex(To,Po,h[28],s[28])=ex[28]
ex(To,Po,h[29],s[29])=ex[29]
ex_air(To,Po,h[3],s[3])=ex[3]
ex_air(To,Po,h[4],s[4])=ex[4]
ex_air(To,Po,h[11],s[11])=ex[11]
ex_air(To,Po,h[12],s[12])=ex[12]
ex_air(To,Po,h[13],s[13])=ex[13]
ex_air(To,Po,h[14],s[14])=ex[14]
ex_air(To,Po,h[15],s[15])=ex[15]
ex_air(To,Po,h[16],s[16])=ex[16]
ex_air(To,Po,h[17],s[17])=ex[17]
ex_air(To,Po,h[18],s[18])=ex[18]
ex_air(To,Po,h[19],s[19])=ex[19]
eta*GCV_daf=W_B+W_R+m[26]*h[26]+W_ORC-W_compa
eta_ex*GCV_daf*(1-To/573)=W_B+W_R+m[26]*ex[26]+W_ORC-W_compa
```

## EES Code Written and Used for Calculating the FT Product Enthalpies

```
T0=298.15
{CALL NASA(F$, T: CP, H, S)
h_kJkg=H/MW}
//CH4
"
call NASA('CH4',T0:cp,h,s)
call NASA('C(gr)',T0:cp1,h1,s1)
call NASA('H2',T0:cp2,h2,s2)
dG0=h-h1-2*h2-T0*(s-s1-2*s2)
ex1=410.27*1000
ex2=236.12*1000
1000*ex=dG0+ex1+2*ex2
MW=MolarMass(CH4)"
//C3H8
"
call NASA('C3H8',T0:cp,h,s)
call NASA('C(gr)',T0:cp1,h1,s1)
call NASA('H2',T0:cp2,h2,s2)
dG0=h-3*h1-4*h2-T0*(s-3*s1-4*s2)
ex1=410.27*1000
ex2=236.12*1000
1000*ex=dG0+3*ex1+4*ex2
MW=MolarMass(C3H8)"
//C8H18
"
call NASA('C8H18,isooctane',T0:cp,h,s)
call NASA('C(gr)',T0:cp1,h1,s1)
call NASA('H2',T0:cp2,h2,s2)
dG0=h-8*h1-9*h2-T0*(s-8*s1-9*s2)
ex1=410.27*1000
ex2=236.12*1000
1000*ex=dG0+8*ex1+18*ex2
MW=MolarMass(C8H18,isooctane)"
//C4H10
"
call NASA('C4H10,n-butane',T0:cp,h,s)
call NASA('C(gr)',T0:cp1,h1,s1)
call NASA('H2',T0:cp2,h2,s2)
dG0=h-4*h1-5*h2-T0*(s-4*s1-5*s2)
ex1=410.27*1000
ex2=236.12*1000
1000*ex=dG0+4*ex1+5*ex2
MW=MolarMass(C4H10,n-butane)"
//C3H6
"
call NASA('C3H6,propylene',T0:cp,h,s)
call NASA('C(gr)',T0:cp1,h1,s1)
```

```
call NASA('H2',T0:cp2,h2,s2)
dG0=h-3*h1-3*h2-T0*(s-3*s1-3*s2)
ex1=410.27*1000
ex2=236.12*1000
1000*ex=dG0+3*ex1+3*ex2
MW=MolarMass(C3H6,propylene)"
//C4H8
"
call NASA('C4H8,1-butene',T0:cp,h,s)
call NASA('C(gr)',T0:cp1,h1,s1)
call NASA('H2',T0:cp2,h2,s2)
dG0=h-4*h1-4*h2-T0*(s-4*s1-4*s2)
ex1=410.27*1000
ex2=236.12*1000
1000*ex=dG0+4*ex1+4*ex2
MW=MolarMass('C4H8,1-butene')"
//C5H10
"
call NASA('C5H10,1-pentene',T0:cp,h,s)
call NASA('C(gr)',T0:cp1,h1,s1)
call NASA('H2',T0:cp2,h2,s2)
dG0=h-5*h1-5*h2-T0*(s-5*s1-5*s2)
ex1=410.27*1000
ex2=236.12*1000
1000*ex=dG0+5*ex1+5*ex2
MW=MolarMass('C5H10,1-pentene')"
//C6H12
"
call NASA('C6H12,1-hexene',T0:cp,h,s)
call NASA('C(gr)',T0:cp1,h1,s1)
call NASA('H2',T0:cp2,h2,s2)
dG0=h-6*h1-6*h2-T0*(s-6*s1-6*s2)
ex1=410.27*1000
ex2=236.12*1000
1000*ex=dG0+6*ex1+6*ex2
MW=MolarMass('C6H12,1-hexene')"
//C7H14
"
call NASA('C7H14,1-heptene',T0:cp,h,s)
call NASA('C(gr)',T0:cp1,h1,s1)
call NASA('H2',T0:cp2,h2,s2)
dG0=h-7*h1-7*h2-T0*(s-7*s1-7*s2)
ex1=410.27*1000
ex2=236.12*1000
1000*ex=dG0+7*ex1+7*ex2
MW=MolarMass('C7H14,1-heptene')"
//C8H16
"
call NASA('C8H16,1-octene',T0:cp,h,s)
call NASA('C(gr)',T0:cp1,h1,s1)
```

```
call NASA('H2',T0:cp2,h2,s2)
dG0=h-8*h1-8*h2-T0*(s-8*s1-8*s2)
ex1=410.27*1000
ex2=236.12*1000
1000*ex=dG0+8*ex1+8*ex2
MW=MolarMass('C8H16,1-octene')"
//C2H6
"
call NASA('C2H6',T0:cp,h,s)
call NASA('C(gr)',T0:cp1,h1,s1)
call NASA('H2',T0:cp2,h2,s2)
dG0=h-2*h1-3*h2-T0*(s-2*s1-3*s2)
ex1=410.27*1000
ex2=236.12*1000
1000*ex=dG0+2*ex1+3*ex2
MW=MolarMass('C2H6')"
//C5H12
"
call NASA('C5H12,n-pentane',T0:cp,h,s)
call NASA('C(gr)',T0:cp1,h1,s1)
call NASA('H2',T0:cp2,h2,s2)
dG0=h-5*h1-6*h2-T0*(s-5*s1-6*s2)
ex1=410.27*1000
ex2=236.12*1000
1000*ex=dG0+5*ex1+6*ex2
MW=MolarMass('C5H12,n-pentane')"
//C6H14
"
call NASA('C6H14,n-hexane',T0:cp,h,s)
call NASA('C(gr)',T0:cp1,h1,s1)
call NASA('H2',T0:cp2,h2,s2)
dG0=h-6*h1-7*h2-T0*(s-6*s1-7*s2)
ex1=410.27*1000
ex2=236.12*1000
1000*ex=dG0+6*ex1+7*ex2
MW=MolarMass('C6H14,n-hexane')"
//C7H14
"
call NASA('C7H16,n-heptane',T0:cp,h,s)
call NASA('C(gr)',T0:cp1,h1,s1)
call NASA('H2',T0:cp2,h2,s2)
dG0=h-7*h1-8*h2-T0*(s-7*s1-8*s2)
ex1=410.27*1000
ex2=236.12*1000
1000*ex=dG0+7*ex1+8*ex2
MW=MolarMass('C7H16,n-heptane')"
```